3-1-2013

Investigation of the intermediate and high end initial mass function as probed by near-infrared selected stellar clusters

Christine Trombley

INVESTIGATION OF THE INTERMEDIATE AND HIGH END INITIAL MASS FUNCTION AS PROBED BY NEAR-INFRARED SELECTED STELLAR CLUSTERS

By

Christine M. Trombley

A dissertation submitted in partial fulfillment of the requirements for the degree of Ph.D. in Astrophysical Sciences and Technology, in the College of Science, Rochester Institute of Technology

March 2013

Approved by _____

Prof. Andrew Robinson Date

Director, Astrophysical Sciences and Technology

ASTROPHYSICAL SCIENCES AND TECHNOLOGY

COLLEGE OF SCIENCE

ROCHESTER INSTITUTE OF TECHNOLOGY

ROCHESTER, NEW YORK

CERTIFICATE OF APPROVAL

Ph.D. DEGREE DISSERTATION

The Ph.D. Degree Dissertation of Christine M. Trombley has been examined and approved by the dissertation committee as satisfactory for the dissertation requirement for the Ph.D. degree in Astrophysical Sciences and Technology.

Dr. Donald F. Figer, Thesis Advisor

Dr. Karl Hirschman, Committee Chair

Dr. Judith L. Pipher

Dr. Michael Richmond

Date_____

Abstract

Young stellar clusters serve as powerful natural laboratories for studying the intermediate to high mass end of the initial mass function. The purpose of this dissertation is to measure the slope of the stellar initial mass function (IMF) over the intermediate to high mass range. Previous measurements are consistent with a "canonical" value over this mass regime, though the young massive star population in the Galactic Center may have a "top-heavy" distribution. In order to probe the IMF in stellar clusters that are preferentially more distant and more massive than the majority previously studied in the literature, the cluster sample is drawn from catalogs of infrared-selected candidates. Hubble Space Telescope near-infrared imaging is used to select the most promising candidates for young, massive stellar clusters. Follow-up near-infrared spectroscopy from two telescopes, covering the northern and southern latitudes, is used to identify the main sequence population and confirm a young age. The IMF is inferred from mass-magnitude relations using Geneva stellar evolutionary models. The slope at the intermediate to high mass range is measured for the completeness-corrected, background subtracted data. Deviations from the canonical IMF slope are discussed. No strong evidence in support of or against a stellar upper mass limit is found. The slope of the intermediate to high end slope of the IMF, as probed by the near-IR selected stellar clusters in this sample, is determined here to be Gamma (Γ)=-1.22, to within 0.31 dex, similar to the canonical value of -1.35.

Contents

1. Introduction

While not the primary source of mass in the universe, stars are the dominant source of visible light. Though the majority are unresolved, stars populate the galaxies observed by astronomers in the local and high-redshift universe. Stars are "building blocks" of galaxies. They form in clusters (Lada & Lada 2003) and disperse into the galactic field. Some star formation sites produce tightly bound clusters, such as the young super-star clusters observed in interacting galaxies (e.g. the Antennae, Whitmore et al. 1999). These super star clusters are thought to be modern precursors to old globular clusters. In external galaxies, individual stars cannot be resolved, requiring a study of the integrated light properties in order to fully understand these star-forming regions. These unresolved stellar populations must be modeled using population synthesis techniques, which in turn require basic assumptions regarding age (or age range), metallicity, and stellar mass distribution. While age and metallicity can be derived from integrated spectra, no method to derive a mass distribution based solely on integrated properties exists.

The frequency distribution of stellar masses, dN/dlogM (where dN in the number of stars in a given mass range dlogM), in local, resolved populations is often described as a log-log power law, $\xi(M)$ proportional to $M^{-\alpha}$. This distribution is known as the initial mass function (IMF). Practically speaking, the IMF represents the inferred mass distribution of stars in a star formation event. The *initial* distribution of mass in a star forming event is rarely observed, rather the present-day distribution is observed and mapped back to an initial distribution. The IMF appears to be an essentially universal power law above 1 solar mass ($M_{\odot}$) (Salpeter 1955, Kroupa 2002, Massey 2003, Bastian et al. 2010). The IMF plays a large role in extragalactic astrophysics, as the functional form of the IMF is required for calculating the expected baryonic mass-to-light ratio in an unresolved population. The choice of IMF and star formation history is also used to predict the number of stellar remnants present in a given population, e.g. globular clusters, the Galactic center region.

Massive star formation remains a theoretical challenge (Zinnecker & Yorke 2007) that can be probed by the high mass end of the IMF. If the properties of the star-forming environment are essential in determining the resulting mass spectrum, then the IMF should display some trend with environmental parameter(s). However, this is in direct contradiction to observations of a putative universal power law distribution. Comparing the slope of the IMF among multiple young massive clusters directly tests the claimed universality of the slope. Any significant deviations from the average IMF slope can then be assessed in terms of environment, e.g. Galactic location or metallicity.

This thesis presents a study of the slope of the initial mass function over the intermediate to high mass range for a sample of young, massive stellar clusters. Background topics relevant to this study are briefly

reviewed, followed by a description of the relevant observations, data reduction, and analysis. The results for individual clusters are discussed in the context of deviations from the median slope of the sample as a whole. The thesis concludes with suggestions for future work in this field.

1.1. The Initial Mass Function

The first initial mass function constructed by Salpeter (1955) in his seminal work, "The Luminosity Function and Stellar Evolution", takes the form of the "original mass function,"

$$dN = \xi \, \mathrm{M} \, \mathrm{d} \, log_{10} \, \mathrm{M} \, \frac{\mathrm{dt}}{T_0}$$

Equation 1 Salpeter's Initial Mass Function

$$\xi \, \mathrm{M} \sim 0.03 \, \left(\frac{M}{M_{solar}} \right)^{-1.35}$$

Equation 2 Observationally derived mass function

where M is the mass in $M_\odot$, dN is the number of stars in a given mass interval, dt is the time interval, and T_0 is the main sequence lifetime. Salpeter (1995) finds that, observationally, ξ(M) is well described by Equation 2 with a slope of -1.35, traditionally known as Gamma, Γ. Values of Γ that are more negative than -1.35 are said to be steep or bottom-heavy, as these values will predict fewer massive stars and greater numbers of low-mass stars than the Salpeter value. Alternately, values of Γ that are higher than -1.35 (i.e. less negative) are flat or top-heavy. Through this work, values of Γ that are higher than the Salpeter Γ of -1.35 are also referred to as "shallow" IMF slopes.

Surprisingly, the results of Salpeter (1955) seem to hold true for a number of other studies, over a large mass regime. The low-mass IMF has a shallower slope, before turning over (changing sign) at a characteristic mass before the lower mass cutoff (set by the limit of hydrogen burning), as displayed graphically in Figure 1. The sub-stellar and sub-solar IMFs are not addressed here, but see reviews by Bastian et al. (2010) and Kroupa (2005) for a more comprehensive review of those topics.

While the Salpeter mass function is a single power law over the range 0.8 to 10 $M_\odot$, the Kroupa IMF (Kroupa 2001) is a three-part power law:

$$\xi(\mathbf{m}) = \mathbf{A}\begin{cases} \left(\frac{m}{m_1}\right)^{-\alpha_0}, m_0 < m \leq m_1, n = 0 \\ \left(\frac{m}{m_1}\right)^{-\alpha_1}, m_1 < m \leq m_2, n = 1 \\ \left[\prod_{i=2}^{n\geq 2}\left(\frac{m_i}{m_{i-1}}\right)^{-\alpha_{i-1}}\right]\left(\frac{m}{m_n}\right)^{-\alpha_n}, m_n < m \leq m_{n+1}, n \geq 2 \end{cases}$$

Equation 3 Kroupa IMF

where A is the normalization and the values of α are determined by the following relations:

$$\alpha_0 = +0.3 \pm 0.7\,, 0.01 \leq \frac{m}{Msolar} < 0.08\,, n = 0$$

$$\alpha_1 = +1.3 \pm 0.5\,, 0.08 \leq \frac{m}{Msolar} < 0.50\,, n = 1$$

$$\alpha_2 = +2.3 \pm 0.7\,, 0.50 \leq \frac{m}{Msolar} \leq 150\,, n = 2$$

Equation 4 Kroupa IMF exponents

The Scalo index (Scalo 1998) goes as α_3=2.7+/-0.7 for 1<m/$M_\odot$, n=3, which is consistent within errors of the Salpeter slope of α=2.35 and the Kroupa slope α_2=2.3 (recall α=Γ+1, and note that in Equation 3 α is taken to be a positive value with the negative built into the equation itself) and the results of Kroupa (2001).

Bastian et al. (2010) suggest that an 8-parameter IMF is required to properly characterize the important points of the IMF, duplicated here in Figure 1. These authors identify four primary parameters (characteristic or mean mass, dispersion or sigma as it is labeled in Figure 1, power law slope, and break point or turn-over between "high" and "low" mass regimes) of the IMF. Additionally, Bastian et al. (2010) recommend that a lower and upper mass cut-off are required (parameters 5 and 8), along with a low mass break point (where the distribution changes from a log-normal function to a power-law, parameter 6) and the low-mass power law slope (parameter 7). Both the upper and lower mass limits are debated in the literature; should the IMF describe objects other than stars, such as brown dwarfs or planets? What is the most massive star that can form? The high mass limit is discussed in detail below.

The primary concerns of this study are parameters 4 and 5 as labeled in Figure 1, the high mass slope and upper mass limit respectively.

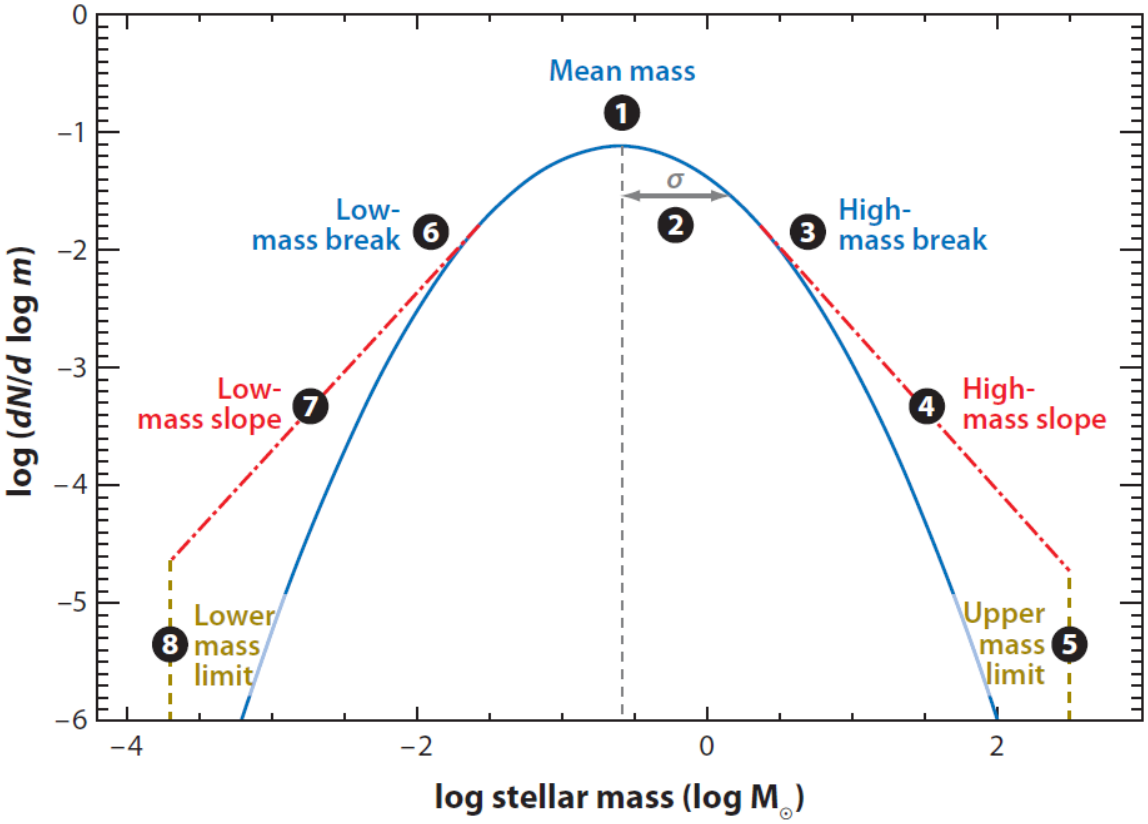

Figure 1 Eight-Parameter IMF from Bastian et al. (2010)

The field-star IMF, the inferred mass distribution of stars in a dispersed population, e.g. the solar neighborhood, is difficult to construct at the high mass regime. Massive stars are rare, short-lived, and seldom found beyond their birthplaces. Estimates suggest 25-30% of O stars are found outside of stellar clusters (Oey et al. 2004) but only 4% of this population of massive stars does not consist of runaway stars ejected from their parent cluster (de Wit et al. 2004, 2005). Additionally, the exact ages of intermediate to moderately high mass stars (B-type stars, 3-20 $M_{\odot}$) are difficult to determine. The main sequence (MS) lifetimes of B stars range up to 100 Myr. Generally, the field star IMF is found to be steeper than the IMF in star clusters (i.e. steeper than Salpeter) at intermediate to high mass ranges (Bastian et al. 2010). Assumptions regarding the star formation history of the parent population (e.g. the Galactic disk, the SMC) are required to produce an *initial* mass function for the observed field population. Another complication is computing the distance to stars in the field, a process which is subject to large errors.

Coeval populations of stars existing at the same spatial location provide for a far more straightforward measurement of the IMF. Such populations are found in stellar clusters and OB associations throughout the Milky Way and Magellanic Clouds. While OB associations have larger ages and age spreads, young massive stellar clusters have small age spreads (typically 1 Myr, though error on the age determination can be larger than 1 Myr). Single-age models are able to accurately represent the stellar populations in stellar clusters and most OB associations.

The slope of the IMF has been measured for several Galactic clusters and OB associations through direct counts (Kroupa 2002, references therein), but rarely for clusters massive enough to fully sample the high end of the mass spectrum (e.g. >10 $M_{\odot}$). Figure 2, taken from Bastian et al. (2010), illustrates this point. Though the data contained in this plot do not represent every IMF slope measurement available in the literature, the data are representative of the literature. Therefore the relative lack of measurements at the high mass regime remains evident. Comparing the slope of the IMF of several young, massive star clusters can directly test the claimed universality of the IMF for the sample examined. The larger the sample, the more statistical weight that can be placed on the results. Statistically significant deviations from the average in the measured slopes can be examined in the context of external environment, e.g. metallicity, Galactic location.

As higher spatial resolution imaging became available, improvements in the measurement of the slope of the IMF across all mass ranges have been made. Larger telescopes allow for faster collection of the same signal-to-noise ratio observations, reducing the integration time required for photometry. Shorter integration time allows for additional telescope pointings, making large-field-of-view studies feasible. Massey et al. (1995b) made the first measurement of the IMF in the Cyg OB2 association, finding a slope of -0.9 using UBV photometry from the Kitt Peak 0.9 meter telescope. Knodlseder (2000) uses 2MASS near-IR (JHK) photometry (1.3 meter telescope) to derive a slope of -1.6+/-0.1 for Cyg OB2. More recently, Wright & Drake (2009) use a combination of 2MASS, IPHAS (INT Photometric Halpha Survey, Drew et al. 2005, 2.54 meter telescope), UKIDSS (United Kingdom Infrared Deep Sky Survey, Lucas et al. 2008, 3.8 meter telescope,), and targeted Chandra X-ray observations to derive a slope of -1.27+/-0.16. Additionally, these authors find evidence for mass segregation in the form of a steepening of the IMF away from the center of the association.

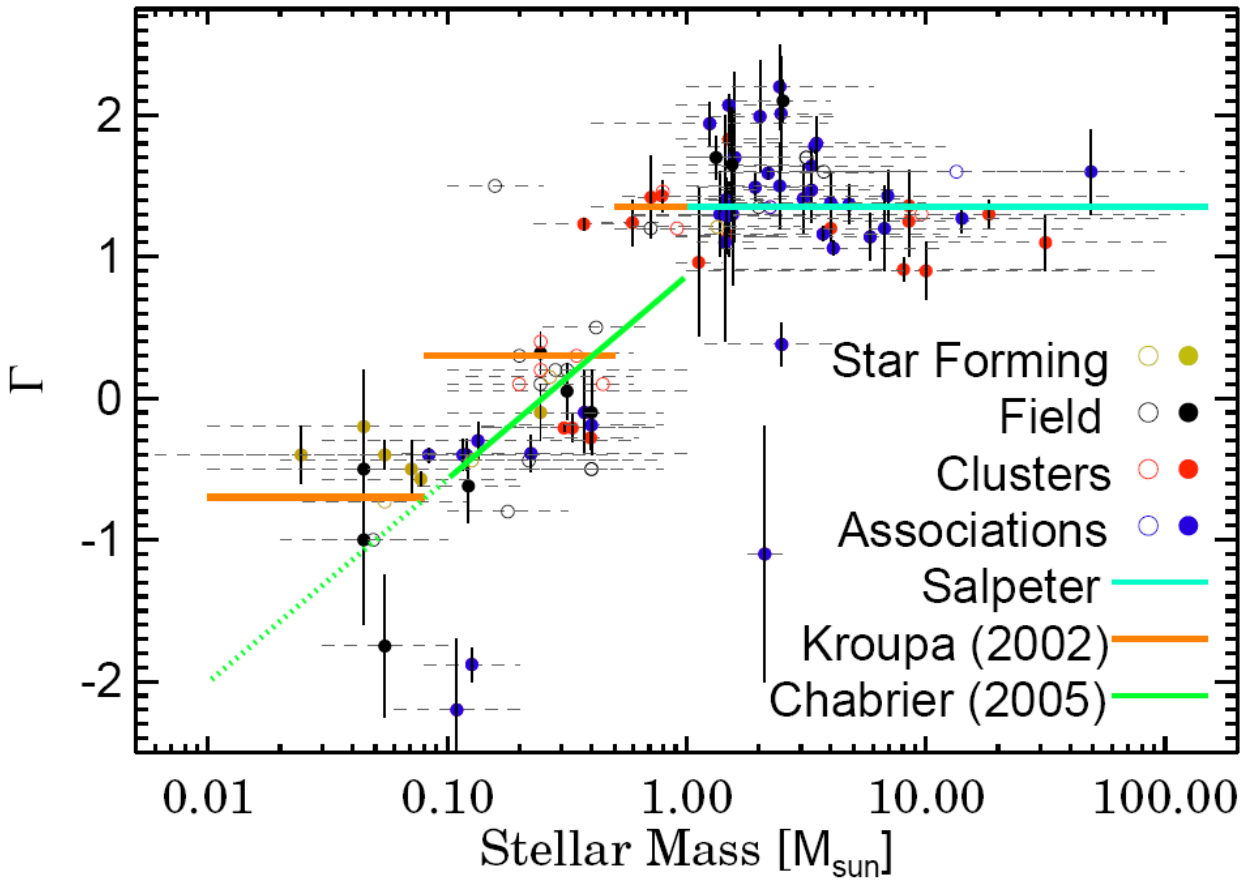

Figure 2 Selection of estimates of the IMF slope as a function of mass range, taken from Bastian et al. (2010)

A very careful definition of the term "initial mass function" is required to understand the goals and results of the investigation presented here. The IMF is defined as the inferred mass distribution of stars produced in a star formation event. Rarely is the *initial* distribution observed; instead the present-day population is observed. The IMF is then inferred from the present-day population.

To construct an IMF for a sample of clusters, evolutionary models are applied to infrared photometry. The photometry is calibrated via spectroscopic observations, which are used to determine luminosity class and distance. The evolved massive star population is used to constrain the age of individual clusters. The present-day mass of main sequence stars in each cluster is determined from magnitude-mass relations of rotating stellar evolutionary models (Maeder & Meynet 2003). From the present-day mass, the initial mass is inferred according to the same stellar evolutionary models.

The cluster age is subject to errors, as are the magnitude measurements. Though generally small, errors in each magnitude measurement propagate through the entire study, leading to errors in the distance

estimates. This is especially evident from the large distance ranges in spectrophotometric distance calculations. Errors in the distance estimate subsequently produce errors in the absolute magnitude of objects in each cluster. The absolute magnitude and infrared colors are used to determine the present day mass of each star. The present day mass is directly related to the initial mass as per the mass-loss prescriptions of the stellar evolution models. The most massive stars have high mass-loss rates (Vink et al. 2000, 2001, 2011), which leads to rapid evolution away from the zero-age main sequence (ZAMS).

1.1.1. Variations

Variations in measurements of the IMF slope can be attributed to any number of observational effects, including the effects of sample size, systematic error, presence of unresolved binaries, and field of view. Studies of the IMF in the Arches cluster show that the slope of the IMF changes with distance from the cluster center due to mass segregation. Restricted field of view limits the identification of observational evidence for mass segregation. Additional physical processes governing star formation, e.g. metallicity, Galactic location, can potentially affect the slope of the IMF.

To date, the strongest claim for a high end IMF slope significantly different from Salpeter arises from studies of the center of the Milky Way. Multiple authors (Bartko et al. 2010; Lue et al. 2013) find evidence for a flattened (larger number of massive stars than predicted by a Salpeter or Kroupa IMF slope) IMF is found in Galactic Center region. These results are consistent with X-ray studies of the Galactic Center. Nayakshin & Sunyaev 2005 find that scaling-up the X-ray population of the Orion Nebula Cluster is inconsistent with the X-ray flux of the Galactic Center.

1.1.2. Stellar Evolution Models: Past and Present

The most important assumption of the stellar evolutionary models discussed here is the singularity of stars: no binary evolution (e.g. rejuvenation due to mass transfer) is incorporated into these grids of models. For a more thorough review of the effects of binarity on the evolution of massive stars, see Langer (2012) and references therein.

Massey (1998) relies on the Geneva grid of stellar evolutionary models from 0.8 to 120 $M_{\odot}$ with convective overshooting and mass loss (Maeder & Meynet 1988) and WR models (Maeder & Meynet 1994). Schaller et al. (1992) present a new grid of models, known as “canonical mass loss” models over the same mass range. These authors use the updated opacities of Rogers & Iglesias (1991) and Kurucz (1991). Meynet et al. (1994) published a grid of “enhanced mass loss” models, with mass loss rates twice as high as the standard models. Figer (2005) uses these models to derive the masses of stars in the Arches cluster.

Broadened line profiles provide observational evidence for rotation in massive stars, which results in an enhancement of mass loss via stellar winds. The effects of rotation are thoroughly reviewed by Maeder & Meynet (2000), who go on to lead efforts to include rotation in stellar evolution models. More recently, Vink et al. (2011) calculates mass loss rates for very massive stars (up to 300 $M_{\odot}$), as an improvement upon previous work (Vink et al. 2000; Vink et al. 2001; Vink 2006). These authors emphasize the importance of rotation in stellar evolution models, calling for a "fundamental revision" in the incorporation of mass loss rates.

Calculations of rotating models have led to many important results. This includes the prediction of red supergiants at higher masses and luminosities than previously estimated from non-rotating models. Brott et al. (2011) show that stars as massive as 60 $M_{\odot}$ can pass through the red supergiant phase at LMC metallcity. Eckstrom et al. (2012) demonstrate that the enhanced mass loss rates during the red supergiant phase can result in evolution back blueward for stars with initial masses in the range 15-20 $M_{\odot}$. These stars were previously thought to end their lifetimes as red supergiants before exploding as supernova. These recent studies emphasize the importance of including the effects of rotation in stellar evolution models.

Using the most recent set of Geneva stellar evolution models, in conjunction with the stellar atmosphere model results of CMFGEN (Hillier & Miller 1998), Groh et al. (2013) predict SNe from luminous blue variable (LBVs) in the initial mass range 20-25 $M_{\odot}$. Previously, stellar evolution models did not predict an LBV phase, potentially owing to the relatively short lifetime of this phase and the inability to reproduce the eruptions that define this phenomenological phase. Crockett et al. (2008) and Georgy et al. (2012) observe type IIb supernova having LBV progenitors, but no theoretical model had predicted that LBVs explode as supernovae until Groh et al. (2013).

Maeder & Meynet (2003) published a grid of rotating and non-rotating stellar evolution models from 8 to 120 $M_{\odot}$. The present study uses these models and the models of Schaerer et al. (1993), which have canonical mass-loss rates and cover the initial mass range of for 0.8 to 8.0 $M_{\odot}$. Brott et al. (2011) present a grid of evolutionary tracks from 5 to 60 $M_{\odot}$, incorporating rotation. Extrapolating these models up to nearly three times their mass (e.g. see R136 section of Results & Discussion) is less certain than extrapolating the Geneva models to only slightly higher masses.

1.1.3. Method

This section describes the methods used to construct an IMF for stellar clusters. The basic steps to constructing an IMF are represented in Figure 3, an IMF flowchart. The strategy here is designed for two purposes: to measure the slope of the intermediate to high mass range of the IMF and to identify an upper

mass cut-off. The importance of the upper mass limit is discussed below, along with techniques for determining such a limit.

The first step in constructing an IMF for the clusters in the sample presented here (discussed in depth in IMF Analysis) is to obtain deep, high resolution near-infrared (NIR) imaging. Optical observations suffer from the heavy extinctions towards these clusters, which are preferentially more distant and extinguished than clusters in previous IMF studies. Control fields are also observed to disentangle the cluster sequence from the fore- and background population. Near-IR photometry is used to select candidate cluster members for spectroscopic follow-up on the basis of color and magnitude. Once spectra have been obtained, spectral types are obtained via qualitative spectral typing. The results are used to determine some of the basic parameters of the cluster stars, e.g. temperature, luminosity class, cluster age. The IR colors and spectral types of the cluster stars are next used to estimate the extinction and spectrophotometric distance towards the cluster.

Figure 3 indicates how stellar atmosphere models can be applied to determine the fundamental properties of evolved massive stars, e.g. temperature and bolometric luminosity. Application of stellar atmosphere models to spectra of sufficient resolution and signal-to-noise (SNR) yields information such as metallicity, mass loss rate, current mass, and effective temperature. From these parameters the initial mass can be derived based on stellar evolution models and position on the Hertsprung-Russell (HR) diagram (see Figure 3). This information is key for determining the initial masses of post-MS stars, which are often located in degenerate parameter space of magnitude-mass relations drawn from evolution models alone.

Once the extinction, distance, and age of the cluster have been established, magnitude-mass relations from stellar evolutionary models are applied to the NIR photometry to determine initial masses of cluster stars. The same process is repeated for the control field photometry. The masses are binned in log space to produce IMFs. The control field IMF is used to characterize the fore- and background population, and subtracted from the cluster IMF. For the purpose of this study, only main sequence objects are considered in the final IMF slope measurement. The upper mass cutoff can only be probed in clusters that are young enough that their most massive stars have not evolved away from the MS.

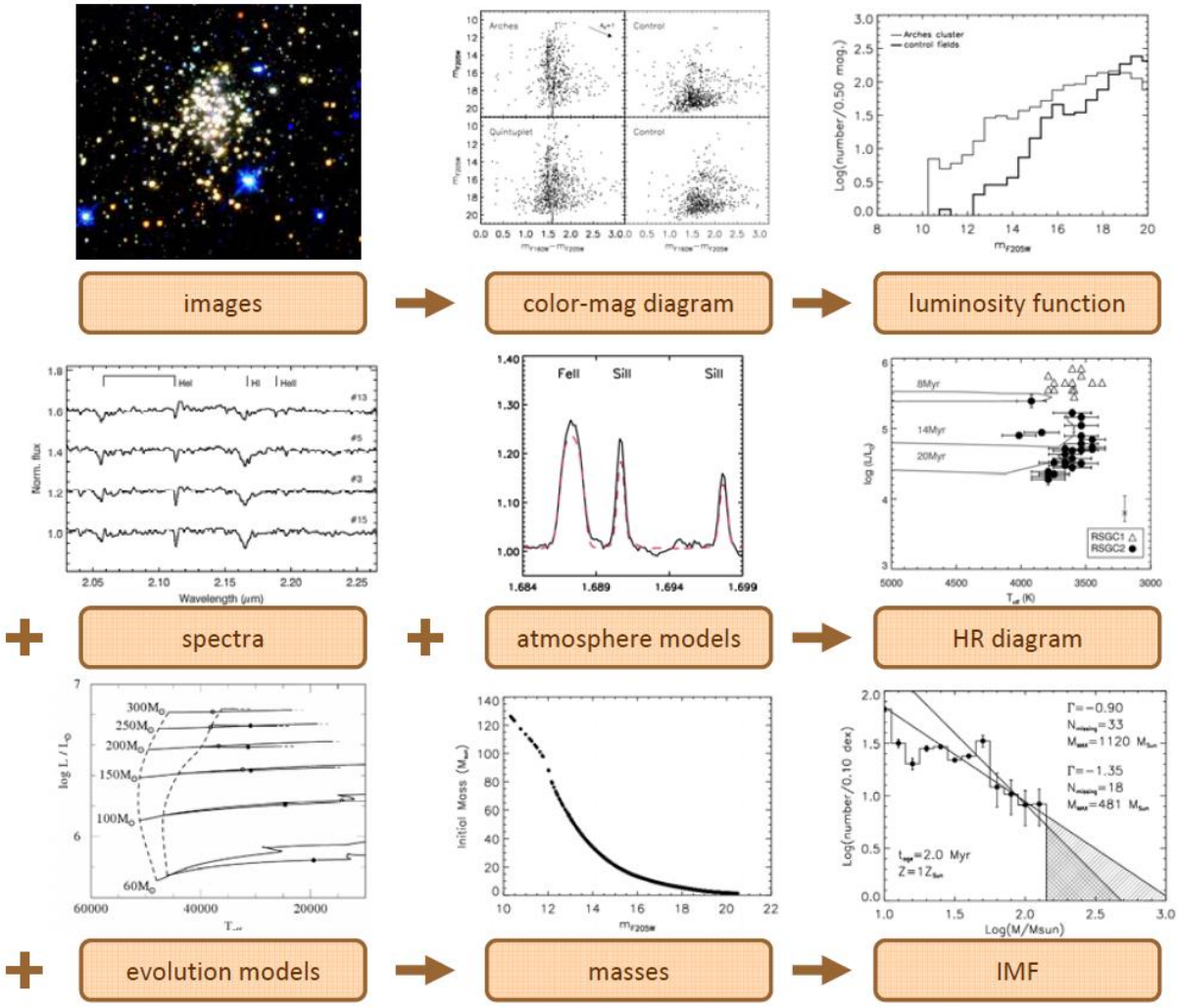

Figure 3 IMF Flowchart: from image to IMF

In the context of this work, spectroscopy is used in a purely qualitative fashion: to calibrate the MS and identify post-MS stars in each cluster. Spectral typing is accurate to +/- 1 spectral type. A quantitative analysis of this spectra is ongoing as part of an analysis of the chemical cartography of the Galaxy (de la Fuente, PhD thesis work).

1.1.4. Utilizing the IMF

Star counting methods provide a means of measuring the slope of the IMF in a given population and also serve as tool for calculating the mass of the cluster. Integrating over the mass range down to 0.8 $M_{\odot}$ (Salpeter IMF) or 0.08 $M_{\odot}$ (Kroupa IMF), yields the total mass of the population. The proportionality constant, A, must first be derived from the observed number of stars, N, over the mass range m_1 to m_2.

Once this constant is determined, the total mass of the population can be found by integrating over the mass function, Φ, from m_l to m_u, where m_l is the lower mass limit and m_u is the upper mass limit (e.g 0.8 to 150 $M_\odot$ respectively for a Salpeter-type IMF). The slope of the mass function, Γ, is either imposed or calculated from the observations at hand. The derivation is as follows:

$$N = A\int_{m_1}^{m_2}\Phi(\mathbf{m})\mathbf{dM}$$

$$N = A\int_{m_1}^{m_2}M^{\Gamma-1}dM$$

$$N = \frac{A}{\Gamma}(m_2^{\Gamma} - m_1^{\Gamma})$$

$$A = \frac{N\Gamma}{m_2^{\Gamma} - m_1^{\Gamma}}$$

$$M_{total} = A\int_{m_l}^{m_h}M\Phi(\mathbf{m})\mathbf{dM}$$

$$M_{total} = A\int_{m_l}^{m_u}M\left(M^{\Gamma-1}\right)dm$$

$$M_{total} = A\int_{m_l}^{m_u}\left(M^{\Gamma}\right)dm$$

$$M_{total} = \frac{A}{\Gamma-1}(m_u^{\Gamma+1} - m_l^{\Gamma+1})$$

Equation 5 Mass derivation

1.2. Upper Mass Cut Off

The Eddington limit (Eddington 1926) was the first theoretical limit to the upper mass of stars, based on the balance between radiation pressure and gravity (Equation 6). This balance is known as hydrostatic equilibrium. Using this relation, stars with mass m>60 $M_\odot$ exceed the theoretical limit and become unbalanced. The Eddington limit describes the theoretical case of fully radiative objects, which is not wholly applicable to massive stars which have convective cores.

$$\frac{L_{edd}}{L_{solar}} \approx 3.5\ 10^4\ m/M_{solar}$$

Equation 6

Schwarzschild & Harm (1959) determined that stars more massive than 60 $M_\odot$ should be unstable to pulsations and the outer layers of the star are destroyed. Later work by Beech & Mitalas (1994) refined the calculation of Schwarzchild & Harm (1959), suggesting that pulsational instabilities could be damped, resulting in a larger theoretical limit. Improvements in the theoretical understanding of opacities (Rogers & Iglesia 1994) led to new calculations of upper mass limits that were also dependent on metallicity (Stothers 1992). Those calculations find that stars of 90-150 $M_\odot$ remain stable against pulsations, while more massive stars are not.

Early statistical studies (e.g. Elmegreen 2000, Larson 2003) point out that random sampling of an IMF with no upper mass limit constraints predicts the existence of stars with M>1000 $M_\odot$. Super massive stars should be observed unless a previously unknown turn-down or truncation in the IMF exists beyond a few hundred $M_\odot$. The authors of these studies also emphasize that despite their predictions and the lack of observational evidence for 1000 $M_\odot$ objects[1], no upper mass limit had been observed.

Massey & Hunter (1998) find stars in R136 with masses of the order 140-155 $M_\odot$. Massey (2003) asserts that this is a statistical limit rather than a physical limit to the upper mass of stars. Figer (2005) finds stars in the Arches cluster with masses ranging up to 130-150 $M_\odot$, producing a cliff-like feature in the IMF (reproduced in Figure 4). Without an upper mass limit truncating the IMF, Figer (2005) predicts an additional 18 to 33 stars beyond the 130-150 $M_\odot$ bin with masses up to 500 $M_\odot$. Extending his analysis of the Arches cluster to R136, Figer (2005) predicts at least 20 stars in R136 with masses greater than 150 $M_\odot$, ranging up to 750 $M_\odot$. Similarly, Weidner & Kroupa (2004) find that 40 stars with M > 150 $M_\odot$ are "missing" from R136, assuming a total cluster mass of $5(10^4)$ $M_\odot$. While the VLT-FLAMES survey has identified massive runaway stars originating from R136, far fewer than 20 of these objects have been identified.

Oey & Clarke (2005) present a statistical argument for an upper mass limit of 150 $M_\odot$ based on a compilation of studies of massive stars and massive clusters in the literature. These authors assume a Salpeter-like IMF. Additionally, Koen (2006) examine the high mass regime of the IMF in R136 using

[1] R136 had been resolved into multiple point sources by this time.

two statistical methods, finding an upper mass limit of 140 to 160 $M_{\odot}$. These results are consistent with the upper mass limit of 150 $M_{\odot}$ found by Figer (2005).

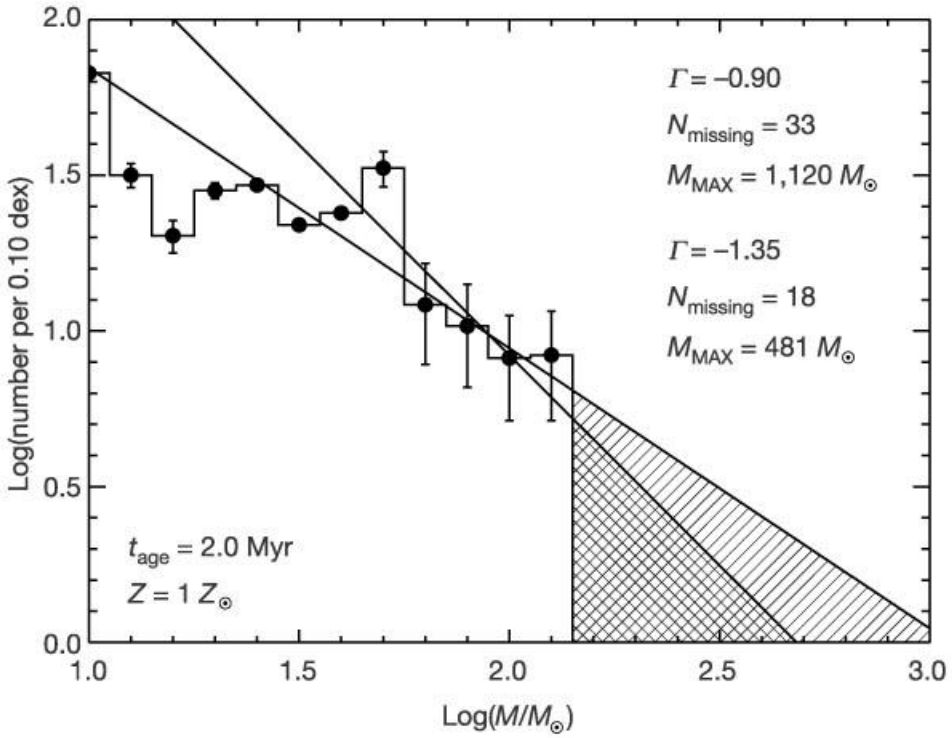

Figure 4 IMF of Arches cluster, reproduced from Figer (2005)

Crowther et al. (2010) claim to have identified stars with initial masses as high as 300 $M_{\odot}$ in R136.These authors do not present an IMF that could potentially show an upper mass cutoff, as done for the Arches cluster. They suggest that 14 stars with initial masses over 100 $M_{\odot}$ should be present in this cluster, identifying 10 objects meeting this requirement. Though they reject binarity as a possible inflating factor for their mass estimates, this cannot be exclusively ruled out (see discussion regarding R136 in Results & Discussion for greater detail). Recent N-body work suggests that very massive stars (so called "super canonical" stars) are the results of dynamical mergers of less massive stars in the centers of young, dense star clusters (Banerjee & Kroupa 2012). Youth (< 3 Myr) is a requirement based on the total lifetimes of the merged very massive stars, which would form in the first one to two Myr of the cluster's lifetime and explode as supernova (SN) within two Myr. If correct, and not the results of dynamical processes, the masses of the four stars in R136 presented by Crowther et al. (2010) require the refinement of the supposed upper mass limit to the formation of stars.

1.3. Young Massive Clusters and Candidate Clusters

Young, massive clusters (YMCs) are excellent probes of the high end of the IMF. YMCs represent coeval stellar populations. Massive star formation in stellar clusters occurs within a timescale that is less than the lifetime of the most massive stars, on the order of 1-2 Myr. Infrared-selected YMCs are preferentially more distant than their optical counterparts, probing a larger parameter space than previously available.

Over the past 15 years, pioneering work in infrared detectors has ushered in a new era of large scale IR imaging surveys. The 2 Micron All Sky Survey (2MASS, Skrutskie et al. 2006) and Galactic Legacy Infrared Mid-Plane Survey Extraordinaire (GLIMPSE, Benjamin et al. 2003) have probed the Galactic Plane as never before. 2MASS began imaging the sky from the ground in 1997, completing the survey in 2001. This all-sky survey covered the entire sky at 1.25, 1.65, and 2.17 microns. The final GLIMPSE survey spans 300 degrees of the Galaxy with IRAC onboard the Spitzer Space Telescope. GLIMPSE provided imaging at 3.6, 4.5, 5.8, and 8.0 microns. Several groups searched through these two surveys for previously undiscovered stellar clusters (Dutra & Bica 2001, Bica et al. 2003, Dutra et al. 2003, Mercer et al. 2005, Froebrich et al. 2007), yielding thousands of candidate clusters.

Froebrich et al. (2007) use star density maps constructed from 2MASS data to search for stellar overdensities in the galactic plane. Other authors, notably Duta & Bica (2001), Bica et al. (2003), and Dutra et al. (2003), perform searches by eye in the direction of optical and radio nebulae. The group led by Froebrich estimates a contamination rate of up to 50% for their candidate cluster catalog, while the latter group make no estimates of contamination. Borissova et al. (2005) follow up 21 clusters from the catalogs of Bica et al. (2003) and Dutra et al. (2003), finding 7 genuine clusters. The remaining candidate clusters are found to be chance stellar overdensities, usually a result of patchy extinction. Mercer et al. (2005) used an automated search algorithm combined with visual inspection of the GLIMPSE mid-IR survey data to find 92 new cluster candidates. This catalog has been particularly successful: resulting in the identification of two new globular clusters in the plane of the galaxy (Mercer 3, Strader & Kobulnicky 2008; Mercer 5, Longmore et al. 2011) and several young, massive clusters (Mercer 30, Kurtev et al. 2007; Mercer 20, Messineo et al. 2009; Mercer 23, Hanson et al. 2010).

Recent identification of this new, rich sample of IR-selected clusters that are preferentially more distant than clusters in previous studies has made possible an updated census of the intermediate to high mass IMF. The dataset presented here consists of candidate clusters from the lists of Bica et al. (2003), Bica & Dutra (2001), Dutra et al. (2003), Mercer et al. (2005), and has been extended to contain the Danks 1 and Danks 2 clusters. Including the cluster R136 in the heart of the 30 Doradus nebula in the Large

Magellanic Cloud (LMC) serves as a check with previous measurements and ensures that the largest mass range possible will be probed by this study. Observations of R136 are included in this work.

The sample presented here is drawn primarily from Hubble Space Telescope (HST) Near-Infrared Camera 3 (NIC3) imaging observations (P.I. Davies). The resolution of NIC3 is a large improvement on earlier imaging capabilities, such as those used in the studies of Massey et al. (1995a,b) for previous IMF determinations. Additionally, Very Large Telescope (VLT) NIR spectroscopy is available for the majority of the HST observations (VLT/ISAAC, P.I. de la Fuente), as well as Chandra X-ray Observatory (CXO) imaging for a smaller subset of the sample. Spectroscopy is used for spectral typing and CXO imaging is used to identify potential colliding wind binary systems.

A direct re-measurement of the IMF of the clusters examined by Massey et al. (1995a,b) results would be of great interest to the IMF community. However, an exact replication of the imaging and spectroscopy would be required to allow for comparisons to embedded Galactic clusters. Improved imaging, with higher resolution and sufficient photometric depth, is not available for the majority of the Massey et al. (1995a, b), Oey & Massey (1995), or Oey (1996) samples. The mass ranges probed by the previously mentioned samples are too low for a study of the high end IMF. Measuring the IMF slope above 10 $M_{\odot}$ requires the discovery of additional young, massive ($>10^4$ $M_{\odot}$) clusters. Such a population is predicted to exist (Hanson et al. 2008, Ivanov et al. 2010), but remains largely undiscovered.

This study examines newly discovered candidate stellar clusters. The goal is to provide a similar investigation of the intermediate to high mass range of the IMF as presented in Massey (1998). To achieve this goal, the slope of the IMF is computed for young, massive clusters drawn from the same set of observations. For example, HST NIR imaging provides all the photometric data presented in this work, with the exception of R136. Spectroscopy of southern objects is obtained with VLT/ISAAC and nothern objects with IRTF/SpeX.

Chapter 2 details the observations and data reduction, and Chapter 3 contains the analysis of the sample of candidate young, massive clusters.. This chapter includes analysis of both photometry and spectroscopy in order to derive parameters such as age, reddening, distance, and mass. Chapter 4 presents an analysis of the errors involved in constructing an IMF along with Monte Carlo simulations of each cluster. Construction of IMFs for the clusters in this sample is described in Chapter 5, and the results presented in Chapter 6. A discussion of the individual and sample results is also given in Chapter 6, with concluding remarks summarizing the study in Chapter7. Chapter 8 includes suggestions for future work, including improvements on the project presented here.

2. Observations

2.1. Sample of Cluster Candidates

The initial sample of candidate young, massive clusters was drawn from an archive of hundreds of candidates built by combining the catalogs of Dutra et al. (2001), Bica et al. (2003), Dutra et al. (2003), and Mercer et al. (2005). For each catalog object, a webpage was created containing a 2MASS 3-color image, a GLIMPSE 3-color image where available, and 2MASS color-magnitude diagrams (H-K vs. K and J-K vs. K) containing all point sources in the 2MASS image. As the project evolved, additional information was added to each candidate webpage where possible, e.g. HST images, HST color-magnitude diagrams, CXO observations, spectroscopic observations, and radio observations.

Before the completion of GLIMPSE-II, a Spitzer/IRAC proposal (Program 30734, PI Figer) was submitted for 76 candidate clusters which showed promise but were not covered by GLIMPSE-I. The observations were specifically designed to mimic the GLIMPSE observing strategy, in order to make the targeted fields directly comparable to GLIMPSE fields. The objects observed in this program are listed below in Table 1. There are no Mercer et al. (2005) objects in the Spizter proposal; the Mercer object list was created by examining 2MASS and GLIMPSE, both by eye and with an automated algorithm.

The "best" candidate young, massive clusters were then drawn from the Spitzer observations of Bica/Dutra clusters and the Mercer catalog. These clusters were chosen based on several criteria: stellar over density discernible by eye, signposts of youth (including the presence of natal material, in many cases a bubble or partial bubble in the surrounding ISM), IR color-magnitude diagram indicating a main sequence. HST proposal ID 11545 (PI Davies) was designed to observe 29 candidate clusters using filters F160W, F187N, F190N, and F222M with NICMOS/NIC3.

Follow-up spectroscopy was obtained to determine parameters, e.g. spectral type, of stars on the main sequence, identify evolved cluster stars, and identify fore- and background non-cluster members for each set of observations. Southern clusters in the sample were observed using VLT/ISAAC (PI la Fuente), and northern clusters were observed using IRTF/SpeX (PI Trombley). Spectra in the work presented here is plotted as flux per unit wavelength.

2.2. Spizter/IRAC Imaging: Reduction and Photometry

Table 1 Spizter/IRAC Targets

Cluster Name	RA	Dec
BDSB2003+1	18 03 41	-24 22 40
BDSB2003+14	19 40 22	+27 18 29
BDSB2003+159	20 29 24	+40 11 14
BDSB2003+16	19 55 00	+27 12 57

BDSB2003+162	2 08 05	+60 45 53
BDSB2003+18	20 01 10	+33 11 09
BDSB2003+35	22 56 17	+58 31 14
BDSB2003+37	22 59 06	+59 28 33
BDSB2003+39	23 05 11	+60 14 44
BDSB2003+48	0 15 27.7	+61 14 18
BDSB2003+49	0 58 40	+61 04 45
BDSB2003+50	1 06 45	+59 40 36
BDSB2003+51	1 08 50	+63 07 40
BDSB2003+52	1 23 06	+61 51 23
BDSB2003+53	2 28 18	+72 37 48
BDSB2003+62	4 03 50	+51 00 55
BDSB2003+63	4 07 12	+51 24 53
BDSB2003+64	4 19 33	+52 58 42
BDSB2003+65	4 11 10	+51 09 58
BDSB2003+66	4 36 50	+50 52 46
BDSB2003+74	5 38 47	+30 41 18
BDSB2003+76	6 01 55	+26 24 58
BDSB2003+77	5 50 14	+23 52 19
BDSB2003+78	6 14 23	+17 44 37
BDSB2003+82	6 14 57	+12 21 03
BDSB2003+84	6 38 28	+00 44 41
BDSB2003+90	6 59 41	-04 51 44
BDSB2003+93	6 57 15	-08 19 48
BDSB2003+94	7 00 51	-08 56 33
BDSB2003+95	7 16 33	-09 25 20
DB2001+16	20 38 29	+42 06 25
DB2001+22	20 42 33.5	+42 56 50
DB2001+23	20 45 37.6	+44 15 21
DB2001+29	6 14 45.1	+19 00 28
DB2001+3	20 4 52.9	+29 11 45
DB2001+33	6 13 21.2	+15 23 56
DB2001+34	6 13 16	+15 22 30
DB2001+35	7 08 39	-04 19 07
DB2001+37	10 45 54	-59 56 58
DB2001+5	20 21 41.8	+37 25 50
DB2001+6	20 29 36.9	+39 01 15
DB2001+8	20 31 45.4	+38 58 00
DB2001+9	20 32 27.8	+38 51 26
DBSB2003T3+10	7 35 27	-22 23 55
DBSB2003T3+106	16 54 17	-45 17 31
DBSB2003T3+109	16 47 11	-41 16 28
DBSB2003T3+110	16 56 41	-40 14 25
DBSB2003T3+113	17 00 35	-40 33 44
DBSB2003T3+114	16 59 10	-40 12 05
DBSB2003T3+17	8 20 54	-36 12 57
DBSB2003T3+18	8 22 52	-42 07 58
DBSB2003T3+22	8 53 09	-42 13 02
DBSB2003T3+23	8 48 48	-42 54 27

DBSB2003T3+26	8 46 34	-43 54 28
DBSB2003T3+28	8 56 28	-43 05 53
DBSB2003T3+33	9 01 54	-47 43 53
DBSB2003T3+35	9 15 11	-47 28 32
DBSB2003T3+36	9 16 44	-47 56 28
DBSB2003T3+37	9 22 12	-48 05 02
DBSB2003T3+38	9 24 25	-51 59 28
DBSB2003T3+4	7 32 10	-16 58 15
DBSB2003T3+44	10 15 51	-57 23 38
DBSB2003T3+45	10 19 11	-58 02 21
DBSB2003T3+48	10 31 29	-58 02 01
DBSB2003T3+54	10 43 57	-59 32 56
DBSB2003T3+59	11 12 18	-58 46 18
DBSB2003T3+60	11 05 37	-62 28 57
DBSB2003T3+67	11 30 07	-62 03 32
DBSB2003T3+7	7 35 34	-18 45 34
DBSB2003T3+74	12 10 00	-62 49 52
DBSB2003T3+75	12 09 02	-63 15 54
DBSB2003T3+76	12 22 30	-63 17 35
DBSB2003T3+8	7 35 39	-18 48 50
DBSB2003T3+87	13 32 47	-60 26 54
DBSB2003T4+125	9 59 32	-57 04 05
DBSB2003T4+126	10 06 40	-57 12 33

Spizter Program 30734 (PI Figer) was designed to mimic the GLIMPSE observing cadence, taking images in all four IRAC bands or channels, 3.6, 4.5, 5.8, and 8.0 microns, and providing a resolution of 0.6 arcseconds. Each set of IRAC basic calibrated data (bcd) was retrieved via the Leopard tool from the Spizter Science Center (SSC), then mosaicked using Mopex, also operated and maintained by SSC. Channels 1 and 2, correspondig to 3.6 and 4.5 microns respectively consisted of 20 overlapping fields, or tiles, while channels 3 and 4, 5.8 ad 8.0 micros respectively, were made up of 10 fields. In some cases, e.g. [BDS2003] 52 in Figure 5, problems in one or more header files made it necessary to mosaic the channel 4 observations by hand.

First, an empty Mopex overlap pipeline was created. This pipeline determines the overlap between fields in an observations. The pipeline run on the basic calibrated data for each channel to determine the overlap between tiles and supply an overlap correction to the mosaic pipeline. The mosaic pipeline combines the dithered images for each target. After overlap parameters were determined, an empty mosaic pipeline was opened and edited to correspond to the correct channel (e.g. channel 1, the 3.6 microns images). For all observations, the same parameters were used in creating the final mosaicked image. Cases such as [BDS2003] 52, where hand mosaicking was required, were obvious from visual inspection of the final 8

micron image. The adverse effects can be seen in Figure 5, in which the left hand panel clearly shows a misplaced tile.

Several bright non-saturated point sources were chosen as references points for mosaics made by hand. The centroid of each source in each overlapping frame was determined using GCNTRD.PRO, from the IDL Astronomy User's Library. One frame was chosen to be the reference frame, or 0^{th} position, and the remaining frames were offset as computed from the positions of the bright sources. Three bright non-saturated point sources with corresponding non-saturated point sources in channel 1 were selected for finding theastrometry solution, applied by using STARAST.PRO from the IDL Astronomy User's Library.

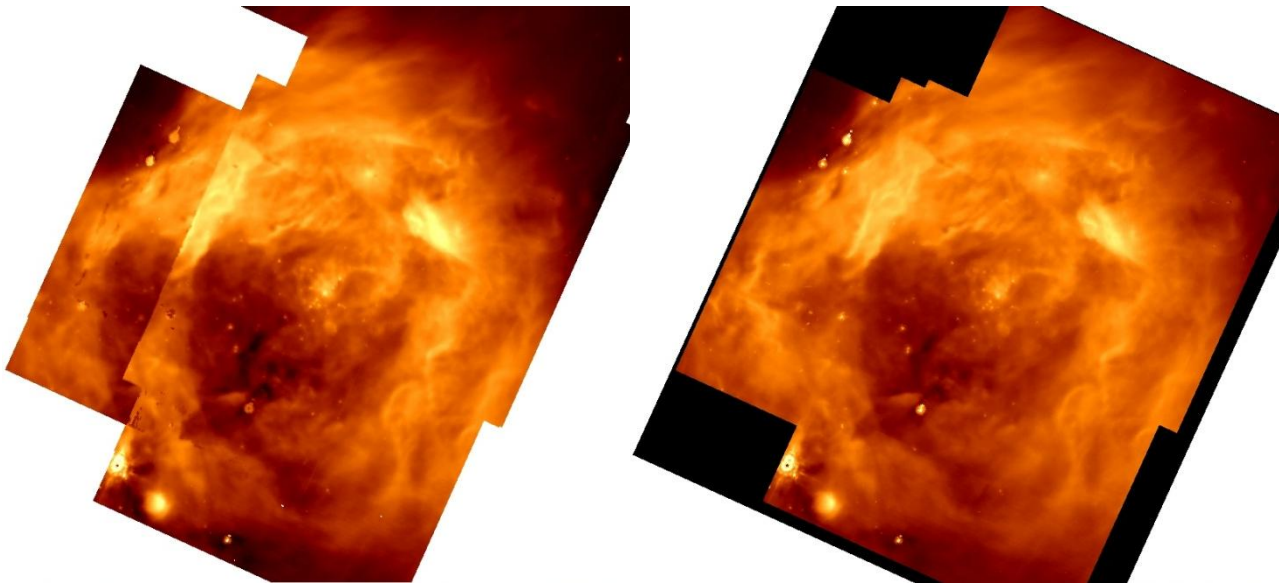

Figure 5 Left: Pipeline mosaicked image of [BDS2003] 52 Right: Hand mosaciked image of [BDS2003] 52

Photometry was performed on individual clusters for each of the four Spizter/IRAC channels, using the IDL-adapted version of DAOPHOT. Customized code was created to perform aperture photometry on any given set of observations. The zero point flux and aperture correction for each band were taken from the SSC IRAC data handbook ;the zero point flux values are also listed as photometric keywords in each header file. Bad pixels (Not a Number/no value) were identified and corrected; the majority of bad pixel issues were contained in channel 4 frames. A median sky value was found for each channel, which was used in setting the detection threshold for FIND.PRO. An aperture size of 3 arcseconds was used for photometry along with an annulus of 6 to 9 arcseconds to characterize the local background. The aperture correction for photometry in each band corresponding to this aperture and annulus size are given in the

SSC IRAC data handbook. Aperture photometry using APER.PRO was done separately on each frame, and the results cross-correlated to build a final catalog of photometry for each cluster candidate. Catalog criteria required valid photometric points in two or more channels to avoid inclusion of spurious sources. The sources in the final catalog were cross-correlated with the 2MASS Point Source catalog, and associations were made when positions of IRAC sources were within 4 arcseconds of a 2MASS source. For (rare) cases of double detections, association preference was given to the closest object.

Aperture photometry was found to be yield better results than point source function (PSF) photometry for the Spitzer/IRAC imaging. This is largely due to the diffuse emission present in nearly every band in every wavelength. The presence of bright, diffuse emission made locating isolated, bright stars for PSF characterization difficult. PSF fitting was further complicated by the diffuse emission, resulting in in poor PSF photometry.

2.3. HST/NIC3 Imaging: Reduction and Photometry

Table 2 HST/NIC3 Targets

Target	Obs Date	RA	Dec	Comments
DBSB2003T3+23	7/20/08	08 48 48.41	-42 54 27.0	
DBSB2003T3+36	7/21/08	09 16 44.46	-47 56 27.5	
DBSB2003T3+45	7/6/08	10 19 11.49	-58 02 18.6	Zhu et al. (2009)
DBSB2003T3+48	7/22/08	10 31 29.54	-58 01 59.3	
DBSB2003T3+78	7/20/08	12 36 03.42	-61 50 56.5	Nebular emission
BDSB2003+18	7/13/08	20 01 10.34	+33 11 07.4	Nebular emission
DB2001+20	7/1/08	20 38 38.01	+42 39 20.6	
BDSB2003+36	7/27/08	22 58 41.39	+58 46 53.6	
MERCER5	7/2/08	18 23 19.92	-13 40 05.9	Globular Cluster, Longmore et al. (2011)
MERCER9	7/3/08	18 34 09.90	-09 14 04.7	Messineo et al. (2009)
MERCER20	6/30/08	19 12 24.01	+09 57 04.4	Messineo et al. (2009)
MERCER23	7/11/08	19 30 13.67	+18 32 06.3	Hanson et al. (2010)
MERCER30	7/18/08	12 14 32.48	-62 58 45.7	Kurtev et al. (2007), de la Fuente et al. (in prep)
MERCER70	7/12/08	16 00 27.67	-52 10 50.4	PEL objects
MERCER14	7/1/08	18 58 06.16	+01 36 31.4	low mass; Froebrich & Ioannidis 2011
MERCER17	7/1/08	19 09 19.48	+08 11 28.0	
MERCER81	8/27/08	16 40 30.03	-46 23 36.0	Davies et al. (2012a)
DANKS1	7/14/08	13 12 26.50	-62 41 56.6	Davies et al. (2012b), CXO obs
DANKS2	7/15/08	13 12 55.95	-62 40 43.4	Davies et al. (2012b), CXO obs
BDSB2003+52	9/9/08	01 23 06.02	+61 52 23.5	CXO obs
DB2001+9	8/23/08	20 32 28.87	+38 51 24.1	PEL objects
BDSB2003+66	8/14/08	04 36 49.46	+50 52 37.1	PEL object, CXO obs

Hubble Space Telescope (HST) Near Infrared Camera 3 (NIC3) observations were taken in the summer of 2008 as part of ProgID 11545 (PI Davies). The observations were taken in a 6-position spiral dither

pattern with an offset of 5.07 arseconds and carefully reduced in order to counteract the known under-sampled PSF of the NIC3 detector. Each candidate cluster was observed in four filters: F160W, F187N, F190N, and F222M, while a near-by control field of identical size was observed only in wide band filters, F160W and F222M.

The raw data for each visit was retrieved using the Barbara A. Mikulski Archive for Space Telescopes (MAST) HST search form. Each raw image was resampled onto a finer grid, then combined using IDL routines NICMOSAIC.PRO and NICSTIKUM.PRO. The overlap parameters were determined by NICMOSAIC.PRO and the final image was combined by NICSTIKUM.PRO to produce a science-quality frame.

Photometry of point sources in each filter for both the cluster and control field was performed using a customized IDL adapted version of DAOPHOT on the final mosaicked image. The routine FIND.PRO was used to identify point sources above a given threshold before photometry was carried out using APER.PRO. A smaller aperture size than that listed in the NICMOS Instrument Handbook was used to avoid overlap in crowded regions, rendering the corresponding aperture corrections inapplicable. For this reason, aperture corrections for filters F222M and F160W were computed by hand using a bright, isolated star in the control field of [DB2001] Cl 9. Figure 6 shows the aperture size in arc seconds plotted against the total encircled F222M flux. The total flux asymptotes towards a final "true" flux value, which was then used to compute the aperture correction at each position. This is a simplification of the actual case, as can be seen in Figure 6 as a continuously – albeit slowly – rising flux. The flux from the central point source falls below the background at some radius, after which point the encircled flux only rises due to the increasing inclusion of the diffuse background. For F160W photometry, an aperture size of 0.4 arcseconds is used with a correction of 1.18193. For F222M photometry, an aperture size of 0.4 arcseconds is used with an aperture correction of 1.21692. An annulus of 1.3 to 2.0 arcseconds is used to characterizes the background contribution. These aperture corrections are higher than those suggested in the HST Data Reduction Handbook because the aperture size used for crowded field photometry is required to be smaller (due to the nature of the crowded field) than the aperture size cited in the Handbook. Photometric zero points for each filter are taken from the appropriate header file.

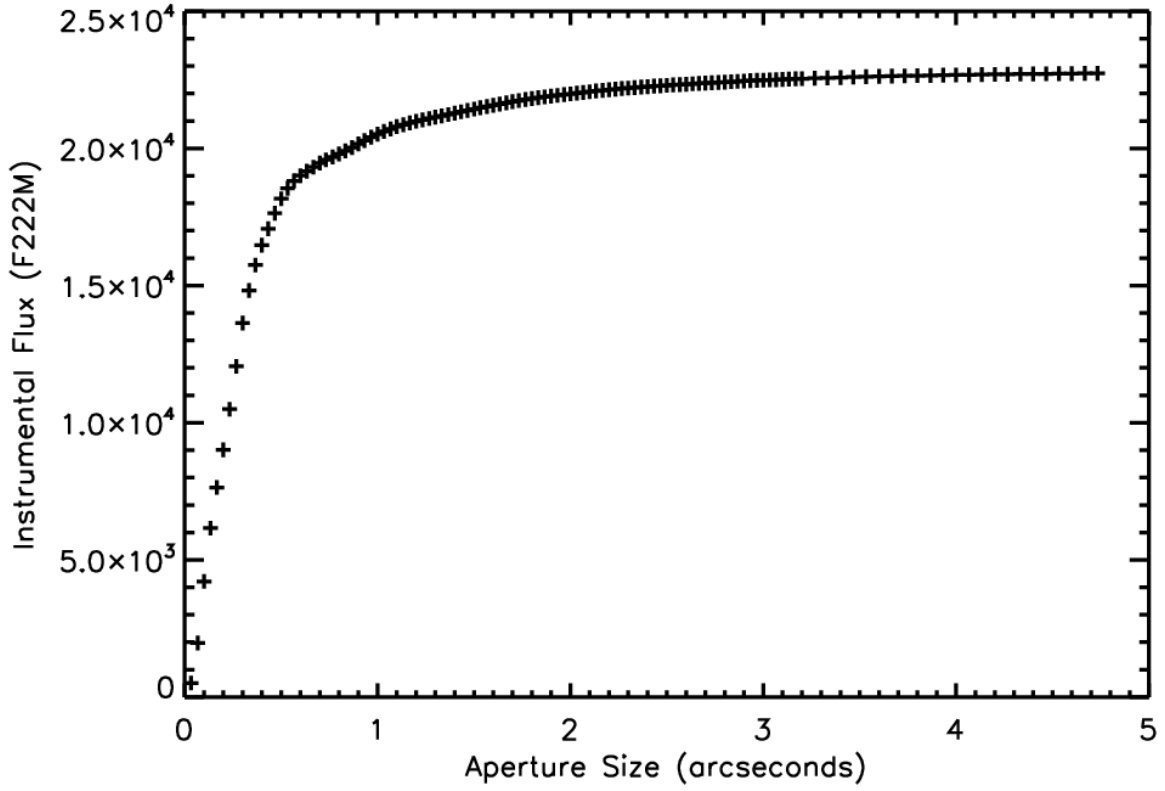

Figure 6 Aperture size vs. encircled flux

The aperture radius was chosen to be 6 pixels, with an annulus of 20-30 pixels for background characterization, corresponding to an angular size of 0.4 arcseconds and 1.3 to 2.0 arcseconds. Similar analysis was done for two clusters using PSF photometry from StarFinder, with minimal discrepancies (Davies et al. 2012b). Sources due to contamination from diffraction spikes and Airy rings of very bright objects were visually identified and removed by hand in order to obtain the best photometric results possible.

Aperture photometry was used in order to provide a consistent method for constructing IMFs. Though the PSF of HST/NIC3 is well characterized by TinyTim, additional observations in this sample were taken using adaptive optics (AO) systems on ground-based telescopes. The PSF of AO images changes across the field of view, making PSF photometry difficult. One consequence of aperture photometry – even very small aperture photometry – is the inclusion of stray light in the aperture. Even when the background is properly characterized, it is possible that light contamination plays a small role. The resulting photometry is slightly brightened, resulting in a mass estimate that is slightly too large. This effect is stronger for faint

stars than for bright stars, potentially flattening the constructed IMF by overestimating the mass of the less massive stars.

Photometry was then used to construct color-magnitude diagrams for each cluster/field combination, where the control field is intended to be used as an indicator of the contaminating fore- and background population. Narrow-band photometry was utilized to identify emission line objects. Both the color-magnitude diagrams and emission line objects are discussed in further detail in the Data Analysis chapter.

2.4. VLT/ISAAC Spectroscopy: Observations and Reduction

Table 3 VLT/ISAAC Targets

Target	RA	Dec	Band(s)
Mercer 81	16 40 24	-46 23 36	H, K1, K2
Mercer 20	19 12 25	+09 57 42	H, K1, K2
Mercer 70	16 00 27	-52 10 48	H, K1, K2
Mercer 23	19 30 13.1	+18 32 09	H, K1, K2
Danks 1	13 12 27	-62 42 06	H, K1, K2
Danks 2	13 12 55	-62 40 56	H, K1, K2
Mercer 30	12 14 32.0	-62 58 49	H, K1, K2

Southern cluster candidates, listed in Table 3, were observed spectroscopically in the near-IR using ISAAC at the VLT. This effort was led by Diego de la Fuente, from proposal to reduction. Examples of his work can be found in Davies et al. (2012a), including the reduction procedure. In a few words, the spectral observations were reduced via customized spectroscopic reduction IDL code written by Ben Davies, and adapted by Diego de la Fuente for use with the VLT/ISAAC observations. For each pointing, nod pairs were subtracted to remove sky features and the result flat-fielded. The resulting 2D frames were rectified and wavelength calibrated using arc frames, after which each spectrum was extracted then divided by a telluric standard star (see section 2.2 and Fig 5 of Davies et al. 2012a for the specific example of Mercer 81) to produce the science spectrum.

ISAAC provides a spectral resolution of R~4000 in H and K bands, ideal for spectral typing to within 1 subtype. Diego de la Fuente was kind enough to share the ISAAC observations in order for collaboration on spectral subtyping. Spectral subtyping was needed for calibration of cluster CMDs as well as spectrophotometric distance estimates. A detailed account of spectral subtyping for both the ISAAC and SpeX data is given in Chapter 3, and a sample of the reduced spectra can be viewed in Figure 28, Figure 33, Figure 36, and Figure 40.

2.5. IRTF/SpeX Spectroscsopy: Observations and Reduction

Table 4 IRTF/SpeX Targets			
Object	Date of Obs	RA	Declination
Mercer 17	7 Sept 2012	19 09 19	+08 11 42
[DB2001] Cl 9	7 Sept 2012	20 32 27.8	+38 51 26
[DB2001] Cl 20	7 Sept 2012 18 Sept 2012	20 38 37	+42 39 24
[BDS2003] 52	7 Sept 2012 18 Sept 2012	01 23 06	+61 51 24
[BDS2003] 66	18 Sept 2012	04 36 50	+50 52 48
HD28794	18 Sept 2012	04 34 45.942	+50 07 28.23
HD196503	7 Sept 2012 18 Sept 2012	20 36 27.869	+41 02 03
HD195377	7 Sept 2012	20 29 28.25	+38 57 05.58
HD8013	7 Sept 2012 18 Sept 2012	01 20 52.149	+60 56 56.10
HD178162	7 Sept 2012	19 07 11.225	+08 20 56.44
HD195377	7 Sept 2012	20 29 28.259	+38 57 05.58

A program to spectroscopically observe northern cluster candidates, again in the near-IR, was undertaken in Semester 2012B at the NASA Infrared Telescope Facility (IRTF), and was on-going through January 2013. SpeX was chosen as an ideal instrument for spectroscopic follow-up in the north: the short wavelength cross-dispersion mode and a 0.3 arcsecond slit provide a resolution of R~2000 across the 0.8-2.42 micron range. This resolution is sufficient for spectral subtyping to the level required for calibration of CMDs and construction of an initial mass function. Only two other instruments in the northern hemisphere fit the required criteria of R~2000-5000 in H and K bands: GNIRS at Gemini North (which was unavailable during Semester 2012B) and NIRSPEC low-res at Keck (a privately funded facility with limited public access).

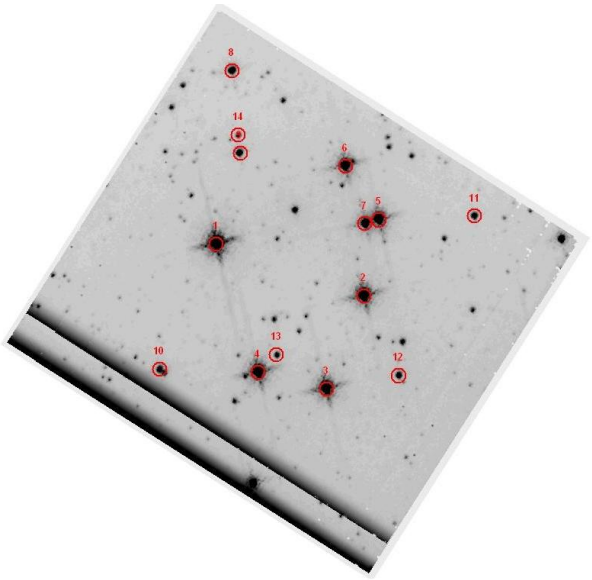
8
14
6
7
5
11
1
2
10
4
13
3
12

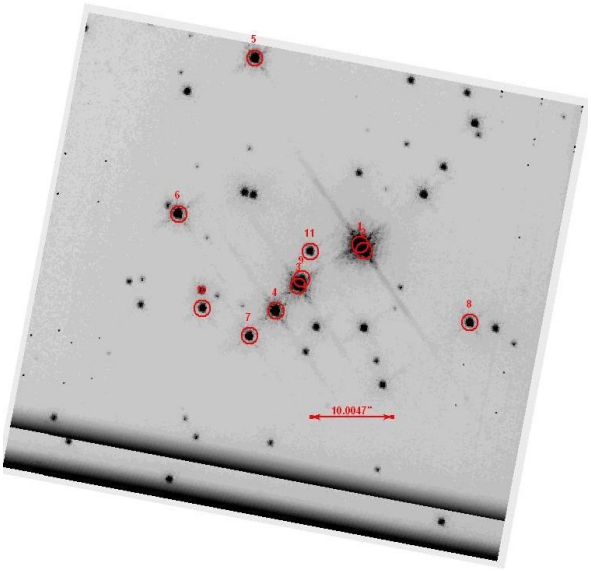
5
6
11
1
9
4
10
7
8
10.0047"

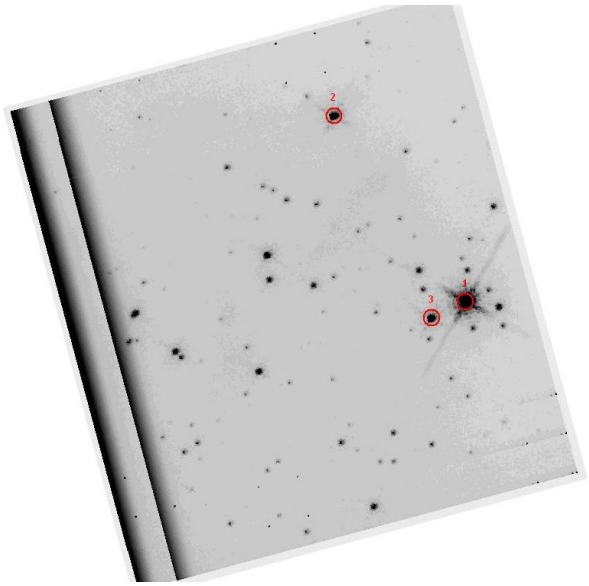
2
4
3

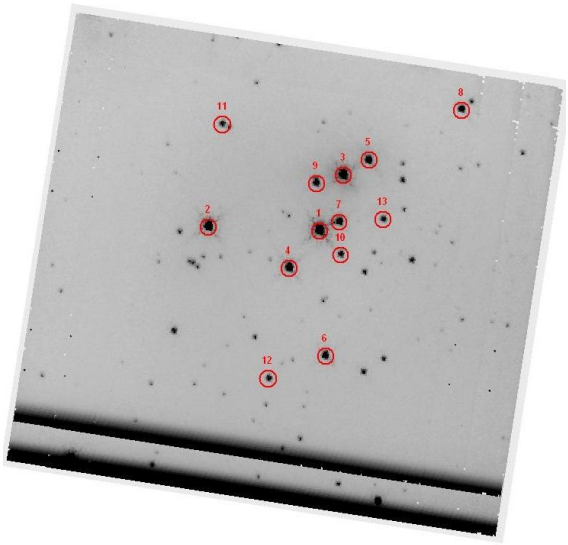
11
8
5
9
3
2
1
7
13
10
4
6
12

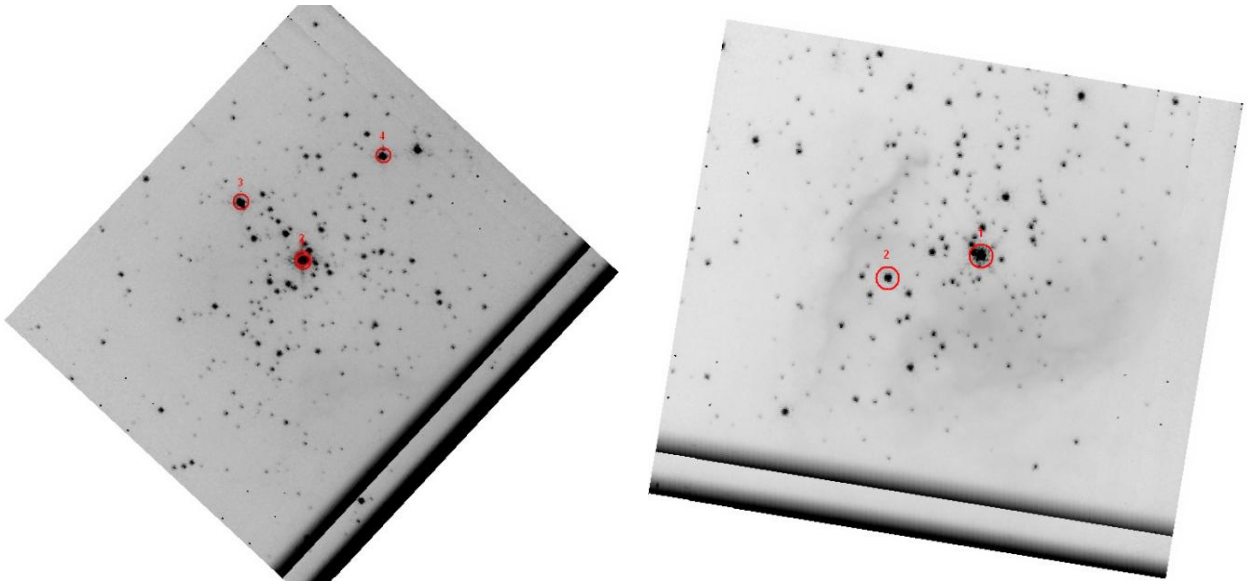

Figure 7 Finding charts for IRTF/SpeX runs. In all images, North is up and East is left. From left to right, top to bottom: Mercer17, [BDS2003] 52, [DB2001] Cl 9, [DB2001] Cl 20, [BDS2003] 66, and [BDS2003] 36.

Reduction of observations taken on 8 September 2012, 18 September 2012, and 20 January were completed using the Spextool 3.4 package (Cushings et al. 2004). Finding charts for each cluster can be found in Figure 7. Spectra were taken in an ABBA nodding pattern throughout all nights. Integration times were based on the sensitivity parameters given on the IRTF webpage for the K band, including use of the SpeX integration time/SNR calculator. Standard stars of A0V spectral type at similar airmass to target stars were observed multiple times. Master arcs and flats were made from calibration files (using the sxd0.3cal macro) taken throughout the night. This process also provides a wavelength solution used to calibrate the raw spectra. Frames were nod-subtracted then flat fielded, and orders with high enough signal to noise extracted and wavelength calibrated. Extracted spectra were next divided by a scaled telluric standard star of similar airmass, resulting in flux-calibrated spectra.

On the night of 18 September 2012, extracted spectra were examined during the run "on the fly" in order to decide if other objects in the field of view should be observed. In the case of [BDS2003] 66, two fainter stars were observed in order to test that a potential main sequence was not actually comprised of foreground giants (both objects were easily identified as hot stars).

Examples of the reduced IRTF/SpeX spectra are can be found in Figure 54, Figure 58, Figure 62, and Figure 71 in the Data Analysis Chapter.

2.6. Keck II/NIRC2 Imaging and Slitless Spectroscopy: Observations and Reduction

Table 5 Keck II/NIRC2 Targets				
Target	Filter	Mode	Int Time (s)	Date
Mercer 5	J	imaging	3	23 August 2008
	H	imaging	3	23 August 2008
	Ks	imaging	1.2	23 August 2008
	CO	imaging	20	23 August 2008
	Kcon	imaging	20	23 August 2008
Control Field	H	imaging	2	23 August 2008
	Ks	imaging	1.2	23 August 2008
Mercer 5	Brγ	grism	40	23 August 2008
	CO	grism	40	23 August 2008
BD-14 5029	Brγ	grism	3	23 August 2008
	CO	grism	3	23 August 2008
Arches	Brγ	grism	240	12 July 2011
	CO	grism	240	12 July 2011
q3	Brγ	grism	30	12 July 2011
	CO	grism	30	12 July 2011

Two clusters were observed in the near-IR using the Near Infrared Camera 2 (NIRC2) at Keck II: Mercer 5 on 23 August 2008 and the Arches on 12 July 2011.

2.6.1. Laser Guide Star Adaptive Optics Imaging

The high density of Mercer 5 was immediately apparent from visual inspection of the HST/NIC3 imaging, suggesting that observations at higher spatial resolution were necessary. To this aim, the cluster was observed using Keck II/NIRC2 in the J, H, and K bands utilizing the laser guide star adaptive optics (LGASO) system. The area corresponding to the HST control field for Mercer 5 was also observed in the H and K filters. Twenty overlapping images were taken, resulting in a total exposure time of 60 seconds in J and H and 24 seconds in K. The observations are nearly diffraction limited, with point sources having a FWHM of ~60 mas in the Ks band.

Detector and instrumental effects were removed by dark subtraction and flat-fielding. The cleaned images were median combined to produce science quality images, as seen in Figure 8. The nearby control field was observed only in the H and Ks bands and reduced in an identical manner.

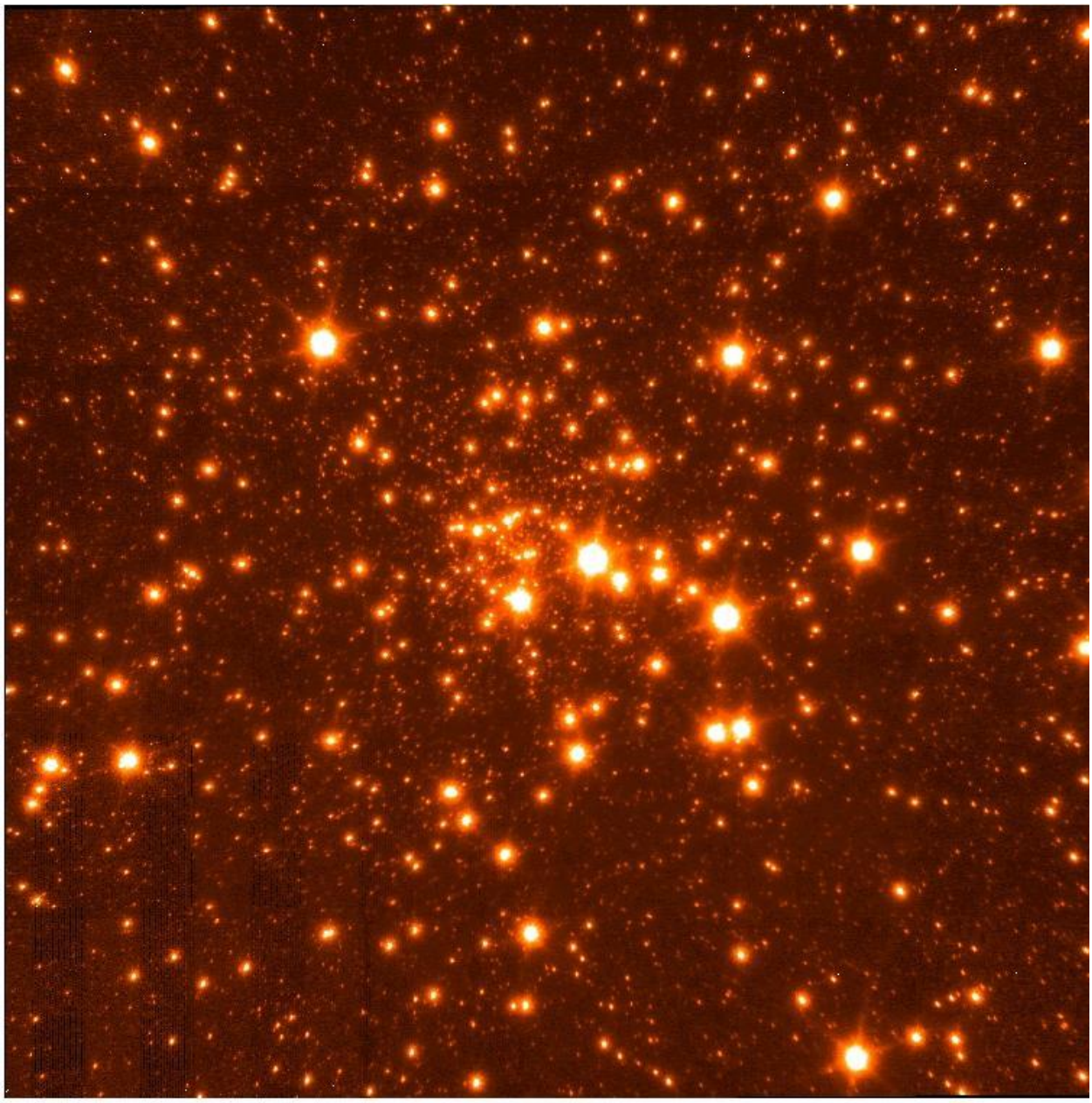

Figure 8 Ks band NIRC2 LGSAO image

A customized IDL-adapted version of DAOPHOT was written to extract aperture photometry of point sources in both the Mercer 5 target frames and control field frames. Photometry was extracted using a radius of 4 pixels (corresponding to 160 mas) and a sky annulus of 5 to 15 pixels (corresponding 199 to 598 mas respectively, given a plate scale of 39.82 mas per pixel). HST photometry of non-saturated stars was used for photometric calibration of the instrumental photometry in both H and Ks bands. J band photometric calibration was performed using photometry of seemingly isolated point sources from the

2MASS point source catalog. Resulting color-magnitude diagrams include those in Figure 16, which are discussed in the Mercer 5 section of Chapter 3.

Astrometric calibration of the NIRC2 frames was calculated using positions of point sources in the HST observations by applying the IDL routine STARAST.PRO; three stars common to both the HST and NIRC2 observations were used to compute a geometric transformation for both the cluster and control field separately.

Mercer 5 was also imaged using two narrowband filters: the K continuum (centered at 2.2706 microns) and the CO bandhead (centered at 2.2891 microns) filters. Photometry was carried out in an identical manner as the J, H, and Ks imaging but no photometric corrections were made to the instrumental magnitudes. The CO index was computed by subtracting the K continuum instrumental magnitude from the CO instrumental magnitude. The resulting color-magnitude diagram is displayed in Figure 9. Stars without any CO feature will have the same CO index, which can be taken as a constant regardless of actual value or offset from 0. Most often the CO feature present will be an absorption bandhead, especially in cool stars. Stars with a CO absorpttion feature will have a value less than the "constant" CO index, which is roughly 0.3 mag in this case. In this manner, stars with strong CO features can be immediately identified, as evidenced in Figure 9.

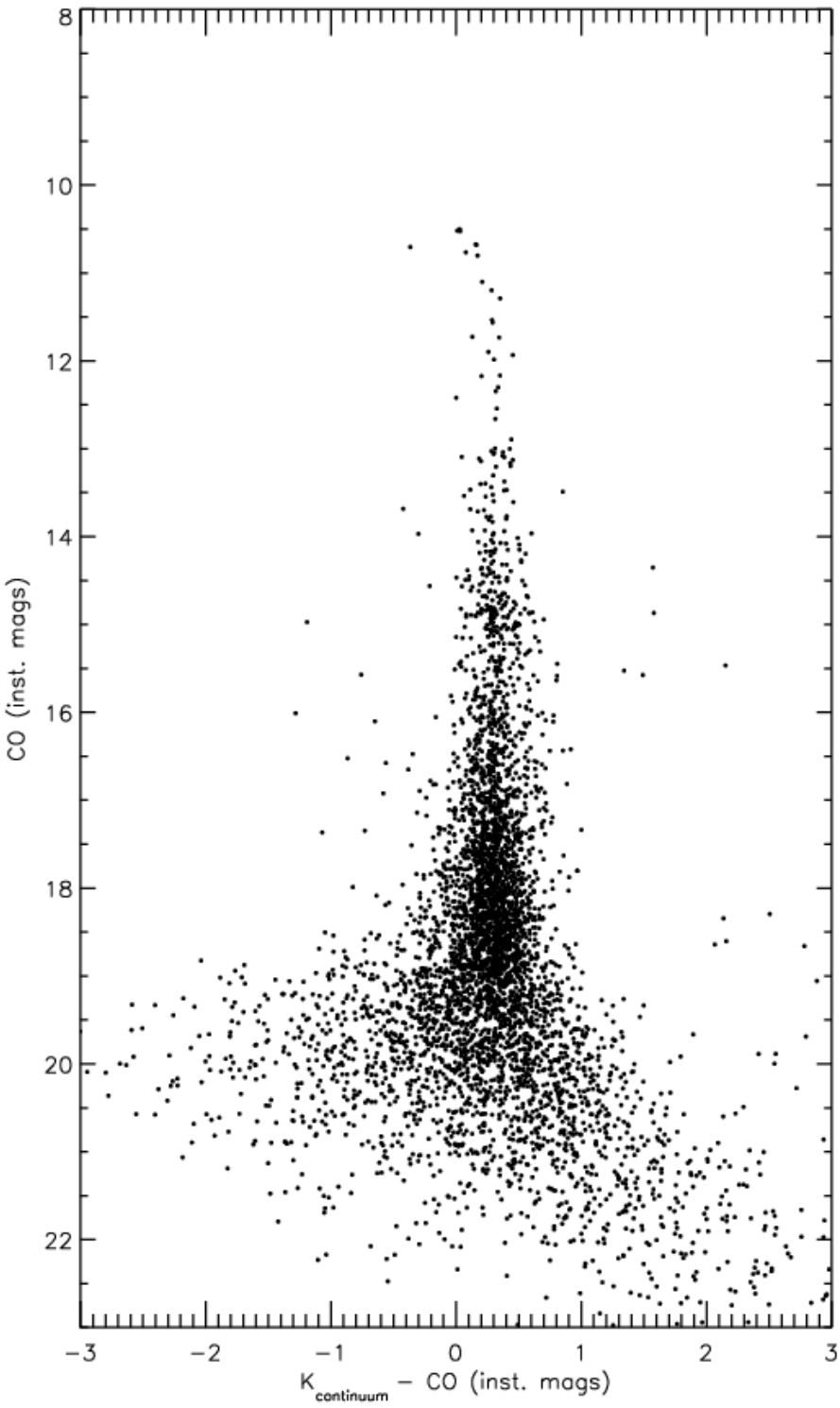

Figure 9 Kcon-CO vs. CO color-magnitude diagram. Objects with CO absorption features are found to the left of the nearly straight feature at Kcon-CO~0.3

2.6.2. Slitless Spectroscopy

Grism spectroscopy was taken for both Mercer 5 and the Arches stellar clusters, using narrowband filters centered on Bracket Gamma (Brγ, 2.166 microns) and the first CO bandhead (2.2891 micros). The use of narrowband filters provides a spectral "snippet" of every star in the field of view of the detector down to some limiting magnitude. The x,y positions of the center of the spectral snippet corresponds to the x,y positions of the target stars in the non-grism imaging field of view. Brγ and CO were chosen because each provides a quick determinate of rough spectral type: Brγ emission or absorption is observed in hot stars while CO features are only present in cool stars, e.g. red giants or red supergiants.

2.6.2.1. Mercer 5

Slitless spectroscopy of Mercer 5 was performed by operating the NIRC2 wide camera with the medium grism and narrowband filters, in this case Brγ and CO. Seven frames at one position angle were observed. This led to difficulties with overlapping spectra, as demonstrated by Figure 10. Inspection of the Brγ frames revealed all spectra to be saturated: entirely flat, featureless spectra (c.f. Figure 13) which did not fit with the characteristic shape of the Brγ filter. The Brγ filter profile from the Keck webpage is displayed on the right in Figure 11. All reduction and extraction was performed used customized IDL scripts written for the specific case of these observations.

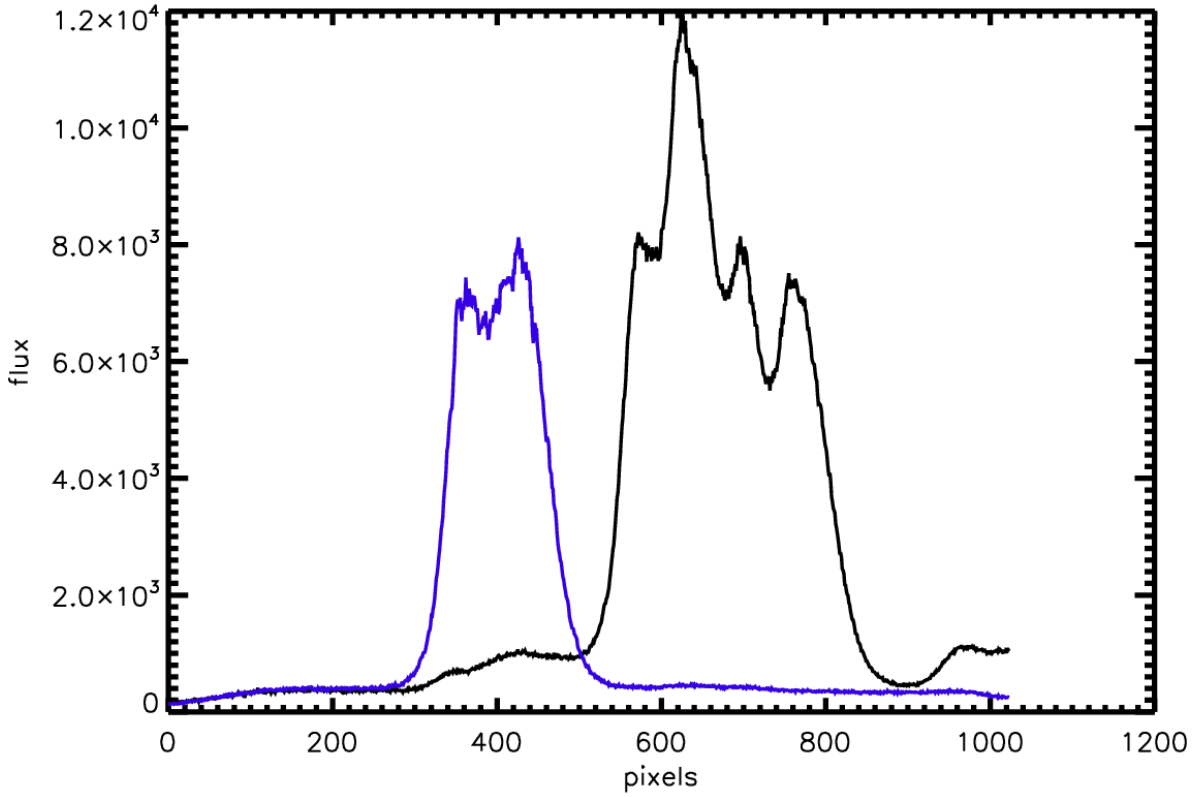

Figure 10 Raw spectra of two objects blend together, in black and on the left, resulting in no information about either object. Example of single spectrum is shown in blue, to the right of the blended spectra.

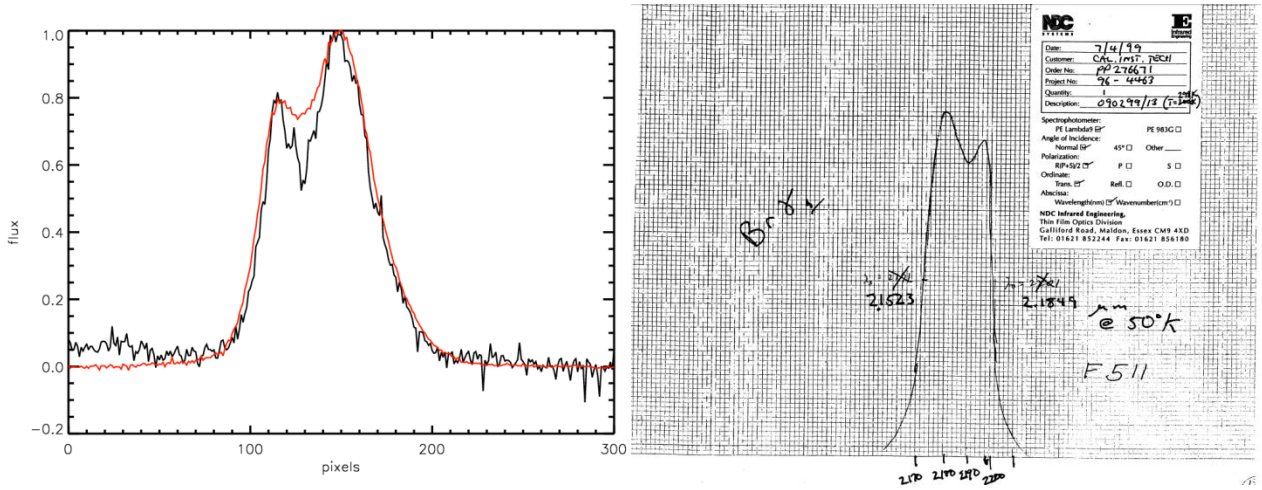

Figure 11 Left: CO narrowband filter profile; Mercer 5 target star shown in black (with deep absorption feature), standard star shown in red. Both spectra have been normalized to 1. Right: Brγ narrowband filter profile, taken from the NIRC2 Filter website.

The raw images were dark subtracted and field fielded in the usual way. Inspection of the Brγ flat fields revealed them to be saturated, but the CO calibration files were within acceptable limits. A standard star (BD-14 5029 of spectral type B1.5b) was observed in the same manner as the cluster and spectra extracted in an identical manner. Again, reduction and extraction could only be done for the CO narrowband observations. An example frame containing CO narrowband slitless spectroscopy of Mercer is presented in Figure 12.

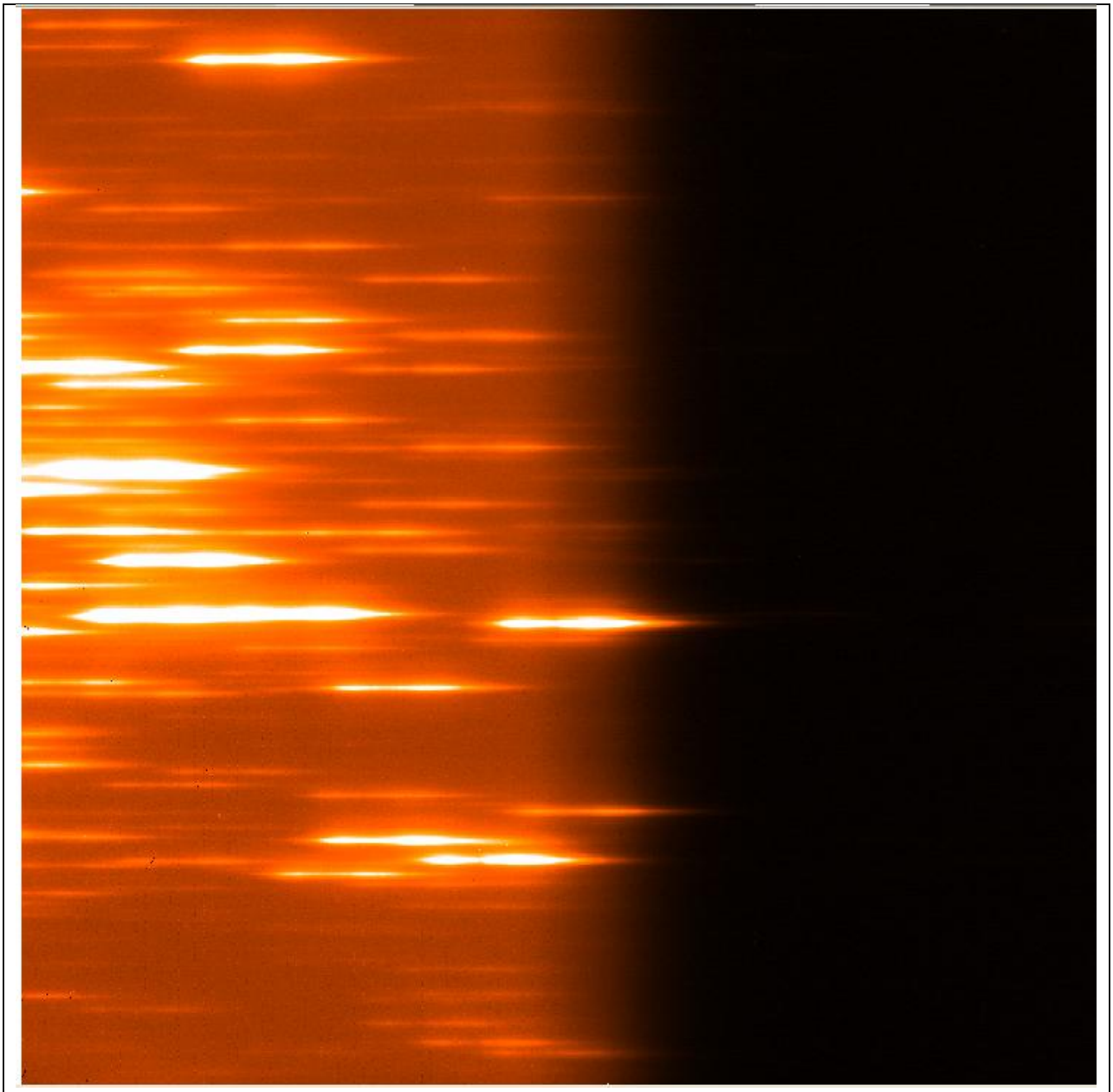

Figure 12 CO narrowband slitless imaging of Mercer 5

Source detection was performed on each frame by stepping across in the x-direction (in steps of 25 pixels) and identifying peaks in the y-direction above a certain threshold. Using this method, columns containing a sharp peak were flagged as containing at least one object, often multiple objects given the high density of the target, then the row containing each peak was searched for spectra. Visual inspection indicated that each spectrum spans roughly 100 pixels (e.g. see Figure 11). A background value was calculated for each flagged row, then pixels above that background were counted. Objects that were cut off by the edge of the frame were discarded as having too few pixels above the background. Some rows contained multiple spectra, all of which were flagged, leading to double detections. Double detections were common and removed via an automated process after source detection. Some sources were missed entirely and added by hand after the detection process was complete.

Spectral extraction began once the detection algorithm reached the end of the frame and double detections were removed from the list of flagged objects. The profile of the CO filter has a shape such that two distinct peaks are present in each spectrum, one higher than the other (as seen in the left panel of Figure 11). As all of the stars in Mercer 5 are expected to be cool, only absorption lines should be present in the wavelength regime covered by the CO filter. An example of this is shown in Figure 11, with the standard star in red displayed as a proxy for the filter profile. This filter profile allows for use of the highest peak as a common defining point in each spectrum. Raw spectra were extracted using a width of 150 pixels and a height of 5 pixels. The five pixel rows were collapsed into a 1D spectrum which was written to a fits file.

Each target spectrum was divided by the normalized standard to remove the filter profile shape and sky contribution. Wavelength calibration was performed using half-power points, in theory corresponding to the cut-on and cut-off wavelengths of the filter. The half-power points were taken from the instrument specifications listed in the manual. The spectral resolution was then calculated by dividing the central wavelength of the CO filter, 2.2891 microns, by the FWHM of the CO image, multiplied by the linear dispersion. This method yielded a resolution of R~1420. Spectra were extracted from all 7 frames then cross-correlated and summed to produce a final spectrum of each star. An example of the raw extraction is shown in Figure 11, the cluster star in black and the standard star in red. Notice the characteristic absorption feature in the center of the filter profile for the cluster star. In the best case scenario, an object was covered in all 7 pointings and the final spectrum built from 7 raw spectra.

Rough spectral types were estimated by comparing the equivalent width (EW) of the CO feature, where present, with template stars from the Kleinmann & Hall 1986 spectral atlas. The atlas stars were first

degraded to the resolution of the target stars, then shifted in wavelength to match the deepest point in the CO bandhead. The results of this comparison are discussed below.

2.6.2.2. Arches

For the Arches observations, three position angles were chosen: 0, 30, and 60 degrees. This was done to allow for characterization of objects which were blended in a single position angle, as shown in Figure 10 above. The Quintuplet star q3 was observed as a telluric standard, chosen on the basis of a lack of spectral features (both emission and absorption) in the K-band. Two observations of q3 were taken using the Brγ filter, with exposure times 120 sec and 30 sec. However, the standard star was found to be saturated in all Brγ exposures and only partially contained in the CO exposure. The saturated spectrum is shown in Figure 13. Luckily, [CEC96] F was present in the field of view of the Arches target observations, and could be used as a standard star in both Brγ and CO. This object is classified as a foreground star based on its photometric properties (i.e. its color appears bluer than the rest of the Arches cluster). Only one of the three target frames contained a suitable spectrum of [CEC96] F; the star was absent or partially cut off in the other frames.

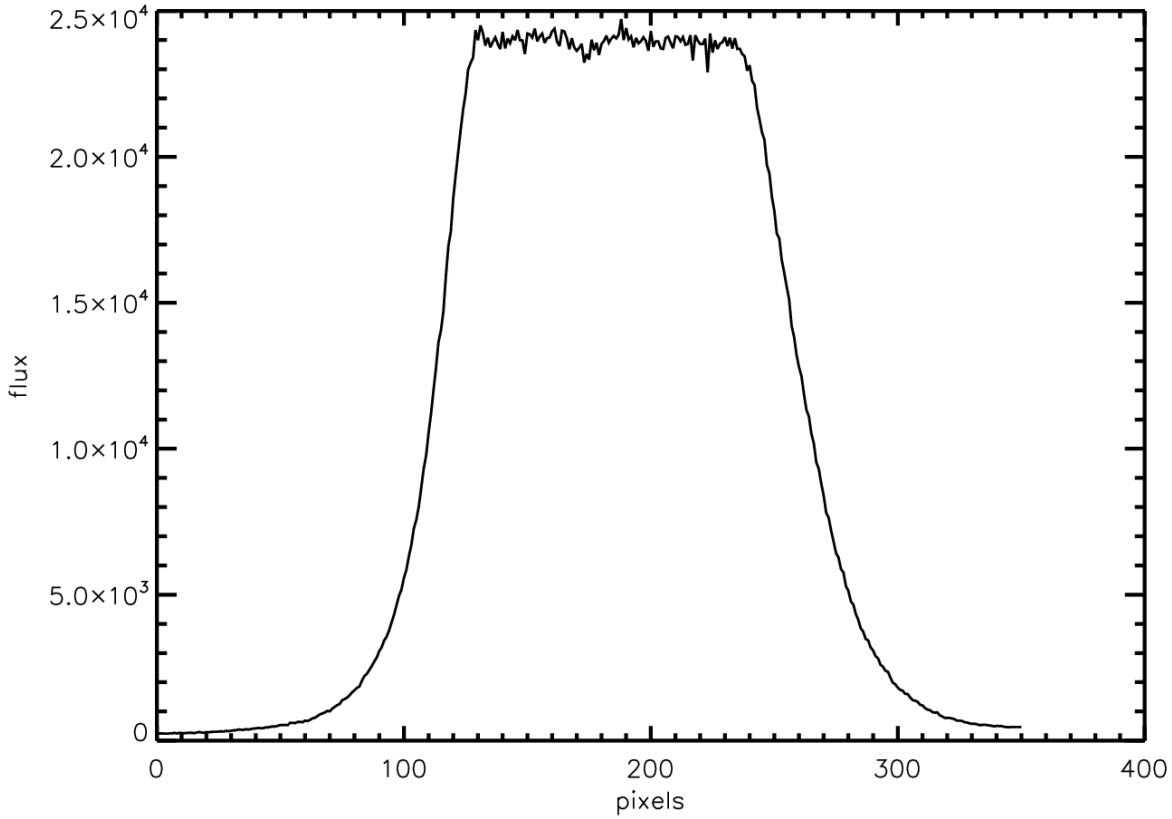

Figure 13 Saturated spectrum of q3.

Calibration files for the Arches observations were not taken the same night as the science observations. Flats from the archive were found to be saturated, and NIRC2 was not used again for several weeks. It was necessary to wait some time for the appropriate calibration files. A modified version of the Mercer 5 IDL code was used to reduce and extract spectra in the same manner. Extraction of spectra in the Arches cluster was complicated by the nature of the target objects: Brγ is found in emission in very hot massive stars, often in excess of the two peaks of the filter profile. This made it difficult to assign the same common defining point in all objects as done for Mercer 5. For some extreme cases, the Brγ emission filled the majority of wavelength space. Spectra of WNL stars heavily dominate the Brγ emission in the Arches slitless spectroscopy frames, often leading to contamination of both near-by and not as near-by objects.

2.7. Chandra/ACIS: Reduction

Table 6 CXO/ACIS Targets

Target	RA	Dec	Int Time (ks)	ID	Comment
[BDS2003] 52	01 23 06	+61 51 24	10	6575	
[BDS2003] 66	04 36 50	+50 52 48	10	7478	
G305	13 12 27	-62 42 06	125	8922	Danks 2 falls on chip gap
[DB2001] Cl 20	20 38 37	+42 39 24	30	8893	Fall on chip gap
Mercer 81	16 40 24	-46 23 36	40	11008	

The CXO deliverable "images" do not need to be reduced. Each set of raw data includes a file named "acisfID#N001_evt2.fits" which contains the level 2 events (level 2 events have been irreversibly filtered for good time intervals, cosmic ray rejection, and pixel position transformation to astromertric coordinates). Generally, observations are binned to a certain extent and visualized in different manners. Point source extraction varies from observation to observation, and is discussed in individual cluster sections along with the point source analysis and cross-correlation of sources.

2.8. VLT/MAD Imaging: Photometry in the core of R136

Campbell et al. (2010) present VLT H and Ks band imaging of three fields in the 30 Doradus region, including R136, as part of a Science Demonstration program with the Multiconjugate Adaptive Optics Demonstrator (MAD). C. Evans kindly provided reduced observations of R136, where the reduction and characterization of the images are discussed at length in Campbell et al. (2010). The central 2.8" are excluded from analysis in that work, but are the focus of photometric efforts towards investigating the high end of the initial mass function here.

Photometry was extracted from the H and Ks band VLT/MAD images using a custom IDL adapted version of DAOPHOT, with an aperture size of 3 pixels and a sky annulus of 5-10 pixels. PSF photometry was not attempted due to the changing PSF characteristic of adaptive optics images. Photometric zero points were taken from Campbell et al. (2010). Only the central region of R136 and two "control" fields were considered for photometry; the majority of the field was studied in depth by Campbell et al. (2010). The location of the control fields and the central region are indicated by labeled green circles in Figure 14.

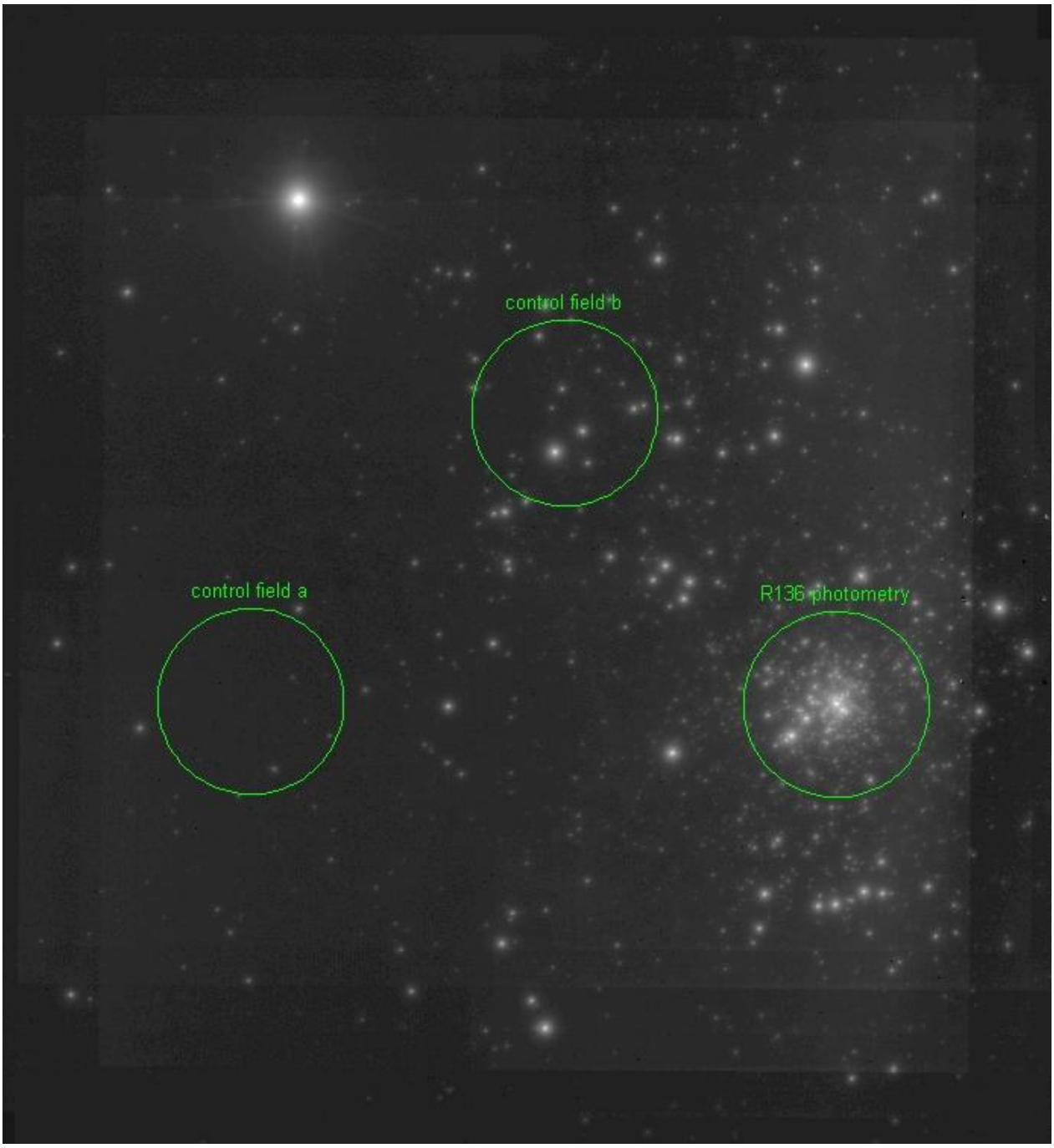

Figure 14 MAD Ks-band image of R136

2.9. Completeness Tests

To test the completeness of the photometry as a function of magnitude, completeness tests were performed for each cluster. For R136, completeness tests were performed on the VLT/MAD observations. For the remaining clusters, completeness tests were done on the HST imaging.

2.9.1. VLT/MAD Completeness Procedure

The core of R136 as observed by VLT/MAD is only complete to roughly 30 $M_{\odot}$. Completeness was investigated via the artificial star method: artificial stars over a wide range of magnitude were added to each frame, for both the cluster center and the two control fields. Photometry was then redone in an identical manner to the science frames in order to characterize the recovery of the artificial stars. This test was repeated 100 times for both H and Ks bands in order to obtain robust completeness results. Identical procedures were run for each field, the core of R136, control field A, and control field B. The results of the completeness test for the R136 cluster core (black plus symbols) and both control fields (red asterisks, blue diamonds) is shown in Figure 15. This figure demonstrates how crowding in the cluster core causes the completeness to drop at brighter magnitudes than in the control fields (beginning around K_S~17 mag).

Each iteration contained 61 artificial stars, varying uniformly in magnitude from 10 to 25 mag in steps of 0.25 mag. A PSF was constructed from isolated stars in control field A, using IDL's GETPSF.PRO procedure, This PSF was scaled to the appropriate magnitude for each artificial star. The position of each artificial star was randomly assigned, then the star added to the field of view. The input position and magnitude of each artificial star was stored in an array and compared to the output photometry. To check for blends, a limit of 2 pixels and 0.5 mag were imposed on "recovered" artificial stars. Beyond these limits the object was considered a non-detection.

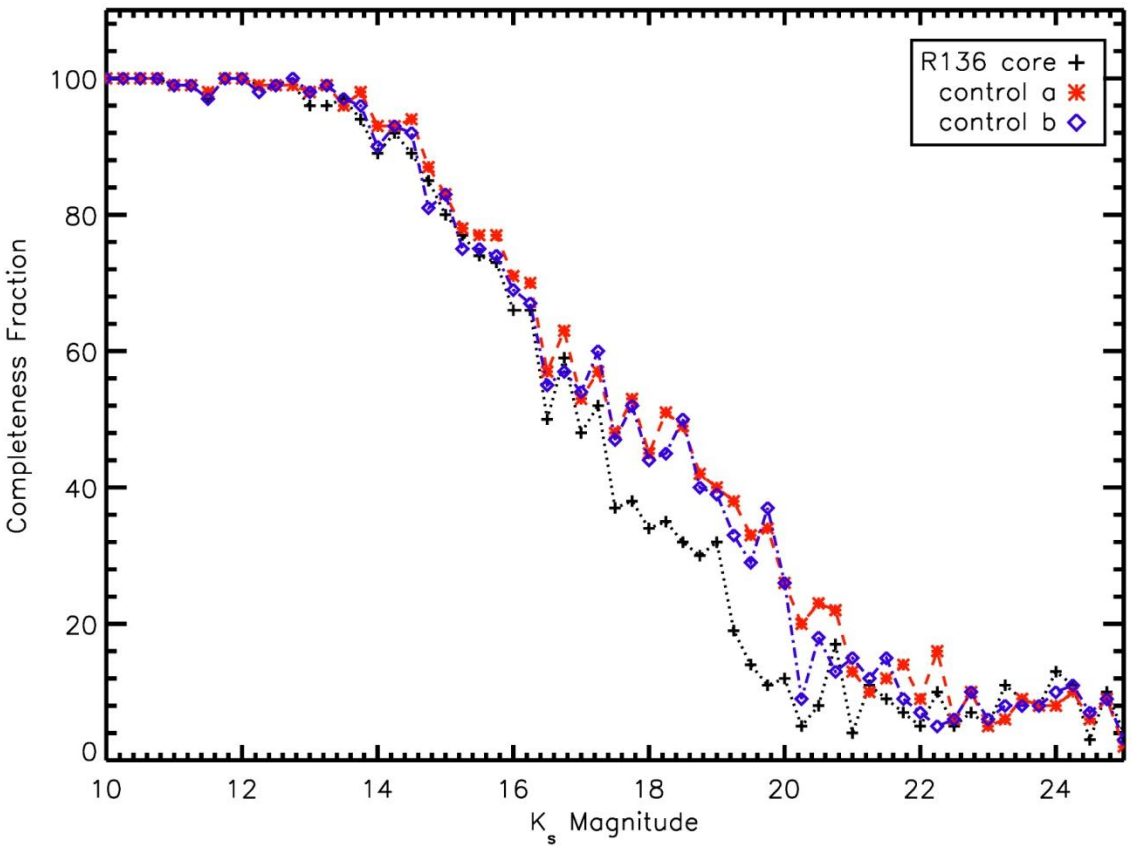

Figure 15 Completeness as a function of magnitude in the core of R136 and both control fields as observed by VLT/MAD.

2.9.2. HST/NIC3 Completeness Procedure

The artificial star method was also used to investigate the photometric completeness of HST/NIC3 observations, though the procedure varied slightly from the VLT/MAD imaging. For each of 100 iterations, 47 artificial stars varying in magnitude from 8.5 to 20 mag were added to each field. The x and y position of each artificial star was randomly assigned in a repeatable way. The PSF of NIC3 has been well modeled by John Krist and Richard Hook, who publish and maintain the Tiny Tim software. Tiny Tim is designed to compute a position-dependent PSF for each of the HST cameras. A parameter file, which can be generated in batch mode, is used to determine the parameters of the resulting PSF(s). These parameters include camera, detector, x and y position, and magnitude, to name a few. For each artificial star, a parameter file was written and Tiny Tim called from IDL to create the appropriate PSF. Each resulting PSF was added to the observed image, and photometry redone in an identical manner to the science photometry.

The input position and magnitude of each artificial star was stored in an array and compared to the output photometry, as for the VLT/MAD completeness tests. To check for blends, a limit of 2 pixels and 0.5 mag

were imposed on “recovered” artificial stars. Beyond these limits the object was considered a non-detection. Identical tests were done on F160W and F222M images, for both target and control fields.

3. Data Analysis

A selection of the candidate clusters listed in Table 2 are discussed in detail in this chapter. The nature of each candidate – genuine cluster or spurious detection – is examined and, in the case of real clusters, the basic parameters such as age, distance, stellar content, reddening, and total cluster mass, are derived. Given the robust selection criteria for identifying young, massive clusters for follow-up, it is of little surprise that most candidates are true clusters. For each cluster, the age, total mass, and stellar content are used to determine whether a measurement of the slope of the initial mass function would be a useful contribution to the overall project goals. In the case of older (>~6 Myr) clusters, the majority of massive stars have already left the main sequence. In these clusters, the high mass limit to the IMF slope measurement suffers. For lower mass (~10^3 $M_\odot$) clusters, the stellar content at the high mass end is prone to small number fluctuations, resulting in high errors on any IMF slope measurements.

3.1. Mercer 5

Inspection of the HST images of Mercer 5 reveal a very dense cluster; the HST CMD reveals a red clump at mF222M ~ 13 mag, suggesting an advanced cluster age (>100 Myr). Though this instantly removes Mercer 5 from the IMF slope project, the cluster on its own is interesting enough to warrant further study. To this aim, higher resolution imaging was required to better investigate the stellar population. Laser guide star adaptive optics (LGSAO) imaging was obtained in the J, H, Ks, Kcon, CO, and Brγ bands using NIRC2 at Keck II. Slitless spectroscopy using the CO and Brγ narrowband filterss was also obtained the same night. Analysis of the LGSAO imaging results is discussed below. In short, Mercer 5 is found to be a newly discovered globular cluster in the Galactic Plane (see also Longmore et al. 2011).

3.1.1. NIR Imaging

The NIRC2 Ks vs. H-Ks color magnitude diagram (CMD) for Mercer 5 is shown on the left in Figure 16. The J-band observation suffers from saturation at bright magnitudes, while H and Ks do not. Inspection of Figure 16 reveals a prominent red giant branch (RGB) and red clump; neither of these features can be identified in the control field CMD on the right in Figure 16. Both of these features are indicative of an intermediate to old stellar population (>~100 Myr).

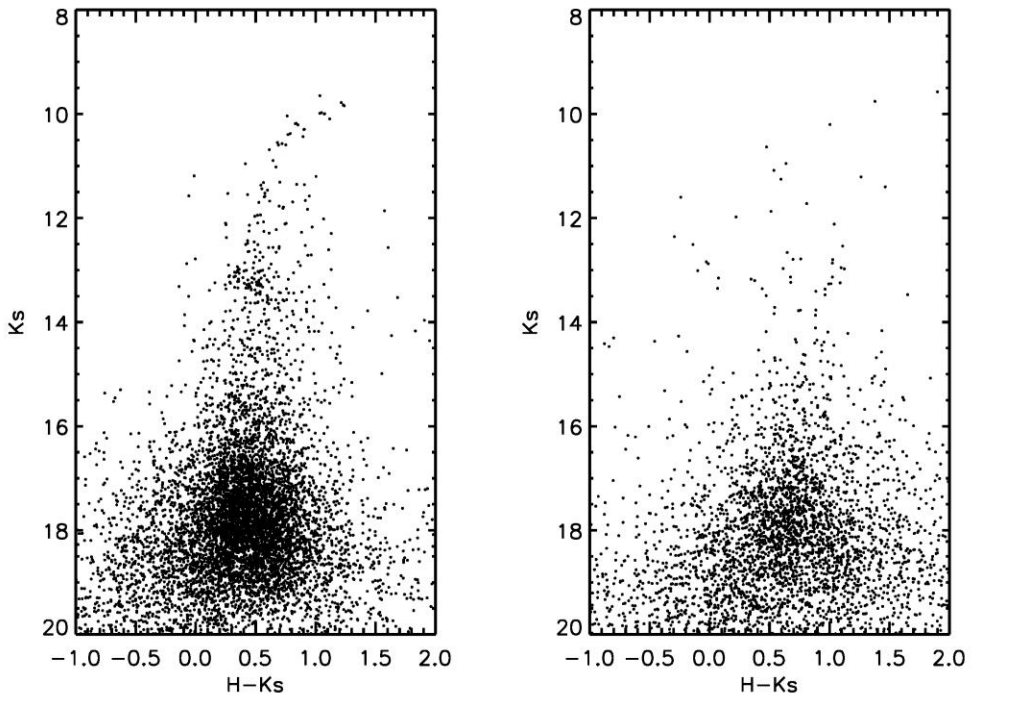

Figure 16 Left: NIRC2 CMD for Mercer 5 Right: NIRC2 CMD for control field. The control field is not overplotted on the cluster field of view to avoid confusion due to the dense nature of both fields.

3.1.2. Slitless Spectroscopy

Slitless spectroscopy of the cluster was extracted from CO narrowband observations. The BrG spectroscopy was saturated in all exposures. No attempt to measure radial velocities was made, rather the deepest part of the CO bandhead feature was used as cross-correlation point. The half power points of the filter were matched to the half power points of the spectra as the turn-on and turn-off wavelengths, but at times this was an imperfect calibrator. The wavelength calibrated spectra for selected stars are displayed in Figure 17. The CO bandhead equivalent width (EW) was measured from 2.2915 microns to 2.2970 microns, and the continuum from 2.287 microns to 2.290 microns. Spectra of cool stars from the Kleinmann & Hall atlas (Kleinmann & Hall 1986) were degraded to the resolution of the NIRC2 slitless spectroscopy, and the same EW measurements were made. The cluster spectra were also visually matched to the atlas spectra in order to determine accurate spectral types (to within 1-2 spectral subtypes).

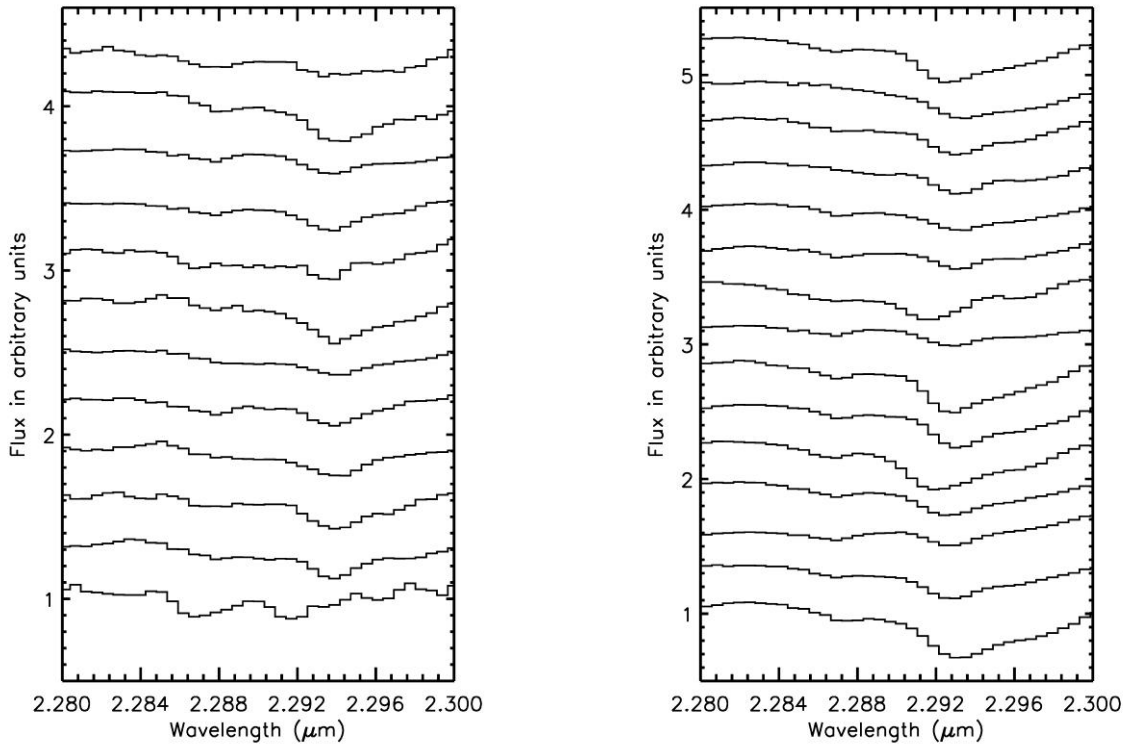

Figure 17 Left: Selected spectra of photometrically selected red clump stars. Right: Selected spectra of bright stars.

The EW of the CO bandhead in giants and supergiants of the same spectral type has been shown to follow two discernible trends (Davies et al. 2007). As in Figure 2 of Davies et al. (2007), a comparison of the EWs vs. spectral type for Mercer 5 showed that the spectra of stars in Mercer 5 were consistent with being cool giants.This can be determined from inspection of Figure 18 and Figure 19. The averaged spectrum of the red clump stars (Figure 17, left) and of the brightest stars (Figure 17, right) are shown in Figure 19, with an atlas example (degraded to the same resolution as the grism spectroscopy) overplotted for each. If these were supergiant stars, the depth of the CO absorption would be deeper, as can be seen from Figure 18. For Mercer 5, the EW of the CO absorption matches the EW measured in giant stars of the same spectral type quite well (see Figure 18).

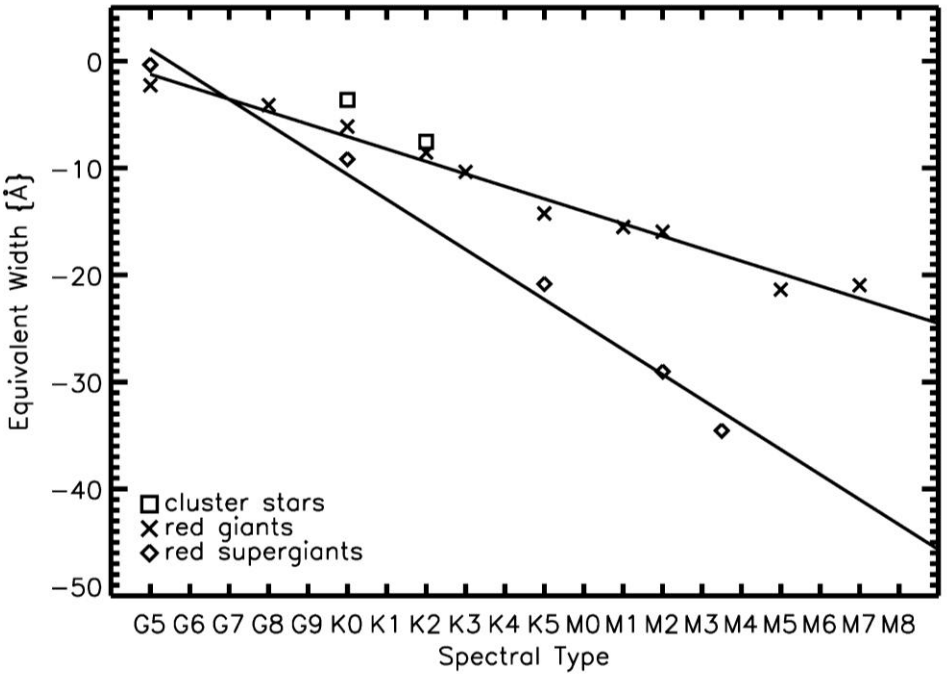

Figure 18 EW vs. spectral type for cool giants, supergiants. Overplotted are the EW and spectral type of the average spectra of red giant branch and red clump stars in Mercer 5.

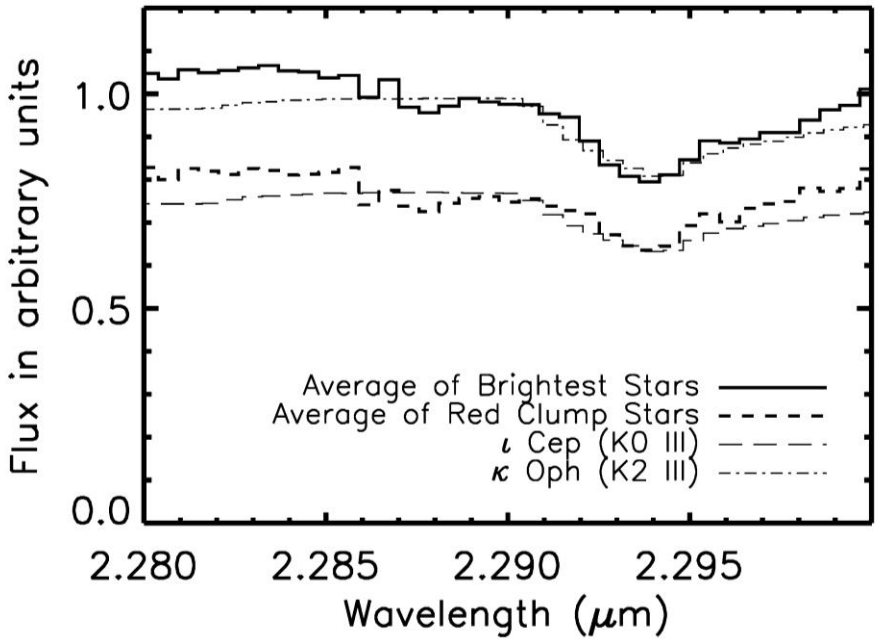

Figure 19 Average spectra of brightest stars and red clump stars in Mercer 5, with KH atlas spectra of the estimated spectral type overplotted.

3.1.3. Metallicity

The two populations of globular clusters belonging to the Milky Way appear to follow a trend. The halo population consists of metal-poor globulars, while the bulge population is made up of higher metallicity globulars. In order to determine if Mercer 5 is merely passing through the Galactic plane or belongs to the bulge population, measurement of radial velocity, proper motion, and/or metallicity are required. Without the availability of sufficiently high resolution spectroscopy to determine radial velocities or multi-epoch monitoring to determine proper motion, only metallicity can provide a hint to the origin of Mercer 5.

It has been shown for other globular and open clusters in the Galaxy that the IR slope of the red giant branch (RGB) in K vs. J-K space varies according to metallicity (Kuchinski et al. 1995; Ferraro et al. 2000; Valenti et al. 2004). Valenti et al. (2004) find the relation [Fe/H]=-22.21x(slope RGB)-2.80, using a linear least squares fit to the decontaminated red giant branch of 10 Galactic Globular clusters. These authors fit the RGB from 0.5 mag to 5.0 mag fainter than the brightest stars. The results of that work are re-examined in Valenti et al. (2007), in which the authors find good agreement between their metallicity determinations and metallicity values published in the literature for 24 bulge globular clusters.

The metal-rich old open cluster NGC 6791, examined in the infrared by Carney et al. (2005), does not follow the RGB slope-metallicity relationships published by Valenti et al. (2004, 2007). These authors determine their own RGB slope-metallicity fit (Eqn 5 in Carney et al. 2005) but find poor agreement between their predictions and spectroscopic metallicity measurements of NGC 6791. As a result, these authors suggest that the RGB slope is only linear in a restricted metallicity range, [Fe/H]<=-0.3, or is not linear in K vs. J-K space.

In an attempt to roughly determine the metallicity of Mercer 5, a 2nd order polynomial was fit to the red giant branch at increasing inclusion radii up to the full angular extent of the NIRC2 imaging. These fits included stars from K_S~14 mag to K_S~9 mag between 3.0 < J-K_S < 4.0. The relationship established in Valenti et al. (2004) was then applied to the results to find a median metallicity of [Fe/H]=-0.78 , suggesting that Mercer 5 is metal-poor (while the majority of bulge globular clusters are metal-rich). These results as applied to Mercer 5 are not extremely robust, for the reasons raised by Carney et al. (2005). In addition, Mercer 5 suffers from patchy extinction, giving rise to a color spread in the red clump. The spread in the red clump could also be attributed to a cluster containing multiple populations with differing metallicity, as has been recently observed in many Galactic globular clusters. However, Longmore et al. (2011) show that in Mercer 5 the smearing of the red clump is due to the effects of strong differential reddening across the face of the cluster, which is even more pronounced when a larger field is considered.

3.1.4. Mass, Age, and Distance

The mass of Mercer 5 was investigated using multiple methods. Integrating the stellar density function over the radial profile of the cluster is one way to estimate the total mass of the cluster, but this method has some drawbacks. The high density of the cluster gives makes this measurement highly incomplete, especially near the cluster center.

Another method of computing the total mass of the cluster is by counting the number of red clump stars (~50) and comparing to Geneva stellar population model predictions, as shown in Figure 20. These models are age dependent, yielding the same result for different combinations of age and total cluster masses. This method yields a mass of $2(10^4)$ $M_\odot$ if the cluster is older than ~1 Gyr, increasing with increasing age. Similarly, for a younger age (~100 Myr) the total mass estimate is lower, below 10^4 $M_\odot$. Thus, it is necessary to determine the age of the cluster in order to place a stronger constraint on the cluster mass.

One method to determine the age of the cluster is to use the Ks-band luminosity function; the ratio of the number of stars in the red clump compared to the number in the nearby gap is a strong function of age. In the luminosity function, Figure 21, it can be seen that this ratio is ~5, corresponding to an age of 1 Gyr or older. Note that for younger clusters, this ratio will be much larger (e.g. ~50 for an age of ~100 Myr). The distance between the red clump and the MS turn-off can also be used as an age estimator, though this was complicated by the effects of differential reddening and the smearing out of the red clump in the K_S band luminosity function across two bins. Figure 21 also contains stellar population models overplotted on the observed luminosity function, built with a Kroupa IMF (Kroupa 2001, see Equation 3 and Equation 4 in The Initial Mass Function) and scaled by mass to fit the number of red clump stars. The best fitting models are those with ages of 10 Gyr or higher.

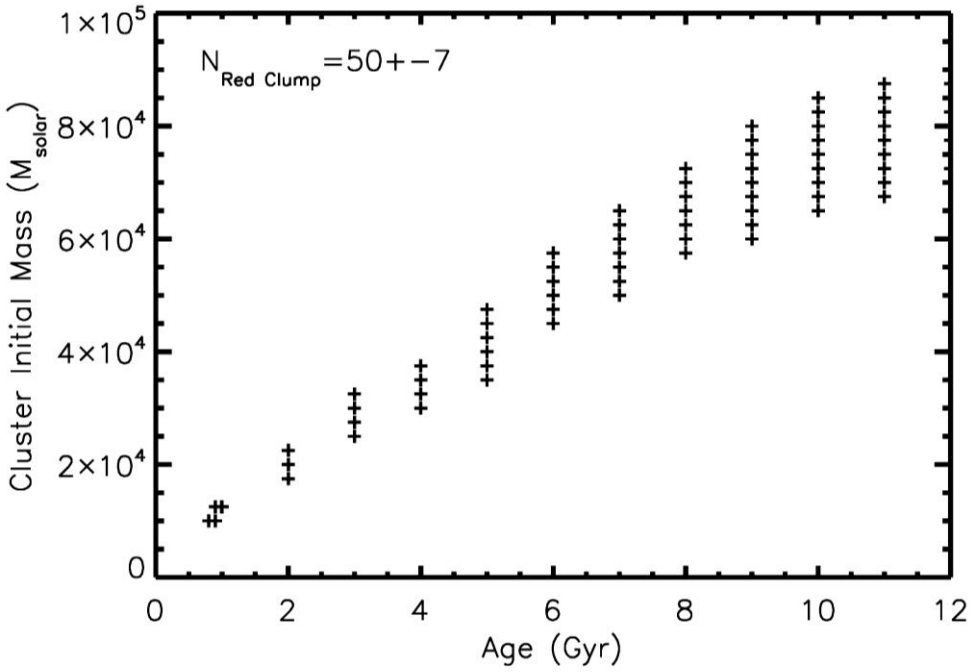

Figure 20 M_{total} vs. expected $N_{red\ clump\ stars}$

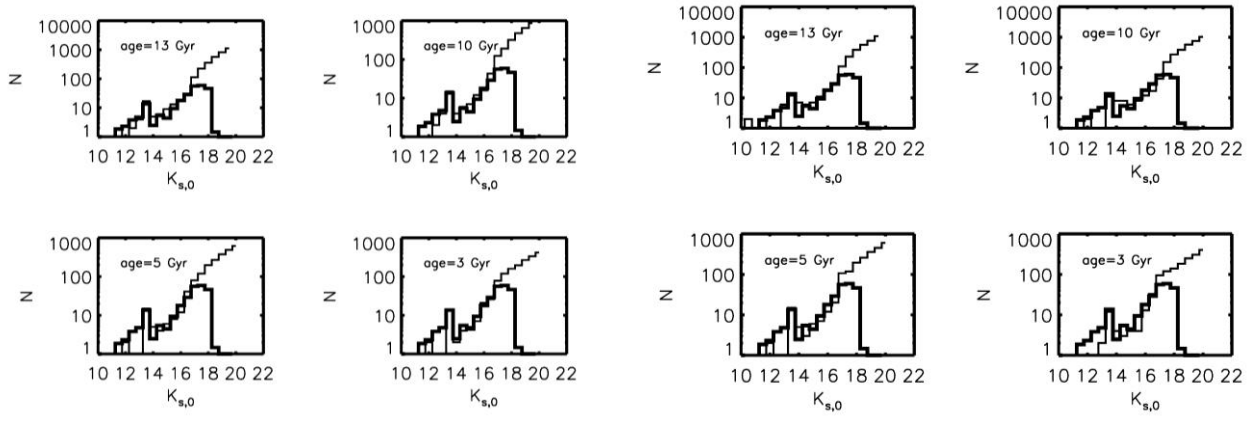

Figure 21 Thick black lines: K_S-band de-reddened luminosity function of Mercer 5; the red clump can be seen as the excess at K_S~13 mag. The left hand panel shows age models (thin black lines) for LMC metallicity, while the right hand panel shows ages models (thin black lines) for solar metallicity. For both metallicities, a model age of 10 Gyr or higher fits the data best. The sharp drop at K_S=18 is due to incompleteness.

The distance to Mercer 5 was computed using the average brightness of the red clump. After de-reddening, the clump brightness is computed as follows:

$$K_{s,0} = K_s - A_{K_S} = 13.0 - 0.2 = 12.8$$

Equation 7

where

$$A_{K_S} = \frac{H - K_S \; - \; H - K_{S\;0}}{\frac{A_H}{A_{K_S}} - 1}$$

Equation 8

given $(H\text{-}K_s)_0 = 0.3$ for red clump stars and $A_H/A_{Ks} = 1.44$ (Rieke et al 1989). For an old (>1Gyr) cluster, this gives a distance modulus $(m_{Ks,0} - M_{Ks,0})$=12.8-1.6=14.4 or roughly 8 kpc.

Another crude distance estimator uses the brightest stars in a globular cluster as a standard candle (Frogel et al. 1981). The absolute magnitudes of these stars are shown to be a function of metallicity; without *a priori* knowledge of the metallicity and cluster membership of Mercer 5, it is only possible to relate the apparent magnitude of the brightest "cluster" star to the average metallicity value. For the case of Mercer 5, the brightest object in the field of view was assumed to be a cluster member. This is a valid assumption as the brightest stars are centrally concentrated, consistent with globular cluster dynamical evolution, and the brightest star is not significantly displaced from the cluster center. For the average over 10 clusters of varying metallicity in Table 6 of Ferraro et al. (2000), it is shown that $M_{K,TIP,0}$=-6.29+/-0.45 (where the error is the standard deviation of the sample). Using this average, the distance modulus can be shown to be:

$m_{Ks,TIP,0} - M_{Ks,TIP}$,- = (9.6- 1.6) – (-6.29) = 14.3 or D~7.2(+2.5,-1.8) kpc

This assumes errors are dominated by the uncertainty in the absolute magnitude. The Frogel et al. (1981) method result agrees with the distance estimate found using the absolute magnitude of the red clump stars in Mercer 5. Using the metallicity derived via the slope of the red giant branch, [Fe/H]~0.78, which corresponds to ~-6.4 mag, yields a distance modulus that is nearly identical to that used for an averaged metallicity and M_{TIP}. Rather than use the equations provided in Ferraro et al. (2000), only a rough estimate is considered. The bolometric magnitude for the brightest star is not determined, and the results of the computations span only a small range (see, for example, Table 7, which M_{TIP} varies by only about one magnitude).

Table 7 Taken from Table 6 of Ferraro et al. 2000. Last row shows averaged values for each column.		
[Fe/H]	m-M	M_{TIP}
-2.12	15.15	-5.67
-1.99	15.14	-5.60
-1.91	14.71	-6.05
-1.61	13.82	-6.07
-0.87	13.95	-6.35
-0.70	13.32	-6.57
-0.68	14.64	-6.84
-0.68	14.64	-6.21
-0.44	13.46	-6.87
-0.38	14.37	-6.73
-1.14	*14.32*	*-6.30*

3.1.5. X-ray Source

XMM observations of the nearby carbon rich WC5 star WR114 reveal an X-ray source coincident with the position of Mercer 5 (Oksinova et al. 2003). This source is located slightly off center from the cluster center, within the positional accuracy of XMM, as shown in Figure 22. The flux of the source is 0.04+/-0.005 counts s^{-1}. Assuming the X-ray source originates in the cluster, e.g. the source is at the same distance as Mercer 5, the X-ray flux is consistent with that expected from a population of unresolved soft X-ray binaries. Deeper X-ray observations are required to determine the exact nature of this X-ray source, and to confirm the possible association with Mercer 5.

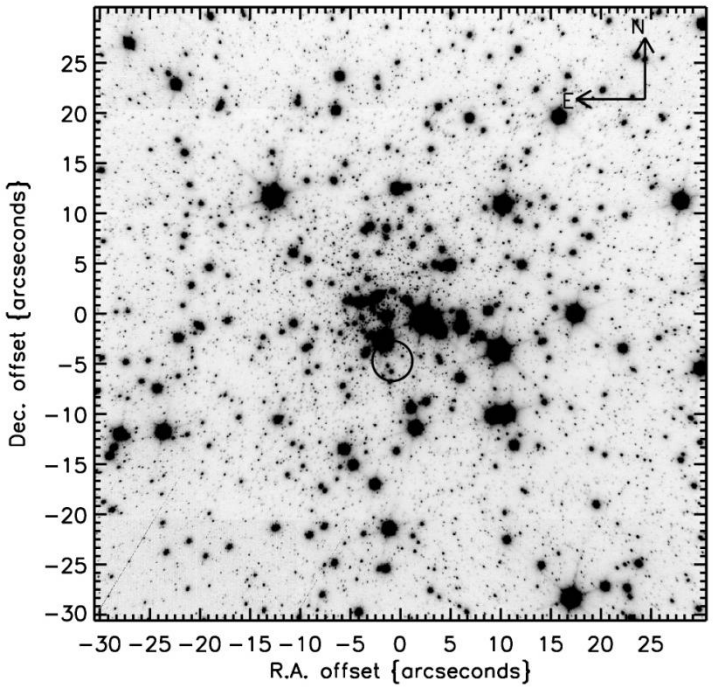

Figure 22 Ks band image of Mercer 5 with X-ray source position indicated. The circle is the size of the positional error of XMMU J182319.8-134011, 2”

3.1.6. Summary

Mercer 5 is a newly discovered globular cluster in the Galactic disk. Due to the nature of globular clusters, it is immediately discounted from the final high end IMF slope study.

3.2. Mercer 14

The HST CMD, Figure 23,of Mercer 14 does not reveal an obvious main sequence. No objects in Mercer 14 were identified as having a m_{F190N}-m_{F187N} excess, suggesting an absence of evolved massive stars.

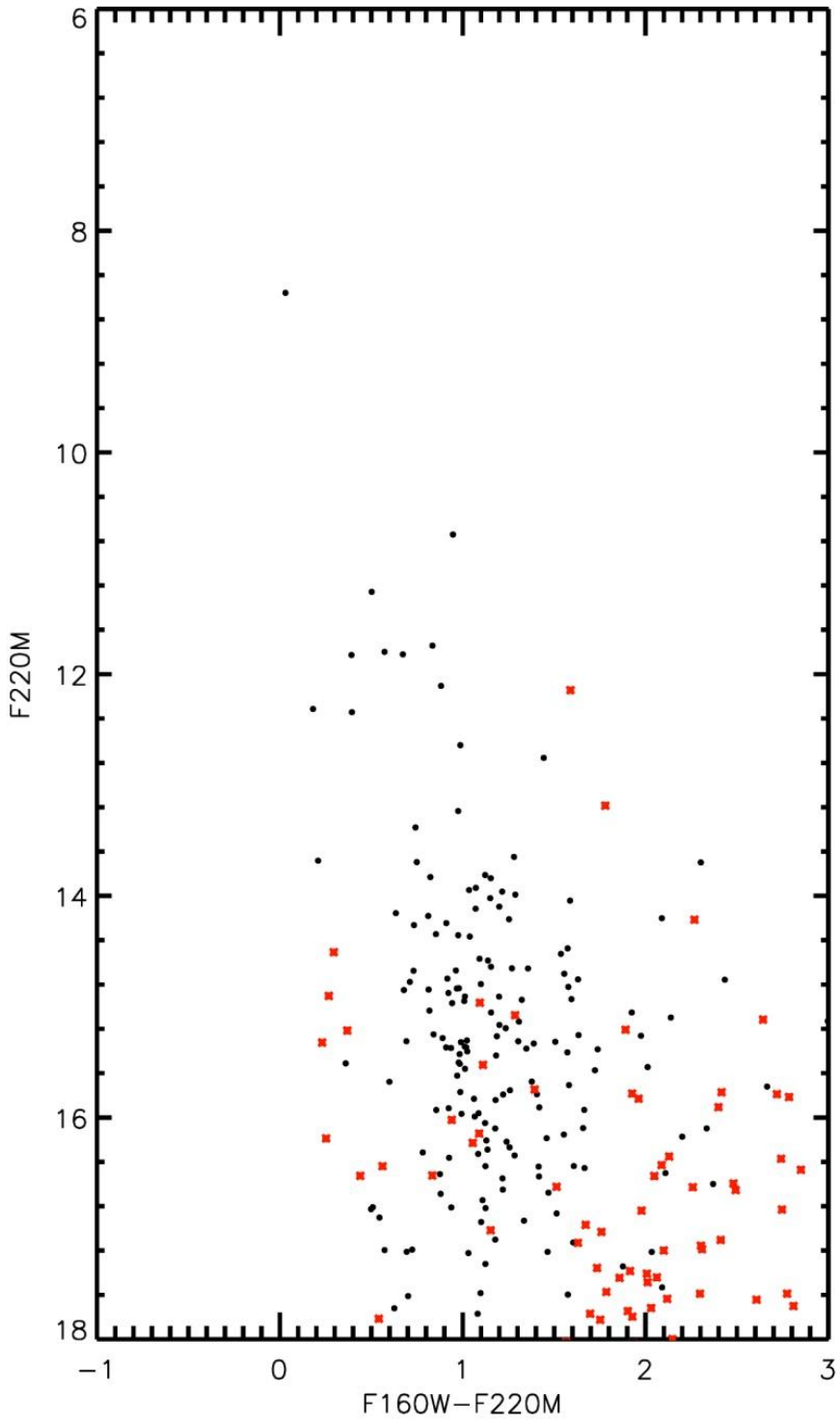

Figure 23 Mercer 14 CMD. Control field photometry is indicated by red astericks while cluster photometry is displayed by black circles.

Mercer 14 is the subject of a study by Froebrich & Ioannidis (2011), who present a multiwavelength analysis of the cluster and surrounding region. These authors find evidence for H_2 flows, signs of ongoing massive star formation, and disk-dominated objects (young stellar objects, YSOs), using archival NIR observations (UKIDSS, GLIMPSE, UWISH2). Freobrich & Ioannidis (2011) determine a distance of ~2.5 kpc to Mercer 14, based on stellar number counts and comparison with Besancon models. While no spectroscopy is presented in the paper, these authors use NIR photometry to estimate that the three brightest stars are roughly 20 $M_{\odot}$ each, and use the M_{max}-M_{ecl} relation of Weidner & Kroupa (2006) to estimate a total cluster mass of 500 $M_{\odot}$.

3.2.1. Summary

The low total cluster mass of Mercer 14, as indicated by the low spatial density and lack of obvious MS in the CMD, along with the shortage of massive stars make this cluster ill-suited for a study of the high end IMF. Mercer 14 is therefore rejected from the final sample.

3.3. Mercer 17

Interpretation of the CMD of Mercer 17, Figure 24, is not entirely clear. Spectroscopic follow-up of the brightest stars in the cluster do not help to clarify the situation, as all objects observed were found to be cool stars. It is possible this is a somewhat spurious detection, similar in nature to Mercer 14. A clear red giant branch or red clump are not discernable in the CMD, as would be the case for a dense older (>100 Myr) cluster. Even for an intermediate aged open cluster, it is likely that some age-defining features would be seen in the CMD. Mercer 13, an older cluster in the sample of Mercer at al. (2005), shows a clear clump of stars in the CMD, which are found to be cool giants (Messineo et al. 2009). The CMD of Mercer 17, however, is devoid of similar features and cannot be easily disentangled from the control field population (plotted with red asterisks in Figure 24).

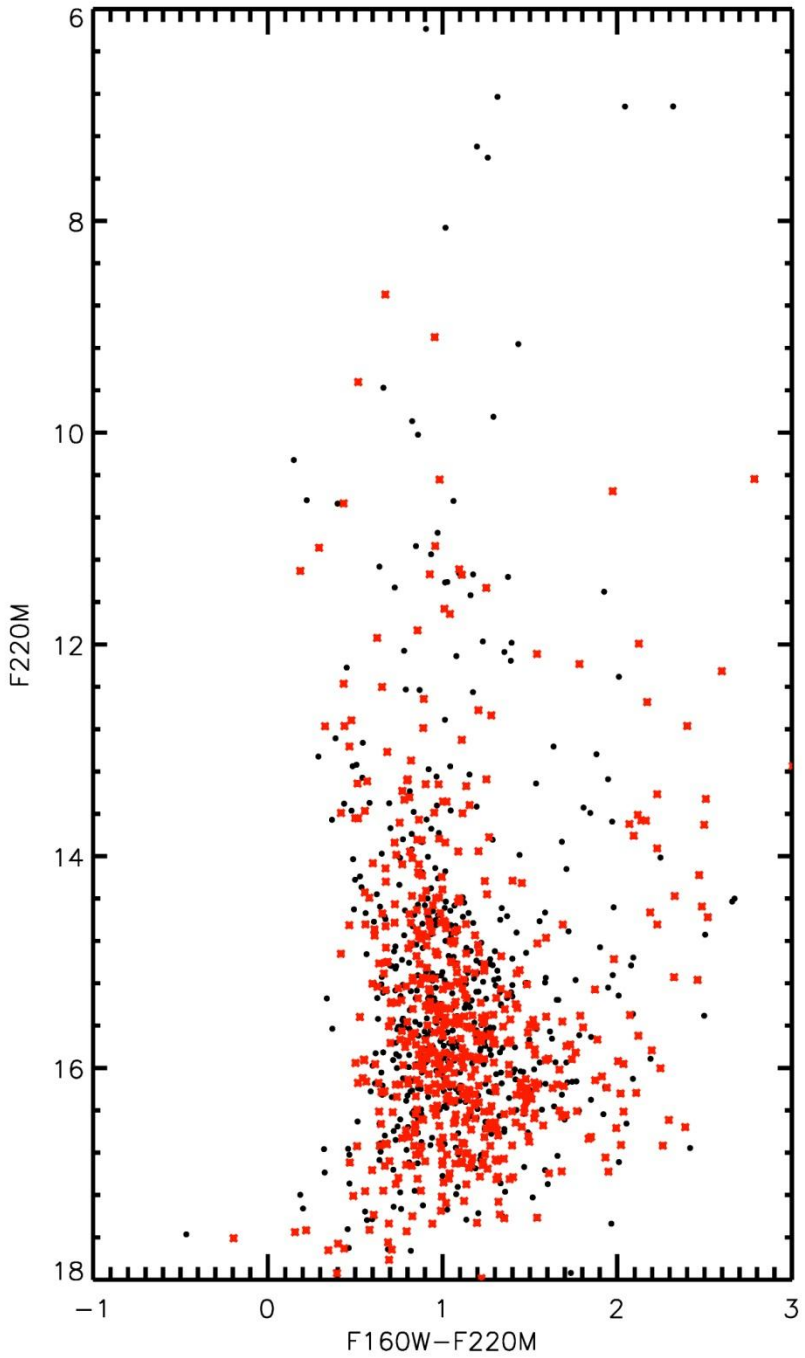

Figure 24 Mercer 17 HST CMD

3.3.1. Stellar Content

Thirteen objects in Mercer 17 were observed spectroscopically as part of the NASA IRTF/SpeX runs on 8 September 2012 and 18 September 2012.

3.3.1.1. Spectral Typing

All spectroscopically observed objects in Mercer 17 contain a CO bandhead feature at 2.29 microns in the K-band, as displayed in Figure 25. All 13 objects are cool, late type stars. In order to determine the precise spectral type of each object, comparison with the IRTF/SpeX IR library of cool stars is required. This analysis is beyond the scope of the work presented here, and has not been completed. After spectral typing, a measurement of the EW of the CO bandhead feature of the Mercer 17 stars and atlas stars would prove beneficial in determining the luminosity class of these objects (see Figure 18 above for an example of this method). For comprehensiveness, the target list with coordinates is listed in Table 8.

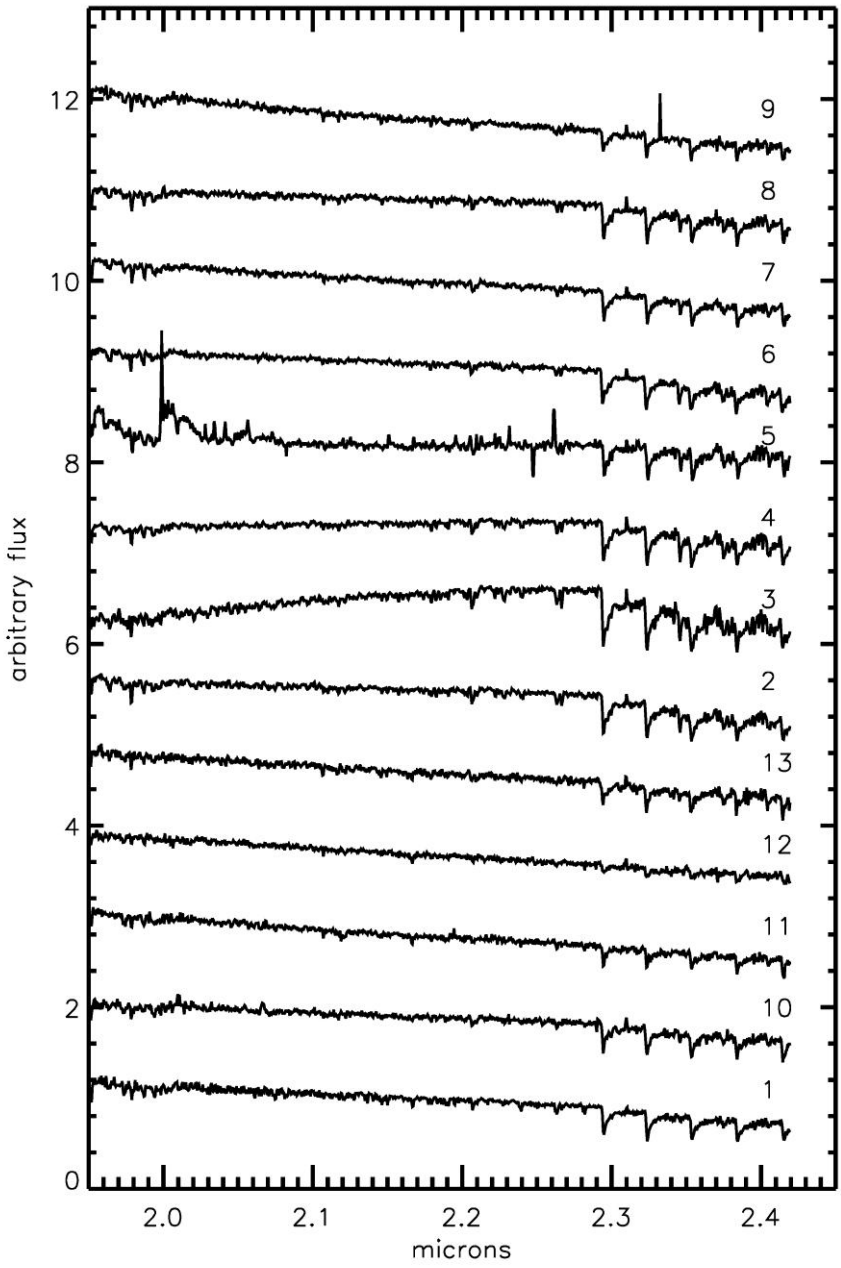

Figure 25 K-band spectra of objects in Mercer 17 observed with IRTF/SpeX

Table 8 Spectroscopic observations of stars in Mercer 17					
ID	RA	Dec	m_{F160M}	m_{F222M}	SpType
1	19 09 20.24	+08 11 34.83	7.09	6.19	late type/cool
2	19 09 18.79	+08 11 27.32	8.14	6.83	late type/cool
3	19 09 19.16	+08 11 13.88	9.24	6.92	late type/cool
4	19 09 19.83	+08 11 16.26	8.96	6.92	late type/cool
5	19 09 18.65	+08 11 38.27	8.50	7.30	late type/cool
6	19 09 18.98	+08 11 46.03	8.66	7.40	late type/cool
7	19 08 18.79	+08 11 37.67	9.08	8.06	late type/cool
8	19 09 20.08	+08 11 59.75	10.60	9.16	late type/cool
9	19 09 20.00	+08 11 47.92	10.24	9.58	late type/cool
10	19 09 20.77	+08 11 16.73	11.14	9.85	late type/cool
11	19 09 17.72	+08 11 38.74	10.72	9.89	late type/cool
12	19 09 18.46	+08 11 15.81	10.88	10.02	late type/cool
13	19 09 19.65	+08 11 18.80	11.71	10.65	late type/cool

3.3.2. Summary

Mercer 17 is rejected from the final sample based on the lack of hot stars.

3.4. Mercer 20

The candidate cluster Mercer 20 was examined by Messineo et al. (2009) and confirmed to be a young, massive cluster. These authors present spectroscopy of the brightest objects and establish the age, distance, reddening, and total mass of the cluster as part of a larger study of newly discovered candidate clusters. Messineo et al. (2009) estimate a distance of 3.5 kpc, an age of 6-8 Myr, and a mass of ~3400 $M_{\odot}$.

3.4.1. Stellar Content

Mercer 20 was observed as part of the VLT/ISAAC southern spectroscopic follow-up program, as well as with the SofI spectrograph at ESO/NTT (4 July 2007), see also Messineo et al. (2009) for details on the spectroscopic data reduction and classification. A MS and emission line objects can be identified in Figure 26, where the latter are shown as green star symbols. The control field photometry is overplotted in Figure 26 in red asterisks, as a representation of the expected fore- and background contamination. Table 9 lists the objects spectroscopically observed as part of the VLT program and important objects from Messineo et al. (2009). The VLT spectra are plotted in Figure 28, and the spectroscopically calibrated CMD is shown in Figure 30.

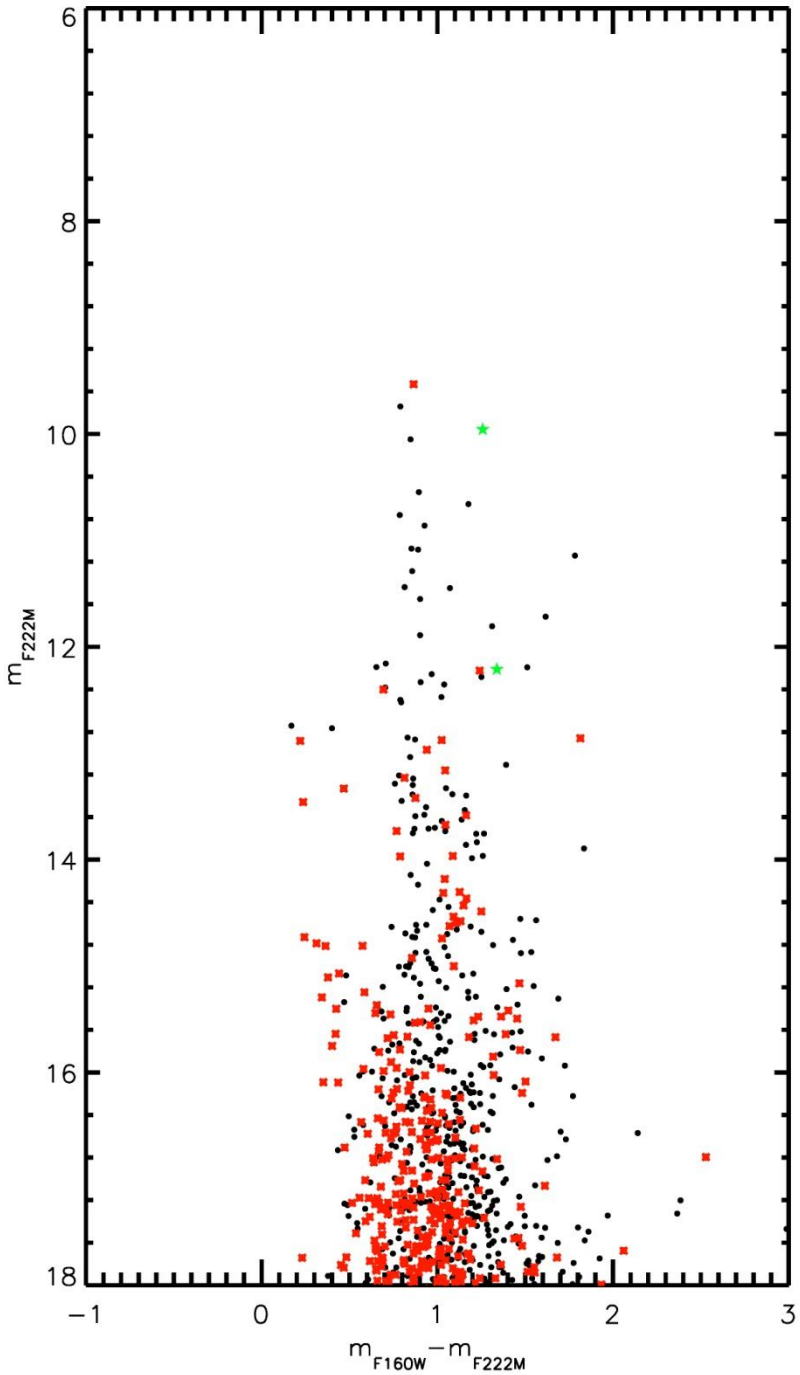

Figure 26 Mercer 20 HST CMD

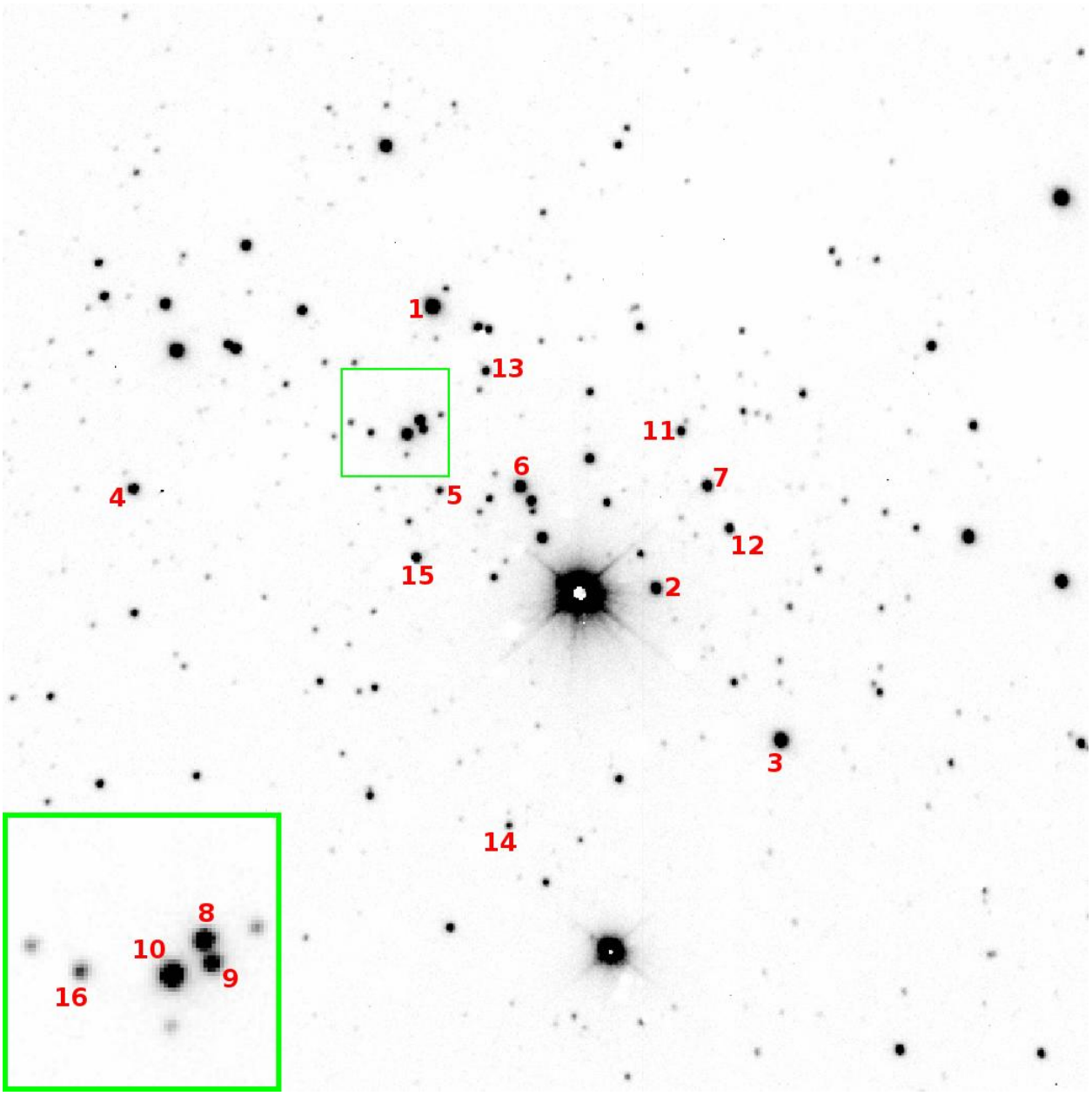

Figure 27 ISAAC finding chart for Mercer 20

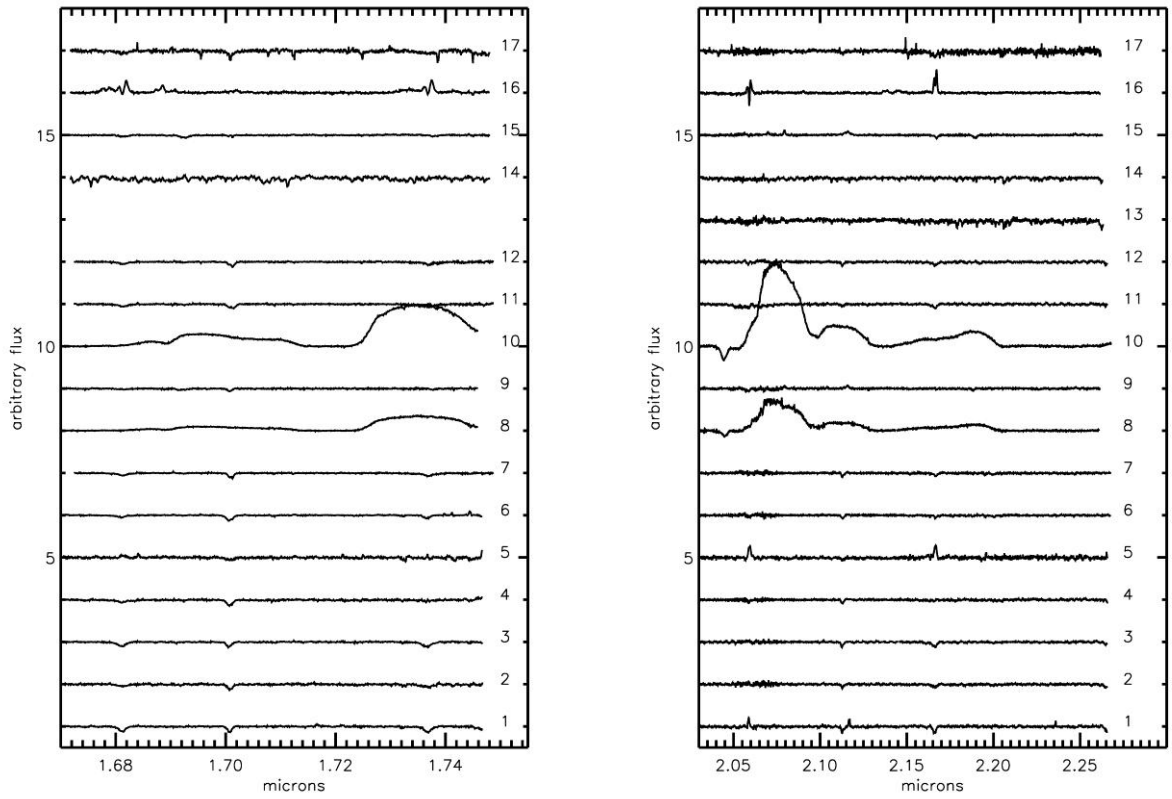

Figure 28 Mercer 20 H (left) and K (right) band VLT/ISAAC spectra

3.4.1.1. Spectral Typing

Two stars in Mercer 20 contain metal lines of FeI, MgI, and NaI, indicative of a cool nature, in their H and K band spectra: Mc20-13 and Mc20-14. These stars are most likely fore- or background objects along the same line of sight as Mercer 20.

Mc20-1, Mc20-3, and Mc20-6 present spectra with HeI absorption features at 1.68 and 1.700 microns, HI absorption at 1.737 microns in the H band, HeI absorption at 2.112 and H absorption at 2.166 (Brγ) in the K band, suggesting spectral types later than O9 but earlier than B4. The shape of the Brγ line in Mc20-1 indicates a supergiant luminosity class, while Mc20-6 and Mc20-3 are more uncertain. Though ambiguous, the Brγ line profile in both stars is more consistent with a giant luminosity class, rather than supergiant class. Additionally, Mc20-6 contains strong emission lines, leading to a final spectral classification of O9-B3 Ve-IIIe for this star.

Though not contained in the HST/NIC3 field of view, Mc20-4 is a likely cluster member. The spectrum of this star displays absorption lines at 1.68 and 1.700 microns, with weak absorption at 1.693 microns,

indicating a spectral type between O7 and O9. The blended HeI absorption/NIII emission multiplet, along with weak Brγ and H absorption at 2.058 microns, are all consistent with this spectral classification.

Four stars in Mercer 20 display very similar spectral features, Mc20-2 (O9-B0 I), Mc20-7 (O9-B0 I-II), Mc20-11 (O9-B0 I-II), and Mc20-12 (O9 I-II). In the H-band, absorption features at 1.68, 1.700, and 1.737 microns are present. Additionally, 2.112 micron and Brγ absorption are present in the K-band spectra of all four stars. Given the line strengths and lack of other absorption or emission features, a spectral type of O9-B0 is assigned to all four objects.

The spectra of Mc20-8 and Mc20-10 are nearly identical, though Mc20-10 has stronger C and He emission lines. The spectra of both stars is strongly similar to WC5-7 stars in the atlas of Figer et al. (1997).

The spectrum of Mc20-5 contains Hydrogen emission lines characteristic of a Be star. No evidence of forbidden emission is observed, ruling out the B[e] classification (interestingly, this object is located at a similar position in the color-magnitude diagram as Mc20-16, see discussion of this star below). HeI absorption at 1.700 and 1.737 microns is present in the spectrum, along with HeI absorption at 2.112/3, indicating a spectral type later than O9.

Strong 1.693 micron absorption, stronger than absorption at 1.680, 1.700, or 1.737 micron absorptions, in Mc20-15 indicates an early spectral type for this star, between O4 and O5. Strong NII and CIV emission lines in the K-band spectrum, along with Brγ and HeII absorption, support the O4-5 If classification. The H-band H and He absorption lines in Mc20-9 are very similar to Mc20-5, with stronger HeI absorption at 1.700 and weaker HeII absorption in the K-band. This suggests a slightly later spectral type, O5.5 to 6.5 If, where the luminosity class is determined by the shape of the Brγ absorption profile.

The spectral type of Mc20-17 is difficult to determine, as the reduction was complicated by three factors: faintness of the source, long exposure time required, and the rapidly varying sky conditions. However, this spectrum displays HeI and HI absorption features commonly observed in O9-B0 type stars.

The spectral type of the brightest star in the field, G20-1, is taken from Messineo et al. (2009). Though unlabeled in Figure 27, this star is easily identifiable as the brightest object in the field of view. In addition, it displays the characteristic signs of saturation in the ISAAC finding chart. Messineo et al. (2009) find G20-1 to be a cool, yellow supergiant associated with the cluster.

G20-3 was observed as part of the ISAAC program, but is also present in the analysis presented by Messineo et al. (2009). These authors find a spectral type of B1-2 I, consistent with the results found here

(the lack of 1.693 micron absorption indicates a spectral type later than O9). The shape of the Brγ absorption feature is consistent with a supergiant luminosity classification. G20-4 was also re-observed and found to be of similar spectral type, though the shape of the Brγ feature is slightly more ambiguous.

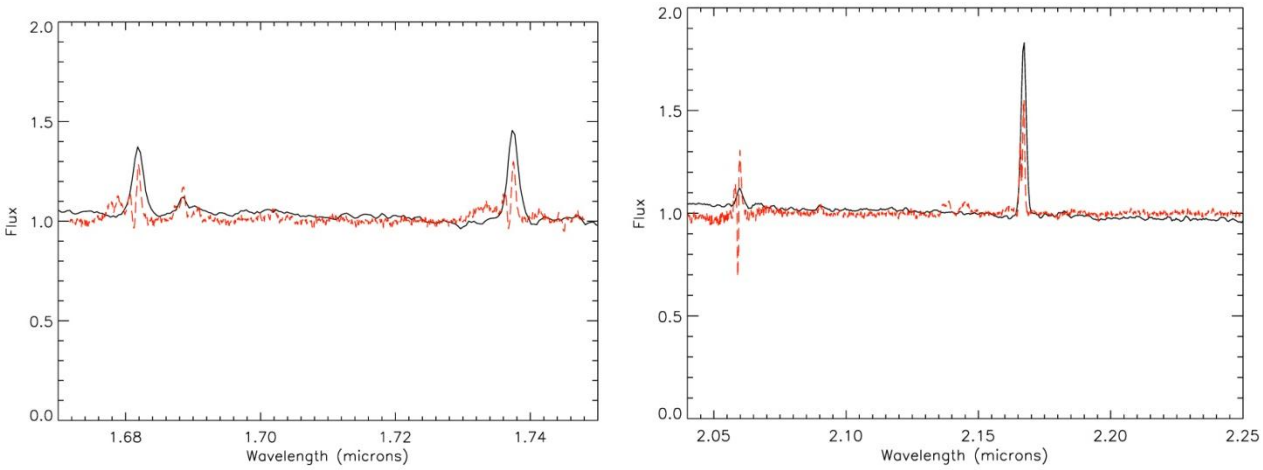

Figure 29 H (left) and K (right) band spectra of IRAS06071+2958 (solid black) and Mc20-16 (dashed red)

The faint star Mc20-16 presents with strong Hydrogen emission lines and forbidden metal lines, as evidenced in Figure 28 (as labeled) and Figure 29 (dashed red lines). Given the photometry of this star, a candidate LBV classification is ruled out (see also discussion of Mc70-14 below), leading to a B[e] classification. Comparison with the spectrum of FS CMa star (non-supergiant, unclassified B[e] star) IRAS06071+2958 (Figure 29, solid black line) reveals many similarities (Miroschnichenko 2007; Miroschnichenko et al. 2009). IRAS0607+2958 was observed at IRTF/SpeX on 20 January 2013. The resolution of SpeX (R~2000) is roughly half that of ISAAC (R~4000), so the double peaked Hydrogen lines present in Mc20-16 are not resolved in IRAS0607+2958. However, this provides compelling support for the FS CMa B[e] classification of Mc20-16.

A summary of the spectral type analysis of objects in Mercer 20 is given in Table 9, and graphically represented in Figure 30. The red dashed line in this figure indicates a 6 Myr MS isochrone. Isochrones are degenerate in the infrared, especially when the color is computed between two close filters, such as F160W and F222M. Larger separation of filters, e.g. J-K rather than H-K, tend to make isochrone features more obvious.

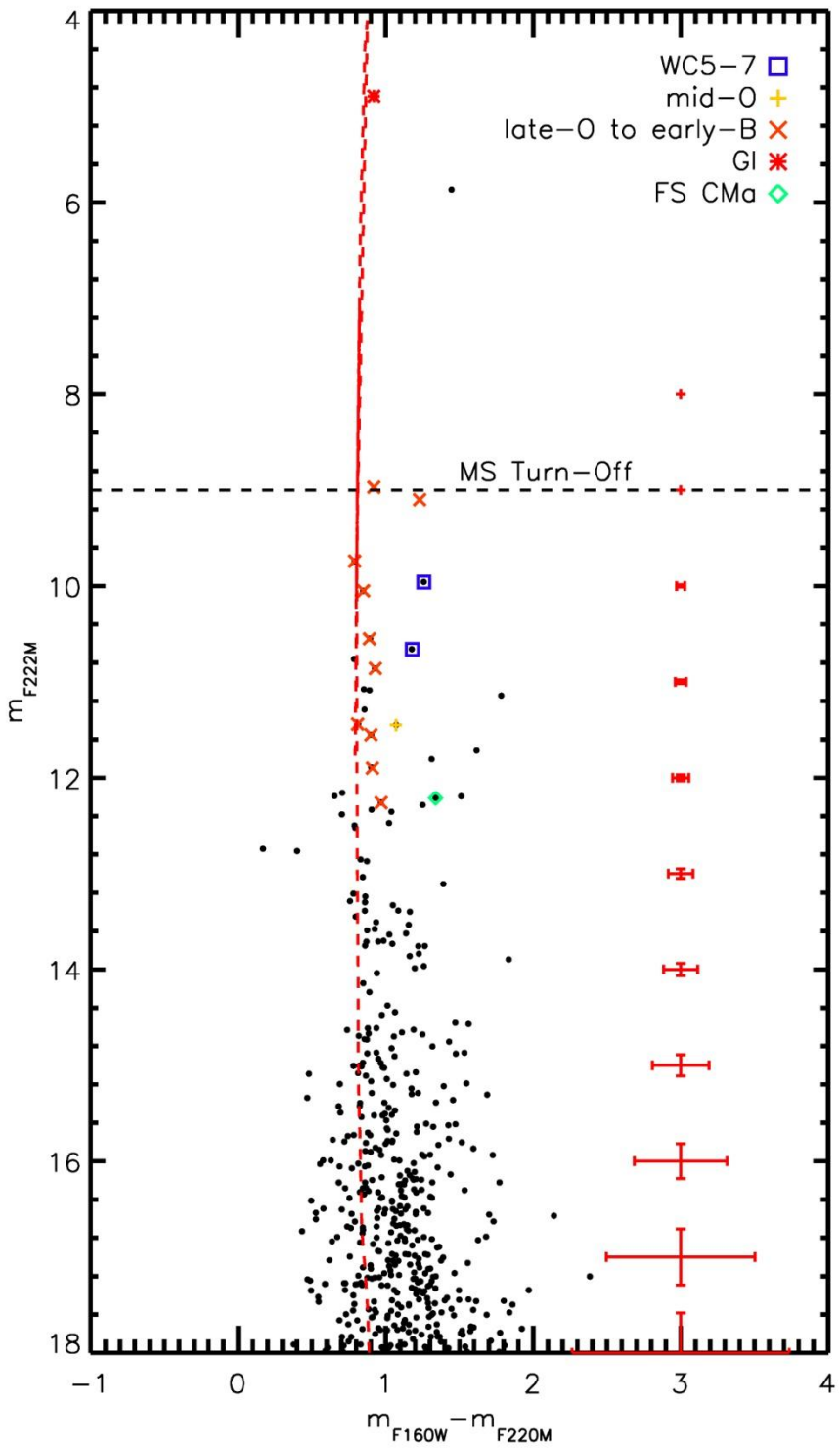

Figure 30 Mercer 20 CMD with spectral types labeled; some spectral types taken from Messineo et al. (2009)

Table 9 Summary of spectroscopic observations of stars in Mercer 20					
ID	RA	Dec	m_{F160W}	m_{F222M}	SpType
1	Not in fov				B0-2 I
2	19 12 23.3	+09 57 4.21	11.44	10.55	O9.5-B0.5 I
3	19 12 23.2	+09 56 46.0	10.53	9.74	B1-3 III-I
4	Not in fov				O7-O9
5	19 12 24.2	+09 57 22.6	13.23	12.26	Be
6	19 12 12.7	+09 57 18.9	10.32	9.1	O9-B3 Ve-IIIe
7	19 12 22.7	+09 57 9.82	11.79	10.86	O9-B0 III-I
8	19 12 24.1	+09 57 29.1	11.84	10.66	WC5-7
9	19 12 24.1	+09 57 28.2	12.52	11.45	O5.5-6.5 If+
10	19 12 14.4	+09 57 28.6	11.22	9.96	WC5-7
11	19 12 22.7	+09 57 15.5	12.45	11.55	O9-B0 III-I
12	19 12 22.7	+09 57 5.34	12.25	11.44	O9-B0 III-I
13	19 12 23.5	+09 57 29.7	12.93	11.14	late type/cool
14	19 12 24.9	+09 56 52.7	13.71	12.19	late type/cool
15	19 12 24.5	+09 57 18.4	11.98	11.09	O4-5 If
16	19 12 24.4	+09 57 30.5	13.55	12.21	FS CMa
17	Not in fov				O9-B3 I-III
2MASS J19122577+0957381	19 12 24.1	+09 57 22.7	12.81	11.9	B0 Ia
G20-1	19 12 23.7	+09 57 08.1	5.81	4.89	GI
G20-3	19 12 23.6	+09 57 38.0	9.89	8.97	B1-B2 I
G20-4	19 12 23.7	+09 57 18.9	10.9	10.05	B0-B1 I

3.4.2. Age, Reddening, Distance, Mass

The presence of the yellow hypergiant is the strongest constraint on the age of Mercer 20. Stellar evolutionary models predict a yellow supergiant phase for stars with initial masses from 12 to 60 $M_{\odot}$. For a 60 $M_{\odot}$ initial mass star, LogTeff = 3.87 is reached after 4.5 Myr. However, this object is predicted to be significantly brighter than that observed in Mercer 20, L/Lsol ~ 6.12. For a 40 $M_{\odot}$ initial mass star, the same temperature is reached after 5.7 Myr, with a luminosity consistent with that of the yellow supergiant G20-1 in Mercer 20. This can be taken as the lower limit on the age of the cluster, assuming coeval evolution. The presence of WR stars set the upper age limit to ~8 Myr, again according to stellar evolutionary models. However, the presence of mid-O supergiants in Mercer 30 contradicts the lower limit on the age set by G30-1. Combined with the presence of WR stars, an age of 3-4 Myr is preferred. For the purposes of this work, the age of Mercer 20 is taken to be 6-8 Myr. As demonstrated below, the age of the cluster does not have a large impact on the measured slope of the IMF.

Extinction towards the cluster is computed by examining the NIR colors of "normal" O and B type stars, i.e. emission line stars or clearly heavily reddened stars are excluded. For Mercer 20, an average value of A_K=1.37 is found (using 7 stars).

Spectrophotometric distance estimates based on VLT/ISAAC observations indicate a distance of 4.40+/-0.33 kpc, somewhat larger than the distance found by Messineo et al. (2009) but within the error estimates (these authors find a distance of 3.8+/-1.3 kpc to the cluster). The table of spectrophotometric measurements, Table 10, highlights the most likely distance/luminosity class combination in bold. The MS is the best calibrated in terms of luminosity (e.g. supergiants can span two or three orders of magnitude in luminosity), only objects consistent with belonging on the MS are used to calculate the distance to Mercer 20.

Table 10 Derived spectrophotometric distances of stars in Mercer 20, using the absolute K-band magnitudes of Martins & Plez (2006) and Crowther et al. (2006)

ID	m_{F222M}	SpType	D_V/kpc	D_{III}/kpc	D_I/kpc	D_{WR}/kpc
2	10.55	O9.5-B0.5	2.49-2.84	4.78-5.13	14.58-9.20	
3	9.74	B0-1	1.85	4.06	5.32	
7	10.86	O9-B0	3.00-3.21	5.58-5.79	16.46-10.39	
10	9.96	WC5-7				4.93
11	11.55	O9-B0	**4.19-4.49**	7.81-8.10	23.04-14.54	
12	11.44	O9-B0	**4.25-4.55**	7.91-8.21	23.35-14.73	
2mass-2	11.9	B0	**4.90-5.25**	9.13-9.47	26.94-17.00	
G20-3	8.97	B1-B2 I	0.97-1.35	2.06-2.44	5.06-4.02	
G20-4	10.05	B0-B1	1.92-2.19	3.82-4.23	12.02-7.58	

Messineo et al. (2009)find a mass of ~3400 $M_\odot$ for Mercer 20. A mass of ~2300 $M_\odot$ is found by measuring the slope of the initial mass function and integrating from 0.5 to 150 $M_\odot$. The slope is shallower than Salpeter; the cluster age is set to 6 Myr and the distance set to 4 kpc in this calculation. For more detail on this mass measurement method and the associated errors, see Equation 5.

3.4.3. Summary

Though Mercer 20 has a slightly higher age than the rest of the clusters in the IMF sample, it contains a clear MS and MS turn-off that make an IMF slope measurement robust. The mass interval probed in Mercer 20 is 2-16 $M_\odot$, which is closer to an intermediate mass slope measurement than a high mass slope measurement.

3.5. Mercer 23

The candidate cluster Mercer 23 has been previously studied by Hanson et al. (2010). Mercer 23 contains evolved massive stars, some noted in Hanson et al. (2010) and some newly discovered in the VLT/ISAAC spectroscopic follow-up study. The color-magnitude diagram of this cluster, Figure 31, clearly shows a MS well separated from field stars (as interpreted from the control field photometry, plotted with red asterisks in Figure 31).

3.5.1. Stellar Content

The stellar content of Mercer 23 is derived from previous work (Hanson et al. 2010) and more recently obtained VLT/ISAAC spectra. The newly obtained spectra (see finding chart, Figure 32) are displayed in Figure 33. As evidenced in Figure 34, cool fore- and background stars contaminate the cluster sequence in several places. These objects are not cluster members, and so are removed from the diagram before the application of stellar evolutionary models to avoid artificial inflation of bins in the initial mass function.

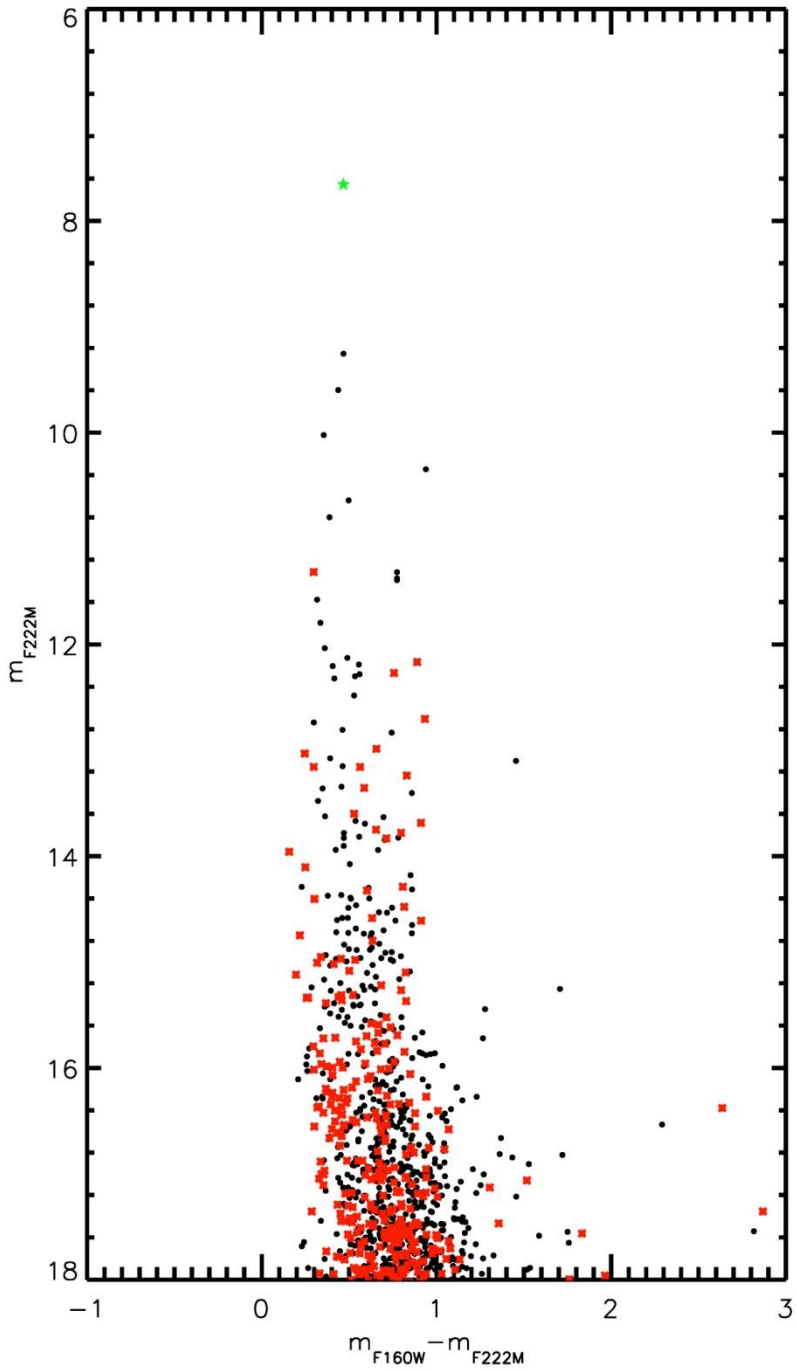

Figure 31 HST CMD of Mercer 23

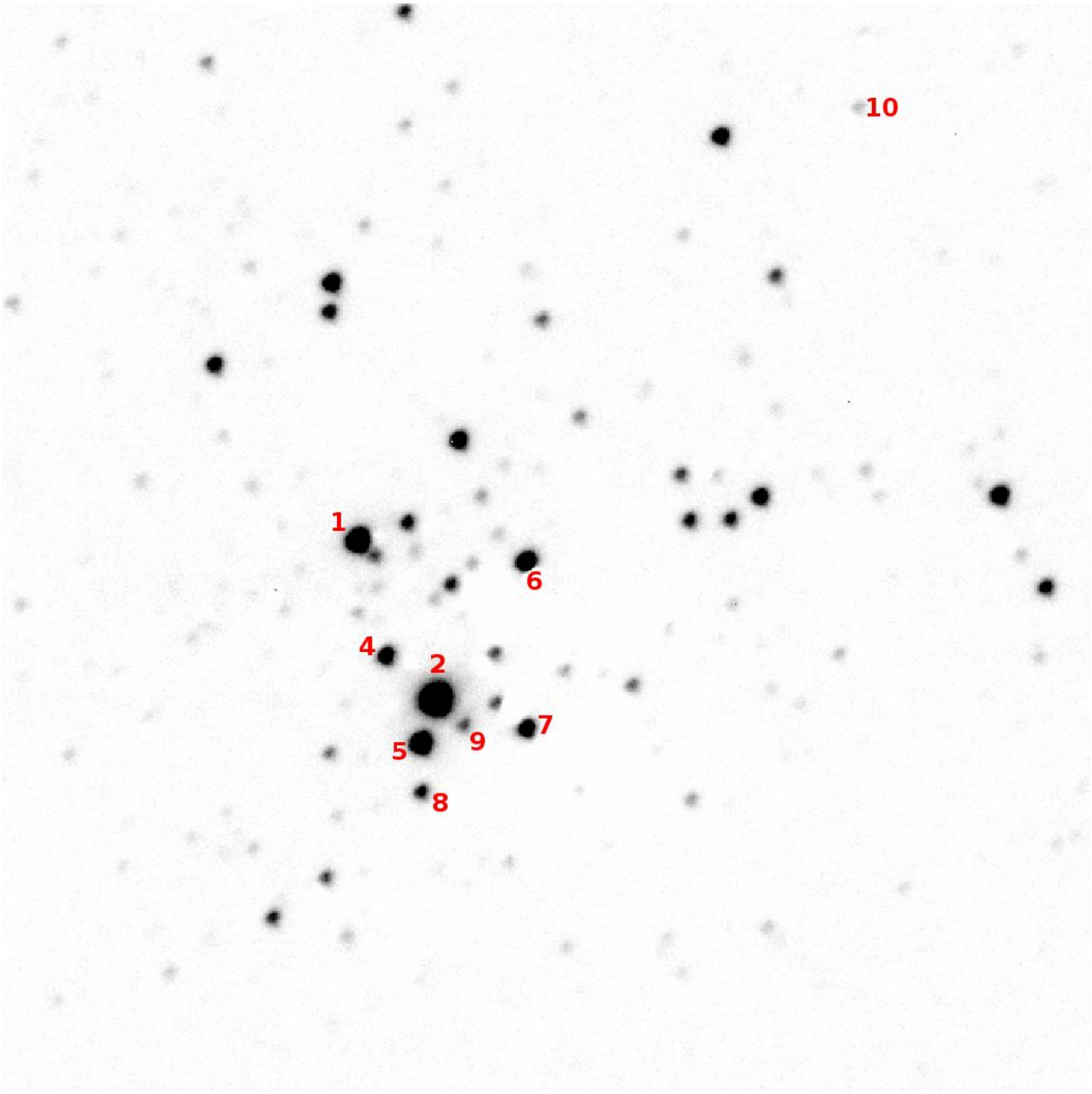

Figure 32 ISAAC finding chart for Mercer 23, showing the position of target stars in the cluster.

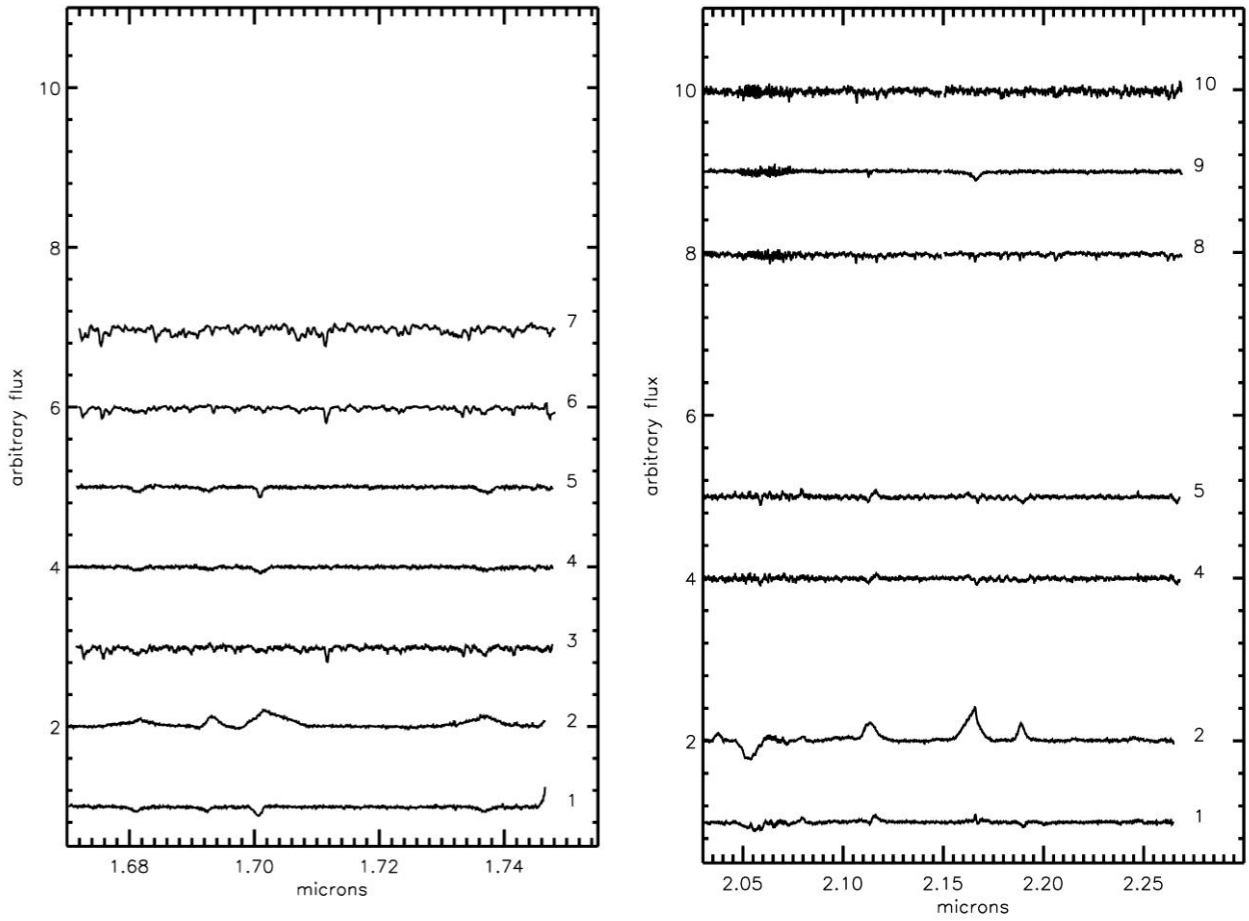

Figure 33 ISAAC spectral of stars in Mercer 23; H-band is on the left and K-band is shown on the right.

3.5.1.1. Spectral Typing

Mercer 23 spectra are shown in Figure 33. Five objects, Mc23-3, -6, -7, -8, and -10 contain metal absorption lines of FeI, MgI, and NaI, characteristic of cool, late type stars and are likely foreground giants. Mc23-3 and Mc23-10 are not in the field of view of the HST/NIC3 observations.

The spectra of Mc23-2 show broad emission lines characteristic of nitrogen subtype WR stars. Comparison with the atlas of Figer et al. (1997) suggests a spectral type of WN7 for this star.

Two stars, Mc23-4 and Mc23-5, show HeI and HeII absorption in the H band at 1.68, 1.70, 1.737, Brγ absorption in the K band as well as HeI(2.112/3) absorption + NII emission, and weak HeII (2.188) absorption. After comparisons with the spectral atlas of Hanson et al. (2005), these stars are classified as O6-7 and O7-8 respectively, based on the slightly different line strengths.

Mc23-1 has a similar H band spectrum to Mc23-4 and Mc23-5, but shows a different Brγ line profile. In addition, CIV emission at 2.078 micron is present, indicating a spectral type of O5-O6.

The last object, Mc23-9, shows Brγ absorption, narrow HeI (2.112/3 micron) absorption, and weak HeII absorption (2.188 micron), consistent with an O9-B2.5 classification.

The results of spectral typing are listed in Table 11 and displayed graphically in Figure 34. The red dashed line in this figure indicates a 4 Myr MS isochrone, while the dashed blue line indicates a 2 Myr pre-MS isochrone. Objects redward of the pre-MS isochrone are interpretted as pre-MS stars younger than 2 Myr still evolving along Hayashi tracks.

Table 11 List of stars spectroscopically observed

ID	RA	Dec	m_{F160W}	m_{F222M}	SpType
1	19 30 13.4	+18 32 18.7	9.25	8.12	O5-O6 III-I
2	19 30 13.6	+18 32 02.7	8.12	7.77	WN7
3	Not in fov				late type/cool
4	19 30 13.7	+18 32 8.66	11.19	10.79	O7-O8 V-III
5	19 30 13.9	+18 31 0.33	10.04	9.60	O6-O7 II-III
6	19 30 12.6	+18 32 7.44	10.38	10.02	late type/cool
7	19 30 13.3	+18 31 55.2	11.28	10.35	late type/cool
8	19 30 14.1	+18 31 56.7	12.15	11.38	late type/cool
9	19 30 13.6	+18 31 59.1	12.74	12.32	O9-B2.5
10	Not in fov				late type/cool

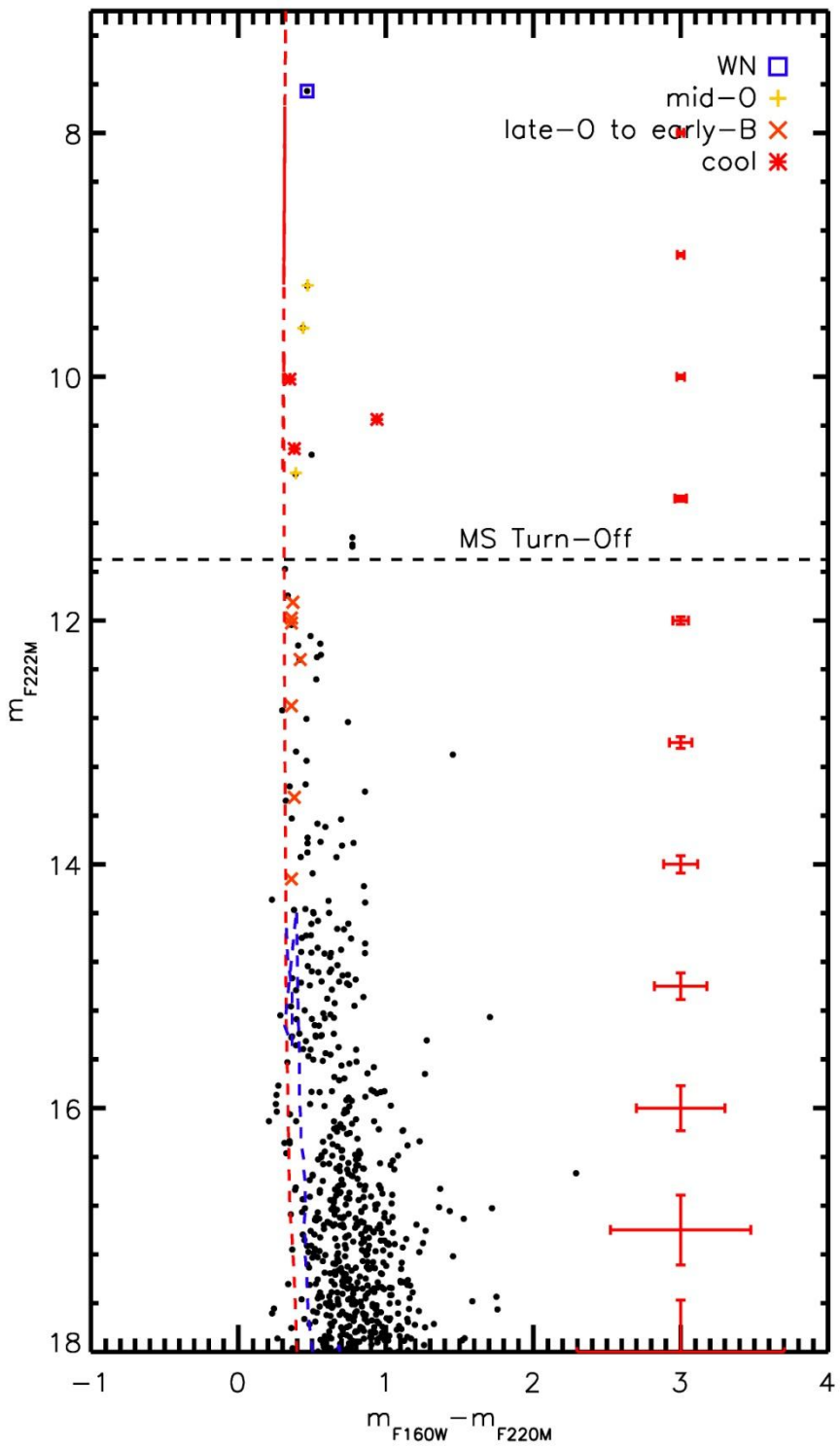

Figure 34 Mercer 23 CMD with labeled spectral types. Some spectral types taken from Hanson et al. (2010)

3.5.2. Age, Reddening, Distance, Mass

Hanson et al. (2010) find an age of 2-4 Myr for Mercer 23 by using the MS turn-on and pre-MS fitting. These authors present non-LTE spectral modeling of the WR star in Mercer 23, finding an 80 $M_{\odot}$ initial mass progenitor for this star. Their results imply an upper limit of ~4 Myr on the age. An upper limit of 5-6 Myr is found, based on the spectral types at the MS turn-off stars (spectroscopically observed by Hanson et al. 2010). The presence of the WN7 star, Mc23-2, suggests a minimum age of 3 Myr.

Extinction towards the cluster is computed by examining the NIR colors of "normal" O and B type stars, i.e. emission line stars or clearly heavily reddened stars are excluded. For Mercer 23, an average value of A_K=0.59 is found for stars with HST photometry and ISAAC spectra.

Hanson et al. (2010) derive a spectrophotometric distance of 6.5+/-0.3 kpc for Mercer 23. Spectrophotometric distance estimates of stars in Hanson et al. (2010) and the mid- to late-O stars observed in the VLT/ISAAC program (Mc23-1, -4, and -5) yield a similar distance estimate of roughly 6.5 kpc, which is consistent with the results of Hanson et al. (2010).

Assuming a Salpeter IMF, Hanson et al. (2010) find a mass of 4-6(10^3) $M_{\odot}$ as a lower limit for Mercer 23. Assuming an age of 4 Myr and a distance of 7 kpc, application of a SalpeterIMF integrated from 0.5-150 $M_{\odot}$ yields a slightly lower mass of 2000 $M_{\odot}$ for the observations presented here.

3.5.3. Summary

Despite a comparatively lower total mass than other clusters in the sample, Mercer 23 contains massive, evolved stars, a clearly massive MS, and a clear MS turn-off, making it an ideal candidate for IMF slope measurement. The mass range for slope measurement is similar to Mercer 20, 2.5-20 $M_{\odot}$, making Mercer 23 a good fit in the IMF slope sample of clusters.

3.6. Mercer 30

Though Mercer 30 has been studied by other authors (Kurtev et al. 2007), a more thorough analysis suggests that this cluster is both more distant and more massive than the literature suggests. Spectrophotometric distance estimates put the cluster at 10-12 kpc from the Sun, while a radial velocity analysis of the BIa star (de la Fuente et al. in prep) assigns a distance of 11 kpc. The narrow-band HST filters reveal the presence of at least five emission line stars, as can be seen in the three color diagram Figure 107 in Appendix A, which are indicated by green stars in the CMD presented in Figure 35.

3.6.1. Stellar Content

The HST CMD in Figure 35 shows several bright emission line objects, suggesting that Mercer 30 is both massive and young. The control field observations imply that the blue plume at m_{F160W}-m_{F222M}~0.25 is due to the contribution of a foreground population, and not related to the cluster.

Mercer 30 was observed as part of the southern spectroscopic follow-up program at VLT/ISAAC, PI de la Fuente. The results of this program are shown in Figure 36, with numbers corresponding to the labels in the finding chart shown in Figure 37.

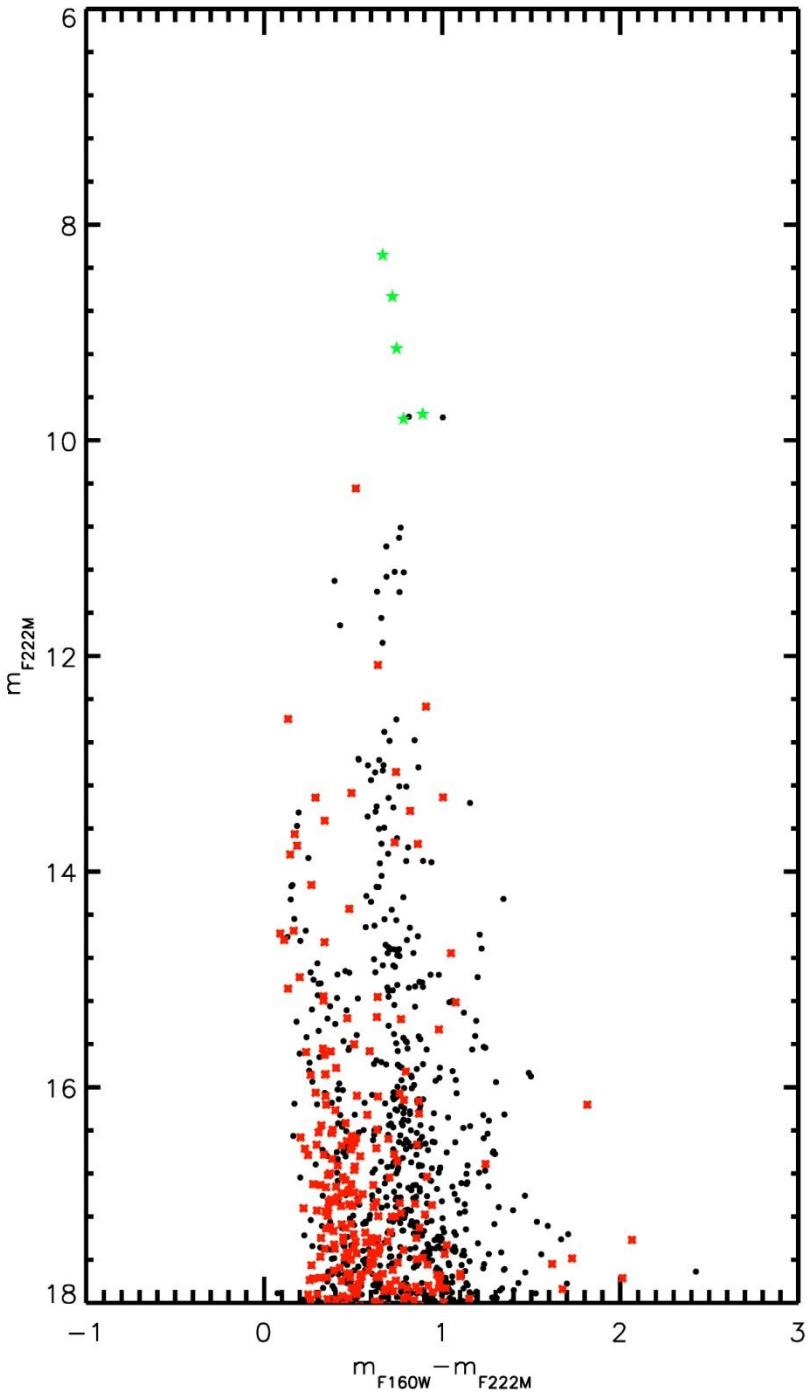

Figure 35 HST CMD for Mercer 30

3.6.1.1. Spectral Typing

Mercer 30 was part of the VLT/ISAAC spectroscopic follow up program of southern clusters (PI de la Fuente). A finding chart for these observations is shown in Figure 37 and the reduced spectra are plotted in Figure 36.

Spectral typing for Mercer 30 was done cooperatively with Diego de la Fuente (de la Fuente et al. in prep). The results of this collaboration are summarized in Table 12, with details of spectral typing to be presented in de la Fuente et al. (in prep). The resulting CMD is displayed in Figure 38, with spectral types labeled. The red dashed line in this figure indicates a 4 Myr MS isochrone, while the dashed blue line indicates a 2 Myr pre-MS isochrone. Objects redward of the pre-MS isochrone are interpreted as pre-MS stars younger than 2 Myr still evolving along Hayashi tracks.

Table 12 List of stars spectroscopically observed

ID	RA	Dec	m_{F160W}	m_{F222M}	SpType
1	12 14 31.5	-62 58 53.8	9.39	8.67	O9 Ifpe
2	12 14 31.6	-62 58 47.6	8.95	8.28	early-B hypergiant
3	12 14 31.7	-62 58 44.6	11.95	11.22	O6 I
4	Not in fov				G
5	12 14 30.8	-62 58 52.7	13.38	12.70	late type/cool
6	12 14 31.7	-62 58 51.6	9.89	9.15	transition star
7	12 14 33.1	-62 58 50.5	10.59	9.80	WN4
8	12 14 33.9	-62 58 48.2	10.65	9.76	WN6
9	12 14 32.7	-62 58 54.5	11.95	11.27	O7 I-II
10	12 14 32.0	-62 58 51.8	12.17	11.41	O5 I
11	12 14 32.1	-62 58 49.1	11.66	10.90	O6 I-II
12	12 14 32.2	-62 58 46.4	13.49	12.79	O8-B1 II-V
13	12 14 33.0	-62 58 41.4	11.58	10.81	O6 I-II
14	12 14 31.3	-62 58 41.8	13.70	13.08	O9-B5 I-III
15	Not in fov				late type/cool
16	Not in fov				KM
17	12 14 32.2	-62 58 50.2	13.33	12.59	O5-9 I-III
18	12 14 32.3	-62 58 47.5	12.31	11.65	O7-O8 I-II
19	12 14 32.5	-62 58 42.3	12.01	11.22	O7 I-II
20	12 14 30.8	-62 58 39.0	10.79	9.79	late type/cool
21	12 14 33.9	-62 58 07.9	12.24	11.57	late type/cool

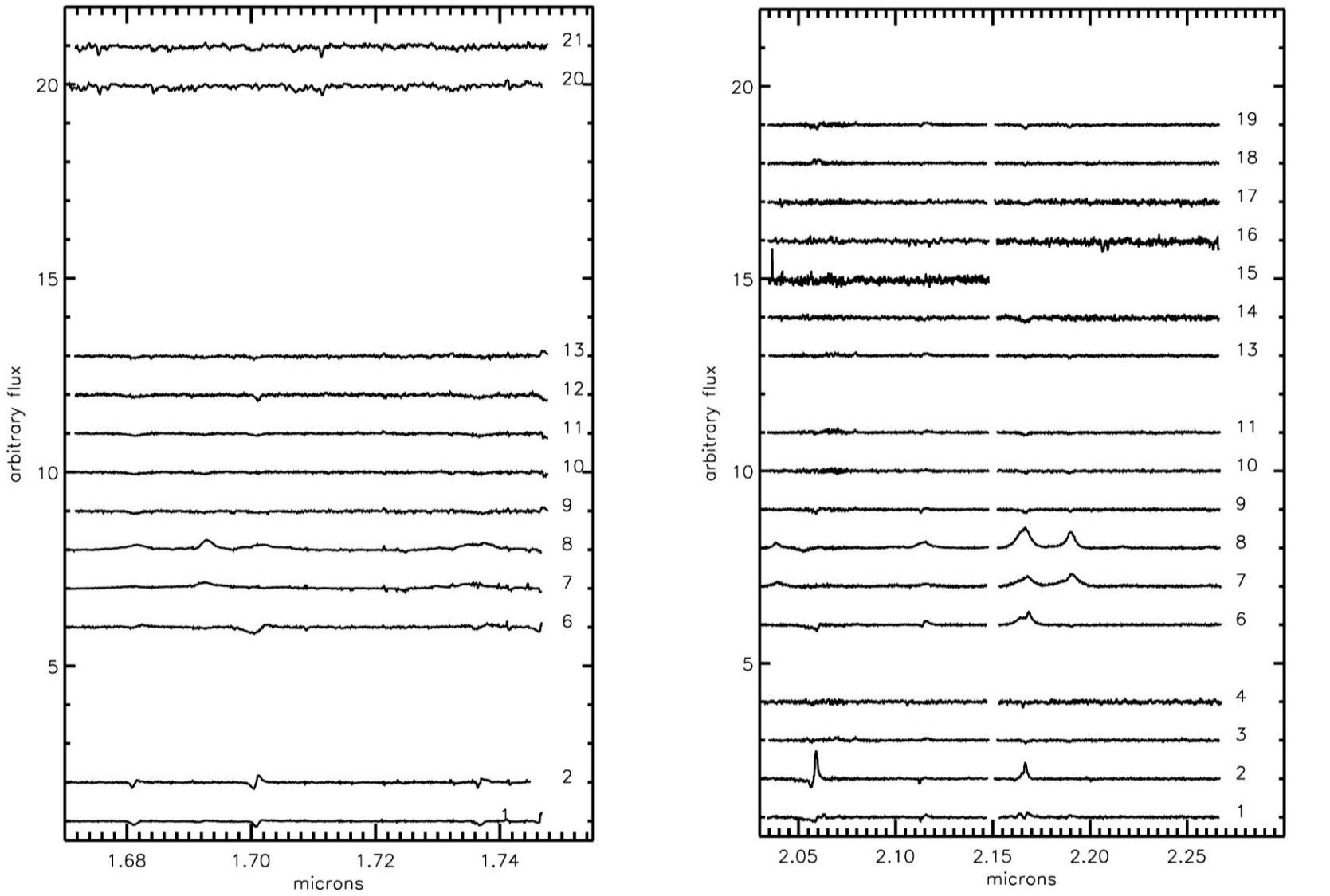

Figure 36 Left: H-band spectra of Mercer 30; Right: corresponding K-band spectra of Mercer 30

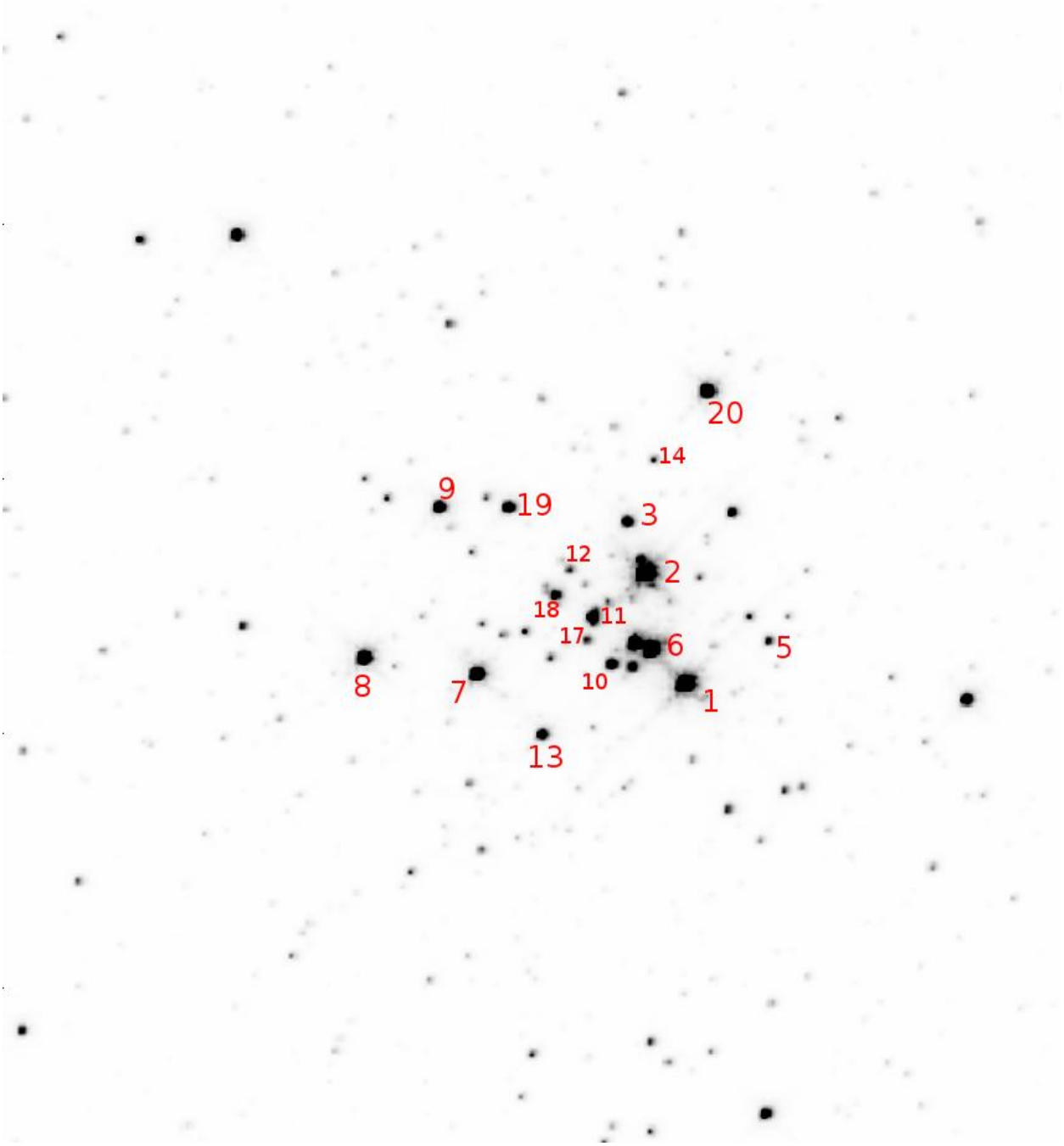

Figure 37 Finding chart for VLT/ISAAC spectroscopic observations of Mercer 30

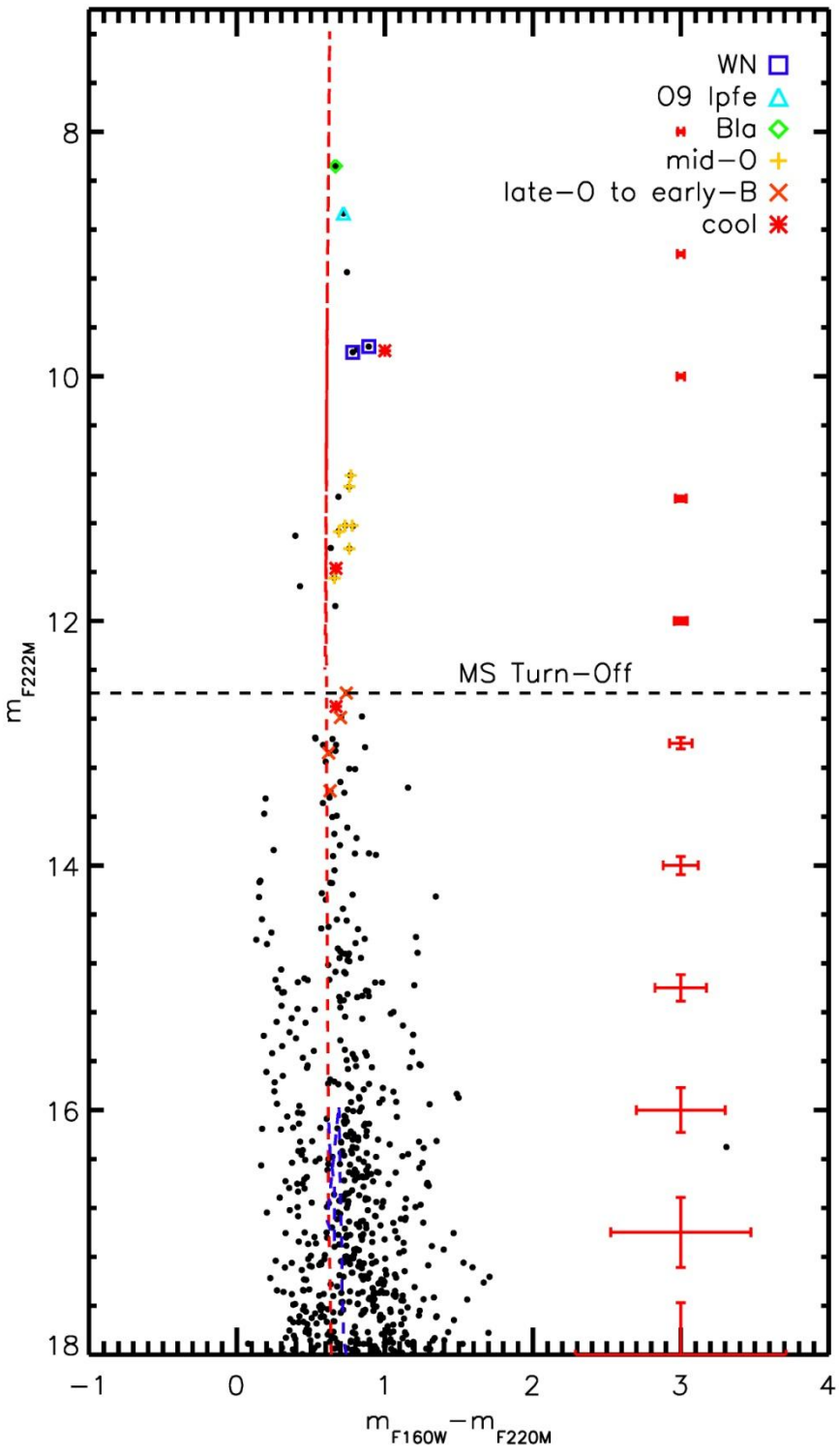

Figure 38 Mercer 30 HST CMD, spectral types labeled

3.6.2. Age, Reddening, Distance, Mass

The presence of WR stars places an upper limit of 8 Myr and a lower limit of 3 Myr on the cluster age, assuming a coeval population. An age of 4 Myr is adopted for Mercer 30, based on the presence of stars evolved from high initial mass stars, namely the mid-O supergiants. As these objects have not yet gone supernova, their total lifetimes (as determined from stellar evolutionary models) provide the best upper limit on the cluster age.

Extinction towards the cluster is computed by examining the NIR colors of "normal" O and B type stars, i.e. emission line stars or clearly heavily reddened stars are excluded. For Mercer 30, an average value of A_K=1.08+/-0.08 is found, based on 12 stars observed by HST/NIC3 and VLT/ISAAC.

A rough estimate of the distance can be derived from spectrophotometric models. Table 13 shows the results of this method, assuming three luminosity classes. Absolute magnitudes are taken from Martins & Plez (2006). The range of distances for each object and luminosity class reflect the errors in spectral typing and the error on the absolute magnitude. As shown in Table 13, later spectral types (late O) are consistent with a luminosity class of V, as other luminosity classifications would result in unreasonable distances estimates. Mid-O stars (O6.5-8) likely belong to luminosity classes III-II. Using MS stars, the average distance is 13.1+/-2.2 kpc. A distance of 11 kpc is derived by de la Fuente et al. (in prep) via radial velocity measurements; as radial velocities provide a more robust distance measurement and is in agreement with the spectrophotometric distance, 11 kpc is used as the distance to Mercer 30.

Table 13 Results of spectrophotometric distances estimates for O-type stars in Mercer 30

ID	m_{F222M}	SpType	D_V/kpc	D_{III}/kpc	D_I/kpc
D10	11.41	O5 I	6.65-8.57	10.16-11.56	14.41-14.48
D11	10.90	O6 I-II	5.28-6.04	8.07-8.65	11.45-11.50
D9	11.27	O7 I-II	5.59	10.06	14.28-14.34
D13	10.81	O6 I-II	5.74	8.23	10.89-10.94
D19	11.22	O7 I-II	6.0	7.17	13.01-13.07
D18	11.65	O7-O8 I-II	6.21-9.18	10.78-13.15	17.41-17.49
D3	11.22	O6 I	7.12	10.19	13.50-13.56
D12	12.79	O8-B1 II-V	7.82-10.13	15.54-17.60	28.54-22.56
S4-1	13.39	O9 II-III	14.16	24.60	31.55
D14	13.08	O9-B5 I-III	9.86-18.71	23.77-32.51	52.72-41.69
D17	12.59	O5-9 I-III	8.99-15.00	15.63-20.23	25.35-25.23

Counting the number of objects still on the main sequence (5-20 $M_\odot$), measuring the IMF slope (Γ = -1.47), and integrating from 0.5-150 $M_\odot$ yields a total cluster mass of ~1.6(10^4) $M_\odot$, making Mercer 30

one of a handful of young, massive clusters in the Galaxy. Kurtev et al. (2007) find a MF slope of -1.01+/-0.03, and a mass of a few 10^3 $M_\odot$ when integrating from 1 $M_\odot$. The results presented here are an improvement on previous work in the literature as new spectroscopic observations of a larger number of clusters stars provides a more robust determination of cluster properties such as age, distance, and total mass.

3.6.3. Summary

Given the young age and abundance of massive stars, Mercer 30 is an excellent example of a cluster for which the high end IMF slope can be measured. A clear MS turn-off is present, along with a detailed knowledge of the spectral types – and therefore masses – of both evolved objects and MS objects. This information results in a straightforward construction of an IMF.

3.7. Mercer 70

Mercer 70 contains several Paschen-alpha emission line (PEL) objects that are identified as WR stars, B supergiants, and a newly discovered B[e] star. Spectra of the brightest stars in the cluster reveal early B supergiants, then a "cluster" of fainter O giants in the CMD, and at even fainter magnitudes the MS turn-off. After inspection of the faint B[e] star in this cluster, another spectroscopically similar object was identified in Mercer 20. Mercer 81 potentially contains a similar source, a relatively faint PEL object slightly redder than the MS, but this object remains spectroscopically unobserved.

3.7.1. Stellar Content

The color magnitude diagram of Mercer 70, Figure 39, shows a likely massive main-sequence, with a clump of brighter stars at similar color that are likely to be supergiants. Spectroscopic follow-up reveals these to be blue supergiants, with another clump of hot giants just brighter than the MS turn-off.

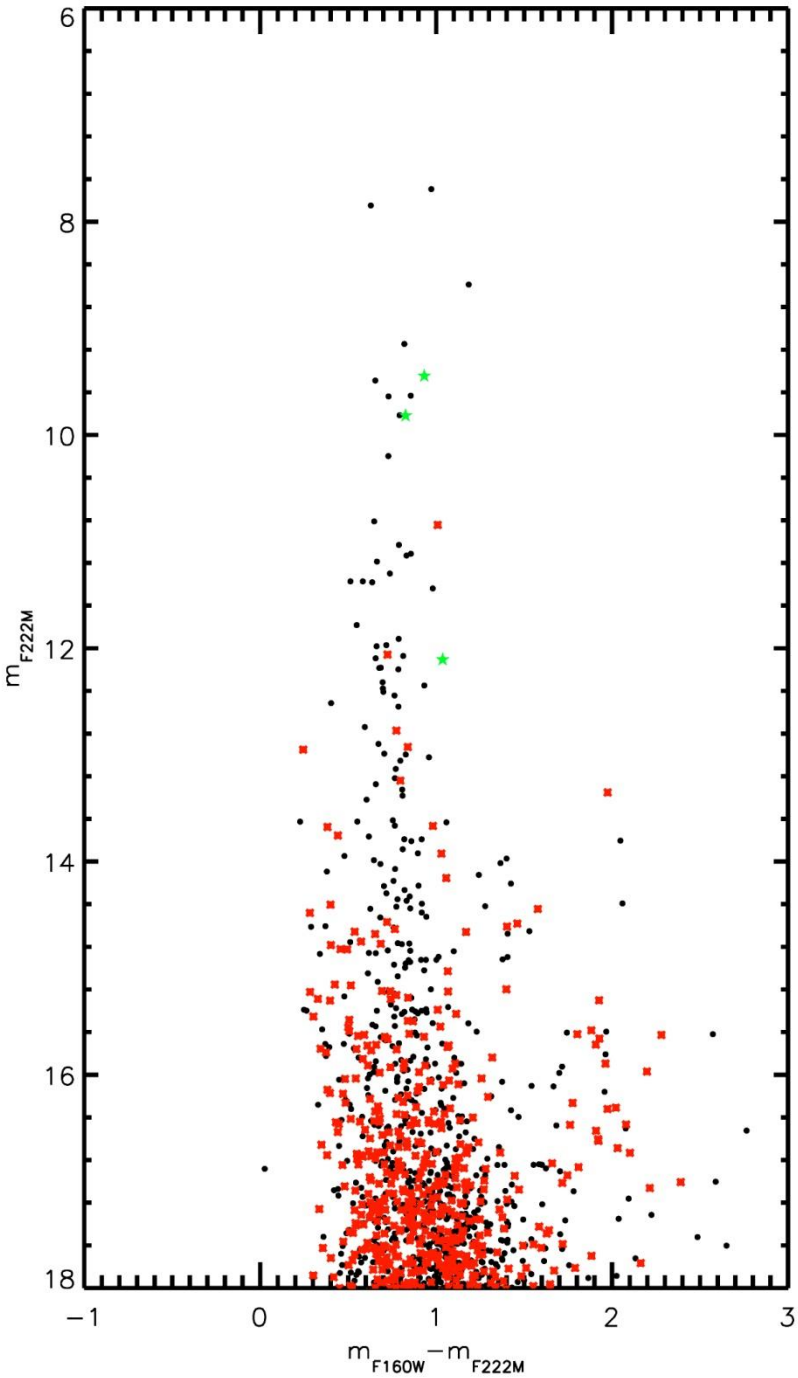

Figure 39 Mercer 70 HST CMD

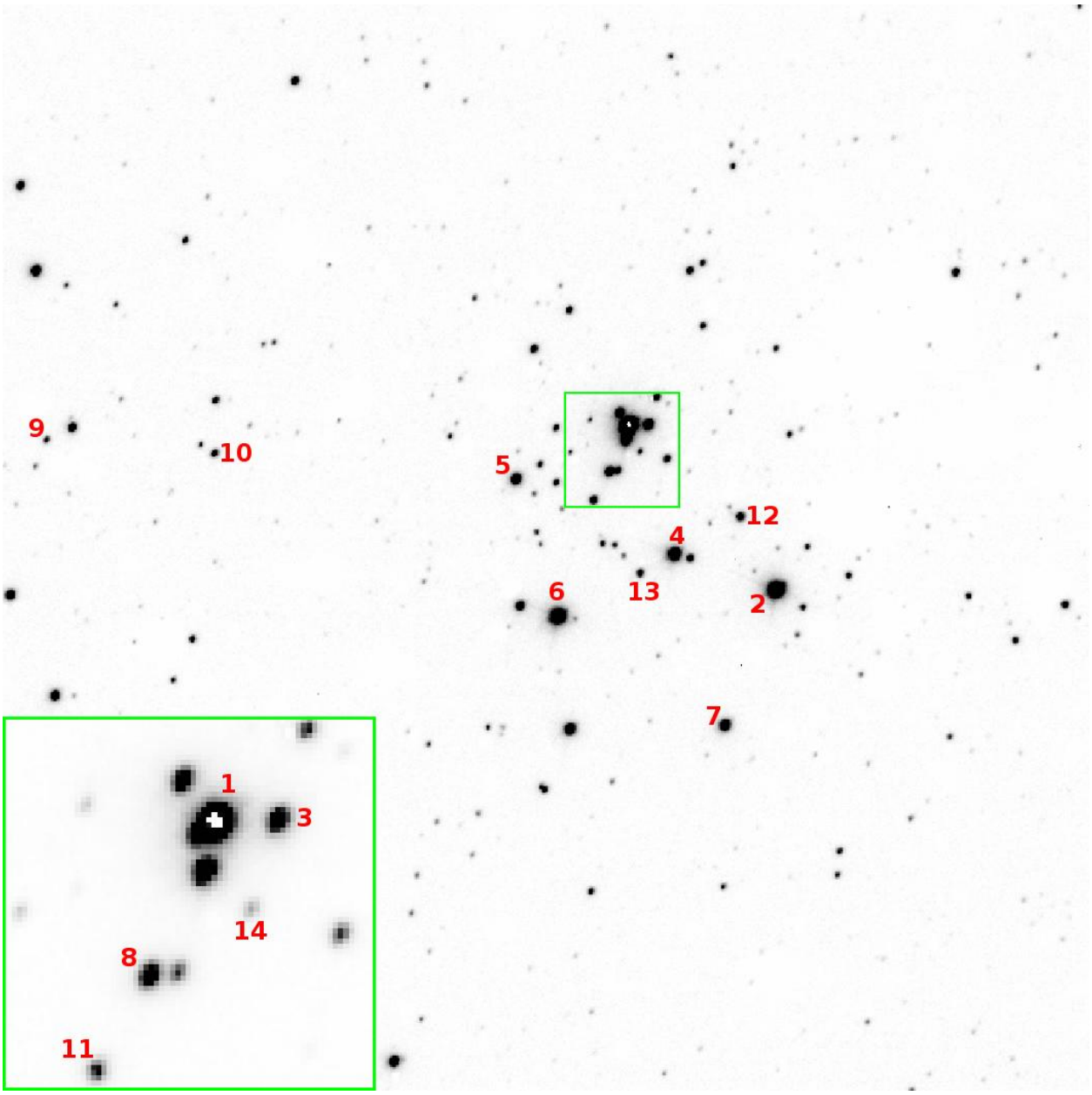

Figure 40 ISAAC finding chart for Mercer 70, with spectroscopically observed stars labeled.

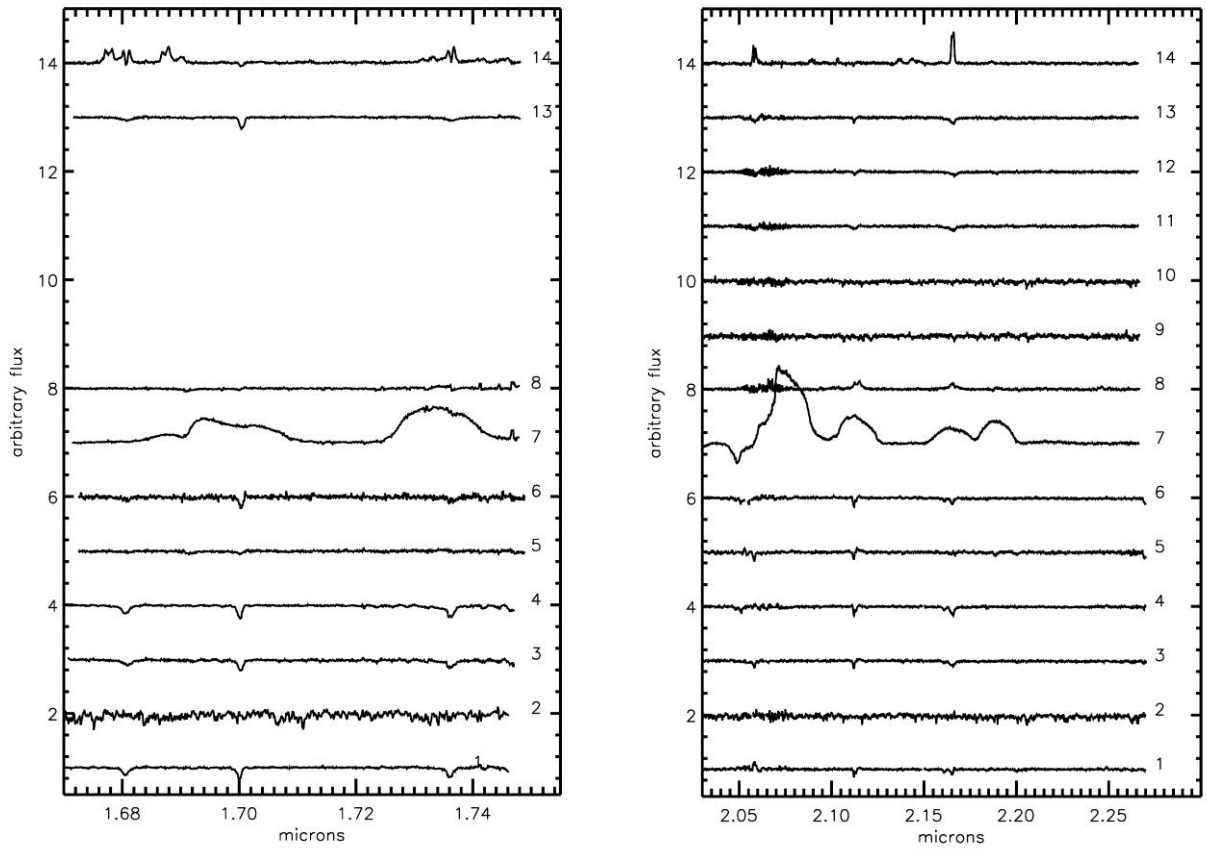

Figure 41 VLT/ISAAC spectra of stars in Mercer 70

3.7.1.1. Spectral Typing

The spectra of Mc70-2, Mc70-9, and Mc70-10 show metal absorption lines from of FeI, MgI, and NaI, characteristic of cool, late type stars. Without the CO bandhead feature at 2.30 microns it is impossible to characterize the CO EW and determine luminosity class of these stars. Most likely these objects are foreground giants.

Mc70-1 shows narrow but fairly deep HeI absorption at 1.68, 1.700, and 1.737 microns in the H band, with no evidence for absorption at 1.687 microns, indicating a spectral type later than O8. The K band spectrum shows HeI 2.112/3 and HeI 2.161/2 absorption, narrow Brγ absorption, and weak HeII 2.118 absorption. These features are indicative of a B0-B3 type star. The shape of the Brγ a absorption is consistent with a supergiant luminosity class. The spectra of Mc70-3, Mc70-4, and Mc70-6 are nearly identical to Mc70-1, and thus have similar spectral classification (see Table 14).

Mc70-5 shows weak Brγ a absorption,strong narrow absorption at 2.058 microns, narrow absorption at 2.188 microns, and a narrow HeI absorption feature at 2.112/3 microns which is contaminated by NIII emission. Weak CIV emission is seen at 2.078 microns. The H band spectrum contains weak absorption at 1.687, with stronger absorption at 1.693 and1.700 microns, indicating a spectral type earlier than O9, closer to O6-O8 based on the HeI/NIII feature.

Strong, broad C and He emission lines indicate that Mc70-7 is a Carbon-type WR star. Inspection of the H and K band spectra as compared to the spectra atlases of Figer et al. (1997) and Mauerhan et al. (2011) yield a spectral classification of WC8 for this star.

The spectrum of Mc70-8 shows Brγ emission, HeII emission, and NIII multiplet emission blended with HeI 2.112/3 double absorption in the K band. HeII and HeI absorption at 1.693 and 1.700 indicate a spectral type earlier than O9. These features in H and K bands, combined with 1.74 micron emission, and close inspection of the spectral atlas of Hanson et al. (2005), result in a spectral type of O3-O4 If (+/* ?).

Stars Mc70-11 and Mc70-12 have very similar K-band spectra, with Brγ and HeI absorption. Mc70-12 has a stronger absorption feature at 2.188 microns, and a stronger NIII multiplet contribution, resulting in a slightly earlier spectral type than Mc70-11. With the addition of H-band spectral information, Mc70-13, which is similar to Mc70-11 and -12, is classified as O8-O9, albeit with marked similarities to O9.5Ia/b objects in Figures 5 and 7 of Hanson et al. (2005).

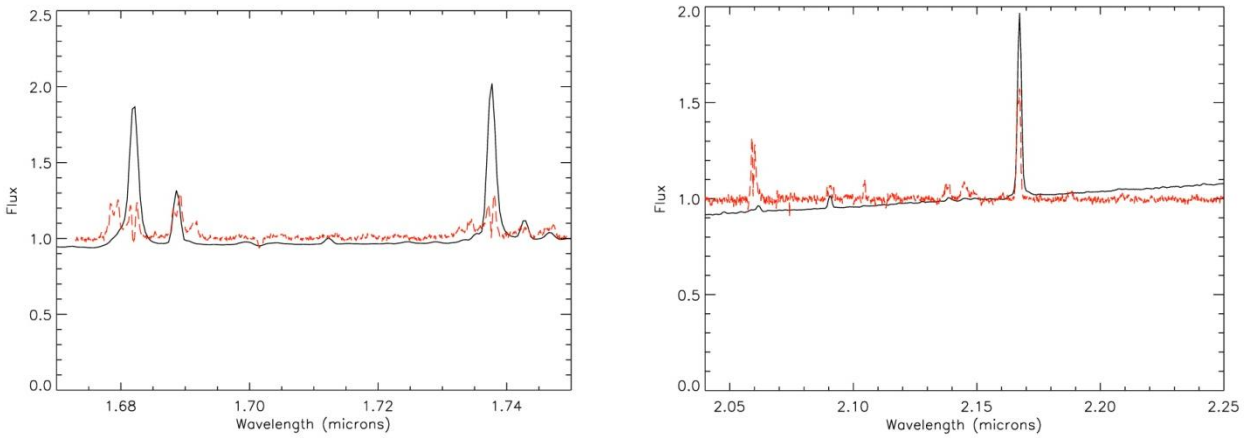

Figure 42 H (left) and K (right) band spectra of FS CMa (solid black) and Mc70-14 (dashed red)

The remaining, and faintest, object exhibits strong Hydrogen emission lines, in addition to He, Fe, Si, and Mg features. Comparison with similar resolution spectra of the Pistol Star and other (c)LBVs in the atlas

of Morris et al. (1996) reveals many similarities between Mc70-14 and these LBVs, suggesting that Mc70-14 is a candidate LBV. Photometry of this star reveals that it is fainter than the MS turn-off in Mercer 70, and has a slightly redder color than the "average" MS color. Inspection of GLIMPSE and WISE images reveal no point-like or diffuse emission associated with Mc70-14. Given the much lower resolution and large positional uncertainties on GLIMPSE and WISE point sources compared to HST/NIC3, mid-IR excess cannot be conclusively ruled out. It remains possible that an ejection nebula surrounds the star, unresolved in either IR survey. Without evidence for an extreme outburst or mass-loss event, Mc70-14 would remain a candidate low-luminosity LBV. Assuming a distance of 5 kpc and a BC_K of -1.6, as found for the Pistol Star (Figer et al. 1998), LogL for this star is 3.73, well below the typical luminosities of LBVs in the literature. Given the results of the luminosity calculation, this star cannot be an LBV and is thus classified as a B[e] star. There exists a sub-category of non-supergiant, unclassified B[e] stars known as FS CMa stars (Miroschnichenko 2007, Miroshnichenko et al. 2009). Comparison with lower resolution IRTF/SpeX observations (R~2000) reveals many similarities between Mc70-14 and FS CMa, as shown in Figure 42, leading to the ultimate classification of Mc70-14 as a FS CMa B[e] star.

The red dashed line in Figure 43 indicates a 4 Myr MS isochrone, while the dashed blue line indicates a 2 Myr pre-MS isochrone. Objects redward of the pre-MS isochrone are interpreted as pre-MS stars younger than 2 Myr still evolving along Hayashi tracks. However, the photometric uncertainty at the magnitude range of pre-MS stars is too large to conclusively identify objects in Mercer 70 belonging to a real pre-MS.

Table 14 List of spectroscopically observed stars in Mercer 70

ID	RA	Dec	m_{F160W}	m_{F222M}	SpType
1	16 0 27.8	-52 10 44.4	8.48	7.49	B0-B3 Ia
2	16 0 26.0	-52 10 57.4	8.67	7.69	late type/cool
3	16 0 27.6	-52 10 44.0	10.49	9.63	B0-B1 I
4	16 0 27.1	-52 10 55.7	9.77	8.59	B2-B3 I
5	16 0 28.8	-52 10 51.0	10.37	9.64	O6-O8
6	16 0 28.2	-52 11 3.13	8.48	7.85	B0-B3 I
7	16 0 26.3	-52 11 10.7	10.38	9.45	WC8
8	16 0 27.9	-52 10 49.0	10.64	9.82	O3-O4 If*/+
9	Not in fov				late type/cool
10	Not in fov				late type/cool
11	16 0 28.0	-52 10 51.6	11.82	11.03	O9-B3
12	16 0 26.5	-52 10 51.2	11.46	10.81	O7-O9
13	16 0 27.4	-52 10 57.9	11.96	11.37	O9.5 I
14	16 0 27.6	-52 10 46.7	13.14	12.11	FS CMa B[e]

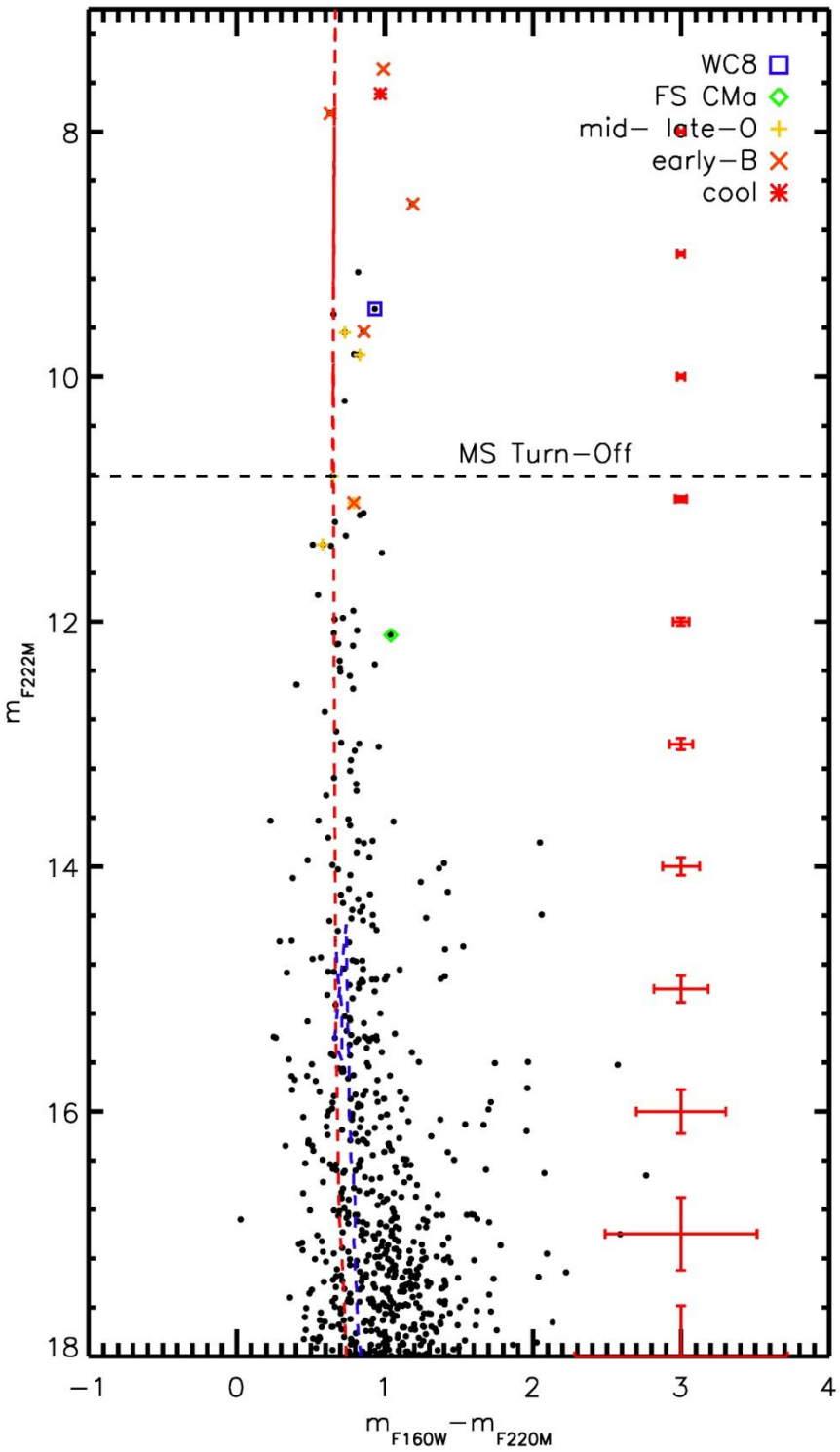

Figure 43 Mercer 70 HST CMD with spectral types labeled

3.7.2. Age, Reddening, Distance

An upper and lower limit on the age of Mercer 70 of 6 Myr and 3 Myr can be set by the presence of the WC8 star in the cluster. The combination of a late WC star, B supergiants, and the similar properties of the CMD make Mercer 70 a lower mass analog to the Quintuplet cluster, likely of similar age (4 to 5 Myr).

Extinction towards the cluster is computed by examining the NIR colors of "normal" O and B type stars, i.e. emission line stars or clearly heavily reddened stars are excluded. For Mercer 70, an average value of A_K=1.18+/-0.30 is found, based on 9 stars observed by HST/NIC3 and VLT/ISAAC.

Inspection of the CMD in Figure 43 suggests that the spectroscopically observed stars are giants and supergiants, clustering in two bunches above the MS turn-off. Table 15 shows the results of spectrophotometric distance calculations, with absolute magnitudes taken from Martins & Plez (2006). The range in distance for each luminosity class reflects the uncertainty in spectral type and absolute magnitude. Supergiants span a large range in luminosity, making these objects less than ideal for spectrophotometric distance estimates. As an exampleif the absolute luminosity of Mc70-1 spans a magnitude range of 4 mags (M=-5.0 to M=-9.0), the resulting distance ranges from 1.59 to 9.88 kpc, nearly a factor of five. MS stars span a smaller luminosity range, yielding better results for this type of distance estimate. The results of the spectrophotometric distance estimates are summarized in Table 15.

The distance to the cluster can also be estimated based on photometry of the WR star; using the absolute magnitude and intrinsic colors from Crowther et al. (2006) and Mauerhan et al. (2011) for non-dusty WC8 stars, a distance estimate of 3.43 kpc is derived. Again, this method is less than ideal as only a handful of data points were used to find the average magnitude and intrinsic colors in Crowther et al. (2006) and Mauerhan et al. (2011).

Based on the MS spectrophotometric distance results, a value of 5.25 (+/-0.37) kpc is adopted as the distance to Mercer 70.

Table 15 Spectrophotometric distance estimates for spectroscopically observed stars in Mercer 70.					
ID	m_{F222M}	SpType	D_V/kpc	D_{III}/kpc	D_I/kpc
1	7.49	B0-B3 Ia	0.42-0.62	1.02-1.20	1.58-2.51
6	7.85	B0-B3 I	0.66-0.97	1.49-1.87	2.47-3.91
4	8.59	B2-B3 I	0.69-0.89	1.46-1.72	2.27-3.59
3	9.63	B0-B1	1.43-1.85	3.03-3.58	4.72-7.48
5	9.64	O6-O8	2.17-2.66	3.17-3.85	6.53-6.56
11	11.03	O9-B3	2.52-4.23	5.70-7.35	9.42-14.93
12	10.81	O7-O9	4.25-5.45	7.39-8.41	11.93-11.99
13	11.37	O9-O9.5	5.45-5.79	9.83-10.06	12.91-20.45

3.7.3. Summary

The presence of evolved massive stars, in addition to a clear main sequence and identifiable main sequence turn-off allows for a measurement of the intermediate to high mass slope of the IMF in Mercer 70. The age and distance of the cluster can be varied to produce many IMF plots, and the results discussed in more detail in Results & Discussion.

3.8. Mercer 81

Mercer 81 presents a very interesting discovery history. Originally in the catalog of Mercer et al. (2005), this cluster appears to be composed of a set of four bright stars, likely the reason the cluster was detected by the algorithm. These stars turn out to be unrelated foreground objects, serendipitously in front of a young, massive cluster containing multiple Paschen-alpha emission line objects. These nine objects are indicated by green star symbols in Figure 44, where the control field contribution (red asterisks) is nearly identical to the cluster field (black points).

Mercer 81 has been studied by Davies et al. (2012a) and de la Fuente et al. (2012), and is the subject of a forthcoming paper (de la Fuente et al. in prep) designed to fully comprehend the nature of this cluster. Mercer 81 has been observed with HST/NIC3, VLT/ISAAC, and CXO/ACIS, providing a rich data set for the characterization of this young, massive cluster.

3.8.1. Stellar Content

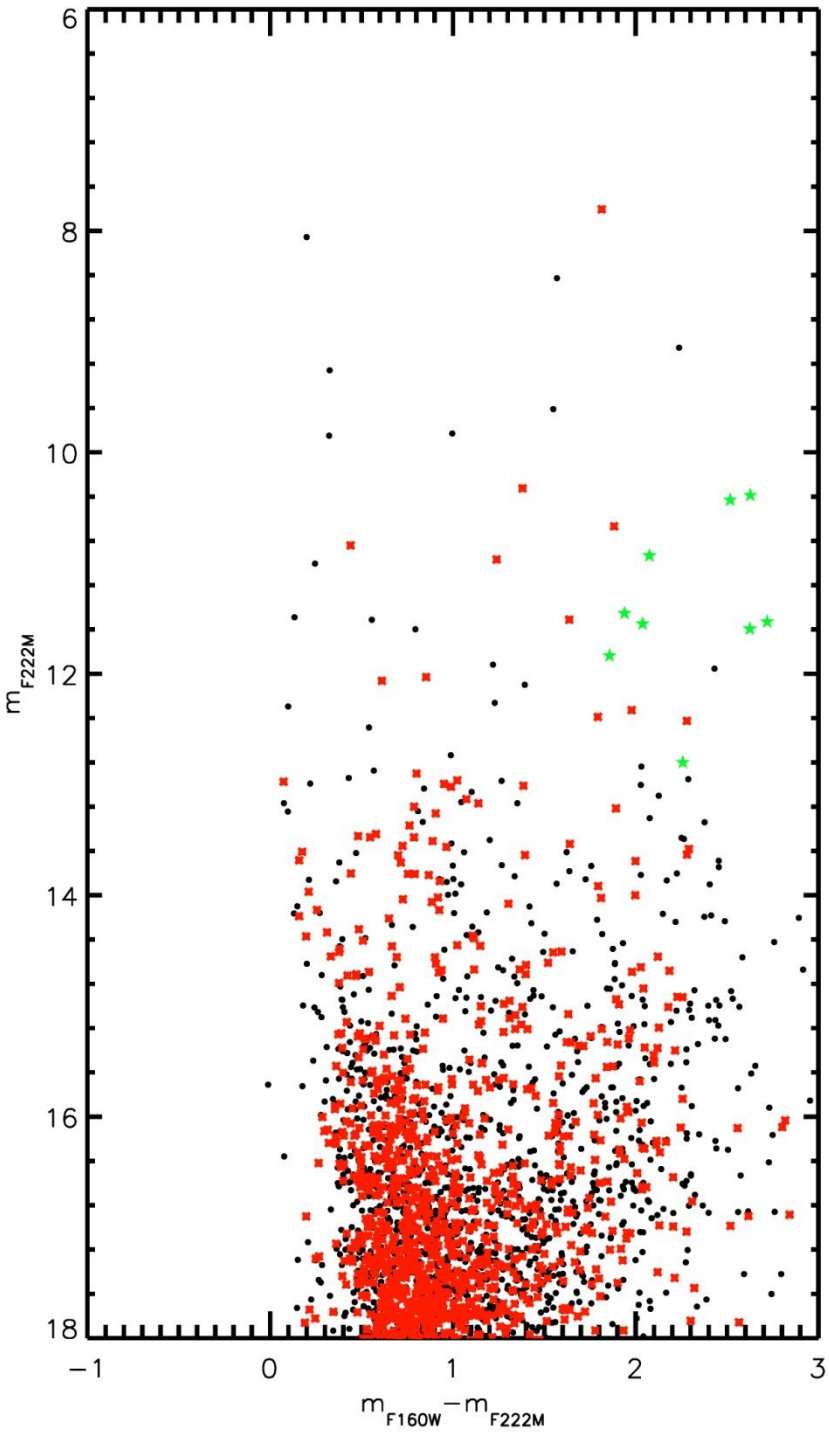

Figure 44 HST CMD of Mercer 81. Note the high field contamination towards this cluster, as indicated by the control field photometry (red asterisks).

Mercer 81 was part of the southern VLT/ISAAC program of de la Fuente et al. designed to characterize massive stars in newly discovered young, massive cluster candidates. The reduced spectra from this program is shown in Figure 46, with nomenclature corresponding to the labels in Figure 45, the ISAAC finding chart.

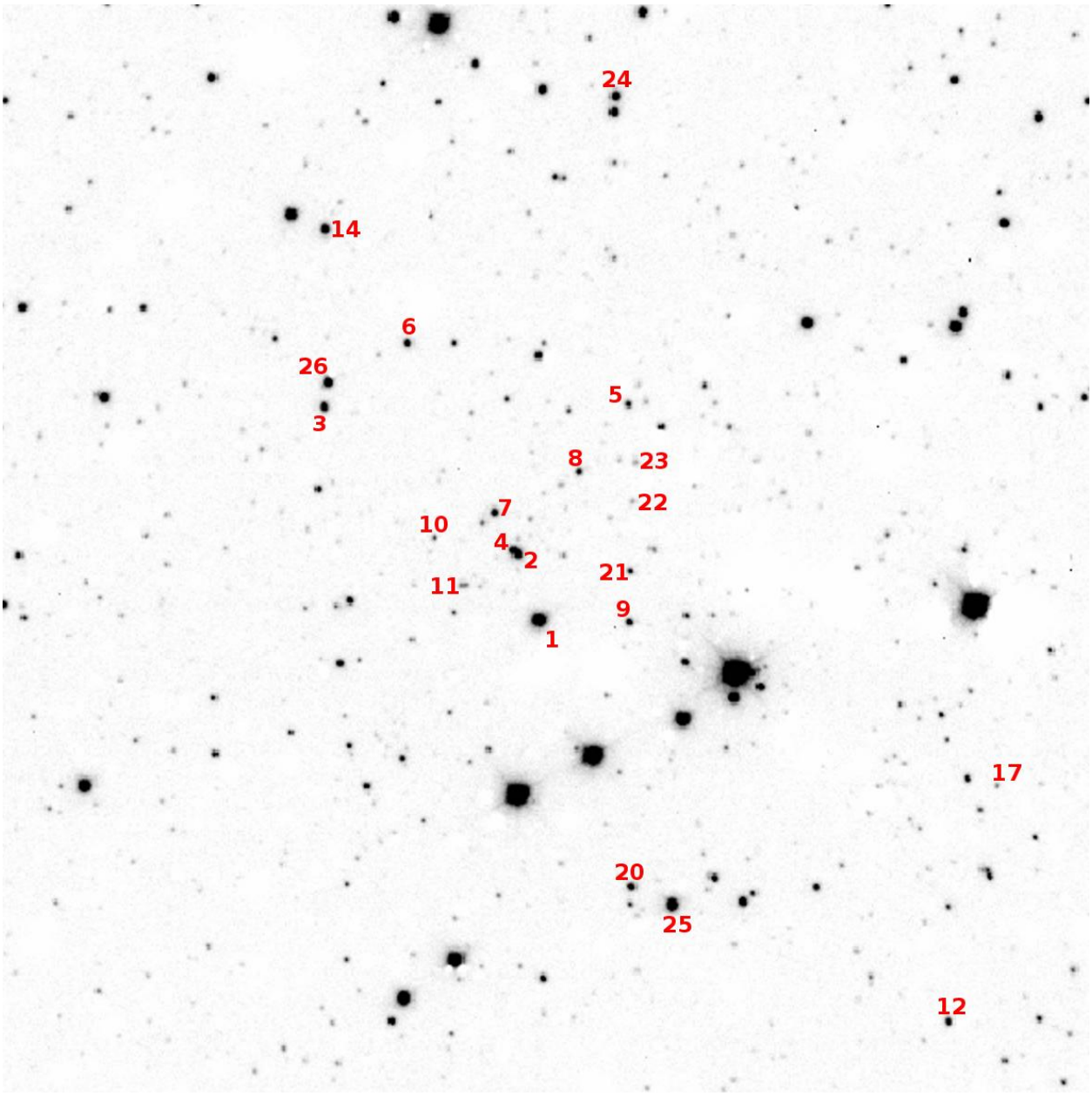

Figure 45 ISAAC finding chart for Mercer 81 spectroscopic observations. Some objects labeled in finding chart were not observed.

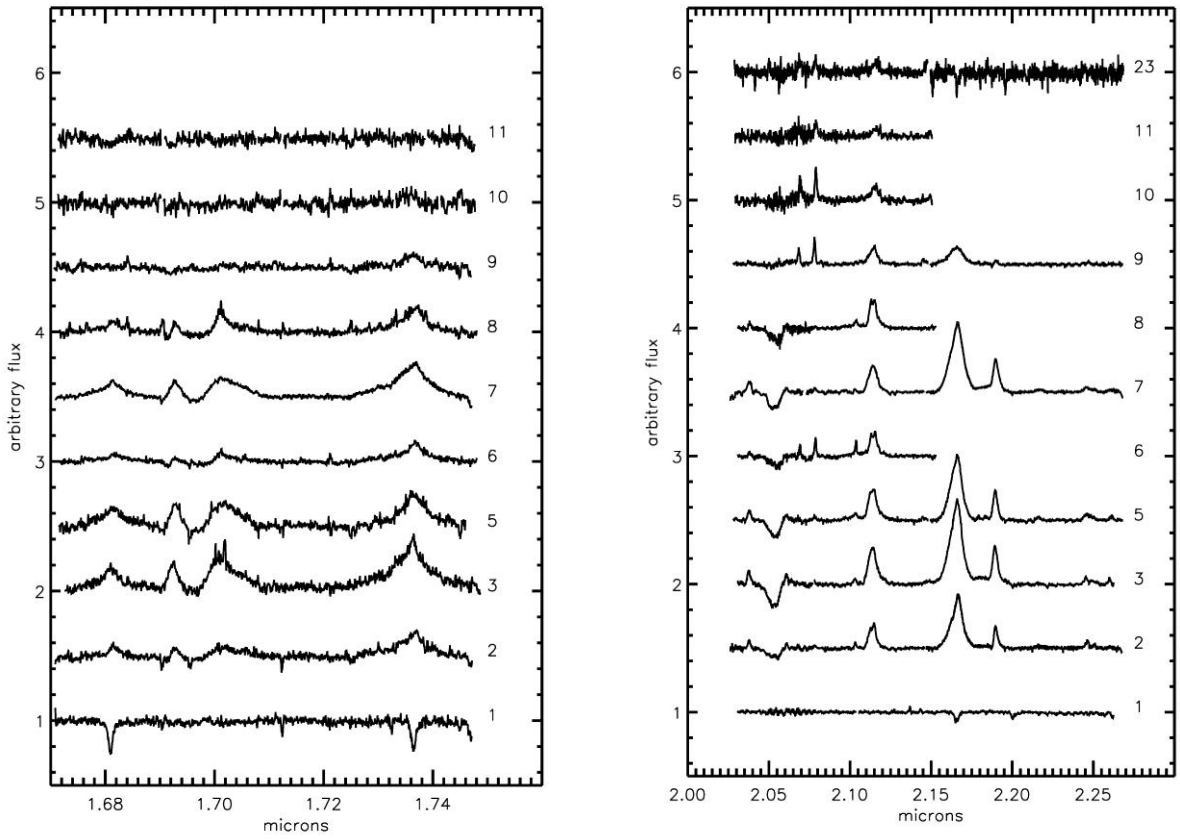

Figure 46 Spectra of hot stars in Mercer 81. Left: H band; Right: K band. Mc81-23 was not observed in H band.

3.8.1.1. Spectral Typing

The spectra of four stars in Mercer 81, Mc81-2, -3, -5, and -7, are almost identical. Broad, strong HeI, HeII, and NIV lines indicate that these stars are late-type Wolf-Rayet stars of the nitrogen subtype, WN7-8. Mc81-4 is blended with the ISAAC spectrum of Mc81-2, and is very likely of the same spectral type. Both stars are identified as emission line objects in HST narrow-band photometry, though Mc81-2 is brighter and possibly dominates the combined spectrum.

Four stars have spectra consistent with intermediate O supergiants; Mc81-6, -9, -10 and likely -11 have spectral type O5-6 I. This is evident from narrow CIV emission lines in the K band and NIII multiple emission, also in the K band. One other object appears to be a mid-O (5-7) star, but with spectra more indicative of a V or III luminosity class (Mc81-23): HeI emission at 2.058 microns, HeI absorption at 2.112/3 microns, NIII multiplet, Brγ absorption, and CIV emission at 2.078 microns are all present. The spectrum of Mc81-23 is very similar to O5-7 V and III stars in the atlas of Hanson et al. 2005.

The brightest cluster star, Mc81-1, was found by Davies et al. (2012a) to be a B/A supergiant.

There is a newly observed object, Mc81-8, whose spectrum shows emission intermediate between a WN star and an O supergiant. This object is classified as in a transition phase; there is no evidence at the time of writing that this is a blend of multiple stars.

The results of spectral typing are listed in Table 16 and labeled on the Mercer 81 CMD in Figure 47. The red dashed line in this figure indicates a 3 Myr MS isochrone, while the dashed blue (very bottom right) line indicates a 2 Myr pre-MS isochrone. Due to the distance and extinction towards Mercer 81, any pre-MS population cannot be distinguished from the fore-and background population.

Table 16 List of stars spectroscopically observed

ID	RA	Dec	m_{F160W}	m_{F222M}	SpType
1	16 40 29.8	-46 23 34.1	11.29	9.05	B/A I
2	16 40 29.7	-46 23 29.2	13.02	10.39	WN7-8
3	16 40 30.1	-46 23 11.5	13.01	10.93	WN7-8
5	16 40 28.4	-46 23 25.6	14.22	11.60	WN7-8
6	16 40 29.3	-46 23 11.7	13.39	11.45	int.O I
7	16 40 29.6	-46 23 25.7	13.59	11.55	WN7-8
8	16 40 28.9	-46 23 27.3	14.25	11.53	transition OI/WN
9	16 40 29.3	-46 23 38.3	13.69	11.84	int.O I
10	16 40 30.1	-46 23 24.4	15.06	12.80	int.O I
11	16 40 30.1	-46 23 28.4	14.87	12.84	int.O I ?
20	16 40 30.5	-46 23 53.8	13.03	12.48	late type/cool
21	16 40 29.1	-46 23 35.5	14.17	13.34	late type/cool
22	16 40 28.8	-46 23 31.5	15.33	14.94	Nosiy
23	16 40 28.6	-46 23 29.3	15.72	13.34	O5-O7 V
25	16 40 30.4	-46 23 56.8	11.25	11.01	late type/cool
26	16 40 30.0	-46 23 10.3	12.39	11.60	late type/cool

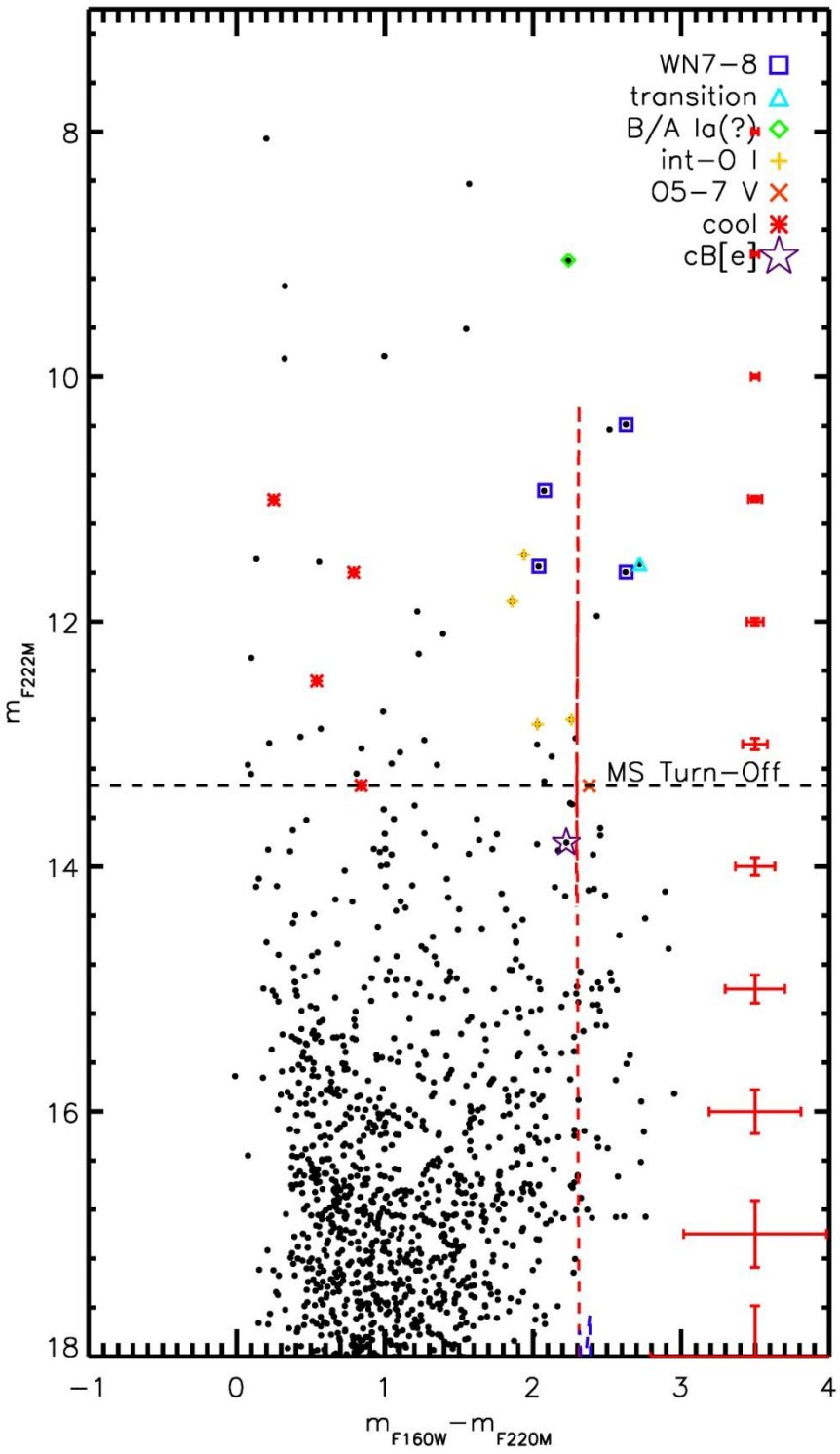

Figure 47 Mercer 81 CMD with spectral types labeled.

3.8.2. Age, Reddening, Distance, Mass

The WR stars in Mercer 81 immediately set limits o the cluster age between 3 and 8 Myr. Davies et al. (2012a) present detailed modeling of Mc81-2, a WNL star, for which they derive an age of 3.7 Myr (see Figure 8 of that work). More recently, de la Fuente et al. (2012) present new spectroscopic observations of cluster stars in Mercer 81 which suggest the cluster age is lower than the 3.7 Myr found by Davies et al. (2012a). Their results are based on newly observed stars with early spectral types (O5-6 I), wich have lifetimes shorter than 4 Myr.

Extinction towards the cluster is computed by examining the NIR colors of "normal" O and B type stars, i.e. emission line stars or clearly heavily reddened stars are excluded. For Mercer 81, an average value of A_K=3.24+/-0.25 is found, based on four O stars observed by HST/NIC3 and VLT/ISAAC. Mercer 81 is located at the far end of the Galactic bar, and as such the extinction towards this cluster is extremely high (for a comparison with other known Galactic clusters, see Figure 98).

Davies et al. (2012a) derive a distance of 11 kpc to Mercer 81, based on radial velocity measurements of the molecular clouds surrounding the cluster. These authors also point to radial velocities of nearby massive young stellar objects and compact HII-regions (Hoare et al. 2005; Urquhart et al. 2007a, b). Radial velocities provide near and far kinematic distances; Davies et al. (2012a) resolve this degeneracy by identifying that HI absorption emission associated with the compact HII-regions is seen at velocities up to the tangent point of the Galactic rotation curve, indicating that the HII-regions lie at the far distance of 11 kpc (see also Lemiere et al. 2009). As an additional check, Davies et al. (2012a) calculate the absolute brightness of the WNL star assuming a distance of 11+/-2 kpc and compare with similar objects at known distances. They find agreement within the errors.

The mass of Mercer 81 is derived by measuring the slope of the IMF and integrating from .5 to 150 $M_{\odot}$, yielding ~1.4(10^4) $M_{\odot}$. This is in agreement with the estimations of Davies et al. (2012a), who based their mass estimate on the assumption that all unobserved PEL objects are WN stars.

3.8.3. X-ray Properties

Targeted X-ray observations of Mercer 81 reveal the presence of hard, hot X-ray sources coincident with emission line stars in the cluster. This emission is attributed to colliding wind binaries (CWB) in the cluster. The binary fraction of massive stars is high (0.7 to 1.0, Clark et al. 2008, Sana et al. 2012), so the discovery of CWBs in Mercer 81 is not surprising. Hard X-ray emission from MS stars could indicate the presence of unresolved binaries. Inclusion of unresolved MS binaries results in a flattening of the measured IMF slope. The X-ray point source population of Mercer 81 is examined in order to identify any MS CWBs.

The brightest X-ray emission is associated with Mc81-2 and Mc81-4, which are unresolved by CXO/ACIS and VLT/ISAAC, though appear as separate emission line objects in the HST/NIC3 observations. Fitting a wabs*apec model to the X-ray spectrum of this source in XSPEC yields n_H=12.1+/-2.0 (10^{22}), which is consistent with the extinction towards Mercer 81 as derived by Davies et al. (2012a). The temperature of the best fitting model is 1.57+/-0.31 keV, which is higher than typically observed for single stars. At a distance of 11 kpc, L_X for this source is 2.62(10^{33}), consistent with what is expected from a CWB (for examples, see Table 2 of Gange et al. 2012).

The other X-ray point sources in the CXO observation did not contain enough counts to model with a high degree of accuracy. No evidence for diffuse emission was identified. None of the hard X-ray point sources were spatially coincident with MS stars.

3.8.4. Summary

Given the young age, high mass, presence of evolved massive stars, massive stars in transition, and identifiable main sequence in Mercer 81, the cluster is well suited for a IMF measurement. The high mass slope can only be measured down to the completeness limit in Mercer 81, ~10 $M_\odot$, which is relatively high as compared to other clusters in the final sample.

3.9. Danks 1 & Danks 2

Located in the G305 star forming complex, the young massive clusters Danks 1 and Danks 2 are possibly the exciting sources for the central cavity of the larger region. In addition to the late WC star WR48a, both clusters and the surrounding "halo" host a variety of evolved massive stars with a small spread in age (Davies et al. 2012b, Mauheran et al. 2011).

3.9.1. Stellar Content

The HST CMDs are shown in Figure 48, a slight reproduction of Figures 5 and 6 in Davies et al. (2012b). Photometry of the brightest star in Danks 1, in the left hand panel, is erroneous. For science purposes, 2MASS photometry of this star is adopted.

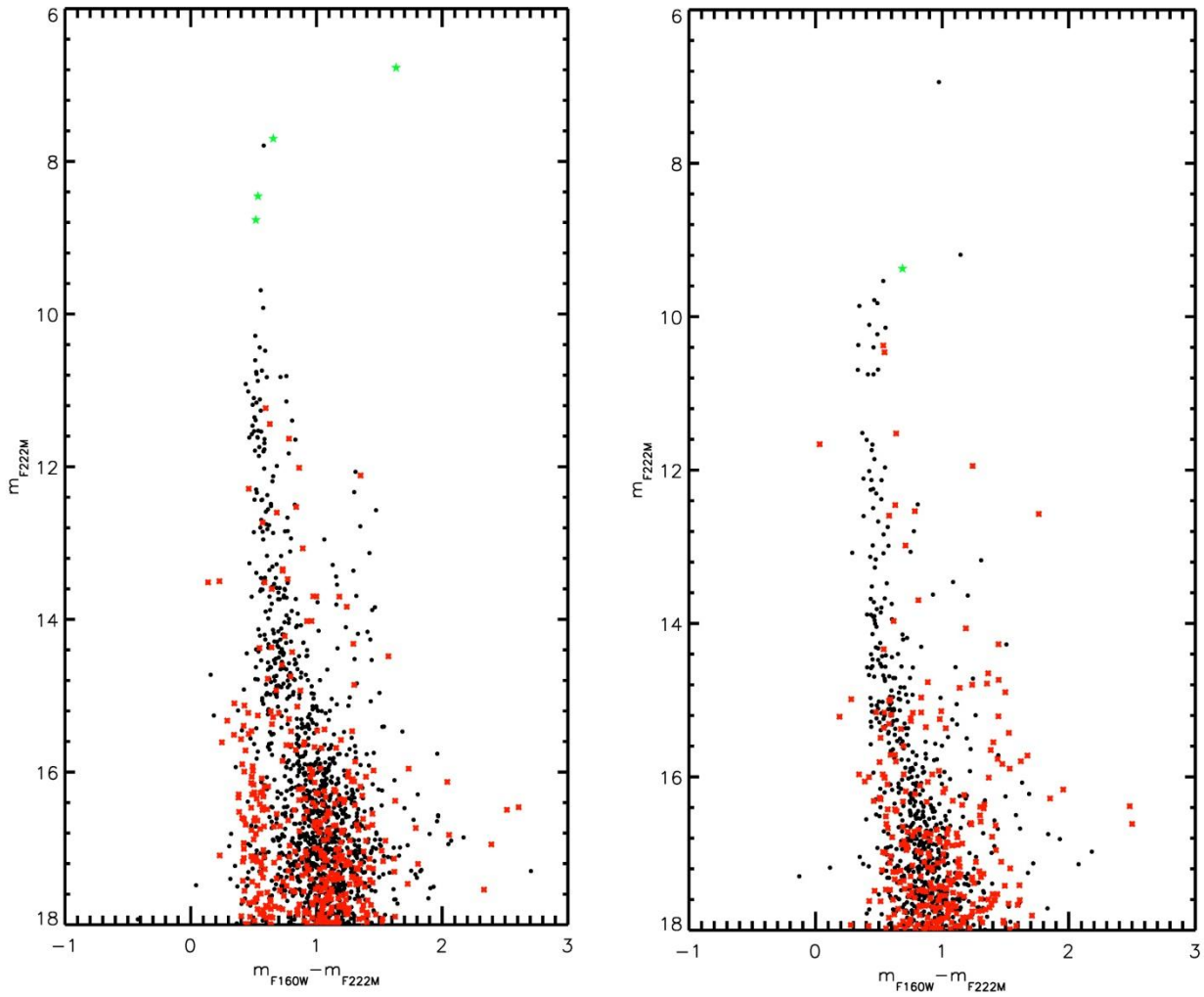

Figure 48 Right: Danks 1 HST CMD. Left: Danks 2 HST CMD

The stellar content of Danks 1 and 2 is examined in depth by Davies et al. (2012b), where the spectral typing methods are discussed in detail. The results of spectral typing are displayed in Figure 49, for comparison to other clusters in this sample.

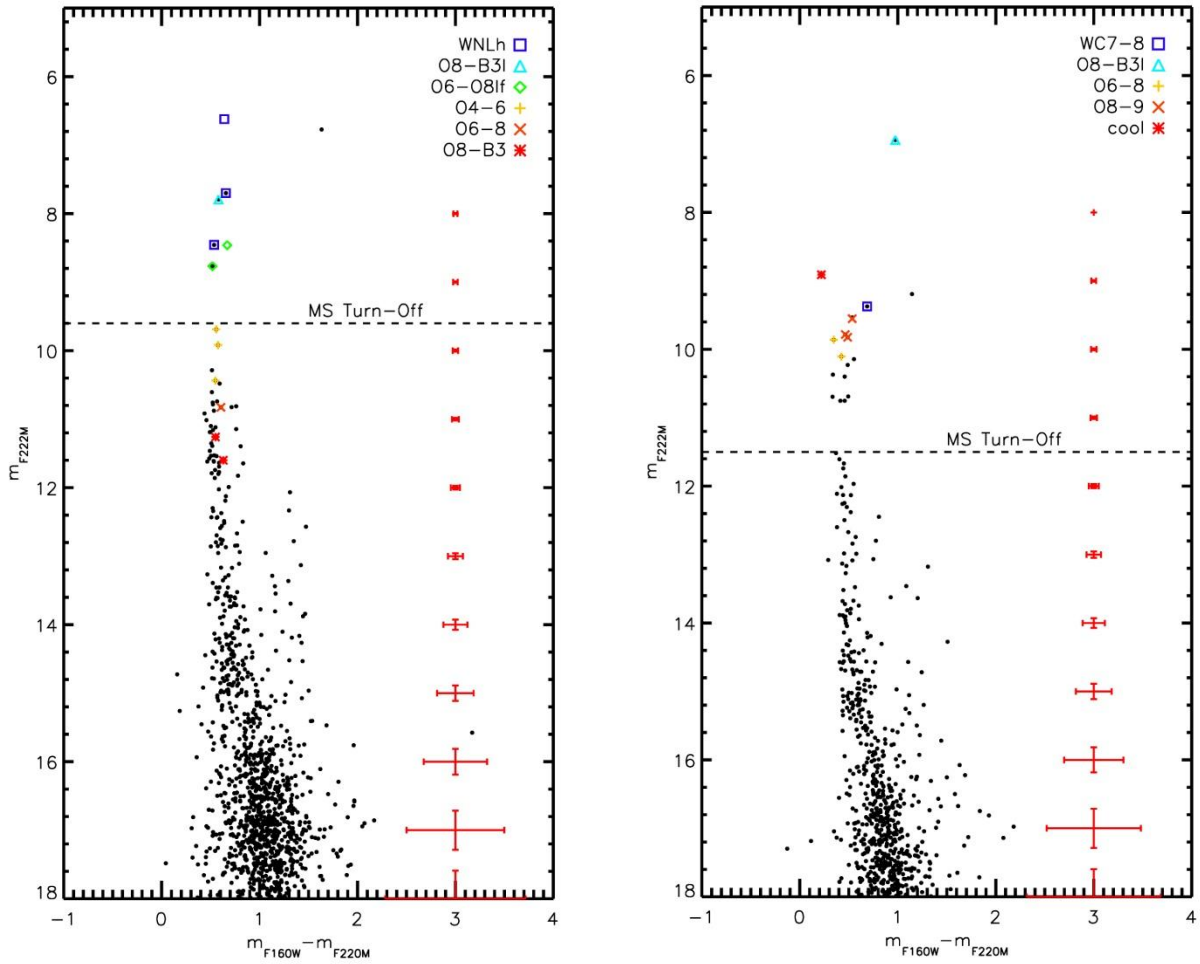

Figure 49 Left: Danks 1 CMD, spectral types labeled. Right: Danks 2 CMD, spectral types labeled.

3.9.2. Age, Distance, Mass

The WNLh star present in Danks 1 provides a strong constraint on the age of the cluster, as does the pre-MS population (or MS-turn on point). Using both the massive star population and MS turn-on, Davies et al. (2012b) derive an age of 1.5 Myr. Danks 2 contains a slightly older population. The spectral types of the hottest O-type stars are later than those in Danks 1 and the lower mass MS turn-on (~2 $M_{\odot}$) indicates an age of ~3 Myr. The carbon WR star in Danks 2 provides an upper limit of 6 Myr to the cluster age.

The distance to the clusters can be derived using the same spectrophotometric method as earlier for several Mercer clusters. Davies et al. (2012b) use this method to derive a distance of 3.8 kpc to both Danks 1 and 2.

The mass of both clusters is estimated by Davies et al. (2012b) to each be a few 10^3 $M_{\odot}$, based on a Kroupa IMF with a (measured) IMF slope consistent with the Salpeter slope.

3.9.3. X-ray Properties

X-ray observations of the region suggest active, ongoing star formation at the peripheries of the central cavity. WR42a is one of the most luminous X-ray WR stars in the galaxy (Zhekov et al. 2011), suggesting it is a colliding-wind binary. The age of WR48a is consistent with either cluster, Danks 2 more so, and was likely ejected from one or the other along with several other WR stars in the surrounding region (Mauheran et al. 2011, Davies et al. 2012b). Targeted CXO observations of the region include Danks 1 and Danks 2, though the majority of Danks 2 lies on the chip gap of the ACIS-I array onboard the Chandra X-ray Observatory (CXO). Only a single X-ray point source is coincident with HST point source population of Danks 2, while 13 HST point sources in Danks 1 are coincident with CXO sources, possibly indicating that the binary fraction of massive stars in Danks 1 is at present underestimated. The position of the X-ray sources in Danks 1 are shown in Figure 50, where X-ray sources coincident with an unnumbered Danks 1 star have the nomenclatureD1-X##.

The X-ray point sources coincident with Danks 1 are examined in order to identify possible MS binary systems. Inclusion of unresolved binaries acts to flatten the measured IMF.

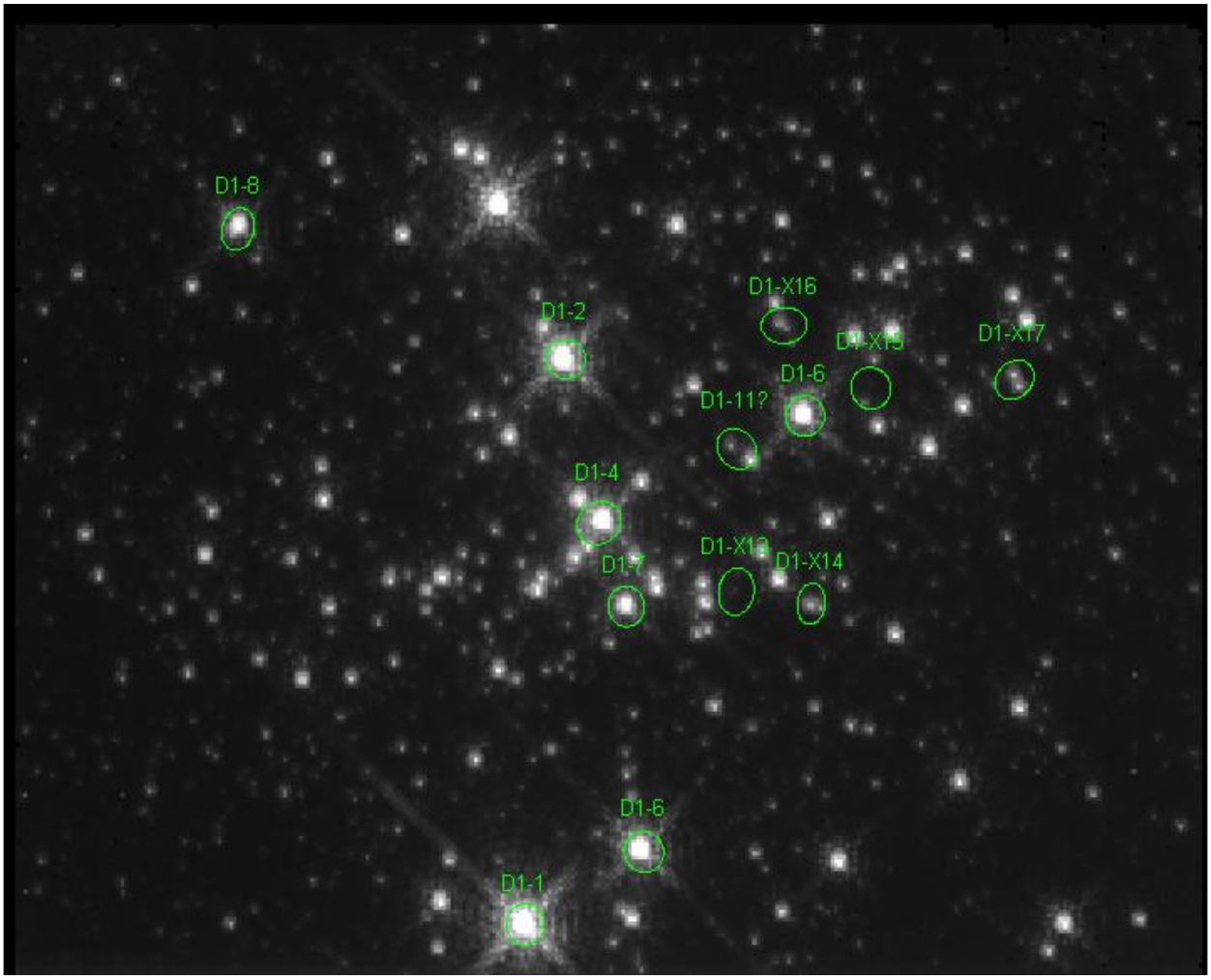

Figure 50 HST/NIC3 F222M image of Danks 1, with X-ray sources labeled. The size of the ellipse indicates the 90% enclosed X-ray flux.

The surrounding area has been examined by Mauerhan et al. (2011) and found to host a "halo" population of WR stars not associated with either of the central clusters, similar to WR48a. Several of these stars are X-ray point sources, and were included in this X-ray analysis of massive stars in the G305 star forming region.

X-ray emission from hot massive stars originates from four main mechanisms: soft X-rays originating in the wind of the star itself, likely due to self-shocking in the wind at X-ray luminosities of 10^{31}-10^{33} erg s^{-1} (Skinner et al. 2010); hard X-ray emission at high temperatures originating from wind-wind collisions (or colliding wind binaries, CWB) with L_X an order or magnitude or so higher; magnetic confinement (Gagne et al. 2005); or accretion onto a compact companion e.g. Be X-ray binaries, high mass X-ray binaries (HMXBs). The latter two mechanisms are more rare than the former.

The single X-ray source in Danks 2 is spatially coincident with D2-1, an O8-B3 I. Single O stars are known to be soft X-ray emitters, with $\log L_X/\log L_{bol} = -7$.

Table 17 X-ray sources in the G305 region

ID	RA	Dec	Counts	SpType	m_K	kT (keV)	L_X (ergs/s)
D2-1	198.23514	-62.674444		O8-B3I	6.81	0.90+/-.08	$2.00(10^{31})$
D1-1	198.11883	-62.695439	375	WNLh	6.62		
D1-2	198.10399	-62.700033		WNLh	7.46		
D1-4	198.109	-62.699269		O6-O8If	8.26		
D1-5	198.11872	-62.697461	624	WNLh	8.31		
D1-6	198.10933	-62.702644	304	O8-O8If	8.65		
D1-7	198.11172	-62.699011	357	O4-O6	9.54		
D1-8	198.09525	-62.696839		O4-O6	9.69		
D1-11	198.10915	-62.701544					
D1-X13	198.11305	-62.700506					
D1-X14	198.11457	-62.701364					
D1-X15	198.10961	-62.703672					
D1-X16	198.10625	-62.703031					
D1-X17	198.11165	-62.705544					
MDM3	198.0378	-62.724025	464	WN8-9	7.58		$1\text{-}18(10^{32})$*
MDM4	198.08833	-62.6700		WC8	8.77		$3\text{-}11\ (10^{31})$ *
MDM5	198.10613	-62.744858		WN9	7.65		$6\text{-}33\ (10^{30})$ *
Halo 1	198.11064	-62.719536			8.47		
Halo 2	198.09151	-62.666517			8.98	2.3+/-0.96	
Halo 3	198.08853	-62.666381			9.46	1.5+/-0.41	
Halo 4	198.07964	-62.743872			9.70		
Halo 5	198.13322	-62.685772			8.97		

*taken from Mauheran et al. (2011), who assumed a distance of 3.5 kpc

The low resolution X-ray spectrum of MDM3 show prominent emission lines at 2.4 keV and 3.1 keV, attributed to highly ionized S and Ar respectively. Another feature at 3.9 keV can be attributed in He-like Ca.

The stars Danks 1-1 and Halo 2 show emission features at 1.8 and 2.4 keV, due to Si XIII and S XV, while Halo 3 has strong emission at 1.8 but weaker 2.4 keV emission than Danks 1-1 or Halo 2, indicating a slightly cooler plasma temperature. Alternately, Danks 1-7 shows strong emission at 1.8, 2.4, and what appears to be emission at 2.9 keV, attributable to slightly hotter temperatures than would be derived by Danks 1-1 or Halo 2.

Danks 1-2 has an emission feature at 1.8 keV but no other prominent X-ray lines, suggesting a cooler plasma temperature for this object than for Danks 1-1 or Danks 1-5. Similarly, Danks 1-6 shows strong emission at 1.8 keV but lacks other strong emission lines.

Danks 1-5 shows strong emission at 1.8 keV and 2.4 keV, with weaker emission at 3.1 keV and possibly 3.9 keV. Similarly, MDM3 contains the same lines in its low-resolution X-ray spectrum. Given that both objects are late WN, the similarity in X-ray emission is expected.

No X-ray emission is found to be spatially coincident with MS stars in Danks 1. The nature of the halo population of X-ray sources remains unknown, as no optical/IR spectroscopic observations of these objects are available at this time.

3.9.4. Summary

Davies et al. (2012b) present the IMF for both clusters Danks 1 and Danks 2, along with a slope measurement from the MS turn-on to turn-off. Using the same data and a similar method makes these two clusters an excellent double-check on the results of this project. To clarify, the IMF results of Davies et al. (2012b) are not used in this work. Instead, the IMF of Danks 1 and Danks 2 will be constructed in the same way as other clusters in the sample presented here then compared to the results of Davies et al. (2012b).

3.10. [BDS2003] 66

The color-magnitude diagram of BD66 closely resembles that of BD52, the "bubble cluster." In fact, BD66 is enclosed in a similar (but less circular) IR bubble, shown in Figure 51, indicating that the cluster is just beginning to clear its natal material. Similar to BD52, a pre-MS is visible to the lower right of the MS (see Figure 52 and Figure 55).

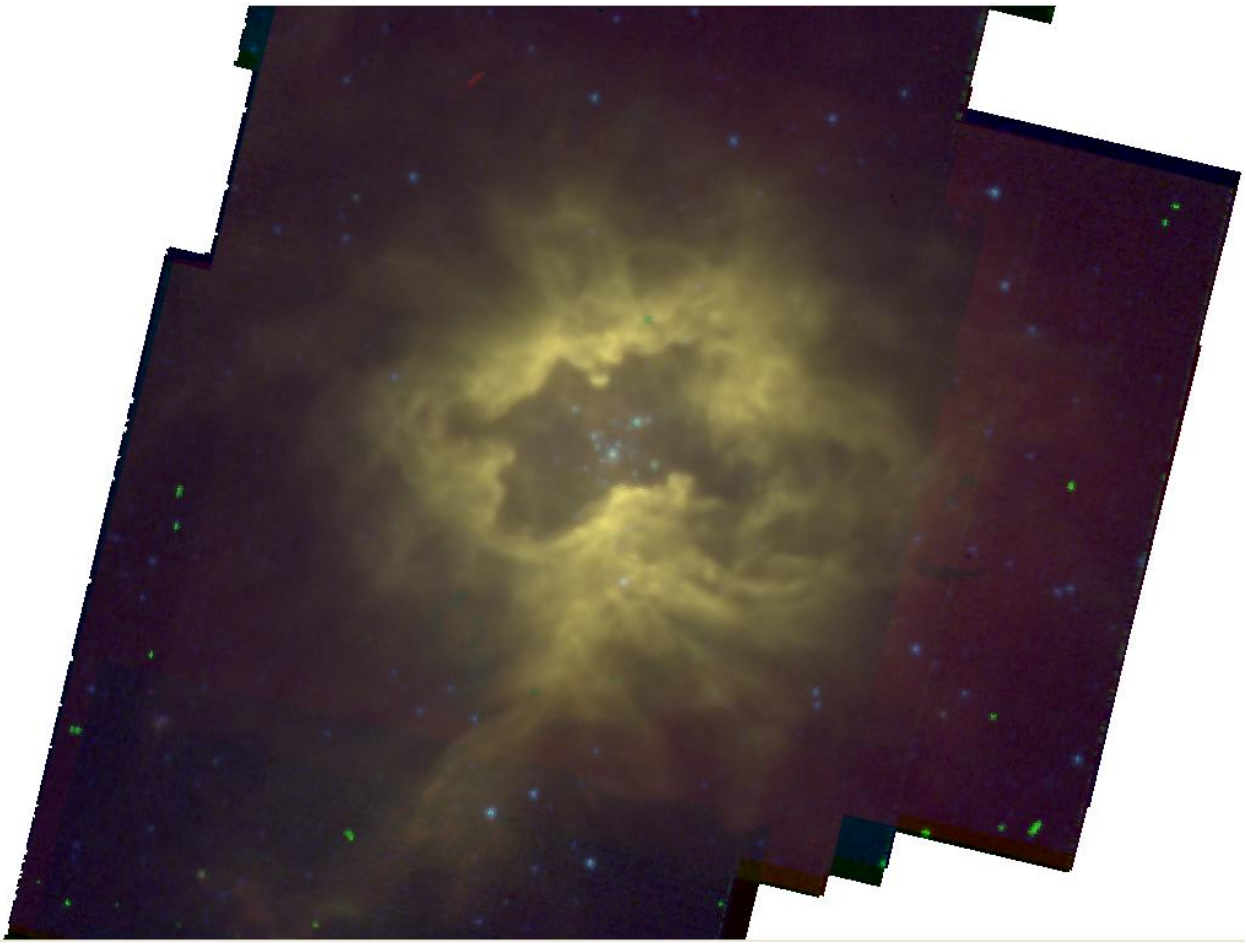

Figure 51 Spizter 3-color image of BD66. Blue: 3.6 micron; Green: 5.8 micron; Red: 8.0 micron. North is up, East is left.

3.10.1.Stellar Content

Target stars in BD66 were observed spectroscopically as part of the September 2012 and January 2013 IRTF/SpeX observing run. The finding chart is shown in Figure 53, and the reduced spectra in Figure 54.

This cluster contains a PEL object, BD66-4, revealed to be a reddened Be star. A search of the SIMBAD database reveals that the center of the cluster is a poorly studied but populous place; a 2MASS source classified as a galaxy is coincident with BD66-4. Given the spectral type and high reddening towards this object, in addition to the IR bubble surrounding the cluster, it is unlikely that the 2MASS source is extragalactic in origin.

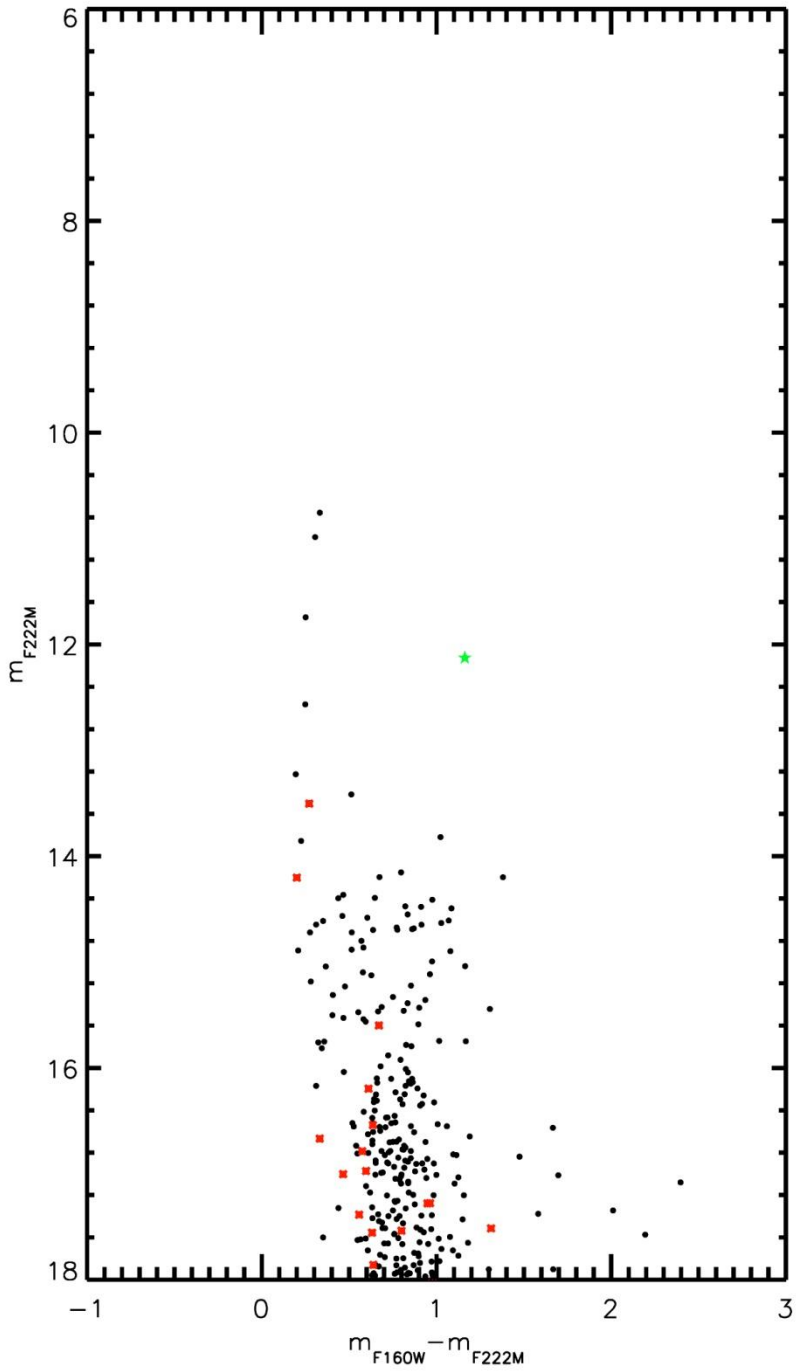

Figure 52 HST/NIC3 color-magnitude diagram of BD66. Emission line object is indicated by the green star symbol.

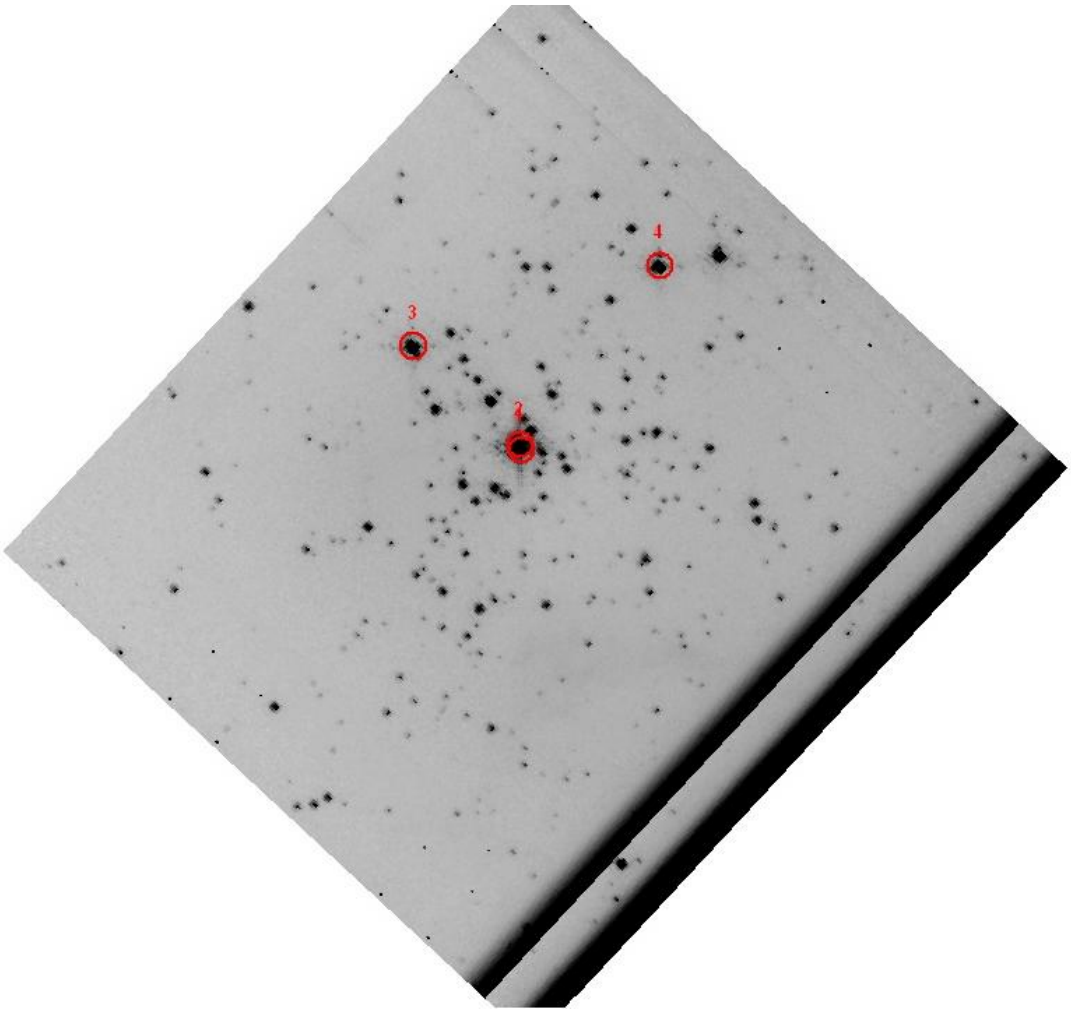

Figure 53 HST F222M finding chart; spectroscopic targets labeled. North is up, East is left. The separation between targets 1 and 2 is smaller than the size of the label, resulting in overlapping labels in this figure.

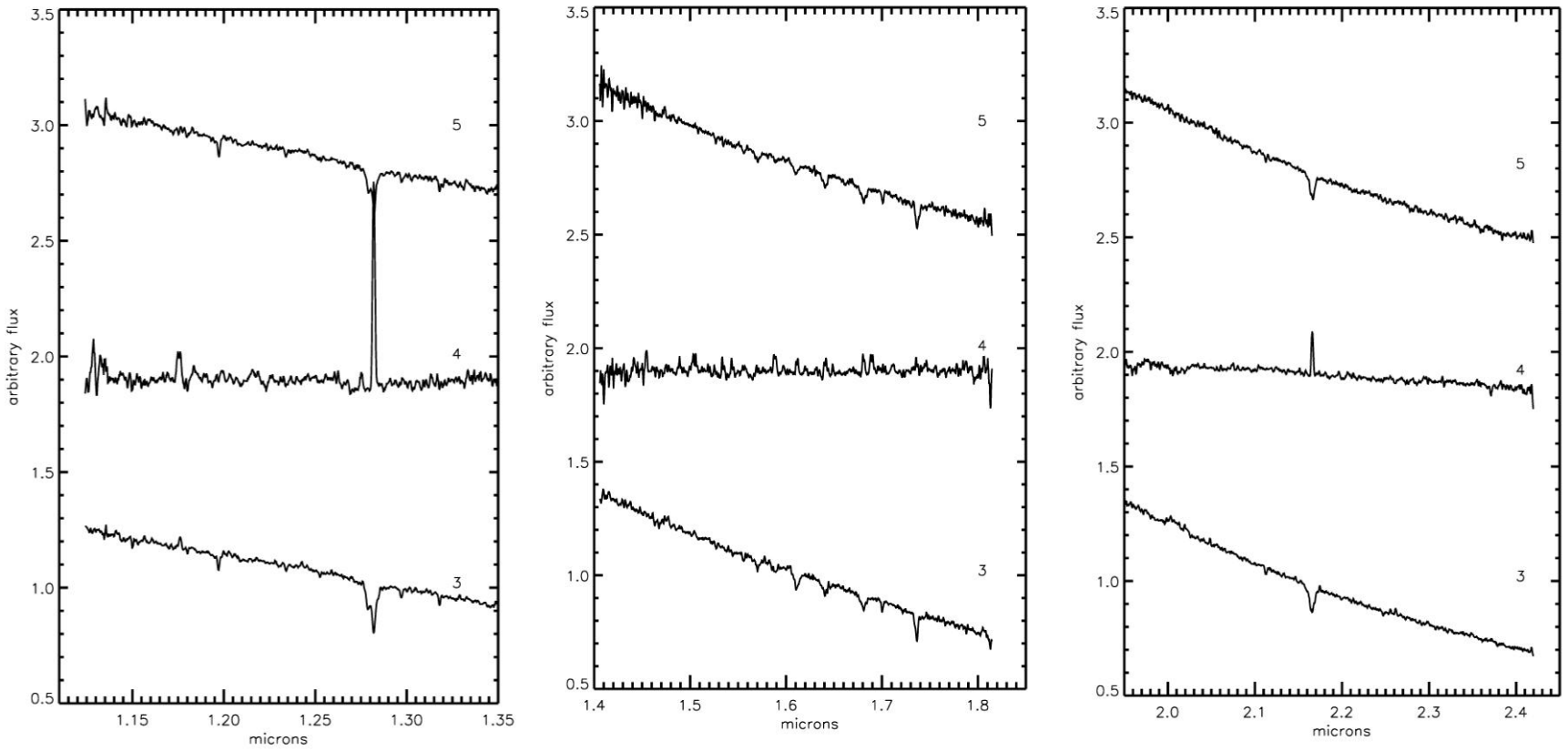

Figure 54 Right to left: J-band, H-band, and K-band spectra of spectroscopically observed objects in BD66

3.10.1.1. Spectral Typing

Strong hydrogen emission lines in the H and K band spectrum of BD66-4 indicate a Be nature for this object.

BD66-3 shows HeI (2.112 micron) and Brγ absorption in the K band, with HeI and HI absorption in the H band as well (1.641, 1.68, 1.700, 1.73 micron). No evidence for HeII is present in the H band spectrum, indicating a spectral type later than O8. Based on these lines, BD66-3 is classified as O9-B1 V.

The spectrum of BD66-5 is very similar to that of BD66-3, with similar HI and HeI absorption lines. The slightly weaker HeI absorption at 2.112 is suggestive of a possibly later spectral type than BD66-3, resulting in a classification of O9-B2 V for this star.

Results of spectral typing for BD66 objects are summarized in Table 18 and shown on the HST CMD in Figure 55. The red dashed line in this figure indicates a 2 Myr MS isochrone, while the dashed blue line indicates a 2 Myr pre-MS isochrone. Objects redward of the pre-MS isochrone are interpreted as pre-MS stars younger than 2 Myr still evolving along Hayashi tracks.

Table 18 List of stars spectroscopically observed

ID	RA	Dec	m_{F160W}	m_{F222M}	SpType
1	04 36 49.57	+50 52 41.75	11.09	10.76	Blended w/BD66-2
2	04 36 39.58	+50 52 42.27	11.29	10.99	Blended w/BD66-1
3	04 36 50.46	+50 52 49.91	11.99	11.74	O9-B1 V
4	04 36 48.41	+50 52 56.28	13.29	12.13	Be
5	04 36 47.92	+50 52 56.92	12.82	12.57	O9-B2 V

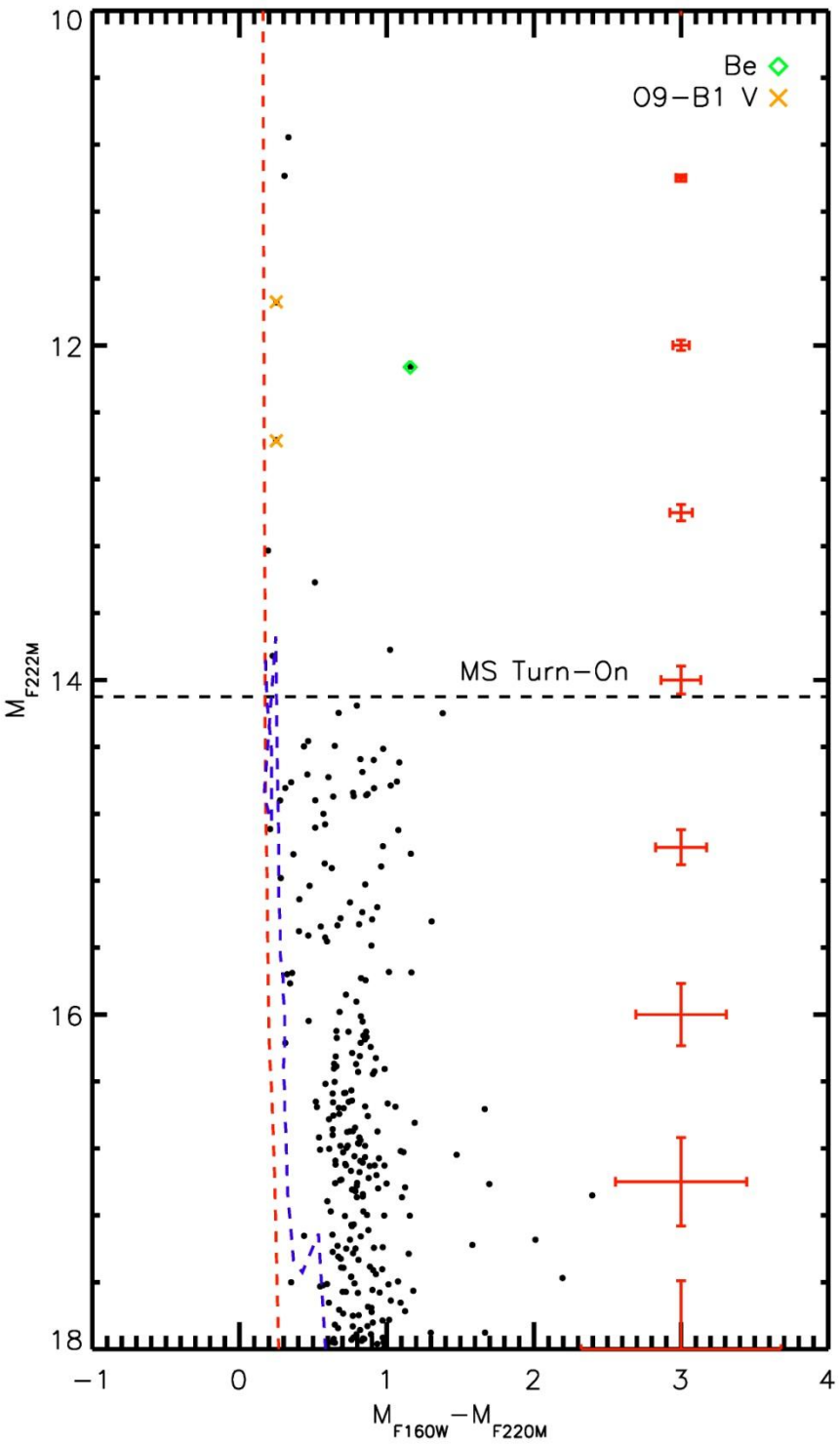

Figure 55 CMD of BD66 with spectroscopically observed stars labeled. Typical photometric errors are shown on the right.

3.10.2. Age, Reddening, Distance

At the time of writing, there is not enough information on BD66 to determine the age, distance, or mass of the cluster. This analysis was hoped to be completed after 20 Jan 2013, at which time the spectra of objects BD66-1 and BD66-2 were obtained. Due to high winds and variable seeing, the two objects could not be sufficiently resolved to disentangle the spectrum of BD66-1 from that of BD66-2. The five brightest stars in the cluster are late-O to early-B type, and a pre-MS feature is observed to the right (red) of the MS. The pre-MS feature suggests a very young age, 1-3 Myr.

Spectrophotometric distance estimates range from 4.5 to 8.0 kpc for the three brightest objects in the cluster. No definitive distance estimate can be derived at this time.

The average reddening towards BD66 can be computed from the two O stars, and is found to be A_K=0.28.

3.10.3. Summary

Due to the relative dearth of stars occupying the main sequence, the large number of likely pre-MS stars, the low mass estimate, and the upper age limit suggested by the presence of no objects earlier than ~O9 an analysis of the IMF of BD66 would not significantly contribute to the overall goal of this project.

3.11. [DB2001] Cl 20

The cluster [DB2001] Cl 20 (hereafter DB20) is identified by Dutra et al. (2001) from the 2MASS catalog. This object is not covered by GLIMPSE or any targeted Spitzer observation. The cluster is, however, covered by the WISE all-sky survey. The resolution of WISE is much poorer than that of HST, making it difficult to assign WISE sources to specific stars in DB20. What is evident, however, is the large IR excess associated with DB20-1, the brightest star in the HST field of view.

The HST color magnitude diagram is presented in Figure 56. Emission line objects, as determined by F190N-F187N colors, are indicated by green stars, while the control field contribution is shown by red asterisks.

3.11.1. Stellar Content

DB20 contains three early Be stars, two of which were identified as PEL stars from narrow-band HST imaging. Multiple Be stars are found in the h and chi Persei clusters, shown by Marsh Boyer et al. (2012). These authors also identify several transient Be stars in these clusters, suggesting that Be stars are common in stellar clusters.

The CMD of DB20 is shown in Figure 56, where the two PEL objects are indicated by green stars. The results of control field photometry are indicated in the same figure, overplotted as red asterisks.

DB20 was part of the northern spectroscopic follow-up program at IRTF, PI Trombley. The finding chart for these observations is shown in Figure 57 and the reduced spectra in Figure 58.

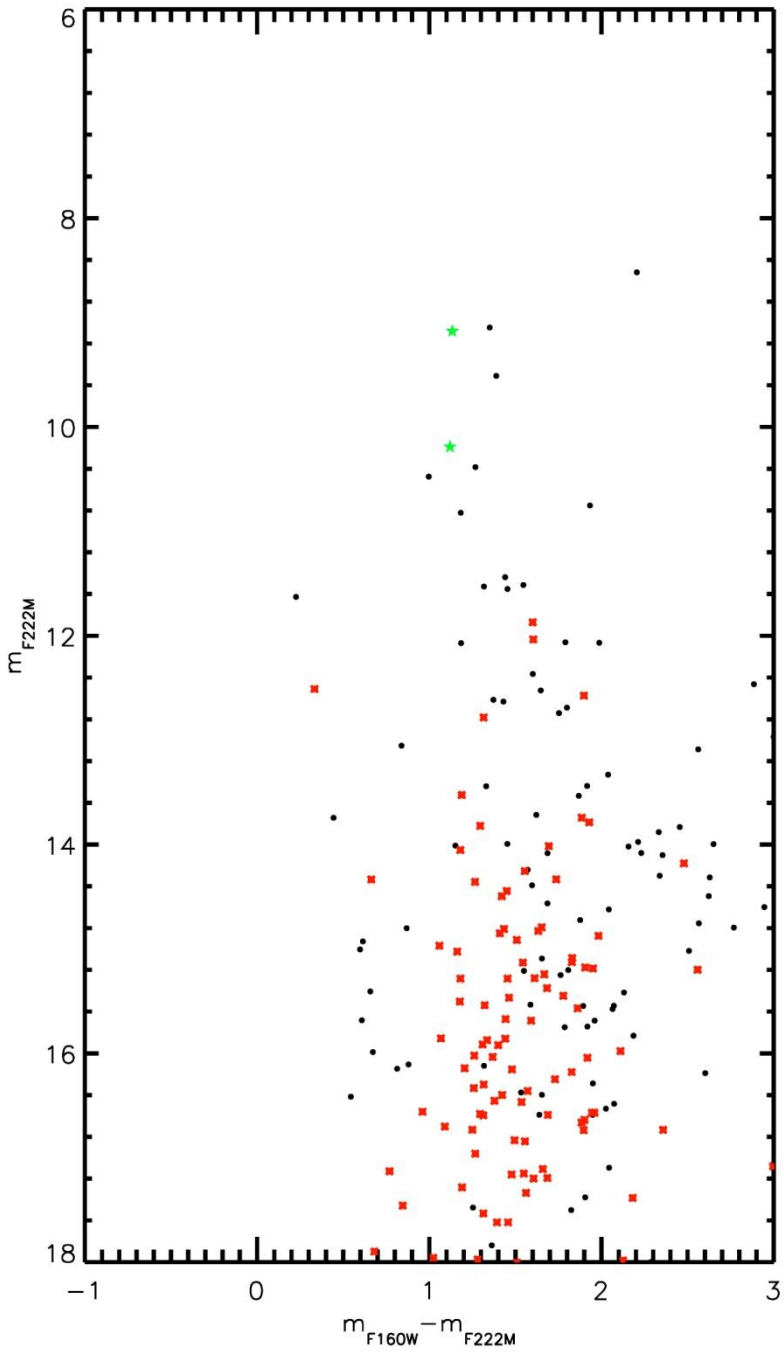

Figure 56 HST CMD of DB20. Emission line objects are indicated by green stars, stars in the cluster FOV by black filled circles, and stars in the control field by red asterisks.

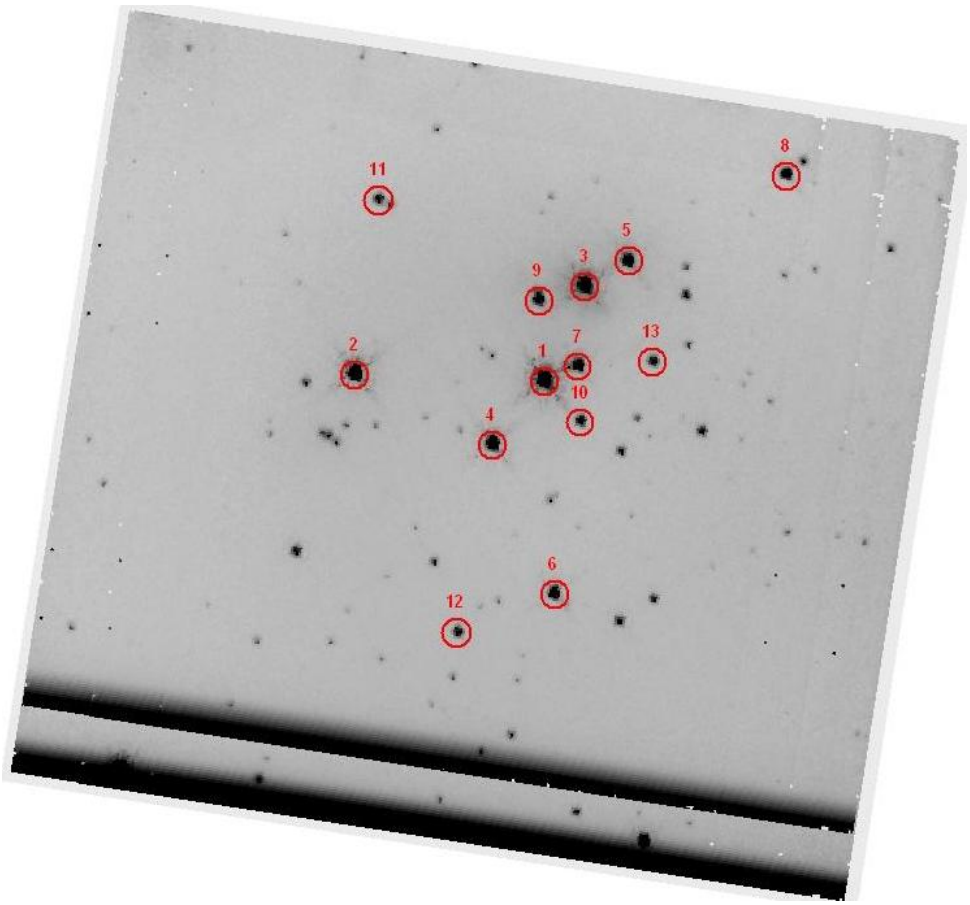

Figure 57 Finding chart for DB20. North is up, East is left.

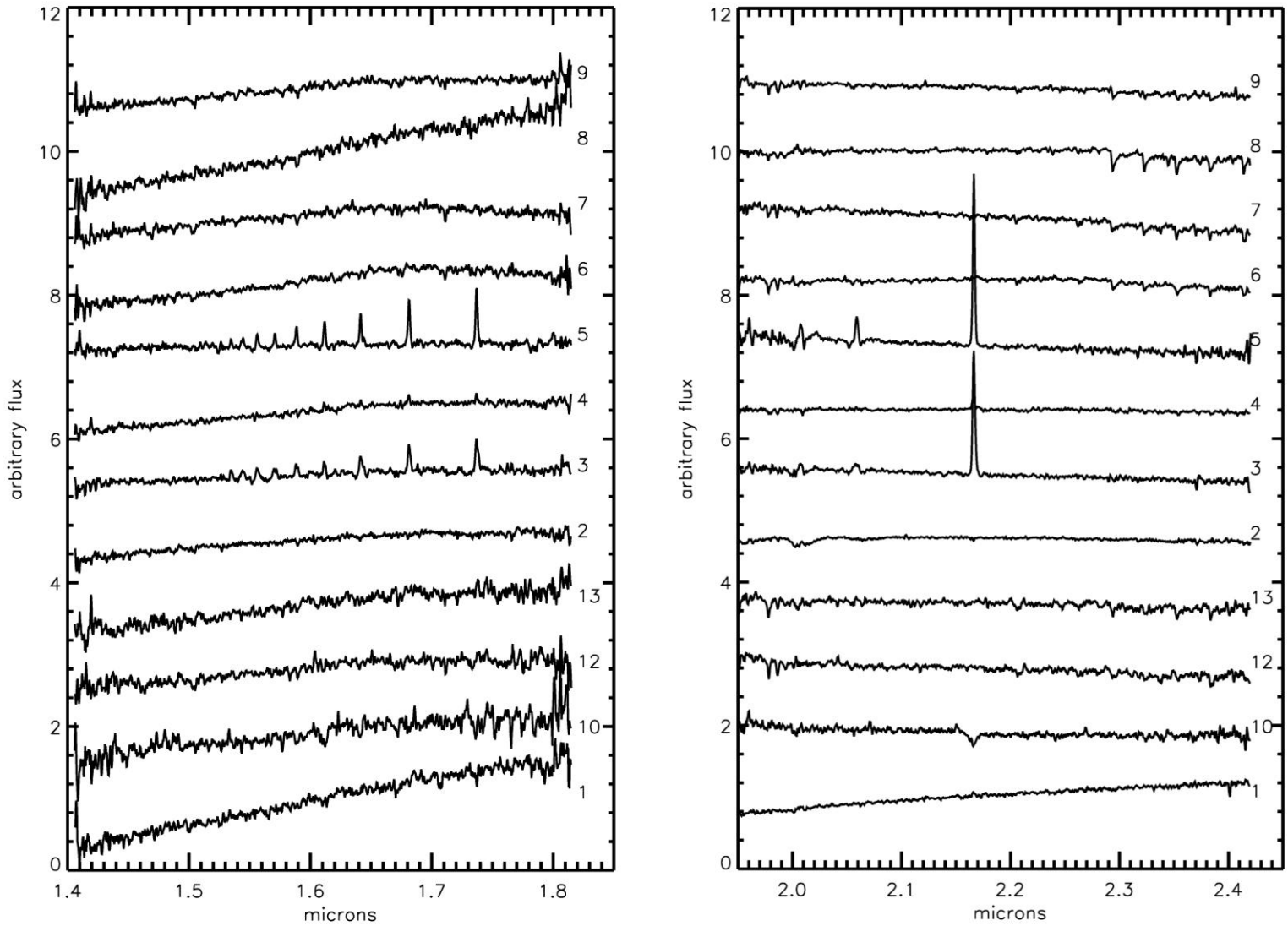

Figure 58 Left: H-band spectroscopic observations of DB20 stars. Right: K-band spectroscopic observations of DB20 stars.

3.11.1.1. Spectral Typing

Spectral types for DB20-3, -4, and -5 are found based on the complete Hydrogen Paschen series seen in emission in these three objects. The Be nature of these three stars is not unexpected: Be stars are often "contaminants" in WR emission line searches. Clark & Steele (2000) group Be stars into five groups, dependent on IR spectral morphology. Two of the Be stars, DB20-3 and -5, are classified as Group 1 according to this nomenclature, showing the Bracket series in emission and HeI at 2.058. Group 1 objects are, according to Steele & Clark (2001), of early spectral type (O9e-B3e) while Group 5 objects (DB20-4) have slightly later spectral types (B4e-B9e).

The brightest object in the cluster, DB20-1, is complex in H and K bands as it suffers from high extinction (which is confirmed by the flux-calibrated spectra). Bracket Gamma emission in the K band suggests some type of weak emission line star, but H band absorption lines are not consistent with this spectral type. DB20-2 is also somewhat of a mystery, displaying what appears to be a featureless spectrum in both H and K.

DB20-10 shows Brγ absorption and HeI absorption, consistent with an early to mid-B spectral type, most likely of luminosity class V.

The remaining objects in DB20 show CO bandhead absorption beginning at 2.30 microns, indicating cool, late type stars. These are likely foreground giants, but warrant further inspection to rule out a supergiant luminosity class.

The results of spectral typing for DB20 are summarized in Table 19 and graphically presented in Figure 59, the HST CMD labeled with spectral types.

Table 19 List of stars spectroscopically observed

ID	RA	Dec	m_{F160W}	m_{F222M}	SpType
1	20 38 37.62	+42 39 25.89	10.72	8.52	Brγ emission
2	20 38 38.89	+42 39 26.41	10.40	9.05	featureless
3	20 38 37.35	+42 39 32.81	10.21	9.08	O9e-B3e
4	20 38 37.97	+42 39 21.22	10.90	9.51	O9e-B3e
5	20 38 37.05	+42 39 34.72	11.31	10.19	B4e-B9e
6	20 38 37.55	+42 39 10.20	11.65	10.38	late type/cool
7	20 38 37.39	+42 39 26.95	11.47	10.48	late type/cool
8	20 38 36.00	+42 39 41.00	12.68	10.75	late type/cool
9	20 38 37.65	+42 39 31.78	12.00	10.82	late type/cool
10	20 38 37.38	+42 39 22.82	12.88	11.44	early-mid B
11	20 38 38.72	+42 39 39.25	13.06	11.51	unobs'd
12	20 38 38.20	+42 39 07.41	12.85	11.53	late type/cool
13	20 38 36.89	+42 39 27.32	13.01	11.55	late type/cool

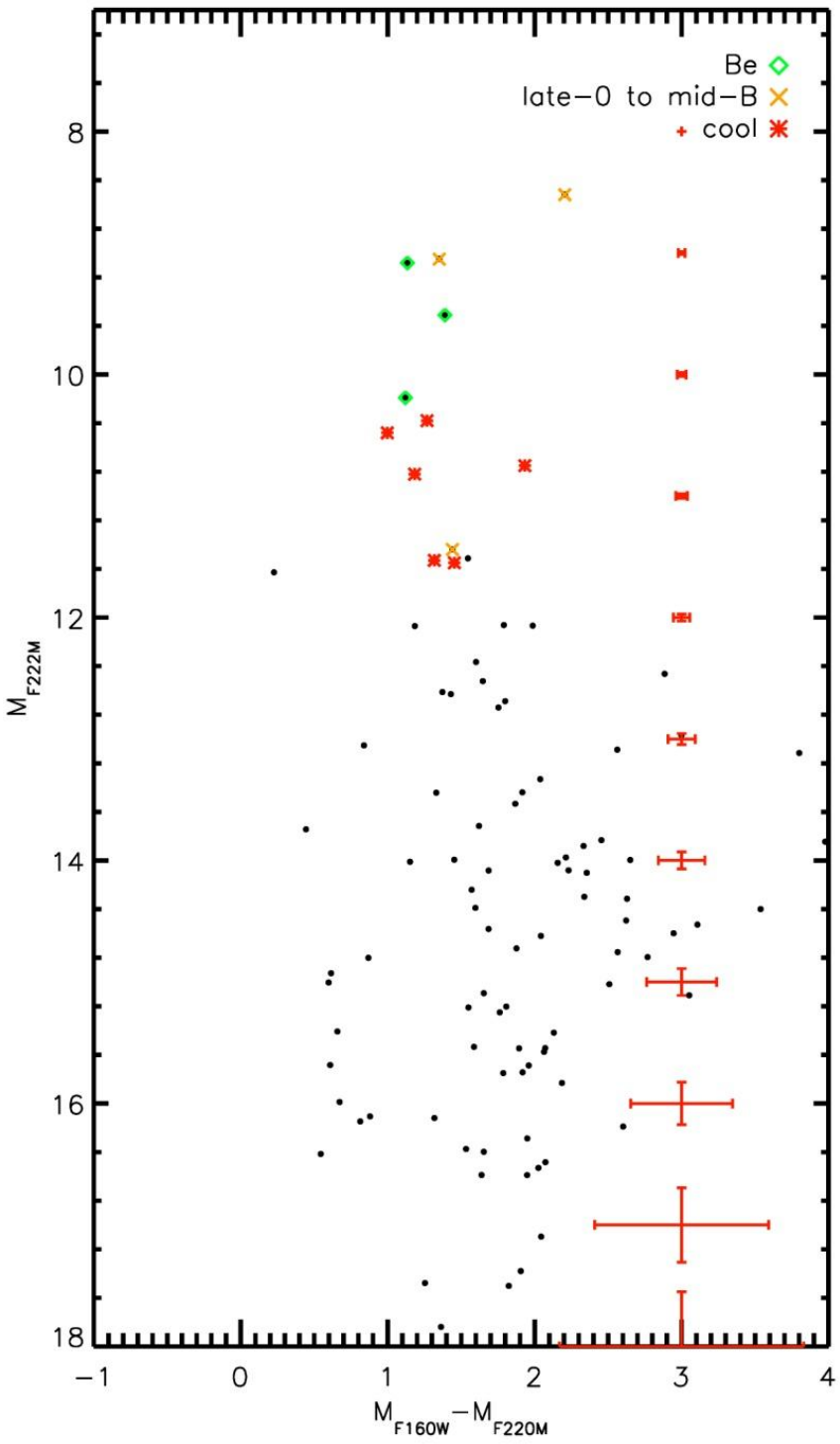

Figure 59 CMD of DB20 with spectroscopically observed stars labeled. Typical photometric errors are shown on the right.

3.11.2. Age, Reddening, Distance, Mass

The age of the cluster remains ambiguous. Early B-type MS stars place an upper limit on the age of the cluster based on their MS lifetimes, roughly 10 Myr. The Brγ emission line object and Be stars place no better constraints on the age of DB20.

Extinction towards the cluster is computed by examining the NIR colors of normal OB type stars, i.e. clearly heavily reddened stars are excluded. For DB20, an average value of A_K=2.12+/-0.22 is found, based on 5 stars observed by HST/NIC3 and IRTF/SpeX. The brightest star in the cluster is excluded as it displays IR excess in addition to what is observed towards fainter cluster sequence.

Spectrophotometric distance estimates suffer from high extinction towards the cluster. The low SNR of the spectroscopic observations results in poorly defined spectral types, increasing the spectrophotometric distance ambiguity. Table 20 shows the results of spectrophotometric distance estimates towards two of the cluster stars, DB20-1 and DB20-10. The median distance is ~2 kpc, assuming a MS luminosity class for DB20-10. It is possible that DB20-10 represents the MS turn-off, as Be stars are typically supergiants and the photometry of DB20-1 is consistent with a supergiant luminosity class.

Table 20 Spectrophotometric distance estimates

ID	m_{F222M}	SpType	D_V/kpc	D_{III}/kpc	D_I/kpc
1	8.52	Brγ emission	0.39-0.42	0.73-0.76	1.37-2.16
10	11.44	Early-mid B	1.43-2.72	4.45-5.25	6.93-10.98

The mass of the cluster is ill-defined as no IMF can be constructed to provide a mass estimate via the method outlines in Equation 5. The high number of contaminating cool stars also complicates the determine of cluster mass.

3.11.3. Summary

Due to the enigmatic nature of the two brightest objects, the seemingly high fore- and background contamination by cool stars in the upper parts of the CMD, and to the upper limit on the cluster age as derived by the early type stars, DB20 is rejected from IMF analysis. The high fore-and background contamination of cool, late type stars is not predicted, as no objects in the control field fall in this area of the CMD (e.g. see Figure 56).

3.12. [DB2001] Cl 9

The candidate cluster [DB2001] Cl 9 (hereafter DB9) is located at 20 32 27.8, +38 51 26, in the direction of the CygOB2 association. Identification of diffuse interstellar bands (DIBs) in DB9 stars are similar to those seen in CygOB2, suggesting that both objects lie at similar distance. The cluster is enclosed in a

large, ~5 pc, infrared bubble which also contains the candidate star cluster [DB2001] Cl 10. At mid- to far-infrared wavelengths, this bubble becomes almost two-lobed, e.g. Figure 64. This figure displays bright emission centered on the brightest star in DB9 and the central region of DB10.

3.12.1.Stellar Content

DB9 was part of the northern spectroscopic follow-up program at IRTF, PI Trombley. Spectroscopic targets were chosen based on the properties of the CMD, Figure 60. The finding chart is shown in Figure 61 and the reduced spectra in Figure 62.

Inspection of the HST NIC3 CMD in Figure 60, indicates that the brightest object in the field is an emission line object, the green star symbol, stars in the cluster field of view are displayed by black circles, and stars in the control field are indicated by red asterisks.

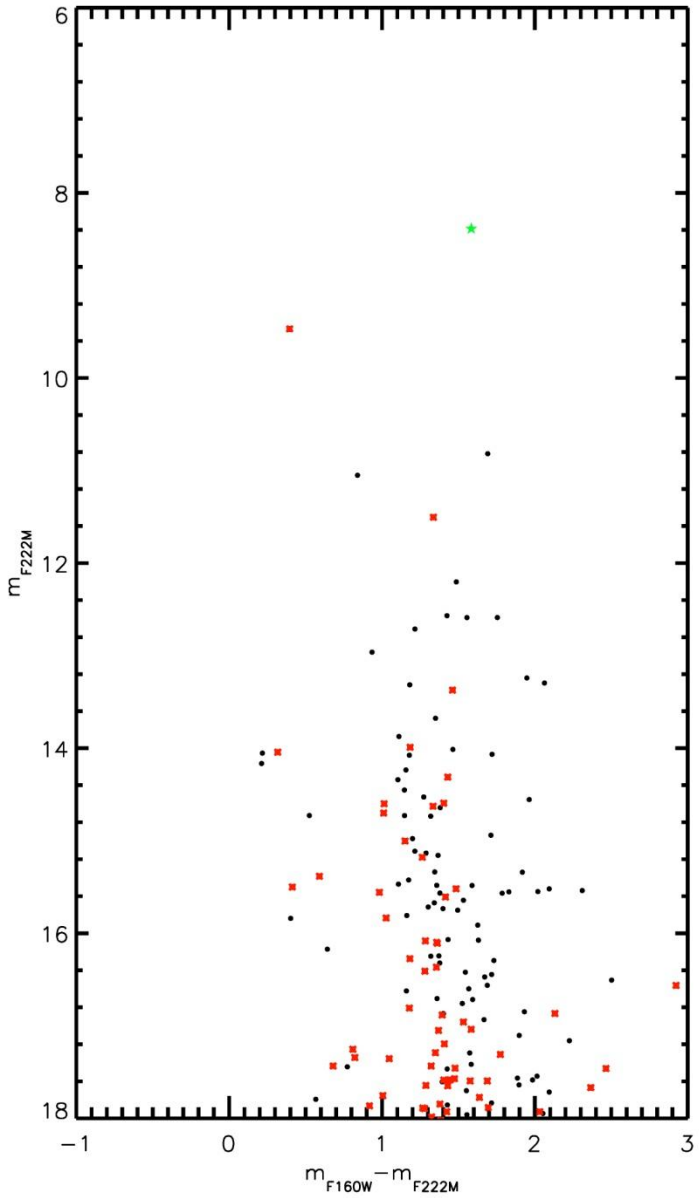

Figure 60 HST CMD of DB9. The emission line object is indicated by a green star, and the control field photometry overplotted as red asterisks.

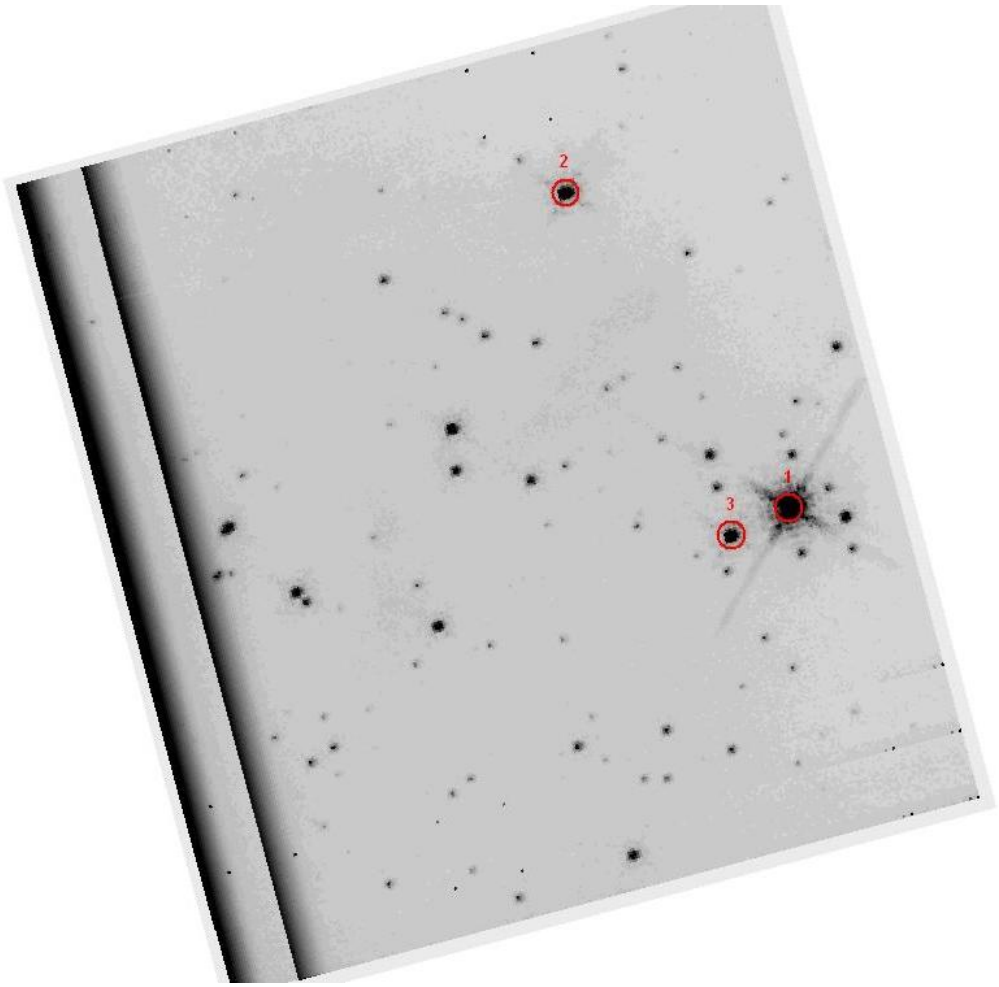

Figure 61 Finding chart for IRTF/SpeX observations

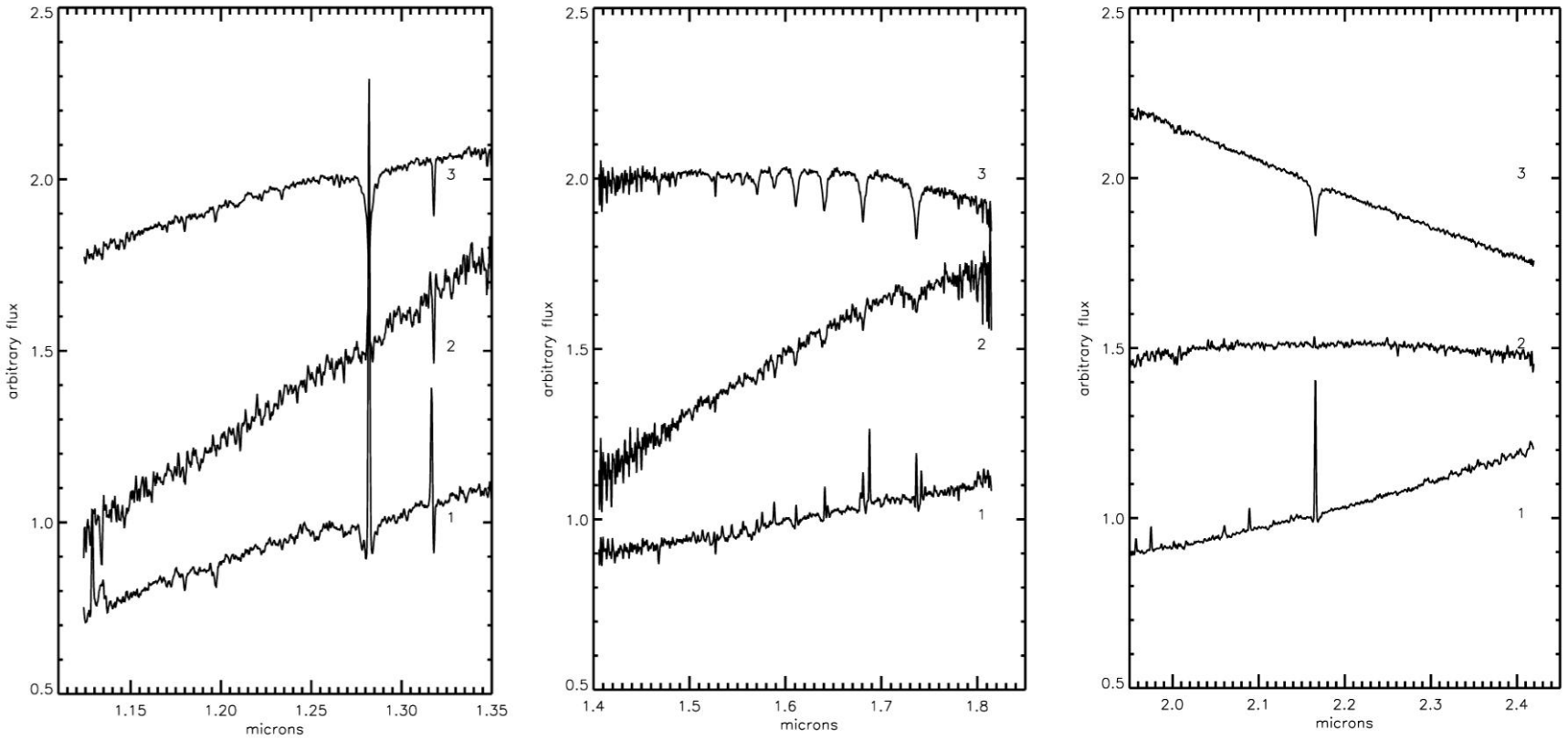

Figure 62 From left to right: J-band, H-band, and K-band spectra of DB9 stars

3.12.1.1. Spectral Typing

The brightest star in the HST observations, DB9-1, has a clear infrared excess and saturates in 8 micron Spizter/IRAC images. WISE observations do not suffer from this issue (see Figure 64 and Figure 65) and exhibit a clear point-source morphology at the position of DB9-1. The IR spectra of this object contain prominent narrow Hydrogen emission lines superimposed on (broader) Hydrogen absorption features in J, H, and K bands, as seen in Figure 62 and in more detail in Figure 66. The presence of [FeII] at 2.09 microns confirms this object as a newly discovered Galactic B[e] supergiant. The B[e] spectral type suggests that the infrared excess originates in a circumstellar disk around DB9-1. Figure 64 and Figure 65 demonstrate the near- to mid-IR excess associated with DB9-1, both as a point source at the same position and as a large IR nebula region surrounding the cluster. The nebulosity begins to dim long-wards of 12 microns, where point source emission from DB9-1 and another source to the southwest begin to dominate the IR emission.

DB9-2 shows an infrared excess which can likely be attributed to patchy extinction towards the cluster. This star is not a point source similar to DB9-1 in mid-IR images (Figure 64, Figure 65). Inspection of the HST 3-color image, Figure 115, and mid- to far-IR images reveals a diffuse IR excess towards this star, while DB9-1 and DB9-3 are not contained in the same nebulosity. Inspection of a wider area surrounding the cluster indicates that DB9-2 sits towards the center of what appears to be a shell of dust, as shown in the three color image presented in Figure 64 and the grey scale images in Figure 65. The additional extinction towards DB9-2 makes spectra typing difficult as this source has a lower SNR than expected for its mF222M magnitude. There is weak Brγ emission in the K band, and H band absorption at 1.61, 1.64, 1.68, and 1.736 microns, suggesting a mid- to late-B spectral type.

The spectrum of DB9-3 shows strong HI absorption features consistent with a spectral type of A1 V (see Fig 14 of Hanson et al. 2005, for example).

The results of spectral typing are summarized in Table 21 and displayed graphically in Figure 63.

Table 21 List of spectroscopically observed stars

ID	RA	Dec	m_{F160W}	m_{F222M}	SpType
1	20 32 27.04	+38 51 26.0	9.97	8.39	B[e] I
2	20 32 28.45	+38 51 49.3	12.51	10.82	B5-B9 V
3	20 23 05.27	+38 51 24.0	11.89	11.05	A1V

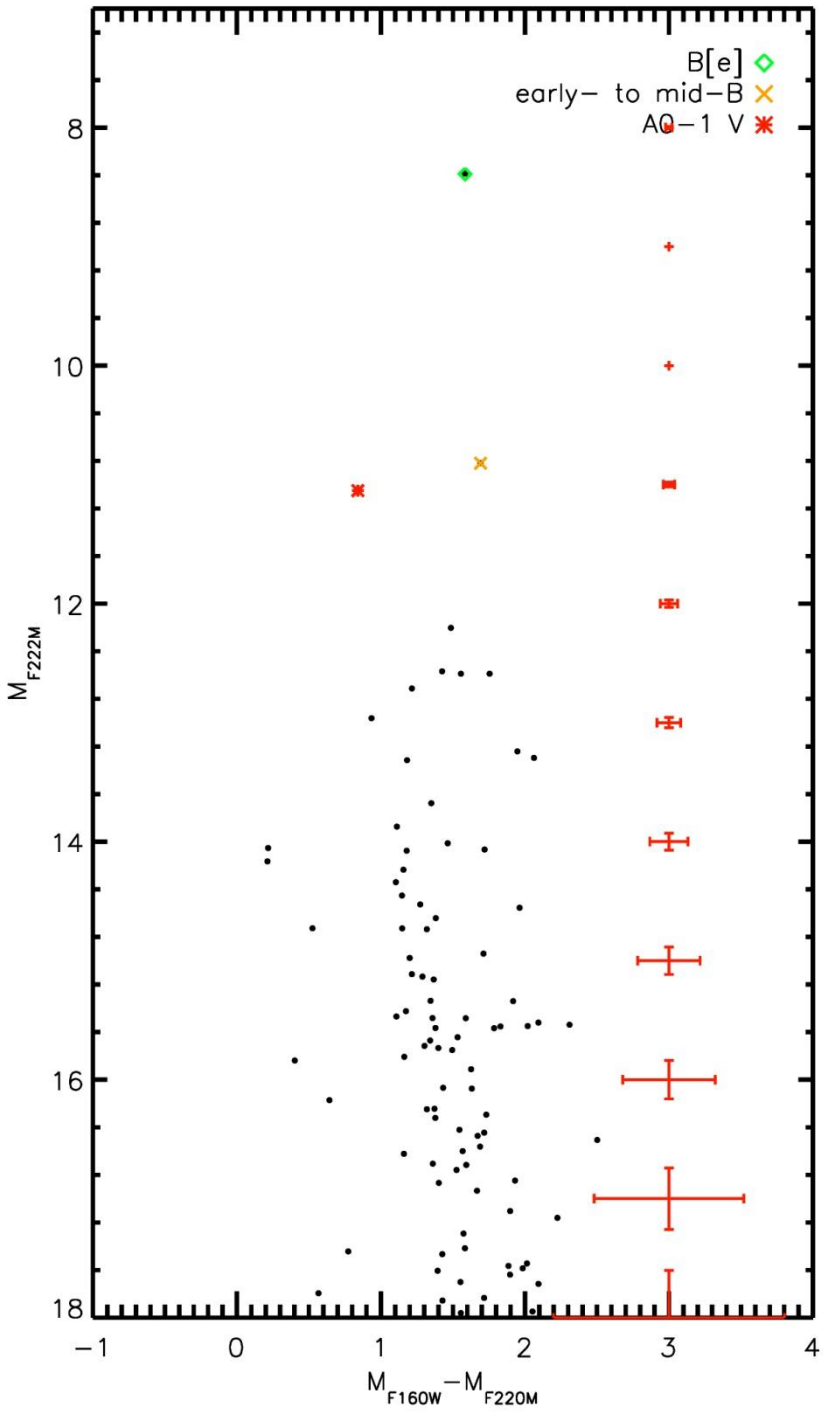

Figure 63 CMD of DB9 indicating spectroscopically observed objects in the cluster.

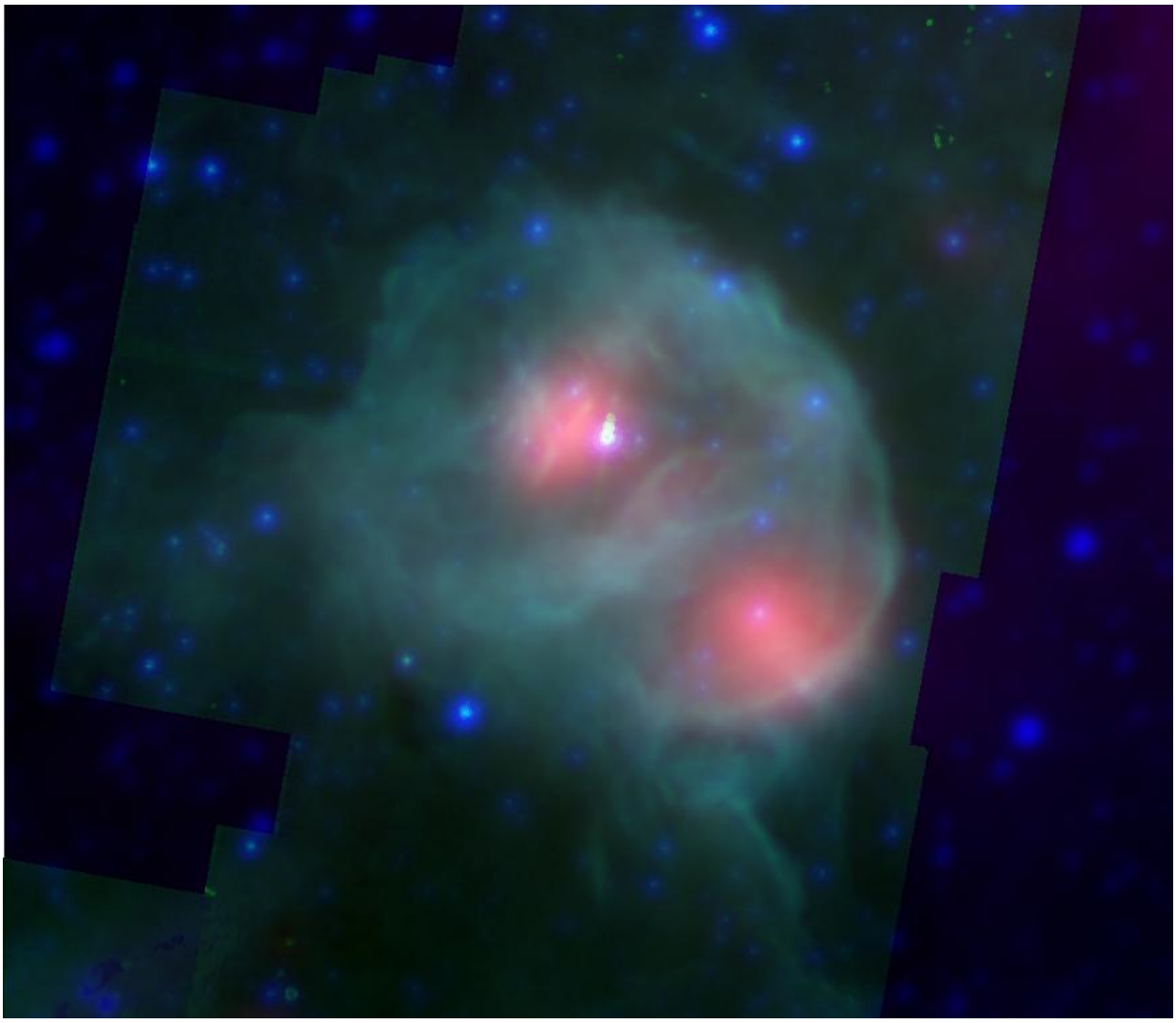

Figure 64 Spizter/WISE 3-color image. Blue: 3.4 micron, green: 5.8 micron, red: 22 micron. DB9-1 is saturated at 5.8 microns.

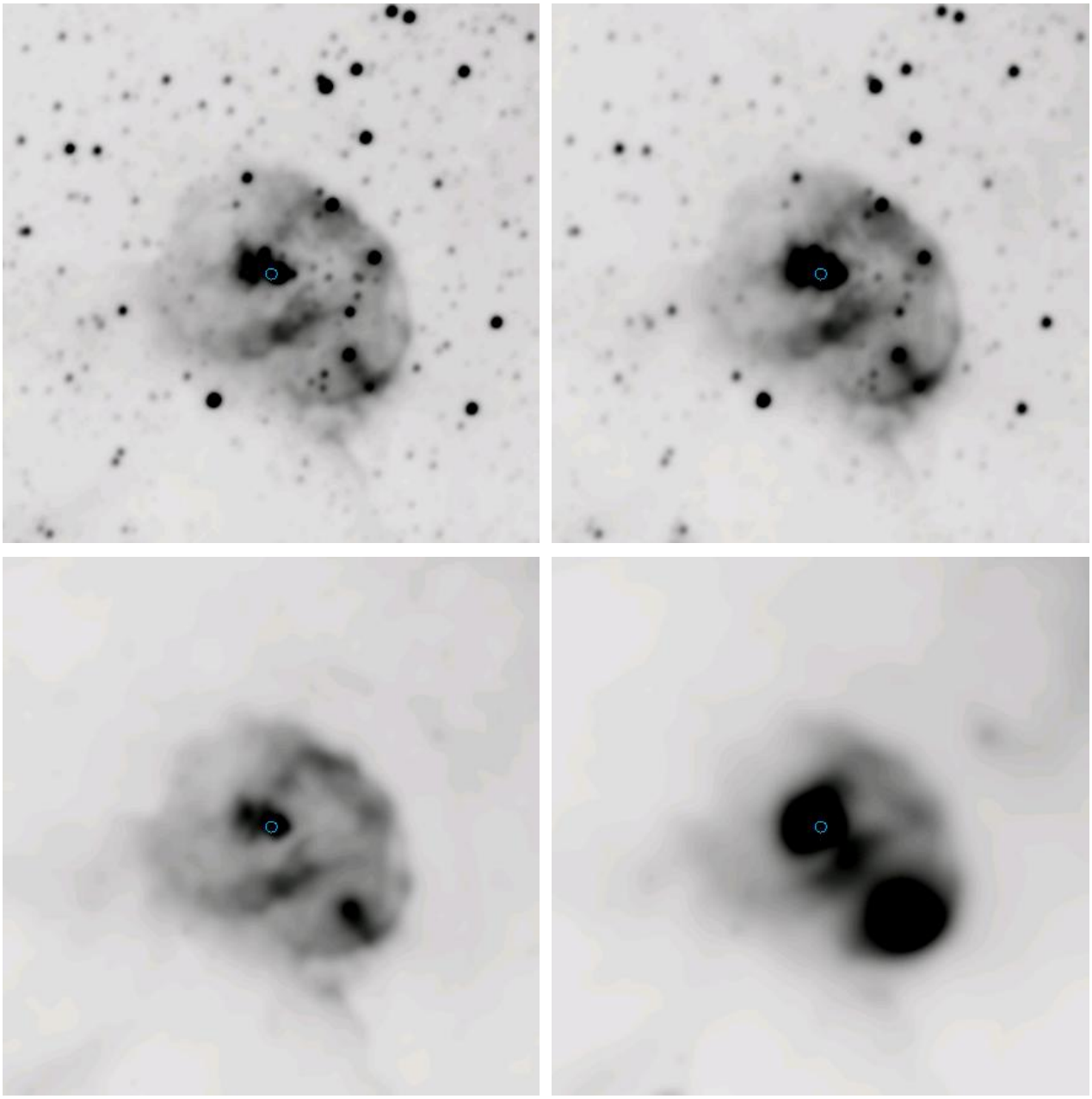

Figure 65 From left to right, top to bottom: WISE ch1, ch2, ch3, ch4 images with the position of DB9-1 indicated by a circle.

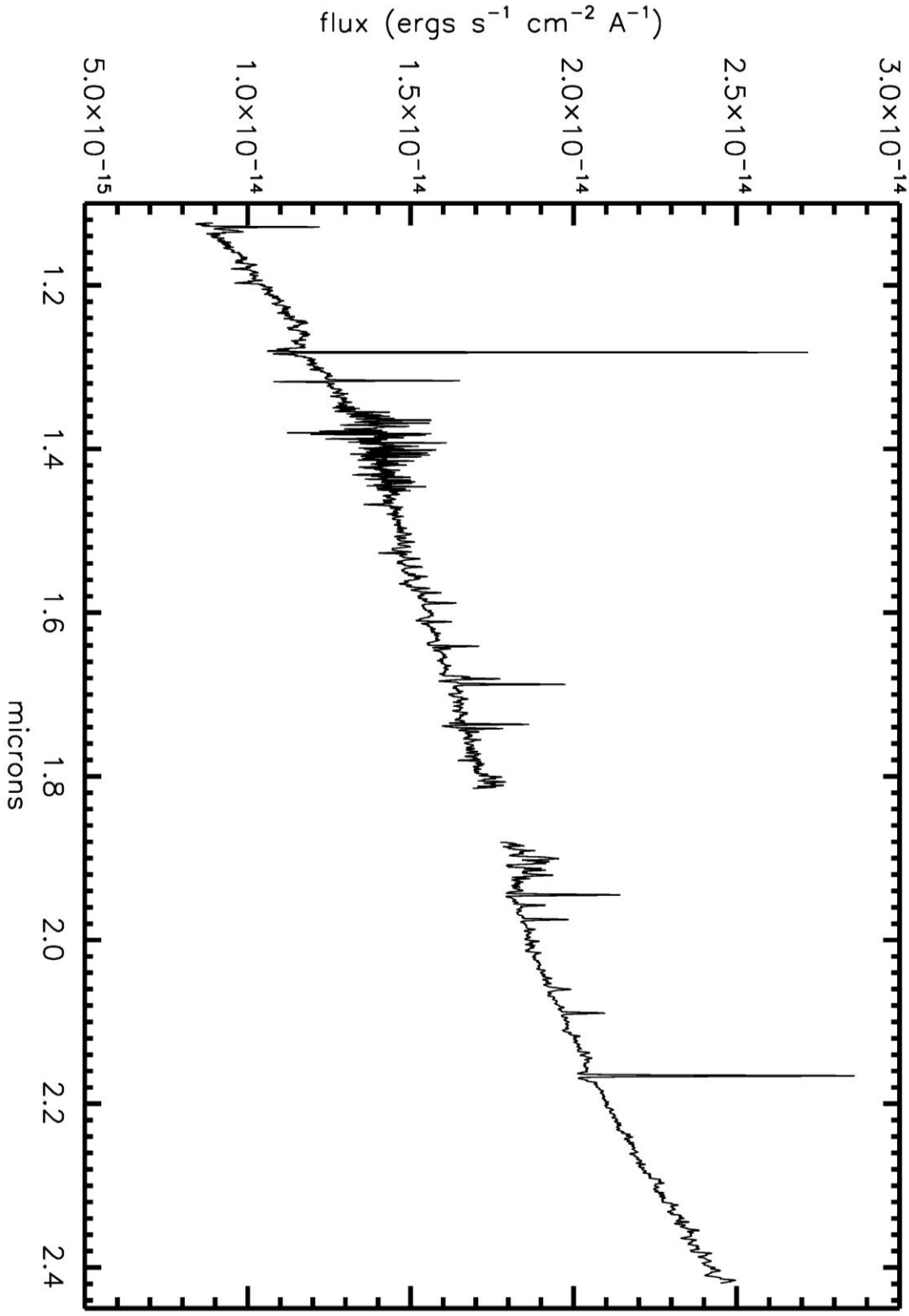

Figure 66 Full spectrum of B[e] star DB9-1

3.12.2. Age, Reddening, Distance, Mass

The distance to DB9 is determined by assuming an association with CygOB2, 1.5 kpc, which is not unreasonable as the two clusters share similar DIBs.

Computation of the extinction towards DB9 is complicated by the presence of the diffuse nebular emission surrounding the cluster, leading to differential reddening across the cluster face. Inspection of HST images shows that DB9-2 is embedded in a tendril of emission, while DB9-1 and DB9-3 lie in areas free of diffuse emission. Given the bright IR excess of DB9-1, this object cannot be used as a reddening indicator for the entire cluster. Assuming a $(H-K)_0=0$ for A stars, A_K computed for DB9-3 is 1.40. Since this is a measurement for a single star, the result is not precise.

B[e] star are believed to be post-red supergiant (RSG) phase objects (Kastner et al. 2006). A post-RSG evolutionary class for DB9-1suggests that the cluster is older than 8 Myr and has lost massive stars to SN.

The mass of the cluster is difficult to determine from the imaging and spectroscopy presented above. It is possible the cluster is more extended, as evidenced by the IR point source to the southwest of DB9-1 with similar mid-IR properties. The nebular emission surrounding the cluster, possibly an ejection nebula of mass lost during the RSG phase, makes it difficult to confirm that the entire cluster is visible. Given that the B[e] star can be the product of a RSG, it is likely to be evolved from an object with an initial mass of 30 $M_\odot$ or lower. If this is the most massive star in the cluster, which cannot be assumed *a priori*, then the total cluster mass is likely to be lower than 1000 $M_\odot$.

3.12.3. Summary

Though an interesting object, DB9 is rejected from the final IMF sample, for a variety of reasons: the lack of high mass MS stars, the degenerate age provided by the B[e] star, the large upper limit on the age as determined from the A1-0 star, and the inferred low total cluster mass.

3.13. [BDS2003] 52

Known informally as “the bubble cluster,” [BDS2003] 52 (hereafter BD52) lies at the center of a large, nearly complete bubble hosting the Sharpless HII region S187. This bubble is bright in the infrared, especially at 8.0 microns, as shown in Figure 67, and punctuated with signs of current and ongoing star formation, e.g. water masers (Henkel, Gueten & Haschick 1986), YSOs (Zavagno, Deharveng & Caplan 1994), dark nebula, and molecular clouds. Radio observations of the HII region enclosed in the bubble suggest that the winds from the massive stars in the cluster are excavating a cavity in the cluster’s natal material. The bright radio sources S187 1b and 1a are most likely the two lobes of a background FRII radio galaxy, as can be discerned from the 5 GHz map (their Figure 3) of Snell & Bally (1986), reproduced here in Figure 74. This source is unresolved in VLA observations of BD52 (Richards et al.

2012) but has a non-thermal spectral index, consistent with an extragalactic source. See Figure 68 for a more detailed local geography of the region. The NIC3 field of view is labeled for reference.

Russeil et al. (2007) estimate a spectrophotometric distance of 1.44+/-0.26 kpc to the cluster, based on observations of a single star. This is in agreement with a kinematic distance of 1.03+/-0.49 kpc to the HII region (Fich & Blitz 1984) based on a CO velocity of -14.9 km/s. A distance of 1.5 kpc yields a bubble size of approximately 5 pc in diameter.

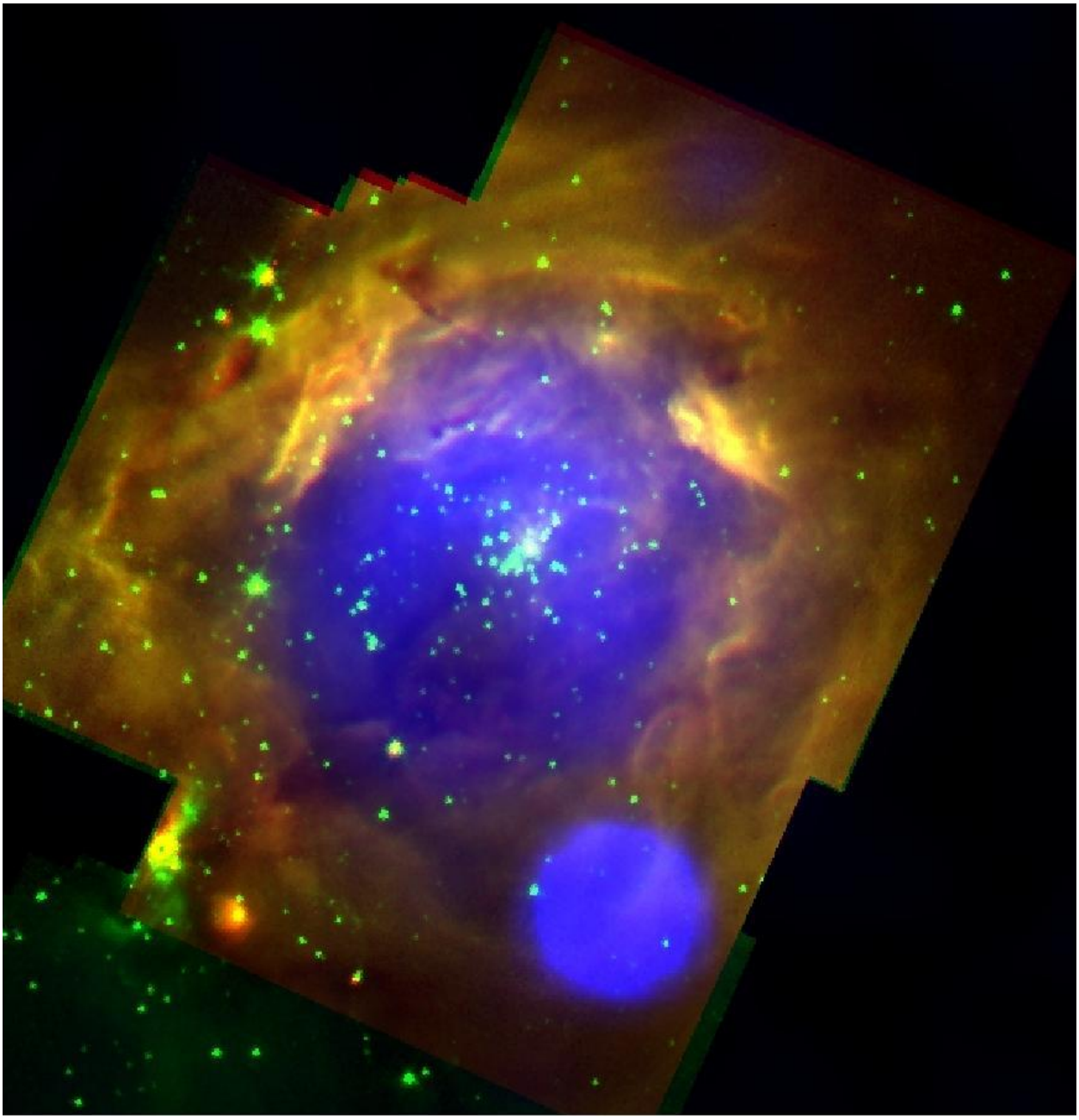

Figure 67 Spizter/IRAC and VLA 3 color image of [BDS2003] 52, north is up and east is left. The 8.0 and 3.6 micron emission is shown in red and green respectively, and the radio emission is shown in blue. North is up, East is left. The very bright radio source to the lower right is likely extragalactic in nature (see text).

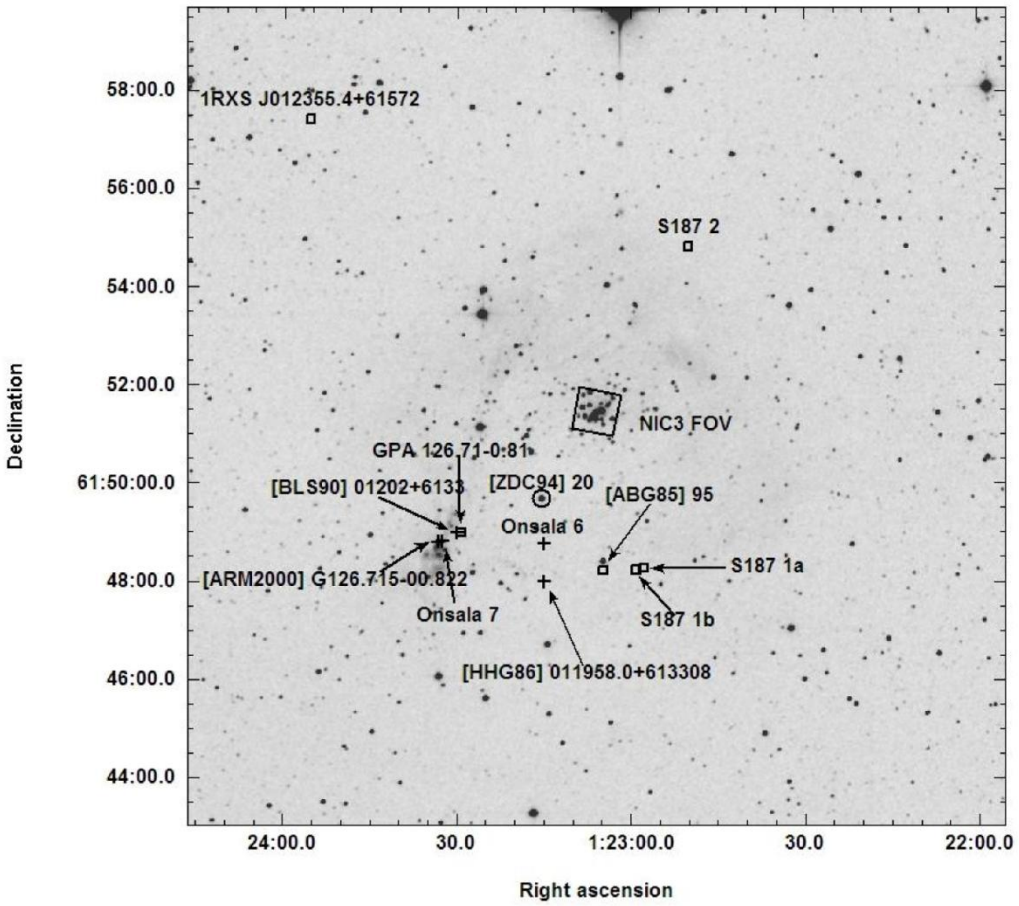

Figure 68 2MASS Ks band observation of the region around BD52; Simbad objects are labeled.

3.13.1.Stellar Content

The HST CMD of BD52, Figure 69, displays a series of stars at similar color from mF222M ~11 to 8 mags, then a fainter, redder population. This second, fainter population is likely to be the pre-MS of the cluster, indicating that only the most massive stars have evolved to the Hydrogen burning stage on the MS.

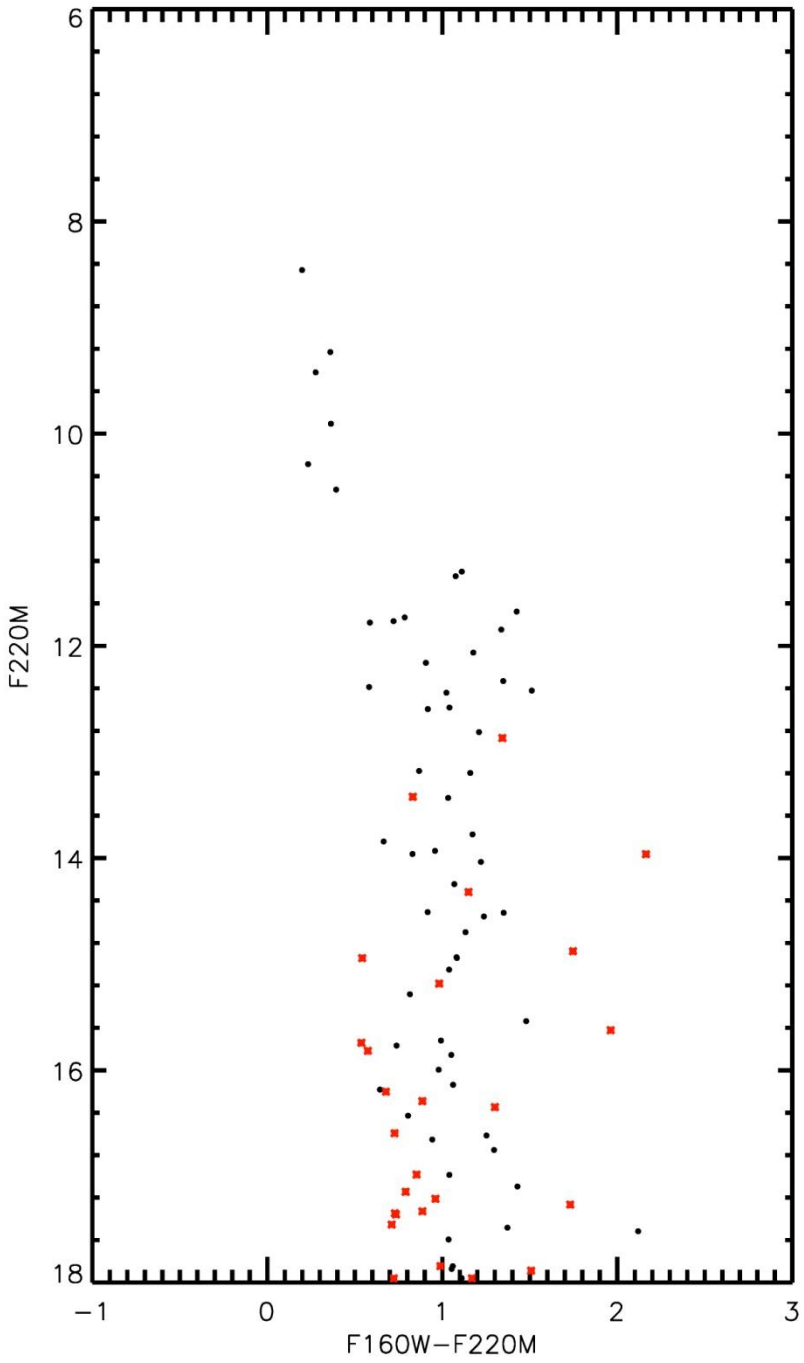

Figure 69 HST CMD for BD52 (black points). Objects from the control field are shown by red asterisks.

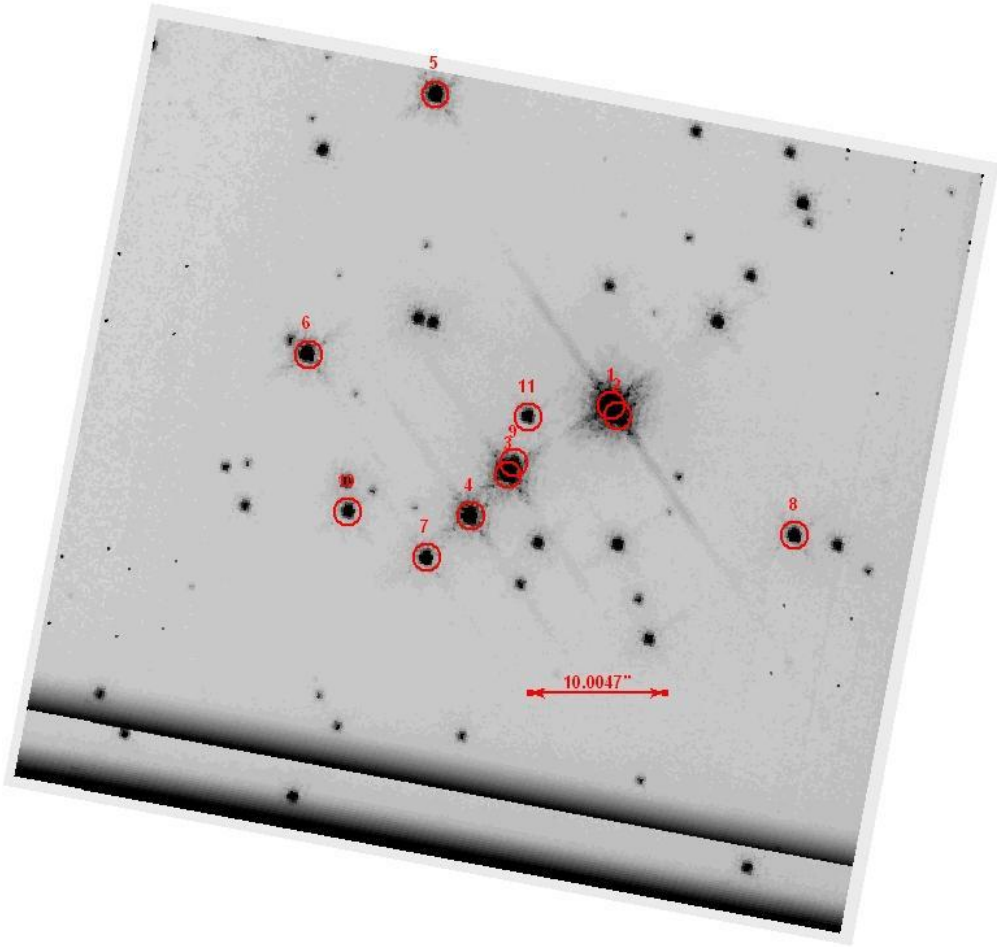

Figure 70 HST/NIC3 Image of [BDS2003] 52, finding chart w/labels. North is up, East is left. The two brightest stars in the cluster are at a small spatial projection, leading to misidentification in the literature (e.g. thought to be a single object until higher spatial resolution imaging became available).

Follow up spectroscopy of BD52 was obtained on 8 September 2012 and 18 September 2012 at NASA's IRTF using SpeX. Figure 70 displays the finding chart for BD52, with targets for spectroscopic follow-up labeled in decreasing order of brightness. The reduced spectra of 10 target stars are shown in Figure 71.

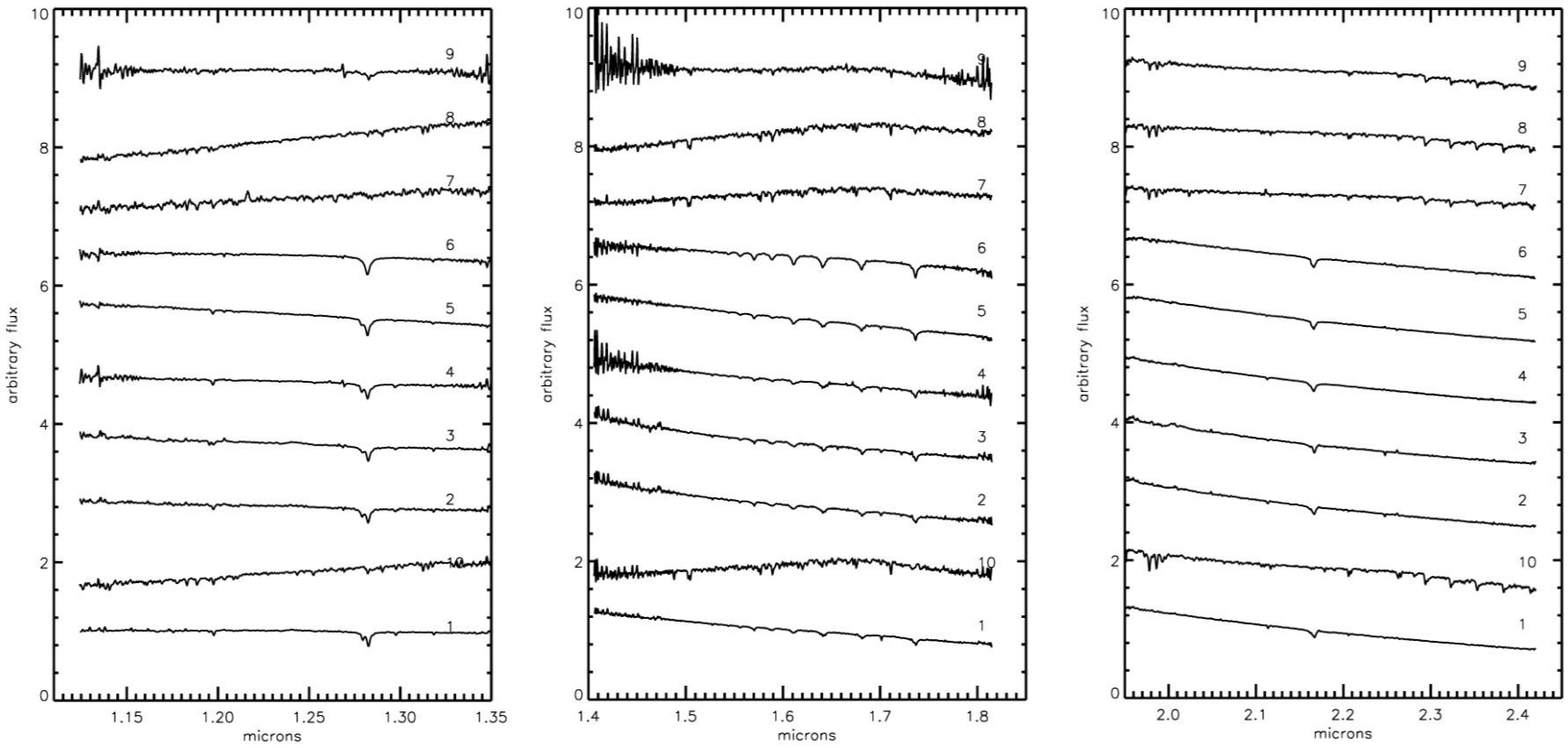

Figure 71 From left to right: J-band, H-band, and K-band spectra of BD52 stars

3.13.1.1. Spectral Typing

The spectra of stars BD52-1, -2, and -3 are nearly identical in H and K bands. All three spectra show Brγ absorption, and HI and HeI absorption at 1.61,1.641/3, 1.681, 1.700, 1.737, and 2.113 microns. The absence of HeII absorption at 1.693 indicates a spectral type later than O8. In the J band, BD52-3 has a more prominent Paschen series, as shown in Figure 71. All three stars are classified as O9.5-B2.5 V.

The lack of HeII absorption at 1.693 in BD52-4 indicates a spectral type later than O9. HI and HeI absorption indicate that this object has a temperature consistent with a mid-B star or earlier. For these reasons, BD52-4 is classified as early- to mid-B.

The spectrum of BD52-5 is similar to that of BD52-4, but with weaker 1.700 micron absorption. The weaker absorption line indicates that BD52-5 is slightly cooler than BD52-4, leading to a spectral classification of mid- to late-B.

Comparison of the spectra of BD52-6 with the spectral atlas of Hanson et al. (2005) indicates a spectral type of A0-A1, based on strong HI absorption lines and a full Paschen absorption series in the J band.

The remaining four stars, BD52-7, -8, -9, and -10, show clear CO bandhead absorption beginning at 2.30 microns, indicating that all four stars are cool, late-type objects. It is unclear from the CMD if these are pre-MS objects evolving towards the MS or contaminating foreground giants.

The results of spectral typing are summarized in Table 22 and displayed graphically in Figure 72. The red dashed line in this figure indicates a 1 Myr MS isochrone while the dashed blue line indicates a 1 Myr pre-MS isochrone. Objects redward of the pre-MS isochrone are interpreted as pre-MS stars younger than 1 Myr still evolving along Hayashi tracks.

Table 22 List of stars spectroscopically observed

ID	RA	Dec	m_{F160W}	m_{F222M}	SpType
1	01 23 05.27	+61 51 29.79	8.66	8.45	O9.5-B2.5 V
2	01 23 05.20	+61 51 29.03	9.59	9.23	O9.5-B2.5 V
3	01 23 06.34	+61 51 24.66	9.70	9.42	O9.5-B2.5 V
4	01 23 06.74	+61 51 21.65	10.27	9.91	Early-mid B
5	01 23 07.10	+61 51 52.68	10.52	10.29	Mid-late B
6	01 23 08.44	+61 52 33.57	10.92	10.53	A0-A1
7	01 23 07.20	+51 52 18.58	12.41	11.30	late type/cool
8	01 23 03.36	+61 51 20.21	12.42	11.37	late type/cool
9	01 23 06.29	+61 51 21.94	12.52	11.73	late type/cool
10	01 23 08.02	+61 51 28.90	12.49	11.77	late type/cool

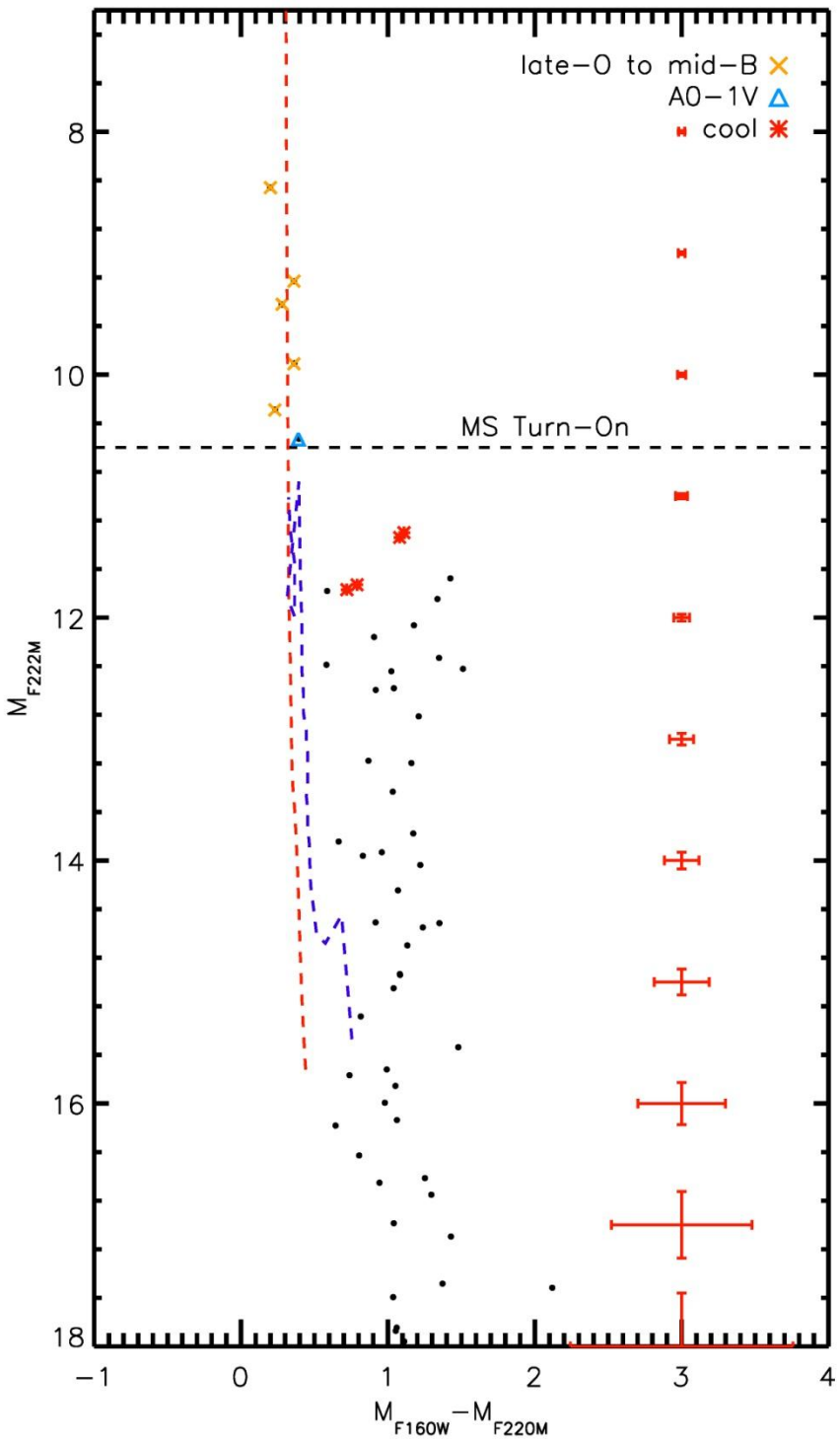

Figure 72 BD52 CMD w/spectral types labeled. Typical errors are idicated to the right of the cluster sequence.

3.13.2. Age, Reddening, Distance, Mass

The pre-MS population suggests a young age for BD52, as objects of <~3 $M_{\odot}$ are still evolving out of the pre-MS stage towards the MS. This is consistent with an age of 1-2 Myr (e.g. see Davies et al. 2012b for similar analysis of the more massive Danks 1 cluster).

Extinction towards the cluster is computed by examining the NIR colors of normal OB stars, i.e. emission line stars and heavily reddened stars are excluded. For BD52, an average value of A_K=0.33+/-0.11 is determined, based on 5 stars observed by HST/NIC3 and IRTF/SpeX. This is consistent with the distance (discussed below) and the Galactic anti-center direction of BD52, where less reddening is expected than for clusters in the heart of the Galactic Plane.

Given the uncertainties in spectral type, spectrophotometric distance calculations yield a wide range of distances, as seen in Table 23. Using the spectrophotometric distance calculations for the three brightest stars, BD52-1, -2, and -3, yields a distance of 2.33+/-0.35 kpc. The kinematic distance to the HII region S187, D=1.44 kpc, is adopted for the purposes of this work, as it is more reliable.

Table 23 Spectrophotometric distance estimates for hot objects in BD52

ID	m_{F222M}	SpType	D_V/kpc	D_{III}/kpc	D_I/kpc
1	8.46	O9.5-B2.5 V	1.79-1.91	3.33-3.45	6.19-9.82
2	9.23	O9.5-B2.5 V	2.25-2.41	4.19-4.35	7.81-12.38
3	9.42	O9.5-B2.5 V	2.61-2.80	4.87-5.05	9.06-14.37
4	9.91	early –mid B	2.38-3.08	5.04-5.95	7.85-12.44
6	10.53	A0/A1	1.04-1.11	3.70-3.95	5.79-9.18

Counting up the mass of stars on the main sequence places a lower limit of roughly 100 $M_{\odot}$ on the total cluster mass. Applying a Salpeter mass function (Salpeter 1955) and integrating over a typical mass range of 0.8 to 120 $M_{\odot}$ gives an upper mass limit of ~1300 $M_{\odot}$.

3.13.3. X-ray & Radio Observations

CXO/ACIS X-ray

Five point sources in the targeted Chandra X-Ray Observatory (CXO) ACIS 10 ks observation of BD52 produced 30 or more net counts. Point sources were detected using the wavelet-based detection code PWDetect, developed at the Osservatorio Astronomico di Palermo (OAPA). Photometry, spectra, and light curves for each point sources were extracted using the CIAO tool ACIS_EXTRACT and HEASOFT version 6.3.1. Briefly, each source was extracted from within a 90% contour of the local PSF and a local background containing at least 100 photons was extracted in an annulus around each source.. The

observed photon flux (in units of photons cm-2 s-1) was computed for each source by dividing the net counts in each of five energy bands by the mean ancillary response function (ARF) and the effective exposure time. Variation in actual exposure time due to chip gaps and dead columns are taken into account by using this method.

The spectra from these sources were adaptively grouped so the data had >7 net counts per spectral bin, increasing the relatively low signal to noise ratio of the unbinned spectra. The spectra for these five sources were modeled as thermal plasma absorbed by interstellar gas and dust along the line of sight using the XSPEC ver12 models "wabs" and "ray." All five sources have IR and mid-IR counterparts, two of which lie within the NIC3 field of view. Both X-ray point sources in the NIC3 field of view are associated with point sources in the HST data (see red diamonds in Figure 73). Five additional (but low count-rate) sources are located within the NIC3 observations. Four of the X-ray sources are associated with cool stars, as identified by IR spectroscopy, two are associated with possible pre-MS objects, and one X-ray source is associated with an OB star in the cluster.

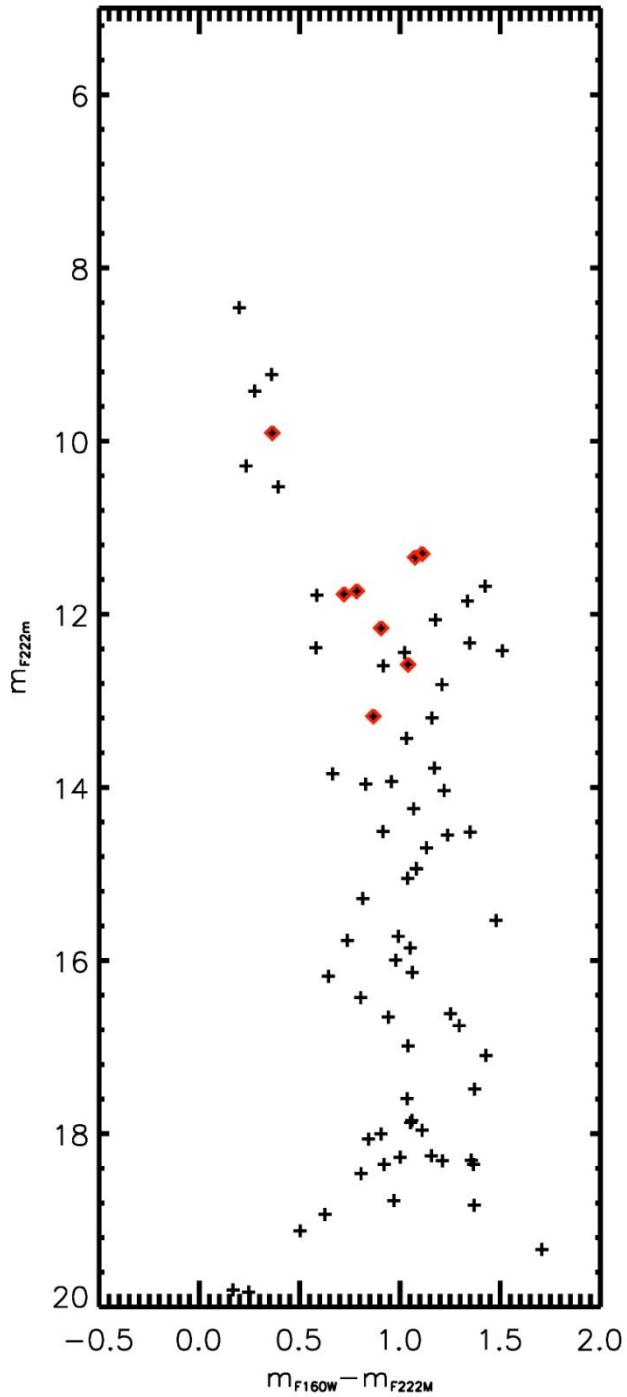

Figure 73 HST CMD where X-ray sources are indicated by red diamonds.

By filtering the observation by energy, it is possible to find large scale structure in X-ray observations, e.g. bubbles or shells. Another method of searching for diffuse emission interior to the IR bubble is to

extract counts from equal size regions interior to, on the edge of, and exterior to the bubble and compare the results. No evidence of diffuse emission was found in the 10 ks Chandra observation of BD52. While it has been shown that massive clusters can fill a cavity similar to that observed in BD52 with diffuse X-ray emission (Townsley et al. 2011, Townsley 2009), BD52 is on the low-mass end of young clusters.It is unlikely that diffuse X-ray emission would be seen in such a relatively short exposure.

VLT Radio

The radio properties of the cluster and surrounding area were studied by Richards et al. (2012). These authors find that gas ionized by the cluster is confined within the IR shell. Richards et al. (2012) also reports missing flux at 8.5 GHz, citing the largest angular size of the 8.5 GHz VLA interferometer in D-array (the configuration at which the observations were taken) of ~3', making larger scale structures undetectable. The 4.9 GHz emission fills the central cavity of the IR shell, roughly ~4' in diameter, indicating that large scale structure (> 3') is present around BD52. These authors find an ionized gas mass of 7 $M_{\odot}$ and a Lyman photon flux of 9.3(10^{46}) for the HII region. The photon flux is consistent with that expected from ~4-5 early B main sequence stars, which are observed.

VLA observations by Richards et al. (2012) also identify a radio point source at 8.5 GHz that is spatially coincident with one of the early type stars in the cluster (see their Figure 3). This source has a flux of 0.3+/-0.1 mJy, and is suggestive of radio emission originating in a stellar wind. Should that be the case, Richards et al. (2012) calculate the mass-loss rate of this point source using Equation 1 of Lang et al. (2001), finding 0.35(10^{-5}) $M_{\odot}$ y^{-1} (assuming a terminal wind velocity of ~1000 km s^{-1} and a distance of 1.44 kpc). A mass-loss rate this high is not consistent with mass-loss rates found for early B-type MS stars (Sternberg et al. 2003).

The brightest source of radio emission in the observations of Richards et al. (2012) is extra-galactic in nature, showing a non-thermal spectral index. This radio source is previously known, S187-1, observed at a variety of wavelengths by Snell & Bally (1986). Figure 3 from that work is reproduced in Figure 74, revealing a dual, extended source nature for S187-1. The morphology of the radio emission suggests that this source is a FRII radio galaxy (Faranoff & Riley 1974).

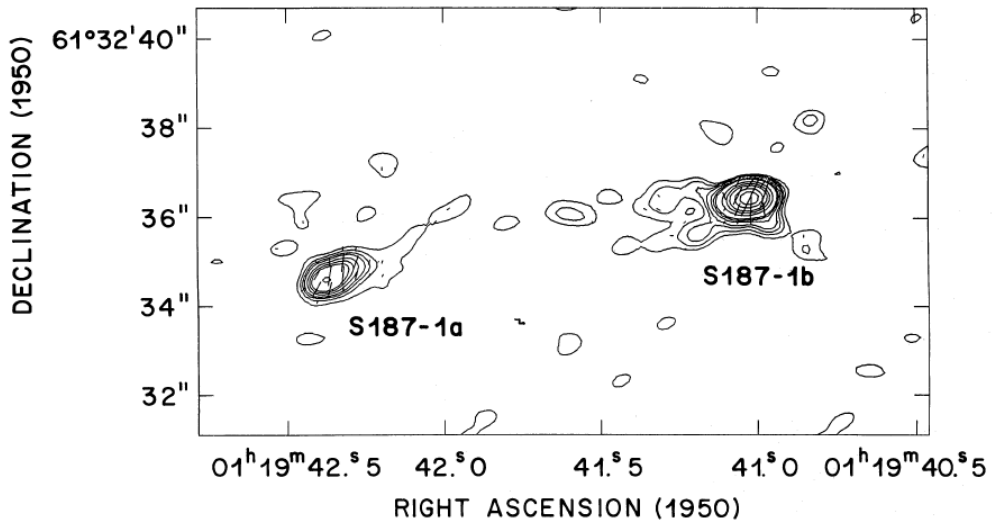

FIG. 3.—A 5 GHz A-configuration map of the nonthermal radio double source south of S187. Contour levels are at 0.1, 0.2, 0.3, 0.4, 0.6, 0.8, 1, 2, 3, 4, 6, 8, and 10 × 68.8 mJy per beam. The lines show the direction of the electric vector of polarized emission, and the length is such that 1″ = 4.57 mJy per beam of polarized flux. The maximum percentage polarization is 7%.

Figure 74 Reproduced from Snell & Bally (1986) Figure 3.

3.13.4.Summary

The distribution of YSOs in the region surrounding BD52 suggests star formation is on-going, though massive star formation has likely ended. Winds from the massive stars in the central cluster are excavating a cavity in the natal material, either triggering or revealing the most recent epoch of star formation.

Due to the lack of massive main sequence stars, BD52 does not make the final cut to be included in the IMF slope sample. The presence of candidate pre-MS objects see to the lower right of the (sparse) MS indicate that the cluster is young and still undergoing star formation. A slope measurement of the high mass slope of the IMF would suffer from low-number statistics and a limited mass interval over which to make the measurement.

4. Error Analysis

This chapter contains the details of the error analysis on the measured IMF slope for each cluster and for the sample of clusters taken as a whole.

4.1. Distance

Varying the distance to each cluster has little systematic effect. For some clusters, the lower limit for the slope measurement changes as the K-band magnitude completeness limit shifts when converted to initial mass completeness limit. For all clusters, the measured slope of the IMF varied only within the errors. This is illustrated in Table 24, which lists the results of slope measurements when distance and age are varied for each cluster. The first column lists the abbreviated cluster name, the second column lists the age of the model in Myr followed by the log of the age, the third column lists the distance in kiloparsecs, and the fourth column lists the upper and lower mass bins used to measure the IMF slope. The age and distance are varied for each cluster, and the resulting slope measurement and error are given in column five and six respectively. In order to demonstrate the importance of the effect of completeness on the IMF slope, the completeness corrected slope and slope error are listed in columns seven and eight. The total mass of the cluster, as computed from the completeness corrected slope, is given in column nine.

Table 24 IMF Slope Measurement Results with Varied Parameters

Cluster	Age, logAge	Dist	$Logm_{low}$, m_{high}	slope	slope err	cc slope	cc slope err	cc mass
Mc20	6, 6.778	4.4	0.3,1.3	-0.44	0.17	-0.68	0.38	2806
Mc20	7, 6.845	4.4	0.3,1.3	-0.46	0.28	-0.71	0.29	2746
Mc20	7.25, 6.860	4.4	0.3,1.3	-0.39	0.27	-0.64	0.30	2914
Mc20	6, 6.778	4.1	0.3,1.3	-0.53	0.26	-0.74	0.29	2412
Mc20	7, 6.845	4.1	0.3,1.3	-0.50	0.27	-0.68	0.26	2642
Mc20	7.25, 6.860	4.1	0.3,1.3	-0.48	0.26	-0.71	0.29	2506
Mc20	6, 6.778	4.7	0.3,1.3	-0.54	0.23	-0.71	0.39	2841
Mc20	7, 6.845	4.7	0.3,1.3	-0.43	0.12	-0.64	0.37	3136
Mc20	7.25, 6.860	4.7	0.3,1.3	-0.40	0.09	-0.63	0.08	3183
Mc23	3,6.477	7.0	0.4,1.3	-1.08	0.39	-1.41	0.40	1664
Mc23	4, 6.602	7.0	0.4,1.3	-1.00	0.42	-1.33	0.42	1881
Mc23	5, 6.699	7.0	0.4,1.3	-0.85	0.35	-1.17	0.37	1641
Mc23	3,6.477	6.5	0.4,1.3	-0.88	0.30	-1.13	0.28	1466
Mc23	4, 6.602	6.5	0.4,1.3	-0.86	0.34	-1.12	0.33	1500
Mc23	5, 6.699	6.5	0.4,1.3	-0.78	0.26	-1.20	0.45	1452
Mc30	3,6.477	11	0.7,1.3	-1.34	0.19	-1.61	0.17	19119
Mc30	4, 6.602	11	0.7,1.3	-1.20	0.23	-1.47	0.23	16460
Mc30	5, 6.699	11	0.7,1.3	-1.14	0.21	-1.43	0.21	15567
Mc30	3,6.477	10	0.7,1.3	-1.27	0.14	-1.57	0.15	16113
Mc30	4, 6.602	10	0.7,1.3	-1.19	0.18	-1.51	0.19	14896
Mc30	5, 6.699	10	0.7,1.3	-1.22	0.11	-1.52	0.10	15224
Mc30	3,6.477	12	0.7,1.4	-1.20	0.16	-1.32	0.20	14415
Mc30	4, 6.602	12	0.7,1.4	-1.28	0.12	-1.45	0.17	16332

Mc30	5, 6.699	12	0.7,1.3	-1.12	0.13	-1.28	0.17	14666
Mc70	3,6.477	5.25	0.4,1.5	-0.42	0.12	-0.70	0.12	2580
Mc70	4, 6.602	5.25	0.4,1.4	-0.27	0.11	-0.56	0.17	3242
Mc70	5, 6.699	5.25	0.4,1.4	-0.53	0.35	-0.86	0.33	2100
Mc70	3,6.477	4.85	0.4,1.5	-0.16	0.27	-0.43	0.26	3308
Mc70	4, 6.602	4.85	0.4,1.4	-0.09	0.29	-0.35	0.26	3672
Mc70	5, 6.699	4.85	0.4,1.4	-0.25	0.55	-0.52	0.53	3031
Mc70	3,6.477	5.65	0.5,1.5	-0.32	0.27	-0.65	0.27	3446
Mc70	4, 6.602	5.65	0.5,1.4	-0.07	0.27	-0.47	0.24	4531
Mc70	5, 6.699	5.65	0.5,1.4	-0.08	0.24	-0.44	0.22	4678
Mc81	2,6.301	11	1.1,1.6	-0.97	0.81	-1.28	0.78	13420
Mc81	3,6.477	11	1.1,1.6	-1.41	0.32	-1.68	0.28	29107
Mc81	3.5,6.544	11	1.1,1.6	-0.96	0.17	-1.23	0.17	12877
Mc81	2,6.301	9.0	1.0,1.6	-0.97	0.37	-1.06	0.41	7521
Mc81	3,6.477	9.0	1.0,1.6	-0.73	0.25	-1.54	0.47	15457
Mc81	3.5,6.544	9.0	1.0,1.6	-0.73	0.88	-1.14	0.78	8297
Mc81	2,6.301	13	1.1,1.6	-0.71	0.31	-0.80	0.36	9804
Mc81	3,6.477	13	1.1,1.6	-0.47	0.56	-0.50	0.62	9554
Mc81	3.5,6.544	13	1.1,1.6	-1.15	0.54	-1.34	0.69	15899

The distance to R136 is well established in the literature. This procedure was performed for Danks 1 and Danks 2 by Davies et al. (2012b), with the same results. The distance to the G305 star forming complex is also well established, both by Davies et al. (2012b) and other authors,

4.2. Monte Carlo Error Simulations

Monte Carlo simulations, designed based on simulations of the Arches cluster by Figer (2005), were used to estimate the error on the IMF slope for each cluster. Each simulation consists of 1000 trials: 500 with a Salpeter IMF slope as input and 500 with the completeness-corrected measured slope of the intermediate to high end IMF. The simulation uses test points with a mass distribution following a single power law from 0.8 to 150 $M_{\odot}$ such that the total mass of each simulated cluster is roughly equal to the cluster mass inferred by integrating over the IMF. The simulated cluster mass corresponds to the mass derived by using the completeness corrected slope.

Geneva stellar evolution models are used to convert initial mass in each simulated cluster into magnitude according to models of a given median age (again dependent on the specific cluster that is being simulated). An age distribution of 0.5 Myr around the median age is applied randomly to each point in the synthetic cluster. An average extinction is assigned to each magnitude point, with the extinction drawn from a Gaussian distribution with a mean of A_K equal to the measured extinction and sigma equal to the error on the extinction. Photometric error, drawn from a Gaussian distribution with a mean of zero and sigma=0.3, is applied to each point.. With the exception of Mercer 81, the slope of IR extinction law is

taken from Rieke et al. (1989), taken to be -1.53. For Mercer 81, an extinction law slope of -2.0 is adopted (see Davies et al. 2012a). The appropriate distance modulus (e.g. using 11 kpc for Mercer 81 and Mercer 30) is applied to the simulated photometry, the last step in converting mass points to apparent magnitude points.

In order to measure the slope of the IMF for each simulated cluster, the simulated apparent magnitudes are compared to the Geneva evolution models as was done for each observed cluster. The slope of the resulting IMF is then computed using the same limits as for the actual cluster; the same bins are used to compute the slope, the same methodology (LINFIT.PRO) is used to compute the slope, and the same stellar evolution models are used to convert magnitude to mass. Results of the Monte Carlo simulations are summarized in Table 25 below.

Simulations were run using a Salpeter slope as input in order to investigate any change in input slope to measured output slope due to systematics in the Monte Carlo simulations. Other simulations (see Figure 76 and discussion below) indicate that the output slope begins to suffer from low number statistics below some threshold, resulting in a shallower "measured" slope.

Table 25 Results of Monte Carlo simulations for each cluster

Cluster	Mass	CC Slope (input)	Median MC Slope (output)	MC StdDev	Salpeter MC (output)	Salpeter sig
Mercer 20	4000	-0.70	-0.70	0.10	-1.36	0.0
Mercer 23	2000	-1.33	-1.35	0.20	-1.39	0.19
Mercer 30	15000	-1.38	-1.35	0.14	-1.37	0.13
Mercer 70	3000	-0.7	-0.70	0.13	-1.40	0.15
Mercer 81	15000	-1.60	-1.74	0.36	-1.40	0.29
Danks 1	5000	-1.21	-1.33	0.13	-1.48	0.14
Danks 2	3000	-1.21	-1.22	0.13	-1.36	0.14

4.3. IMF Simulations: Expectations vs. Reality

Initially, this project was designed to contain 15 young (< 8 Myr), massive (10,000+ $M_{\odot}$) stellar clusters. As it became apparent that every cluster in the original sample did not meet these criteria, the total number of clusters shrank to 7. Monte Carlo simulations designed to measure the slope of the upper portion of the IMF in the dataset, e.g. young clusters of varying total masses, were performed in order to understand the expectations versus the reality of the project. The goal of the simulations was to determine if the results of the IMF slope measurement of the sample taken as a whole can be a statistically significant measurement of the intermediate to high end IMF, with the possibility to identify real statistical outliers from the canonical IMF slope. Monte Carlo simulations suggest that the slope of the IMF can be measured to 0.2 dex for a sample of 15 young, massive clusters if the intermediate to high end

IMF is drawn from the same parent population for all clusters. For a smaller sample size of 7 clusters, the average slope can be measured to 0.3 dex.

The accuracy in the measurement of the IMF slope, whether consistent in the sample or not, depends on several factors: sample size, observations error, model assumptions, and model error. Assuming a canonical IMF slope (Salpeter 1955, Kroupa 2001), Monte Carlo simulations of 10 clusters similar to the Arches cluster (~10^4 $M_\odot$, 2 Myr) were realized 100 times. From this, it can be shown that it is possible to measure Γ to within 0.2 dex for a minimum of 10 young, massive clusters. The simulations are constructed over a mass range of 0.8 to 150 $M_\odot$. Geneva stellar evolution models (Meynet & Maeder 2005) were used to convert $M_{initial}$ into magnitude, according to 2 Myr isochrones. Each test point was then assigned an extinction and photometric error, as described above for the error analysis for each observed cluster.

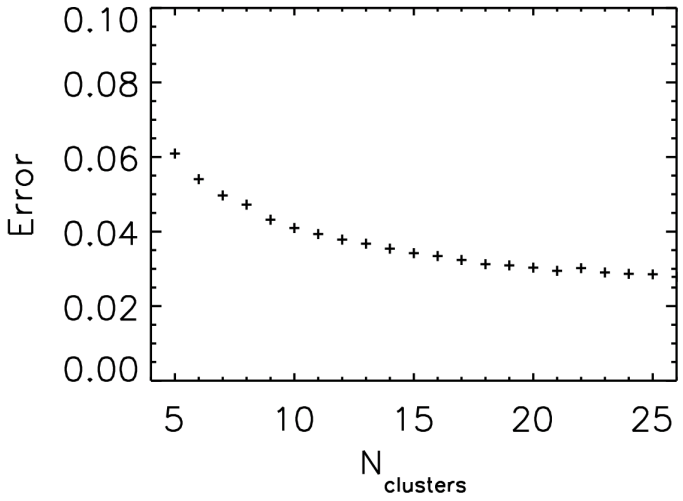

Figure 75 Standard deviation of recovered slopes versus number of synthetic clusters

Unfortunately, the results of the imaging and spectroscopic observing campaigns did not yield 10 or more clusters with masses greater than 10^4 $M_\odot$ and ages of 2 Myr. Instead, eight clusters were identified with ages ranging from 1.5 to 6 Myr and total masses ranging from a few 10^3 $M_\odot$ to roughly 10^4 $M_\odot$. The expectations derived from the Monte Carlo simulations used to motivate the project now require updating in order to understand the IMF analysis results (see Chapter 5, IMF Analysis).

One thousand Monte Carlo simulations were run for a sample of clusters over a wide range in mass (500 to 2x10^4 $M_\odot$), designed to measure the IMF slope between 10 and 120 $M_\odot$. For each trial, a mass function

was built from a Kroupa IMF profile, with a slope of -1.3 for 0.5 < M < 120 using the RANDOMP.PRO function from the IDL Astronomy User's Library. This function generates an array of random numbers distributed according to a power law, such as a mass function or initial mass function. No seed value is given, resulting in a unique result for each trial (RANDOMP.PRO uses the system clock as a seed value when no seed value is specified). The IMF for each simulated cluster is measured twice, once over the entire mass range and again over the range 10-M_{max} $M_{\odot}$. The results of these simulations are shown in Figure 76. Black X's identify the median output slope, as measured across the entire mass range of the cluster, while red asterisks represent the median high end slope. Black and red error bars are the errors on each point for the input and output slopes respectively. It is clear from Figure 76 that the measured slope is lower than the input slope, especially for cluster masses lower than 10^4 $M_{\odot}$.

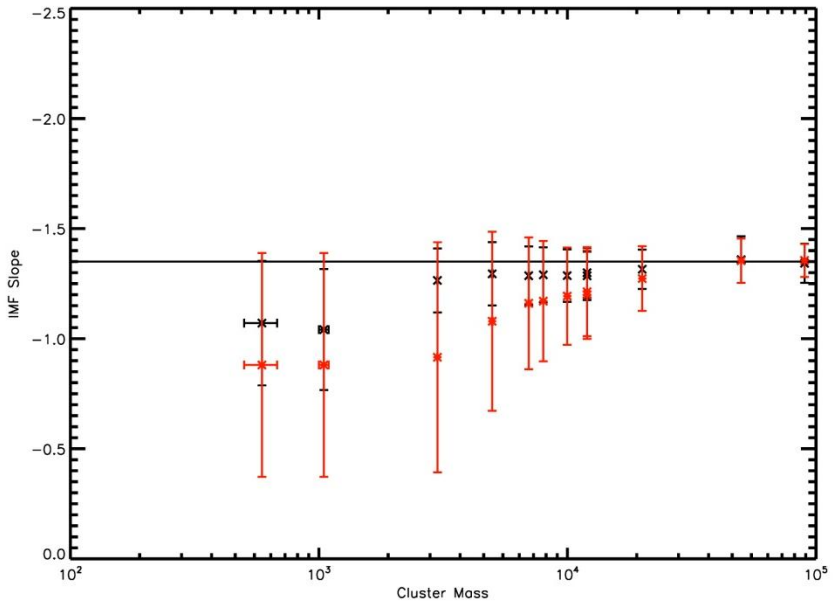

Figure 76 Resulting IMF vs. input IMF for Monte Carlo simulations of clusters over a large mass range.

Though simplistic, this method provides a realistic prediction of the results that can be expected from this project, measuring the slope of the high end IMF for a sample of clusters with a variety of ages and total masses.

Several important properties can be identified in Figure 76. At the low total mass end, $M_{total}<10^3$, small number statistics lead to a widely varying high mass slope. In these instances, there are either no massive stars or the high mass bins are so poorly populated that measuring a slope becomes impractical. This results in a tendency to measure a steeper IMF slope at the high mass range than for the entire cluster

sample taken as a whole. On the high mass end, low number last bins skew the measured slope towards more negative numbers. This effect can be removed by properly weighting the linear fit(s).

The total cluster mass has a large effect on the error measured for the IMF slopes of simulated clusters, as shown in Figure 76 and Figure 77. For clusters with a total mass lower than ~10^4, the error on the measured IMF slope will tend to be higher than 0.2 dex (recall a measurement to within 0.2 dex was one of the original goals of this project).

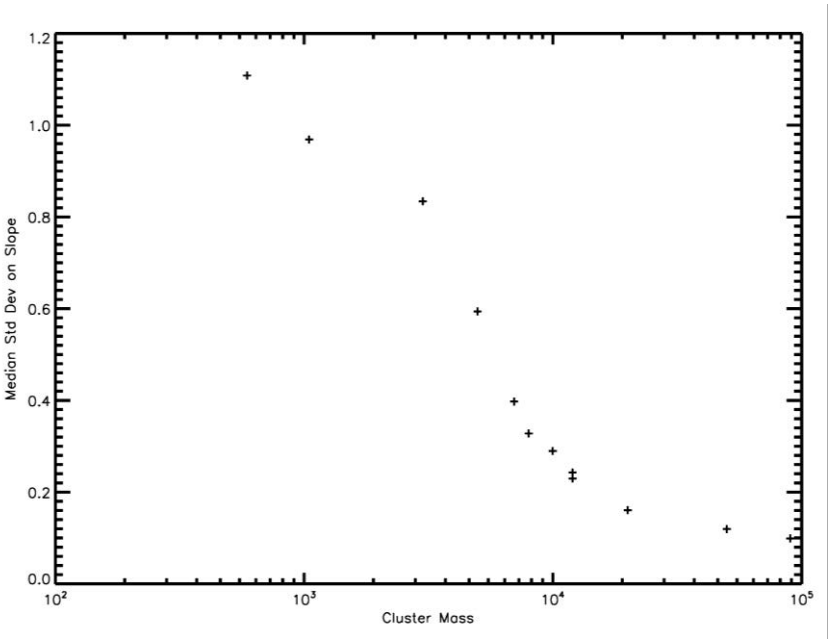

Figure 77 Median standard deviation on the IMF slope vs. total cluster mass. Standard deviation represents the error on the slope measurement, as in Monte Carlo Error Simulations

Another result from the Monte Carlo simulations is shown in Figure 78, which is designed to mimic Oey & Clarke (2005) Fig 1. Overplotted are the average values of m_{max} and LogN for each specified mass. This plot differs from Oey & Clarke (2005) Fig 1 in that these authors consider a smaller mass range, 20-100 $M_\odot$ for their IMF simulations. Figure 78 emphasizes the effects of stochastic sampling of the IMF: it is more unlikely that a high mass star will be found in a low total mass cluster, emphasizing that the high end IMF will remain sparsely populated in relatively low mass clusters.

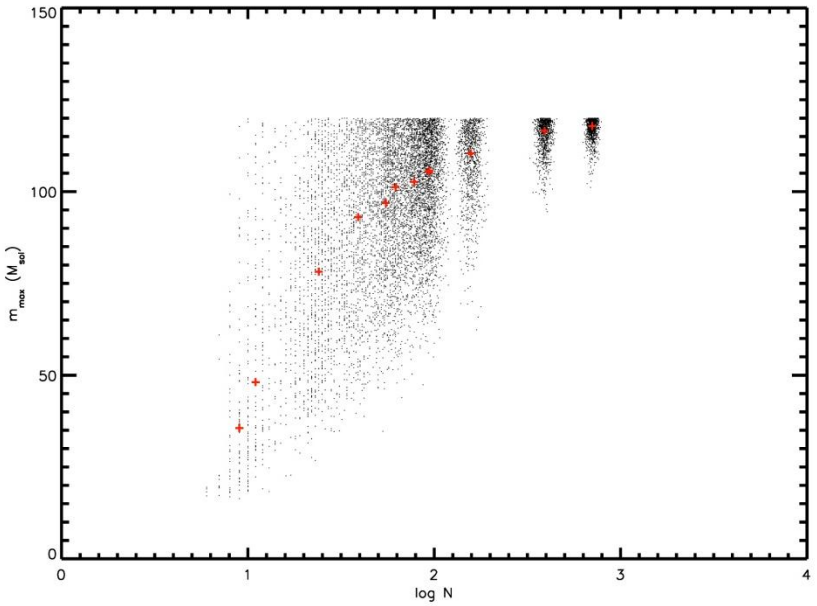

Figure 78 Maximum stellar mass, m_{max}, per simulated clusters vs. the number of stars, Log N, per cluster.

Youth can be simulated by adjusting the upper mass limit of the IMF measurement, i.e. the most massive stars in very young clusters will still be on the main sequence while the most massive stars in slightly older, evolved clusters will no longer be present as main sequence stars (and may even have exploded as supernovae, depending on the age of the cluster). For the simulations above, each cluster is assumed to be young enough to contain stars with masses up to 120 $M_{\odot}$, corresponding to an age of ~3 Myr or less.

4.3.1. Influence of IMF Form: Kroupa vs. Salpeter

Using a different functional form of the IMF yields somewhat different total mass estimate results. A Kroupa IMF assigns more of the total cluster mass to low mass objects, resulting in fewer high mass stars. This makes the high mass slope less defined than if a Salpeter IMF is used. For the case where the total mass is inferred by applying a mass function (e.g. Equation 5), the Kroupa functional form yields a larger total mass than the Salpeter functional form. In the Monte Carlo simulations performed for this analysis, the slope of the IMF is first measured from 0.5 to m_{max}. If a Salpeter functional form was used, all of the mass of the cluster would be contained in this range.

5. IMF Analysis

This chapter details the construction of the K-band luminosity function, including the rejection of non-cluster members and other contaminants, and the application of stellar evolution models to produce an initial mass function for each cluster.

In order to compare the results of this study to the IMF slope and upper mass cut-off of the Arches cluster as measured by Figer (2005), the measurement method and presentation were specifically chosen to follow his work. A similar data set is examined for each cluster, consisting of HST/NICMOS NIR imaging with spectroscopic follow-up of bright objects. The same binning method is used to construct an IMF for each cluster, though different mass limits are imposed to determine the slope.. Different limits are required because 1) the completeness limit of each cluster is different from the Arches cluster and 2) the age of each cluster differs from the age of the Arches cluster. Table 26 below shows the results of Chapter 3, the derived parameters of the clusters making up the final sample for IMF measurements. The parameters listed in this table are those used to construct the IMF for each given cluster.

Table 26 Derived parameters of final sample

Cluster	RA	Dec	A_K (mag)	Dist (kpc)	Age (Myr)
R136	05 38 42.4	-69 06 03.4	0.2	49	1.7
Danks 1	13 12 26.5	-62 41 56.6	1.11	2.8	1.5
Danks 2	13 12 55.95	-62 40 43.4	0.92	3.8	3.0
Mercer 20	19 12 24.01	+09 57 04.4	1.3	4	6.0
Mercer 23	19 30 13.67	+18 32 06.3	0.59	7	4.0
Mercer 30	12 14 32.48	-62 58 45.7	1.1	11	4.0
Mercer 70	16 00 27.67	-52 10 50.4	1.3	5	4-5
Mercer 81	16 40 30.03	-46 23 36.0	2.5	11	2.5-3.5

5.1. CMD decontamination

Two populations of objects act as contaminating objects to the main sequence in each cluster: fore- and background objects that are non-cluster members, and evolved cluster members of uncertain initial mass. First-order removal of foreground stars was probed by the typical cluster MS color compared to the control field photometry. Cuts in color space were performed in order to provide a cleaner background subtraction at later stages of analysis. Statistical subtraction of the remaining field population from the cluster population was done in the last stages before IMF measurement, as discussed in more detail below. Applying a strict binned, number-density method to remove non-cluster objects can have ill-effects on the resulting population. One example of this lies in the Danks control fields, which actually contain massive evolved stars, as shown by Mauheran et al. 2011. This is equally likely to affect the results of R136 as well, as the field population has been shown to contain massive MS and evolved stars (e.g. Bestenlehner et al. 2011; Bressert et al. 2012).

Spiral arm features, seen as blue plumes to the left of each cluster sequence, were removed by color cuts in the mF160W-mF222M magnitude space. In some cases, e.g. Mercer 81 in Figure 47, multiple spiral arms can be identified as contaminating populations along the line of sight towards the cluster. For some clusters, this was either not necessary or not straightforward, in which cases no color cuts were made.

The above removal of spiral arm features is not a statistical decontamination, merely a removal of a fore- or background population that clearly does not belong to the cluster sequence. The same population is removed from the control field, using identical color and magnitude cuts. Table 27 below summarizes the color cuts on each cluster.

Table 27 Color cut limits	
Cluster	mF160-mF222
R136	None
Danks 1	None
Danks 2	None
Mercer 20	None
Mercer 23	None
Mercer 30	< 0.5 removed
Mercer 70	None
Mercer 81	< 1.5 removed

Second order removal of fore-and background objects is reliant on spectroscopic follow-up of each cluster. Objects with colors consistent with the cluster sequence that were spectroscopically identified as non-cluster members (e.g. late-type stars) were removed by hand as contaminants. These objects are labeled, usually by red asterisks, in the CMDs with spectral types labeled (e.g. figure 17, figure 21, figure 25, etc).

Removal of post-MS stars in the same magnitude range as the MS was done by hand. The reasons for this are twofold: initial mass according to models can be highly degenerate, and the magnitude to mass conversion code is not designed to "choose" between two points; secondly, initial masses of single post-MS massive stars can only be reliably measured via application of detailed atmosphere models, e.g. CMFGEN, TLUSTY, FASTWIND, which is beyond the scope of the current project. Stars brighter than the MS turn-off remain in the photometry, K-band luminosity functions, and IMFs to guide the eye in identifying the MS turn-off in these plots (e.g. see the IMF for Mercer 70 in Figure 43 where the supergiant and giant populations are contained in bins clearly beyond the MS turn-off).

5.2. Conversion to K-band Luminosity function

The cleaned HST photometry for each cluster and corresponding control field is written to an ASCII file. Observed photometry is error clipped to include only the most reliable sources, generally the brightest objects in each sample. The K-band photometry error was limited to 0.5 mag or less. This value was chosen in order to include MS stars in Mercer 81, which are fainter than MS stars in other clusters due to the higher distance and extinction towards Mercer 81.

Each K-band luminosity function (KLF) is computed for the observed and completeness corrected photometry, in bins of 0.5 magnitudes. Each star is placed into the appropriate luminosity bin; for the completeness corrected KLF, 100 divided by the completeness fraction is multiplied by the bin total (e.g. for a completeness fraction of 90%, the bin total is multiplied by 1.1).

The KLF is computed identically for the cluster photometry and control field photometry, with the intention of subtracting the control field KLF directly from the cluster KLF. In general, the subtraction affects the faint luminosity bins the most. This method also allows for the direct comparison of the 50% completeness in the control field and cluster. Generally speaking, the control field is complete to a fainter luminosity as the clusters are intrinsically denser fields and completeness suffers more from the effects of crowding.

5.3. Stellar Evolutionary Models

The grid of Geneva stellar evolution models with rotation ($M >= 8\ M_{\odot}$, Meynet & Maeder 2003) were used in tandem with models of canonical mass loss rates (Schaerer et al. 1993) for $M_{initial} < 8\ M_{\odot}$. Except for the case of R136, all clusters in this sample are located in the Milky Way so solar metallicity is assumed. As R136 is located in the LMC, the appropriate metallicity (1/2 solar) is adopted. The effects of rotation and metallicity are important in the high mass ($>12\ M_{\odot}$) model regime; rotating models ultimately result in higher initial masses than enhanced mass-loss (Schaller et al. 1992) or canonical mass-loss (Schaerer et al. 1993). Lower metallicy models predict higher initial masses than solar metallicity and slightly longer lifetimes for the most massive stars.

Isochrone models are built by inputting an age to Fortran code (iso.f) provided by the Geneva group. Briefly, the code interpolates between evolutionary tracks to build an isochrone of a specific age. As evolutionary tracks are only computed at a handful of initial masses, the code is designed to interpolate a track for a given mass at the specified age. A more detailed explanation is given by the Geneva group (http://obswww.unige.ch/Recherche/evol/Geneva-grids-of-stellar-evolution). At present, there exists interactive isochrone calculator and model interpolation tools, which were not available at the time of the current project. The code, iso.f, used to compute model isochrones for this work, was used by Figer

(2005) to compute isochrones for the Arches IMF measurement.Updated stellar evolution models are used for the purposes of this study, rather than those used in Figer (2005).

As stellar evolution proceeds, the model isochrones become degenerate in mass-magnitude space (as demonstrated in Figure 79). Evolved stars which begin to contaminate the MS magnitude space are removed by hand, as discussed above. Briefly, evolved stars can be differentiated from MS stars by their spectroscopic features. Figure 79 also demonstrates that stars with initial masses greater than 100 $M_{\odot}$ have left the MS after less than 2.0 Myr. Inspection of Table 26 above reveals that more than half of the clusters in this sample are older than 3.5 Myr, truncating the upper limit to any slope measurement. As stellar evolution progresses, i.e. the cluster ages, the MS turn-off becomes less and less massive, resulting in a smaller mass regime for which an IMF slope can be measured. This point is discussed in more detail in Results & Discussion.

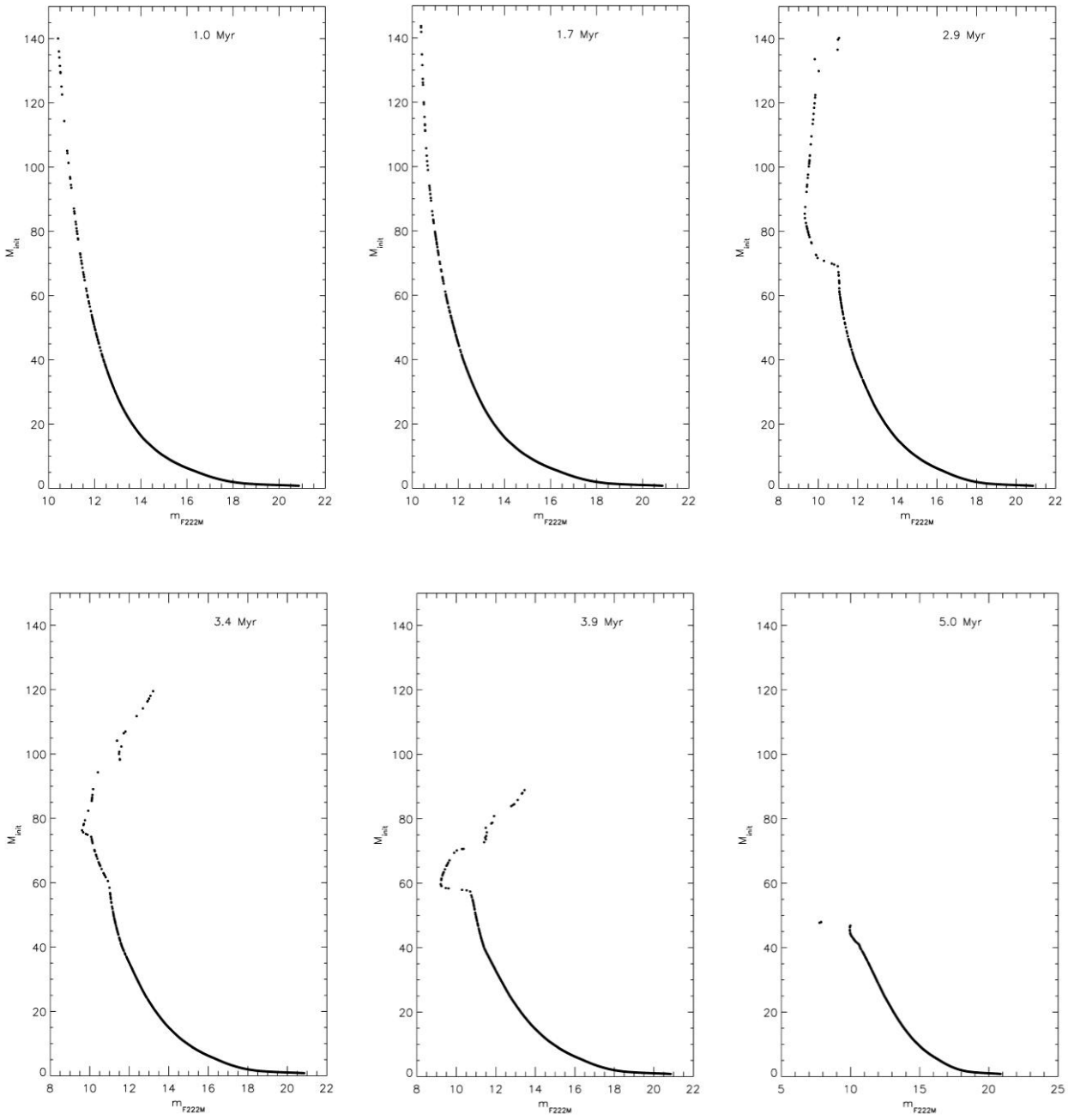

Figure 79 Results of initial mass-magnitude models for a simulated cluster showing that degeneracies in the mass-magnitude relation begin after ~3 Myr.

Geneva stellar evolution models are used to translate magnitude to mass rather than other stellar evolution models, such as the Bonn models. The Geneva models were chosen based on the mass range computed: Geneva models include stars up to 120 $M_{\odot}$ while Bonn models only include evolution models of stars up to 60 $M_{\odot}$. Extrapolating the results of Geneva models to higher masses has more advantages than

extrapolating the results of the Bonn models to similar masses, especially the availability of more points to include in the extrapolation.

The Geneva rotating stellar evolution models were used in determining the ages of the clusters in this sample. The models show, in Figure 80, the lifetimes of MS stars of a given mass, which can be used as an upper limit in clusters where a MS star of a given spectral type is observed at the tip of the MS turn-off in the CMD. In this figure, log of surface gravity is used as an indicator for dwarf luminosity class.

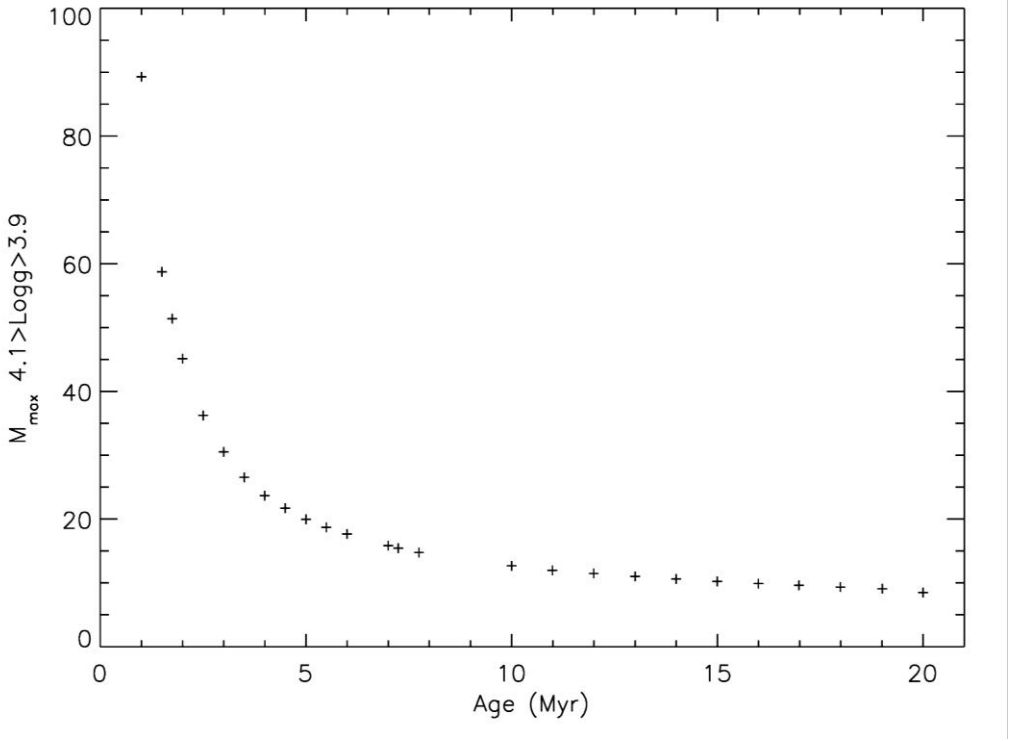

Figure 80 Maximum mass at MS turn-off vs. age

Information on the most massive star expected to remain in a cluster can also be inferred from the Geneva models. Figure 81 shows the evolution of Mmax,init vs. cluster age. For cases where detailed atmosphere modeling yields the mass of hot evolved stars in a cluster, the Geneva models can once again be used to determine the upper limit on the age of the cluster.

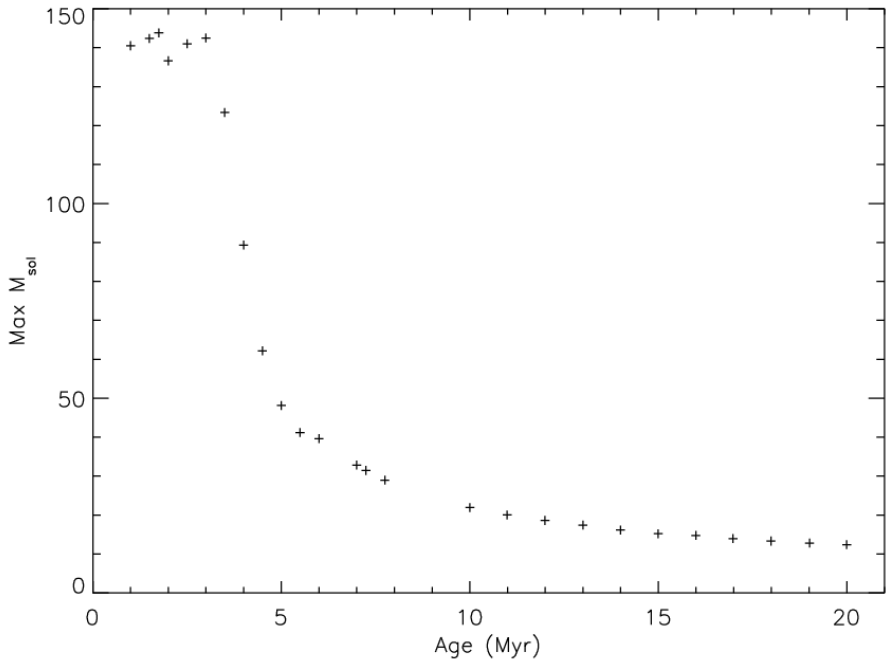

Figure 81 Maximum initial mass before SN vs. age

5.4. Construction of IMF

An extinction correction is applied to the model photometry (i.e. the results in the isochrone table described above) according to average extinction derived towards the specific cluster. The distance modulus is also applied at this time, resulting in a table of values containing $M_{initial}$, J mag, H mag, and K mag, where the magnitudes represent the current state of the star of mass $M_{initial}$ as derived from the models. Though a star might have lost 50% of its mass at a given age (see Figure 82), the object of this study is to measure the *initial* mass function rather than the present day mass function, so only initial masses are followed. Extinction is calculated for each wavelength according to the Rieke IR extinction law, with a slope of -1.53. As in Davies et al. (2012a), the slope -2.0 is adopted for Mercer 81 (see Davies et al. 2012a, references therein).

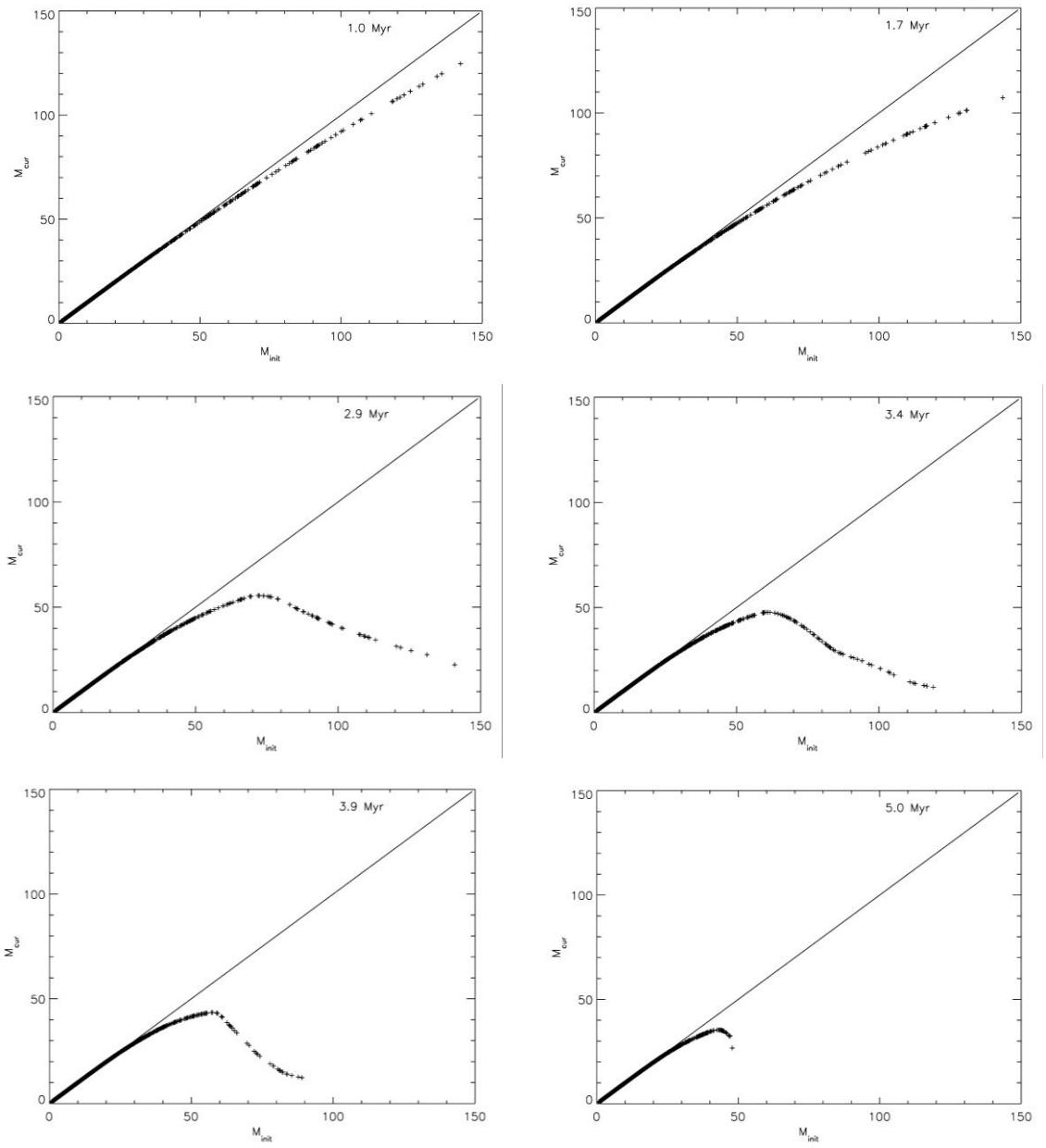

Figure 82 Results of initial mass vs. current mass for a simulated cluster. Each plot contains a line with a slope of 1 to guide the eye in identifying departures from the ZAMS, where all points fall along the line.

The observed K band magnitude is translated to initial mass according to the table containing the results of the model isochrone. As it is highly unlikely that each observed point will perfectly match the results of the model photometry, an interpolation over the model photometry array is utilized to determine the optimum solution. For objects which are brighter than the brightest magnitude in the isochrone table, a linear extrapolation is used to extend the mass range. The same method is applied to the control field

associated with each cluster, and an IMF is built for each cluster and control field. As every object in the cluster field is first assumed to belong to the cluster, a single age model is applied to all stars. Contaminating stars in the cluster field of view, belonging to a fore- or background population, will be assigned an incorrect age. The same model age is applied to the control field photometry in order to accurately reproduce the contaminating population in the cluster field.

The K-band completeness limit for a given cluster falls within the limits of a luminosity or mass bin. This results in a completeness corrected bin that contains fewer counts than actually observed. This bin, which is always the last (faintest magnitude or lowest mass), is removed once the completeness correction is applied to the KLF or IMF. The background is characterized for each cluster by the associated control field, for which the same completeness correction is applied.

Each IMF is constructed by directly subtracting the completeness-corrected background IMF from the completeness-corrected cluster IMF. In general, this removes a large portion of the faint bins. In some cases, this subtraction carries through to affect the slope of the IMF, as discussed below.

An error is determined for each mass bin, beyond Poisson noise. The total error for each bin the quadrature sum of the individual errors in the target and control field bins. The target error is defined as the square root of the number of counts in the non-completeness-corrected bin (e.g. Poisson noise) divided by the completeness fraction of the bin. Similarly, the control field (which serves as the background) error is computed in the same manner, and then scaled by the relative area of the control field to the target field. For the HST observations, the control field and target field have identical areas. For R136 as observed by VLT/MAD, the control fields were chosen to be the same area as the target field.

5.5. Slope Measurement Limits and Method

As in Figer (2005), each mass bin is set to a width of 0.1 in $\log M_{initial}$ space. At high masses, this results in a bin width that is larger in $M_{initial}$ space than bins at lower masses. For example, the bin covering the range of $\log M_{initial}$ = 1.9-2.0 corresponds to 79.4-100 $M_{\odot}$, resulting in a bin size of roughly 20 $M_{\odot}$ in M_{inital} space. Alternately, the bin covering the range of $\log M_{initial}$ = 0.5-0.6 corresponds to 3.2-4.0 $M_{\odot}$, a bin size of only 0.8 $M_{\odot}$ in $M_{initial}$ space. The IMF is plotted in log space in order to allow for a linear fit to the slope. In linear space, the IMF is an exponential function with a power-law (see Equation 2 and Equation 3) which is difficult to fit. This difficulty is overcome by working in log-log space. Other methods used in the literature include the use of an adaptive binning or a minimum count binning (for a discussion of the effects of binning on the results of the IMF see Maiz Apellaniz & Ubeda 2005).

Slope limits for each cluster are set on the low-mass end by the 50% completeness limit and on the high-mass end by the MS-turn off. Including only the MS population removes the degeneracies brought forth by evolved stars (see Figure 79 for examples of these degeneracies). This method becomes age (and therefore model) dependent, as a change in model age will result in an increase or decrease in the high-mass and low-mass limits.

The IDL routine LINFIT.PRO is used to fit the slope of the IMF on the background-subtracted raw and completeness corrected data. This routine fits a linear slope ($y=ax+b$) by minimizing the chi-square error statistic. The 1-sigma uncertainty estimate on both parameters *a* and *b* is returned as output of the routine.

6. Results and Discussion

Five of eight clusters presented here are found to have IMF slopes consistent with each other (Γ=-1.22+/-0.31) and the Salpeter/canonical slope (Γ=-1.3+/-0.7, Kroupa 2005) for intermediate to high mass ranges. This includes R136, though this cluster is discussed in detail below. Table 28 lists the cluster name, age, distance, reddening, upper and lower mass limits on the individual slope measurement, slope, and slope error for each cluster in the sample.

Danks 2 is found to have a IMF slope that is slightly shallower than the canonical slope. Mc70 and Mc20 have shallower slopes than the other clusters in the sample. This could be due to the more advanced dynamical state of these clusters. Mercer 20 is the oldest cluster in the sample, as indicated by the presence of a yellow hypergiant, allowing more time for the effects of mass segregation and cluster dispersal to become dominant in shaping the structure of the cluster. The shallower slopes could also be attributed to the comparitively lower masses of these clusters. However, the mass is determined by integrating over the completeness corrected slope and should be taken as a lower limit; if a Salpeter slope is used, a larger total mass is derived as the population of low mass stars increases greatly. Young massive clusters showing evidence of mass segregation are also found to have a flatter IMF. For example, Γ is found to be ~ -0.8 to -0.9 at the center of the young massive cluster NGC 3603 (Harayama et al. 2008; Pang et al. 2012).

Table 28 IMF Slope Measurement Results

Cluster	Age	Dist (kpc)	A_K	M_{low}	M_{up}	Slope	Error
Mercer 20	6 Myr	4.4	1.37	2	20	-0.68	0.38
Mercer 23	3-5 Myr	7	0.59	2.5	20	-1.33	0.20
Mercer 30	3-5 Myr	11	1.08	2	20	-1.47	0.14
Mercer 70	3-5 Myr	5.3	1.18	5	25	-0.56	0.13
Mercer 81	3 Myr	11	3.24	10	40	-1.38	0.29
Danks 1	1.5 Myr	3.8	1.11	4	32	-1.21	0.13
Danks 2	3 Myr	3.8	0.92	2	16	-1.14	0.13

R136	1.7 Myr	59	0.2	varies	250	varies	varies

6.1. IMF Slope: Individual Results

The individual results IMF slope measurement for each cluster are discussed below. Slope measurements of two clusters resulted in significant (greater than the one sigma error) deviations from the sample median. The IMFs of these clusters are examined in detail. Where possible, the slope of the IMF for a cluster is compared to results in the literature.

6.1.1. Mercer 20

Mercer 20, with an age of ~6 Myr and located at a distance of 4.4+/-0.33 kpc, was previously studied by Messineo et al. 2009. These authors do not construct a mass function for this cluster. Figure 83 displays the background-subtracted IMF (solid histogram) and the completeness-corrected, background-subtracted IMF (dashed histogram) for Mercer 20. The resulting slopes are overplotted in the figure by solid and dashed lines through each histogram respectively. The measured slope and predicted maximum mass for the background-subtracted IMF is displayed in the upper right of the plot. The measured slope of predicted maximum mass for the background-subtracted and completeness-corrected IMF is displayed in the middle right of the plot. For Mercer 20, the completeness-corrected, background-subtracted IMF has a slope of -0.68+/-0.38. Monte Carlo simulations recover this input slope to +/-0.1 dex, as discussed in 4.2 and listed in Table 25. Vertical dotted lines in Figure 83 indicate the mass range over which the slope is computed, corresponding to the completeness limit at the low mass end and the MS turn-off at the high mass end.

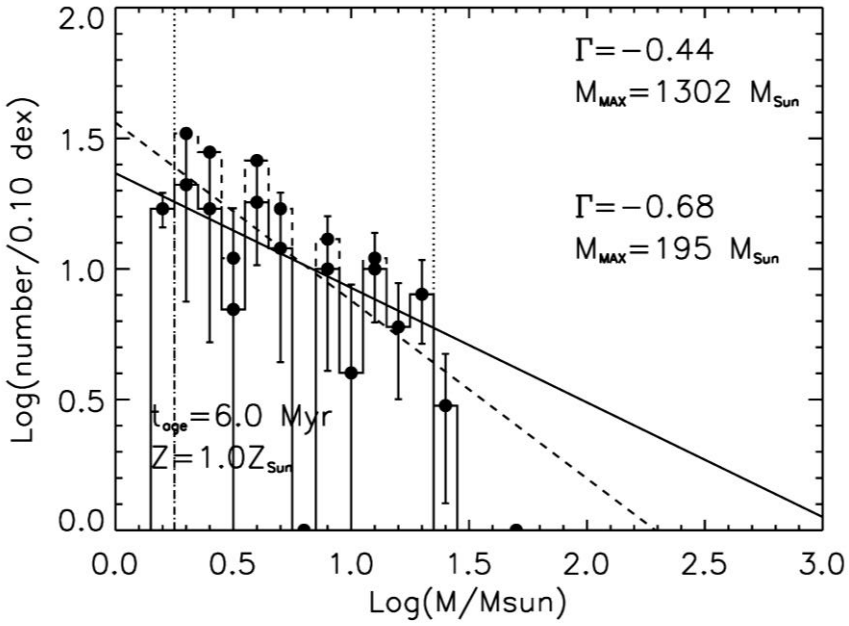

Figure 83 Mercer 20 IMF, as indicated by a solid histogram and fit by the solid line. The completeness corrected IMF is indicated by the dashed histogram and fit by the dashed line.The limits over which the slope was computed are indicated by the vertical dotted lines.

Background subtraction substantially flattens the slope of the IMF, as indicated in Figure 84, and significantly reduces the population of the mass bin at LogM=0.8 (6.3 $M_{\odot}$). Table 29 lists the slope measurement of the IMF for the completeness-corrected, background-subtracted slope in column 5. The completeness-corrected but not background-subtracted slope is listed in column 7. The background-subtracted slope is always flatter than the slope measured before background-subtraction. Should the cluster Mercer 20 extend substantially beyond the NIC3 field of view, it is possible that the control field population does not accurately reflect the true fore- and background contamination but instead contains the extended population of the cluster.

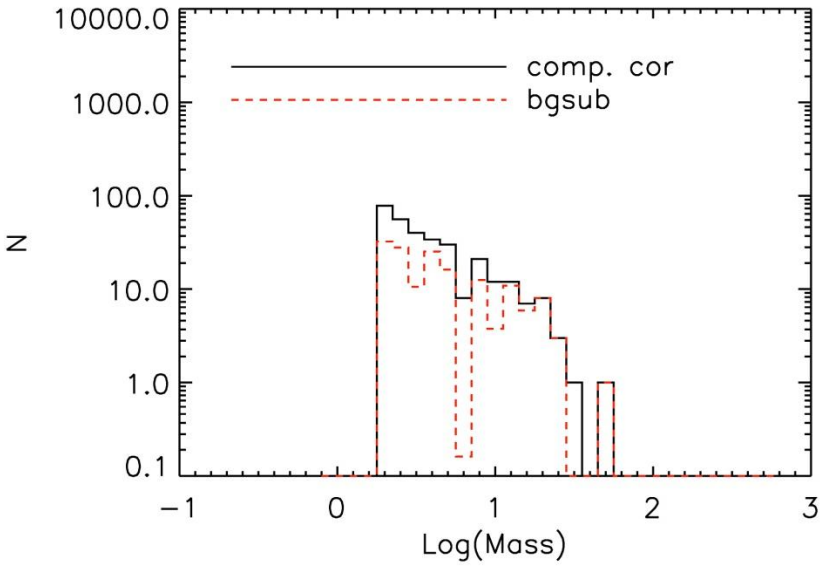

Figure 84 Completeness corrected IMF (solid black) and background subtracted, completeness corrected IMF (red dashed) for Mercer 20

Table 29 Slope measurements for Mc20							
Cluster	Age, LogAge	Dist	Log M_{low},M_{high}	CC, BG Slope	CC, BG err	CC Slope	CC err
Mc20	3, 6.477	4.4	0.3,1.5	-0.60	0.13	-0.80	0.12
Mc20	3.5, 6.544	4.4	0.3,1.5	-0.64	0.15	-0.84	0.13
Mc20	6, 6.778	4.4	0.3,1.3	-0.68	0.38	-1.02	0.15
Mc20	7, 6.845	4.4	0.3,1.3	-0.71	0.29	-1.05	0.14
Mc20	7.25, 6.860	4.4	0.3,1.3	-0.64	0.30	-0.99	0.15

6.1.1.1. 2MASS Radial Density Profile

Figure 85, solid histogram, displays the radial density profile for Mercer 20. This profile is constructed from sources listed in the 2MASS Point Source Catalog (2MASS PSC). The average density of the field is indicated by a red solid line at 11 stars/arcmin^2. The dashed histogram represents a color cut around the average A_K value for Mercer 20, 1.37 mag. This color cut is intended to represent the cluster population as resolvable by 2MASS. The edge of the NIC3 field of view is indicated by the dash-dot line at 0.5 arcminutes. The radial distance to the control field is indicated by the dotted line. Examination of Figure 85 indicates that the radial density of stars around Mercer 20, as probed by 2MASS point sources, extends beyond the NIC3 field of view. The radial density remains above the background level until roughly 2 arcminutes, farther than the distance to the observed control field.

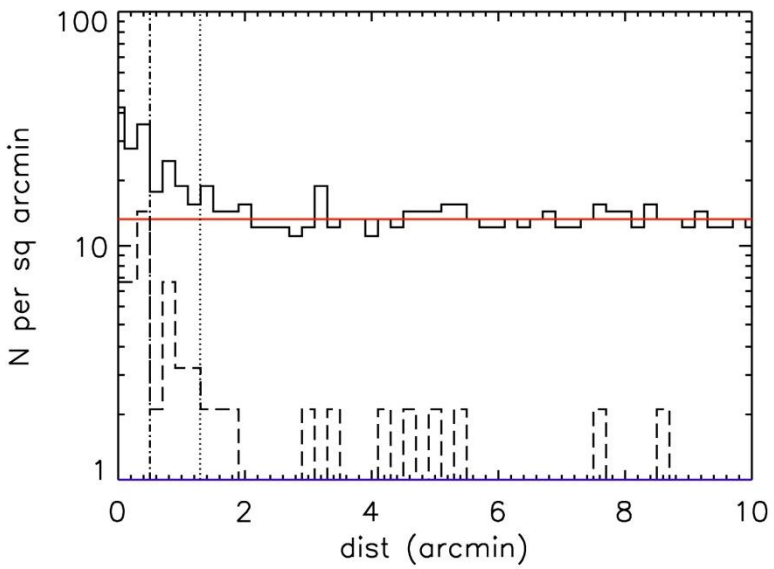

Figure 85 Mercer 20 2MASS radial density profile. Solid histogram shows all 2MASS point sources, while the dashed histogram displays the radial density profile of sources with colors similar to Mercer 20. The edge of the NIC3 field is indicated by the vertical dash-dot line, while the NIC3 control field is indicated by the vertical dotted line.

Comparison of the radial density profile of Mercer 20 with the radial density profiles of other clusters in this sample, Figure 86, suggests that the chosen control field potentially contains cluster members. Subtracting cluster members from the IMF will flatten the resulting distribution (e.g. make the slope less negative). With the exception of Danks 1, the radial density profile drops to the background level at or soon after the edge of the NIC3 frame. The radial density profile of Danks 1 is contaminated by Danks 2. The radial density of Mercer 30, top right of Figure 86, drops at the edge of the NIC3 frame in the general 2MASS source population, but contains few objects in the color-selected dashed histogram. The 2MASS PSC does not contain many members of Mercer 30, as evidenced by the relative dearth of stars with colors similar to Mercer 30 (dashed histogram).This cluster is at least twice as distant as Mercer 20 and the other clusters plotted in Figure 86. 2MASS lacks the photometric depth and spatial resolution to contain members of Mercer 30. Subtracting an improper background, e.g. one which contains cluster members, results in a shallower IMF slope. This is the most likely reason for the shallow IMF slope of Mercer 20.

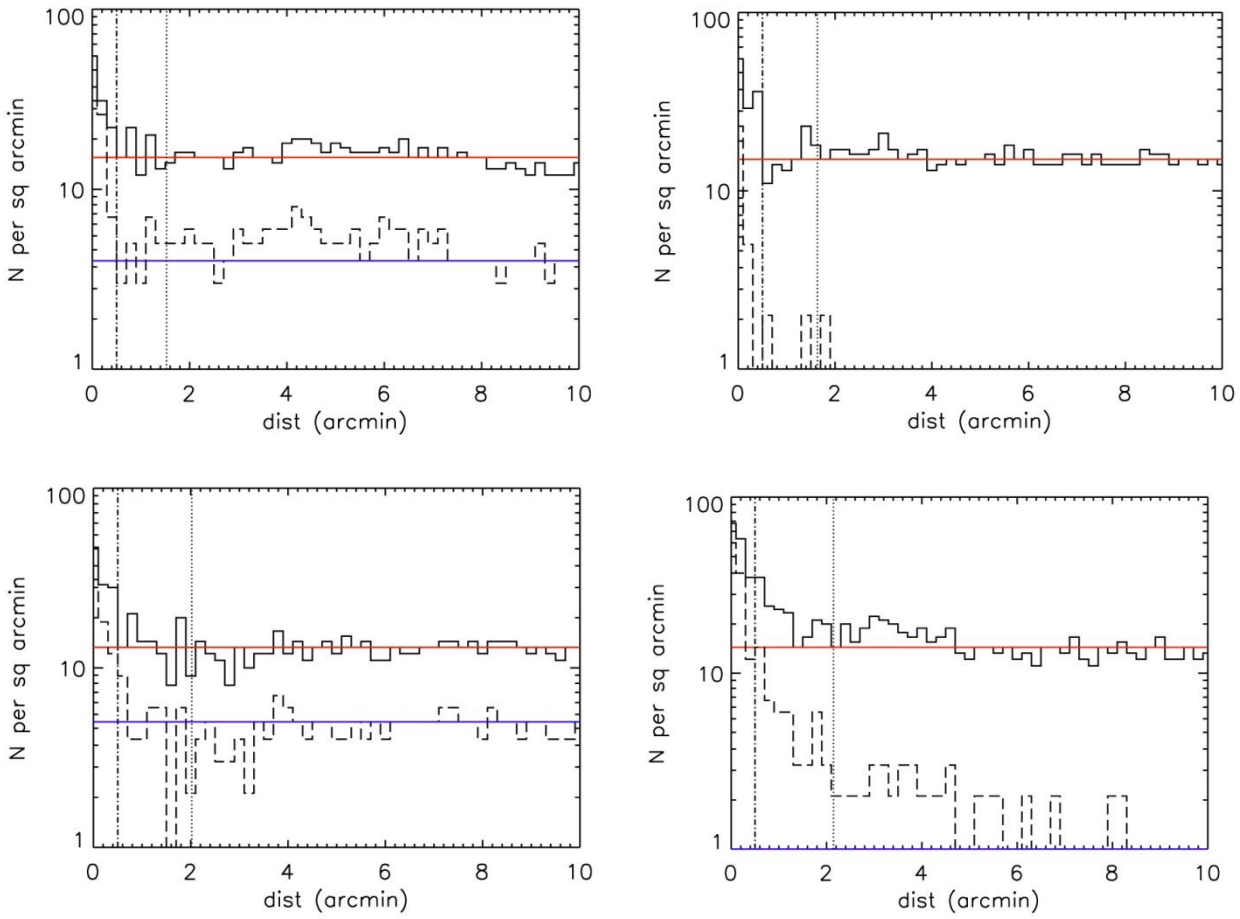

Figure 86 Radial density profiles for other clusters in the sample. Top left: Mercer 23; Top right: Mercer 30; Bottom left: Mercer 70; Bottom right: Danks 1

6.1.1.2. Mass Segregation in Mercer 20?

It has been shown that massive stellar clusters can undergo significant changes early in their dynamical evolution (Harfst et al. 2010, Banerjee & Kroupa 2012), leading to the loss of a possibly significant fraction of massive stars during cluster youth (Poveda et al. 1967; Aareseth & Hills 1972; Gies 1987; Leonard & Duncan 1990; Pflamm Altenburg & Kroupa 2006). Mass segregation has significant effects on the slope measurement of the IMF in dynamically evolved clusters. NGC 3603, for example, is found to harbor an IMF that flattens significantly towards the center (Harayama et al. 2008, Pang et al. 2012). Habibi et al. (2012) demonstrate that the same is true for the Arches cluster, showing that the high end IMF slope steepens when measured in radially increasing annuli.

The origin of mass segregation can also be primordial (Clarke & Pringle 1992; Clarke & Bonnell 2008) rather than dynamical. The Orion Nebula Cluster, with an age of approximately 1 Myr, is thought to have

formed with primordial mass segregation. This cluster contains too few massive stars to robustly populate the high mass bins of either the IMF or present day mass function (PDMF), so the exact effects on the intermediate to high end IMF slope remain undiagnosed in this nearby, well-studied stellar nursery.

Given the presence of the mid-O supergiants in Mercer 20, it is possible that the cluster age is overestimated (recall that the lower limit to the age of Mercer 20 is set by the yellow hypergiant G20-1). If G20-1 is not a cluster member and the age of Mercer 20 in the 3-3.5 Myr range, the above arguments remain valid. Reducing the model age for Mercer 20 results in similar IMF slope values, as displayed in Table 29. The upper limit on the mass range over which the slope is measured corresponds to the MS turn-off mass at 3 to 3.5 Myr. Both the Arches and NGC 3603 are relatively young clusters showing evidence for mass segregation, thus it is not unreasonable to expect signs of primordial mass segregation in Mercer 20, especially if it is younger than previous work (Messineo et al. 2009) asserts.

Deep, wider field imaging of Mercer 20 could potentially resolve the discrepancy between the measured slope and the steeper sample slope. Constructing an IMF for a series of radially increasing annuli, as done by Habibi et al. (2012) for the Arches cluster, would be the best method to search for signs of an IMF slope that changes due to mass segregation. In order to construct a meaningful IMF at radially increasing annuli, the completeness limit for each annuli must be computed. Analyzing the NIC3 observations of Mercer 20 does not provide a large enough radial range to search for signs of mass segregation.

6.1.2. Mercer 23

The slope of the IMF in Mercer 23 is consistent with the Salepter value, -1.35, as presented in Figure 87. Previous work by Hanson et al. (2010) derives the same age, distance, and mass, but these authors do not construct an IMF for the cluster. Monte Carlo simulations recover the input slope of -1.33 to a one sigma value of 0.2 dex, as noted in Table 25.

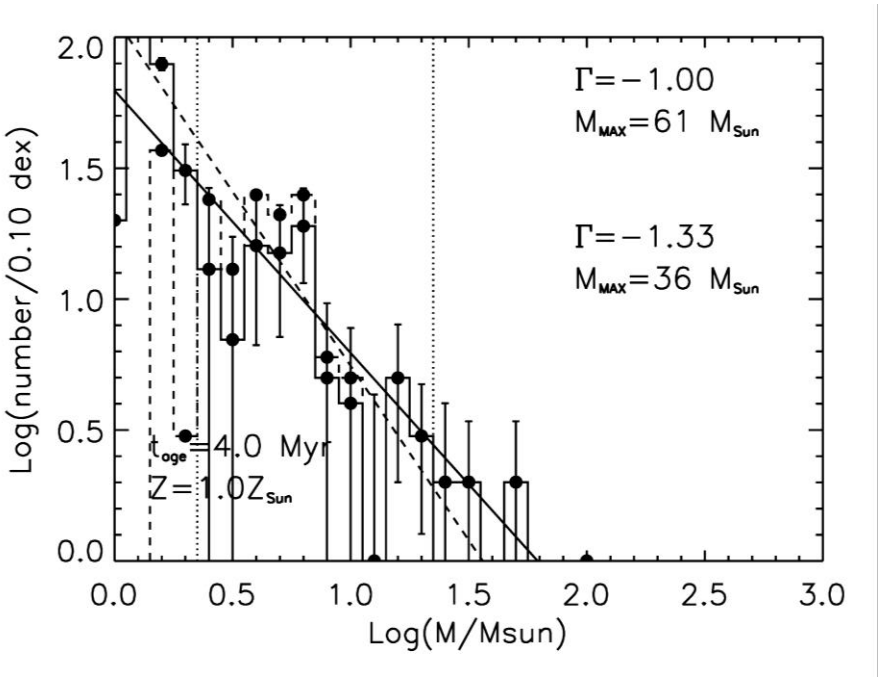

Figure 87 Mercer 23 IMF, same as for Figure 83

6.1.3. Mercer 30

The updated distance measurement for Mercer 30 places it twice as far as previous estimates (Kurtev et al. 2007), resulting in a total cluster mass larger by an order of magnitude and slightly different IMF slope than is found in the literature. The IMF slope is found to be consistent with the sample mean and the canonical Salpeter value, within errors, -1.47+/-0.14 as indicated in Figure 88. Kurtev et al. (2007) find a shallower IMF slope of -1.01+/-0.03. The steeper slope can be attributed to the larger distance and deeper analysis of the stellar content.

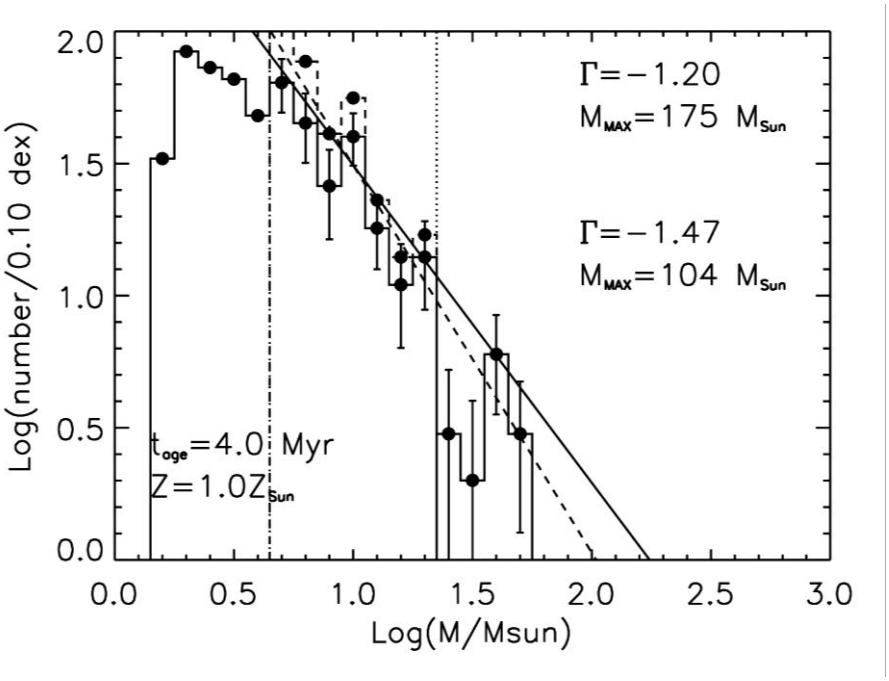

Figure 88 Mercer 30 IMF, same as for Figure 83

6.1.4. Mercer 70

Figure 89 contains the IMF for Mercer 70. The completeness-corrected, background-subtracted slope is significantly shallow than the sample mean and the Salpeter slope, Γ = -1.35, at $\Gamma_{Mercer70}$= -0.56+/-0.17. The model age does have a small effect on the measured slope of the IMF (see Table 30), but the resulting values remain consistent within errors. Monte Carlo simulations recover the input slope of -0.56 to a one sigma error of 0.13 dex, as found in Section 4.2 (see Table 25). The adopted distance of 5.25+/-0.37 kpc to Mercer 70 places it in the Scutum-Crux arm of the Galaxy, as indicated in Figure 98.

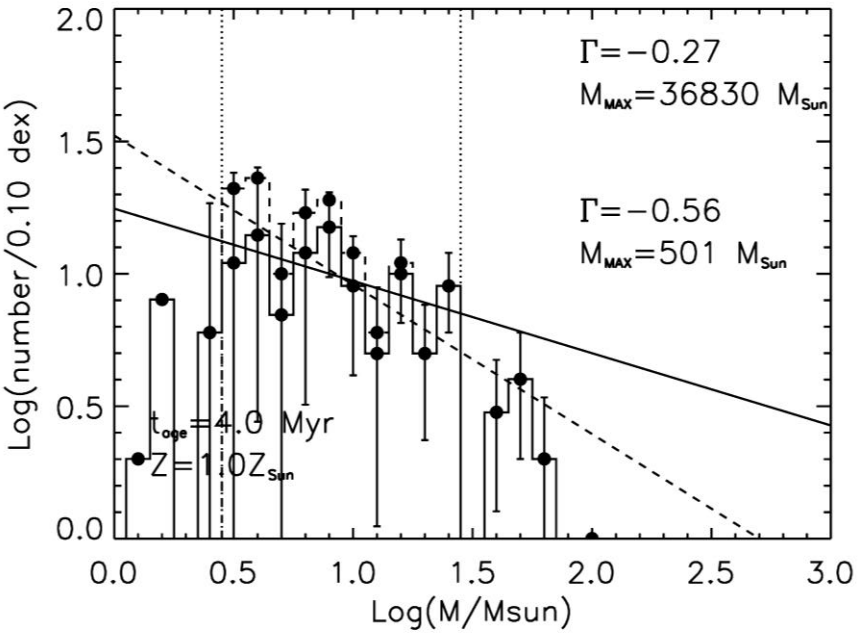

Figure 89 Mercer 70 IMF, same as for Figure 83

As with Mercer 20, background subtraction significantly flattens the slope of the IMF in Mercer 70. This effect is graphically represented in Figure 90, and the exact results (cluster name, age/log of age, cluster distance, log of the lower and upper mass limits for the measurement, completeness-corrected, background-subtracted slope and associated error, completeness-corrected slope and associated error) are listed in Table 30. The slope of the IMF is consistently steeper for the non-background-subtracted IMF. This is expected, as the highest contamination is at the faint (low mass) range (see Figure 39 in 3.7 as an example of this). Inspection of Figure 86 suggests that the radial density profile Mercer 70 does not extend into the control field, making it unlikely that the background subtraction process is flawed in some way. However, the same dynamical arguments for mass segregation made for Mercer 20 apply to Mercer 70.

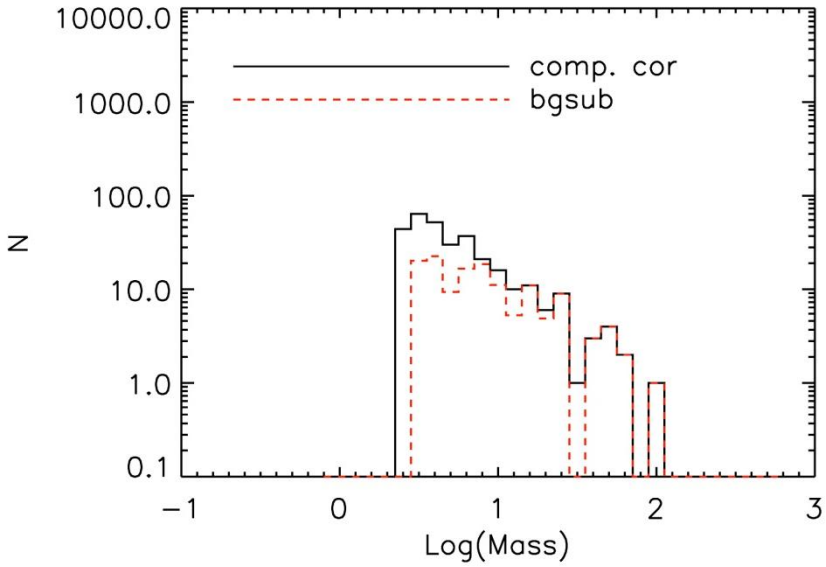

Figure 90 Same as Figure 84, for Mercer 70.

Table 30 Slope measurements for Mc70							
Cluster	Age, LogAge	Dist	Log M_{low},M_{high}	CC, BG Slope	CC, BG err	CC Slope	CC err
Mc70	3,6.477	5.25	0.4,1.5	-0.70	0.12	-1.17	0.08
Mc70	4, 6.602	5.25	0.4,1.4	-0.56	0.17	-1.11	0.11
Mc70	5, 6.699	5.25	0.4,1.4	-0.86	0.33	-1.14	0.15

Mercer 70 appears to represent a true deviation from the average sample IMF slope presented in this work, as well as the canonical IMF slope, for intermediate to high mass stars. Interestingly, both Mercer 70 and Mercer 20 contain FS CMa stars, a fairly rare class of non-supergiant B[e] stars (Miroschnichenko 2007, Miroschnickehenko et al. 2009). This may be a coincidence, as Mercer 81 contains a photometrically selected candidate FS CMa star (however, this exact nature of this object has not been determined via IR spectroscopy at this time). The evolutionary stage of these stars is unknown, but could suggest a more advanced age for Mercer 70 (>= 6 Myr, as for Mercer 20). Using a larger age (6-7 Myr) does not significantly alter the measured slope. The IMF slope measurement for Mercer 70 potentially suffers from the effects of mass segregation, but this cannot be convincingly shown by Figure 86

Why does the IMF of Mercer 70 deviate from the rest of the sample? One possibility is that massive star formation proceeded extremely rapidly in Mercer 70. As the most massive stars reached the MS, powerful winds began to sweep out the cluster's natal material, quenching lower mass star formation.

6.1.5. Mercer 81

Mercer 81, located at the far end of the Galactic bar, is the most heavily reddened cluster in this sample. Despite large error on the extinction of sources in Mercer 81, the slope of the IMF for an age of 3 Myr, Γ =-1.38+/-0.29, is found to be consistent with the canonical slope, Γ = -1.35, and the sample median. The slope of the IMF is measured from the completeness limit at 10 $M_{\odot}$ to the MS turn-off at 40 $M_{\odot}$, indicated by the vertical dotted lines in Figure 91. Monte Carlo simulations recover the completeness-corrected, background-subtracted input slope to 0.02 dex, with a standard deviation of 0.29 dex. The error on the IMF slope measurement for Mercer 81 is higher than the other clusters in the sample, as the exact photometry (and therefore the exact masses derived from the photometry) is less certain due to the higher extinction towards this cluster.

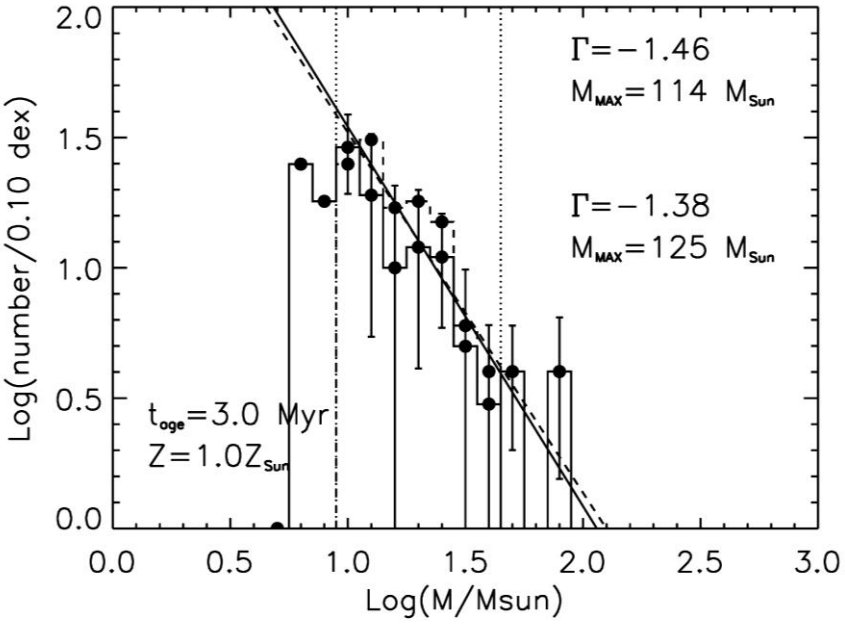

Figure 91 Mercer 81 IMF, same as for Figure 83

6.1.6. Danks 1

The slope of the IMF for Danks 1 is not measured from the completeness limit, but from 2 $M_{\odot}$ up to 32 $M_{\odot}$ as indicated by the vertical dotted lines in Figure 92. Davies et al. (2012b) show that 2 $M_{\odot}$ is the main sequence turn on point in this cluster. Inferring masses from photometry for pre-MS stars is unreliable using the rotating Geneva models, as the calculatiaons are for main sequence stars only. Pre-MS isochrones are required in order to examine the properties of stars less massive than 2 $M_{\odot}$ in Danks 1, but as this is a study of the intermediate to high end IMF, such an analysis goes beyond the scope of this

project. The IMF slope measurement, -1.21+/-0.13, is consistent within the errors of the result found by Davies et al. (2012b).

The results of Monte Carlo simulations indicate that the median recovered IMF slope over the mass range 2 to 32 $M_{\odot}$ is -1.33+/-0.13 when a slope of -1.21 is used as the input. These simulations also result in a steepening of the Salpeter slope, which is recovered within the errors. The IMF slope measurement output by the Monte Carlo simulations is still steeper than the input: a value of -1.48+/-0.14 is recovered when the Salpeter slope of -1.35 is used as input.. Both the completeness-corrected, background-subtracted input slope and the Salpeter slope become steeper by roughly the same amount, demonstrating the robustness of the method and measurement

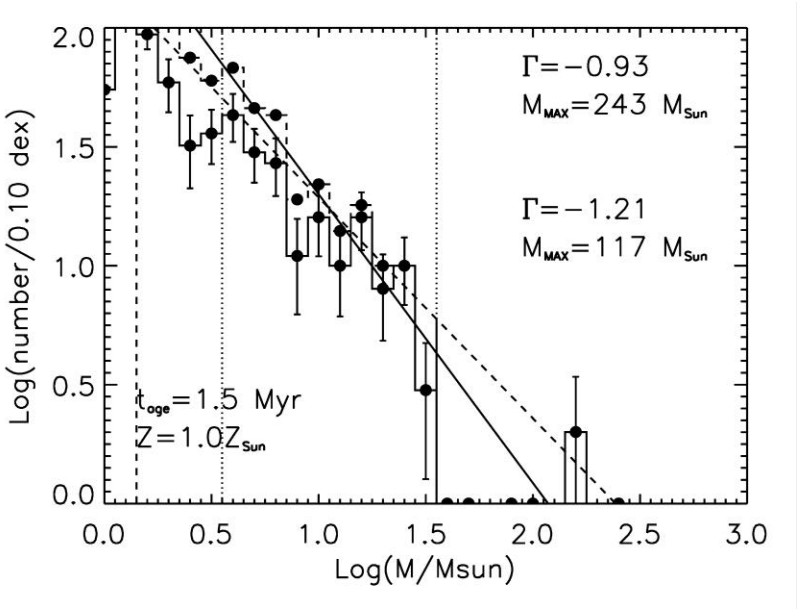

Figure 92 Danks 1 IMF, same as for Figure 83

6.1.7. Danks 2

As with Danks 1, the lower limit on the slope measurement for Danks 2 is set not by the completeness limit of the observations but rather by the MS turn on. The MS turn-off should be around 30-40 $M_{\odot}$ for a cluster with an age of 3 Myr, the age of Danks 2 (see the plot of MS turn off vs. cluster age in Figure 80). The upper limit on the slope measurement is chosen based on the low number counts and empty bin beyond 16 $M_{\odot}$, as displayed graphically in Figure 93. Monte Carlo simulations of Danks 2 recover an input slope of -1.21, to within 0.01 (Table 25), with an average standard deviation of 0.13 dex. Once again, the IMF slope measured here for Danks 2 is consistent with the IMF slope measure by Davies et al. (2012b) within the errors.

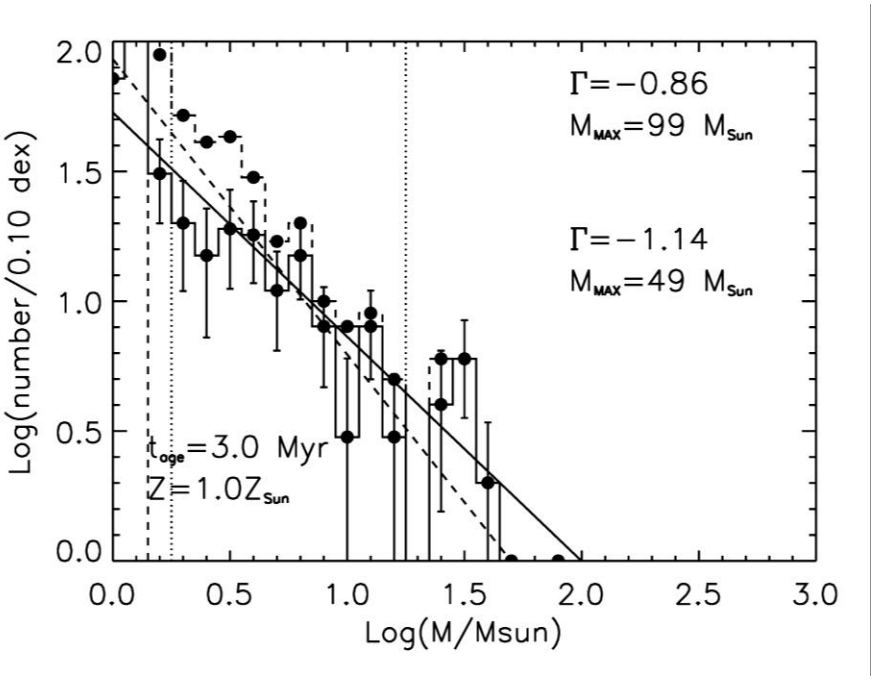

Figure 93 Danks 2 IMF, same as Figure 83

6.1.8. The curious case of R136

The starburst cluster R136 in the Large Magellanic Cloud contains a stellar population drawn from an IMF slope consistent with the Salpeter slope. However, the choice of mass range greatly influences the resulting measurement of the slope of the IMF.

The IMF for R136 is displayed in Figure 94, with the completeness-corrected IMF indicated by the dashed histogram. Star symbols are used to indicate the mass bins used to fit the slope of this IMF. The measured slope (overplotted by a solid line in Figure 94) is consistent with the canonical Salpeter slope (overplotted with a dashed line), Γ =-1.22+/-0.78. The choice of age, 1.7 Myr, is drawn from recent literature and motivated by the opportunity to directly compare the high end IMF slope measurement and other results of this study with work by other authors (e.g. Crowther et al. 2010).

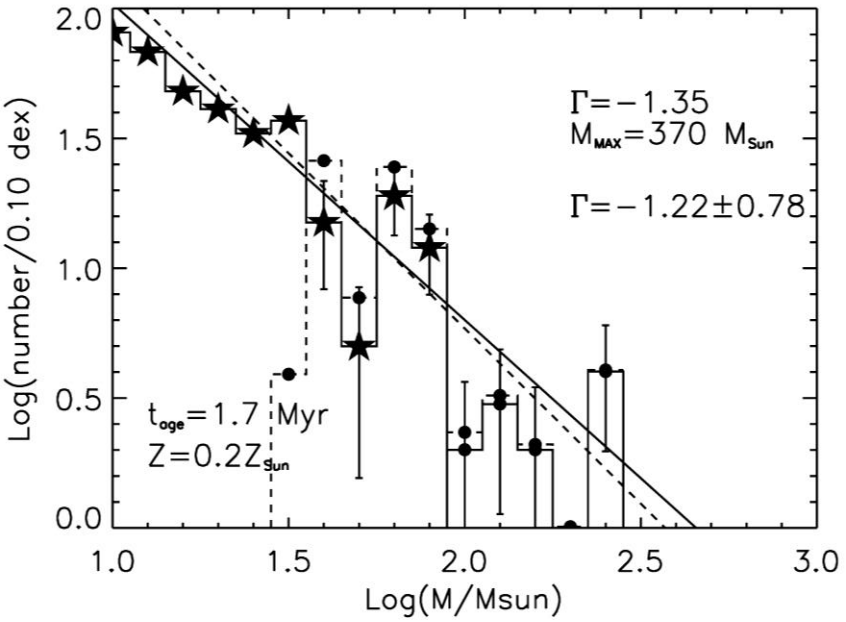

Figure 94 R136 IMF, solid histogram. R136 completeness corrected IMF, dashed histogram. Solid line displays a Salpeter slope fit to the solid histogram. Bins marked with star symbols were used to compute the slope of the IMF, -1.22.

In Figure 94, the highest mass bins (logM > 2.0) are not included in the fit due to low number counts, which would skew the results of the fit. Including all mass bins with more than one star results in a slope of -1.10+/-0.32, within the errors of the slope derived above and still consistent with the Salpeter slope (see the top left panel of Figure 95).

As indicated by the lowest bin in the dashed histogram, the data are only complete to roughly 30-35 $M_{\odot}$. When the completeness limit is taken into account, only 3 or 4 bins remain for the slope determination. The measured slope then becomes much flatter and the error increases by a factor of up to 10. For examples, see Figure 95; in each panel, the Salpeter slope is plotted by a dashed diagonal line and the mass bins used to fit the slope are indicated by star symbols.

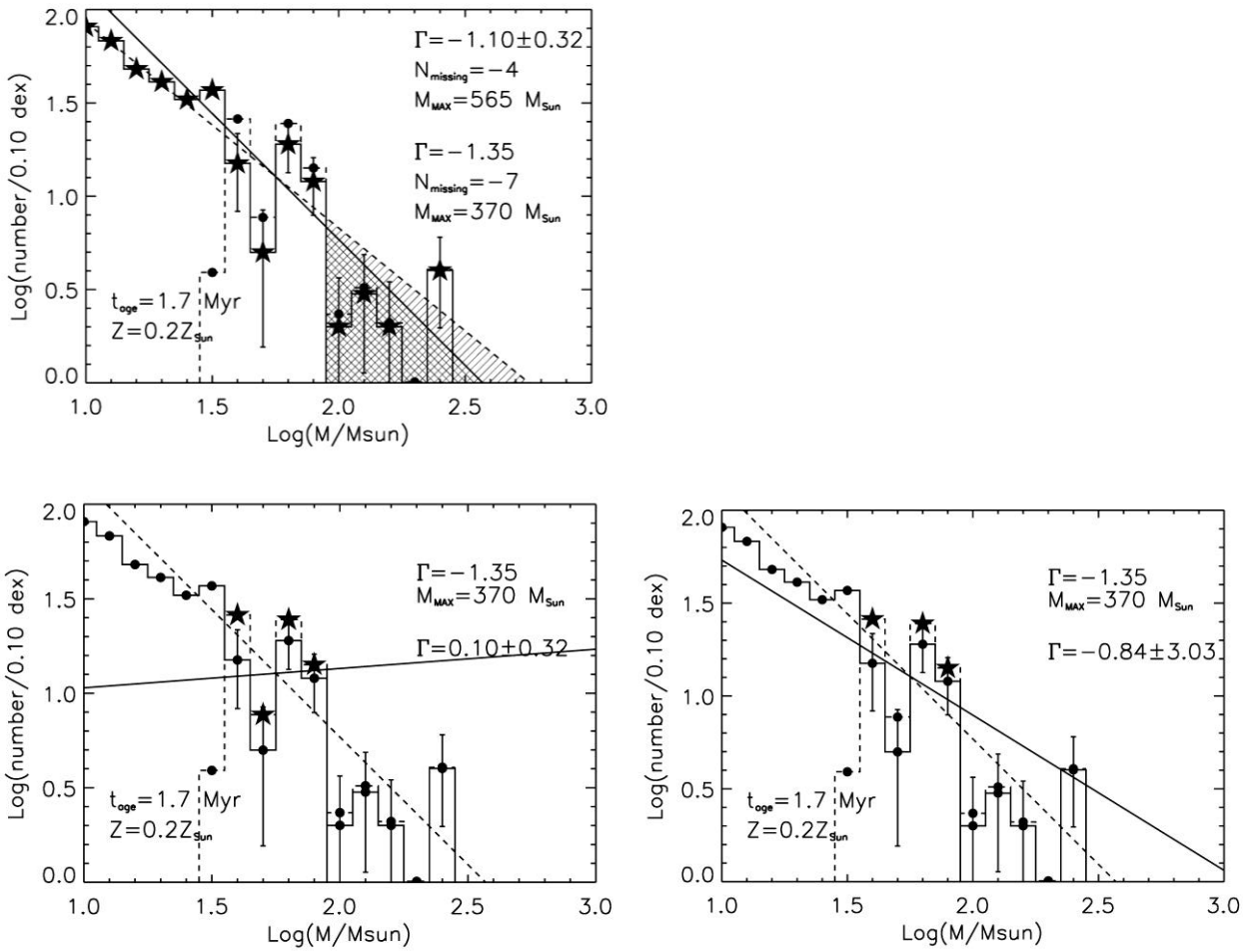

Figure 95 Alternative bin choice for slope determination in R136

Previous IMF slope measurements for R136 have focused on the massive star population only. Parker (1992) finds a slope of -1.3 to -1.5 for stars with masses more than 12 $M_{\odot}$. Massey & Hunter (1998) present two sets of mass derivations based on isochrones from Vacca et al. (1996) and Chlebowski & Garmany (1991), which differ in terms of temperature scale. The temperature scale of Vacca et al. (1996) is hotter than the other work, resulting in higher initial mass estimates for a given spectral type than Chlebowski & Garmany (1996). Using both calibration methods, Massey & Hunter (1998) derive an IMF slope of -1.3 to -1.4 for stars in the range 15 to 120 $M_{\odot}$. These authors find that the number of very massive stars in R136 is consistent with a Salpeter (1955) IMF. Previous work by Hunter et al. (1996) shows agreement with a Salpeter slope in the intermediate mass range, 2.8 to 15 $M_{\odot}$, in the outskirts ($r > 0.11$ pc) of the central cluster. Using only the 29 most massive stars, Koen (2006) derives a slope in the range -0.9 to -1.7 and finds evidence for an upper mass cut-off at 140-160 $M_{\odot}$ but cautions that more reliable mass estimates are required. These previous measurements of the IMF slope of R136 are based on

optical observations, while the IMF presented above is derived from IR photometry. There is good agreement between optical and IR measurements, supporting the robustness of the IMF slope measurement method presented here.

6.1.8.1. Very Massive Stars in R136?

The masses derived here, using rotating Geneva stellar evolutionary models with LMC metallicity, do not exceed 250 $M_{\odot}$. Recent work by Crowther et al. (2010) identifies objects in R136 which appear to exceed the upper mass limit of 150 $M_{\odot}$. These authors investigate the stellar parameters of massive stars in NGC3603 and R136, finding agreement with previous studies for mass estimates of massive stars in NGC3603 by employing non-rotating stellar evolutionary models. Binarity of the brightest objects in R136 cannot be ruled out as a plausible explanation for stars whose masses seem to exceed the upper mass limit of 150 $M_{\odot}$, on the basis of imaging resolution and the results of recent N-body work, as discussed below. Overall, it can be concluded that the nature of the most massive stars in R136 requires further investigation. Such a study must examine both the current mass of these stars and the formation mechanism that produced them.

6.1.8.1.1. RESOLUTION CONSIDERATION

Diffraction limited observations of the core of the massive cluster R136 are limited to resolutions of ~50 mas in the IR using 8 meter class telescopes. At the distance of the Large Magellanic Cloud, 50 mas corresponds to roughly 25000 AU, or 0.12 pc. Binaries and dense stellar systems with separations on the order of 1000's of AU would remain unresolved in diffraction limited observations.

For an equal mass system of 150 + 150 $M_{\odot}$, the equations given by Crowther et al. (2010) predict L_X~6.5(10^{33}) for a CWB system with a separation of 2500 AU, roughly a third of what is observed for the central R136 system. This separation would be unresolved at the distance of R136. Given the high binary fraction observed in other young, massive stellar clusters (e.g. Westerlund 1, Clark et al. 2008), it is very possible that some objects in R136 are unresolved binary systems.

6.1.8.1.2. N-BODY RESULTS

Recent N-body simulations of very massive stars clusters, specifically emulating R136, suggest that stellar mergers producing very massive stars (>150 $M_{\odot}$) are common in young, dense stellar systems (Banerjee, Kroupa, & Oh 2012b). N-body simulations by Banerjee, Kroupa, & Oh (2012a) predict the ejection of very massive stars from a R136-like cluster, producing a halo population of massive stars. Should stars of a given mass be preferentially ejected, a dip would appear in the IMF. With the exception of the bin at logM=1.7 (M=50 $M_{\odot}$), Figure 94 contains no strong evidence for a missing population of

high mass stars. It remains possible that the very massive stars in R136 represent the result of stellar mergers, though higher resolution imaging is required to confirm this.

6.2. IMF Slope: Sample as a Whole

The median IMF slope measurement of the entire sample yields a result of -1.22+/-0.31. Without R136, Mercer 20, and Mercer 70 the resulting median IMF slope is -1.33+/-0.12. Including R136 drops the median IMF slope measurement to -1.28+/-0.11. Considering only Galactic clusters yields a median IMF slope of -1.21+/-0.33. The results taken as a whole are consistent with the canonical Salpeter slope to within the one sigma errors. One interpretation for a shallower IMF slope is very rapid massive star formation that quenches low mass star formation. Primordial mass segregation is also likely to play an important role, as in the case of Mercer 20.

The IMF slope is plotted against cluster age in Figure 96. The solid, horizontal line in the plot indicates the Salpeter value of -1.35. Assuming that the majority of the cluster population is observed, no trend with age is expected and the plot supports this conclusion.

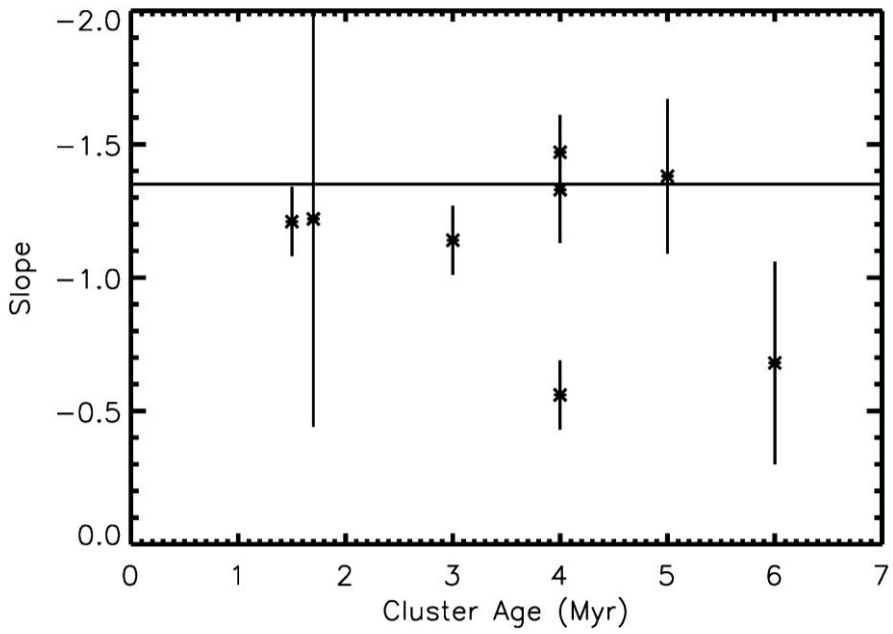

Figure 96 Slope vs. Age

No relationship between distance from the solar neighborhood and IMF slope can be identified in Figure 97. R136 is not included in this plot because it belongs to an external galaxy. If the slope of R136 differed

from the Galactic sample, the difference would be attributed to the variety of different conditions in the 30 Doradus Nebula (e.g. lower metallicity) rather than a simple distance difference.

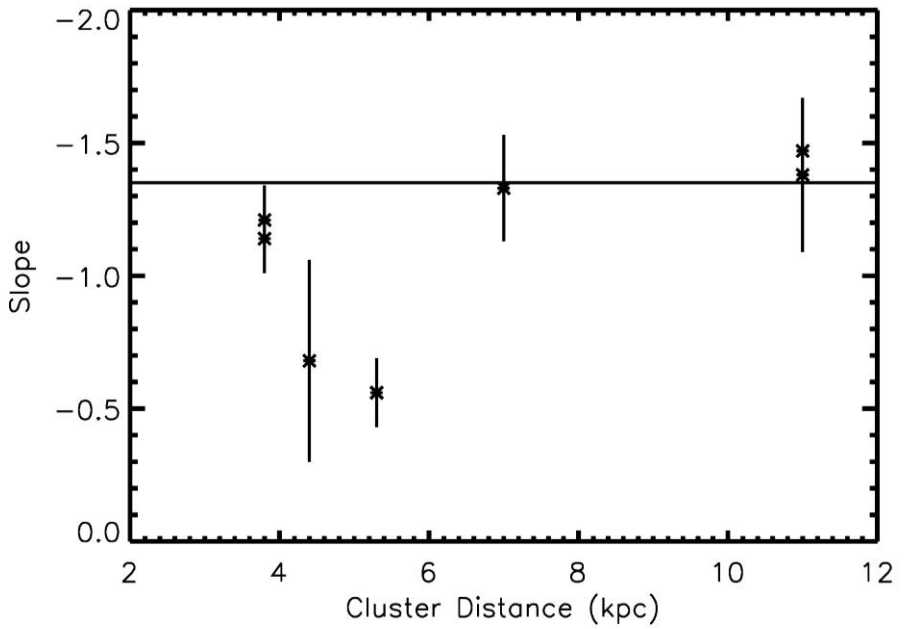

Figure 97 Slope vs. Distance (R136 is not included)

A potentially more interesting conclusion could be drawn from a more specific view of cluster position in the Galaxy rather than distance from the Sun, which is demonstrated in Figure 98. The locations of young, massive clusters are displayed in this figure, with circles indicating the clusters examined in this study. Once again, R136 is not shown in this plot due to its extragalactic nature. Redder colors indicate higher extinction values, as per the color bar in the lower right of the plot.

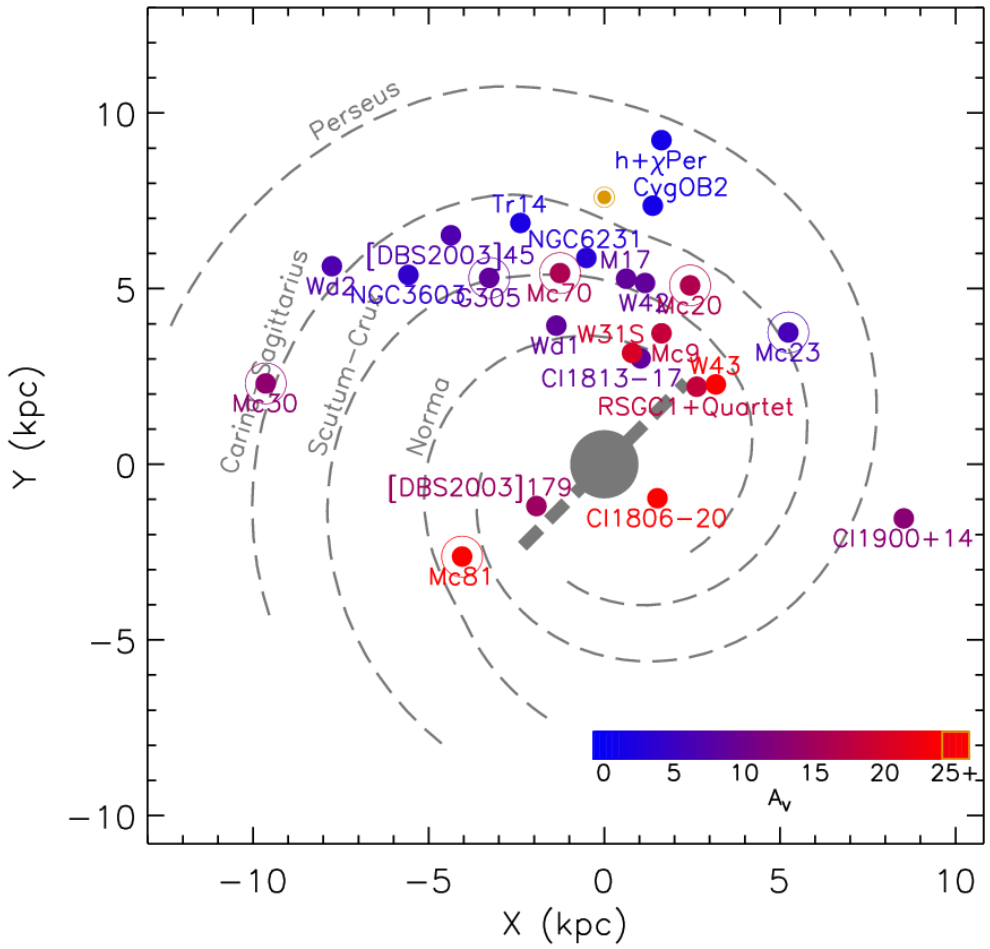

Figure 98 Location of young, massive clusters in the Milky Way. Objects considered in this sample are circled. Symbol color corresponds to extinction, as shown in the lower right of the figure.

No trend of IMF slope with cluster mass can be identified from Figure 99, which contains the IMF slope measurements plotted against the total derived mass of each cluster. Though Mercer 20 and Mercer 70 have total masses towards the low end of the range covered by this sample, the mass estimates are likely lower limits on the true mass. Additionally, two clusters have similar or lower masses than Mercer 20 and Mercer 70, indicating that cluster mass does not affect the slope of the IMF.

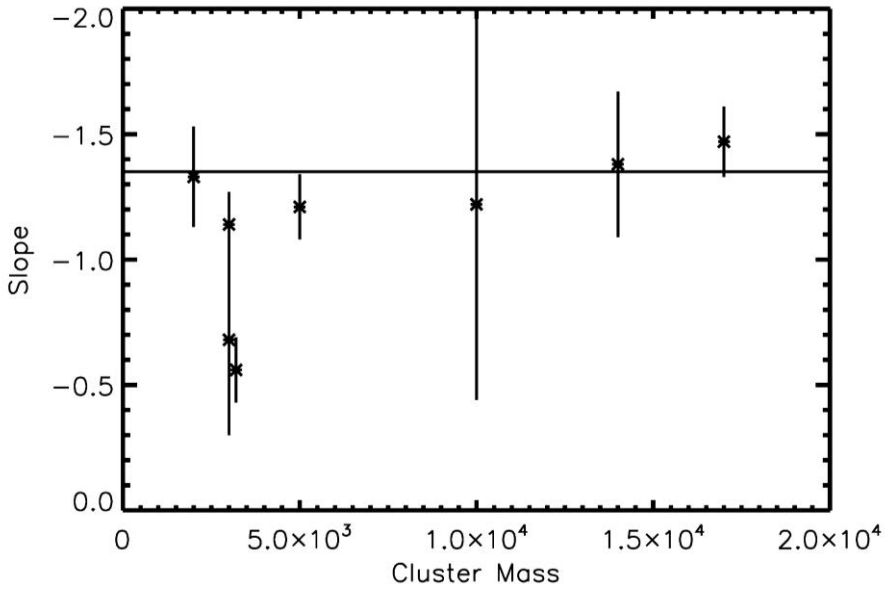

Figure 99 Slope vs. Cluster Mass

Inspection of Figure 96, Figure 97, and Figure 99 reveals no indication of a trend with age, distance, or total cluster mass. Additionally, no evidence is found for a change in slope corresponding to the mass range over which the IMF slope measurement was made (Figure 100). For additional context, see Figure 2 in the Introduction (1.1.1) for a comparison of values in the literature.

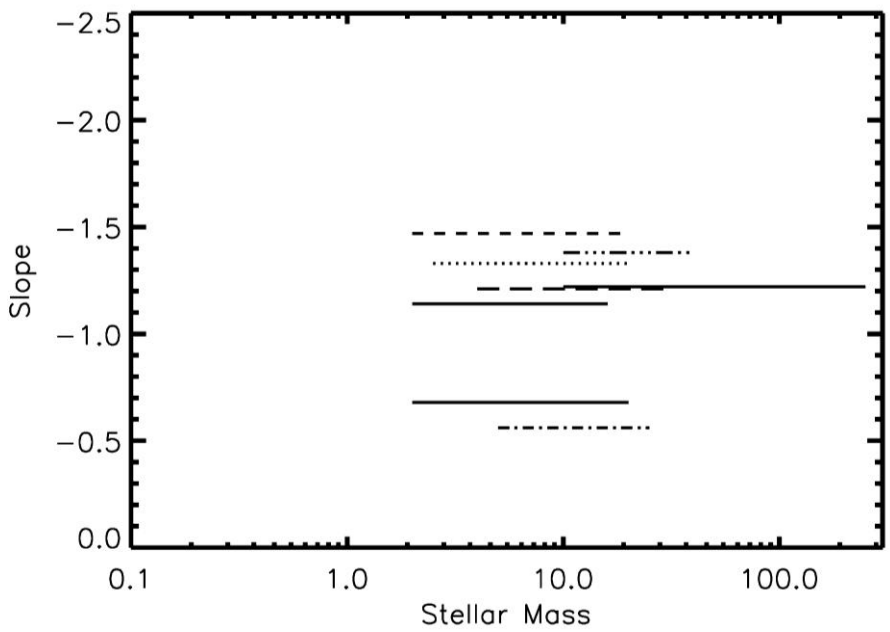

Figure 100 IMF Slope vs. Mass Range

The intermediate to high end slope of the IMF as probed by the near-IR selected stellar clusters in this sample is found to be consistent to within 0.31 dex.

6.3. No Evidence for an Upper Mass Cut-off

In order to identify any evidence for an upper mass cut-off in a given cluster, the cluster must be younger than 3 Myr. This is demonstrated graphically in Figure 101, which plots the maximum initial mass star remaining in a synthetic cluster against the cluster age. The synthetic clusters have an upper mass limit of 150 $M_{\odot}$ with masses drawn from a Salpeter IMF, and a total cluster mass of $3x10^4$ $M_{\odot}$. This plot does not take current evolutionary state into account (i.e. the current mass of the most massive star remaining at a given age is likely to be much lower than that star's initial mass).

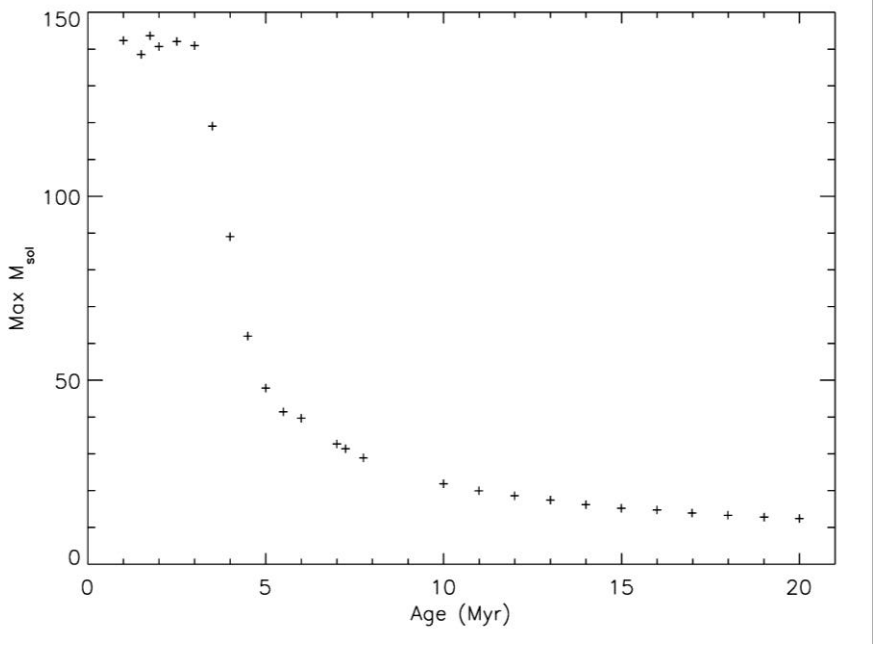

Figure 101 Maximum initial mass before SN vs. Age

In this sample, only four clusters are younger than ~3 Myr: R136, Danks 1, Danks 2, and possibly Mercer 81. R136 is thought to contain stars more massive than the canonical upper mass limit of 150 $M_{\odot}$ (Crowther et al. 2010), but refer to the discussion above. Both Danks 1 and Danks 2 have a total cluster mass less than 10^4 $M_{\odot}$ rendering it unlikely that the highest mass bins will be fully populated. Mercer 81, though massive enough to contain fully populated high mass bins, suffers from high extinction and a somewhat uncertain age (2.5-3.5 Myr, de la Fuente & Crowther, private communication). It is also possible that stars in Mercer 81 have exploded as supernova, as suggested by the potential association with the pulsar wind nebula HESS J1640-465 (Funk et al. 2007).

In summary, no cluster in this sample contains a cliff-like feature as that seen in the Arches IMF at ~150 $M_{\odot}$ or any other value. The majority of clusters in this sample are either not massive or not young enough to display evidence of an upper mass cut-off.

6.4. Dynamical Considerations

In recent years, an increasing observations have been made suggesting the presence of an extended halo of massive stars surrounding young, massive clusters such as those presented in this sample. The clusters Danks 1 and Danks 2 were found to be surrounded by a halo of evolved, massive stars, in addition to the previously known WR star WR48a (Maurerhan et al. 2011, Davies et al. 2012b). These authors find

several WR stars in the G305 star forming region, in addition to WR48a and the Danks clusters (see Table 3 of Davies et al. 2012b).

Gvaramadze et al. (2011) find evidence for several runaway stars, as evidenced by bow shocks in the ISM, originating from the central clusters of NGC 6357. This includes OB main sequence and giant stars, from spectral type B0 to O5.5. NGC6357 contains the young (1-2 Myr), massive cluster Pismis 24, known to host stars with masses near the upper mass limit (Maiz Apellaniz et al. 2007), and the less studied cluster AH053J1725-34.4. The sample of Gvaramadze et al. (2011) is biased towards faster moving runaway stars, as slower moving stars will not sweep up a leading bow shock, making it likely that additional massive stars are present in the halo surrounding the central clusters of NGC6357.

The VLT FLAMES Tarantula survey has identified several very massive stars in the far outskirts of R136 (e.g. 30 Dor 016, Evans et al. 2010), including one very massive star, VFTS 682 (Bestenlehner et al. 2011), with an inferred mass of 150 $M_{\odot}$. N-body work by Banerjee , Kroupa, & Oh (2012a) suggest that this type of "slow runaway" massive star should be common around dense young clusters like R136. These authors also find that "super canonical" stars with masses over 150 $M_{\odot}$ can be produced in R136-like environments via dynamical mergers of binary systems in the cluster core (Banerjee, Kroupa, & Oh 2012b).

For the clusters Danks 1 and Danks 2, the ejection of massive stars into the surrounding medium has little to no effect on the slope of the inferred IMF. In the G305 region, the halo population contains stars that are evolved beyond the MS and therefore beyond the upper limit of the slope measurement. This assumes, however, that only the most massive stars have been ejected from the cluster and that the halo contains no MS stars. This is a reasonable assumption given that recent N-body simulations show that the ejection fraction of stars in a dense stellar cluster increases with increasing stellar mass for masses above 10 $M_{\odot}$ (Banerjee et al. 2012a). The surveys of Mauheran et al. (2011) and Shara et al. (2009) both specifically targeted emission line objects, making it unlikely that MS stars would be detected. No evidence for a preferential deficit over some small mass range can be identified from the IMFs of Danks 1, Danks 2, or R136.

Banerjee & Kroupa (2012) present the results of N-body simulations suggesting that an initially top-heavy or flattened IMF that loses stars due to dynamical interactions will present a canonical PDMF by 3 Myr. Their result suggests that the majority of clusters in this sample formed with a flatter IMF that then steepened due to a loss of stars at the intermediate to high mass range. However, only a handful of massive stars are found to populate the halos around young stellar clusters. The halo stars are either evolved from stars with initial masses above the upper mass limits considered for the IMF slope

measurements presented here (as in Danks 1 and Danks 2) or belong to mass bins that too poorly populated to be included in the IMF slope measurements (as in R136). Inclusion of massive runaways located relatively far from the center of R136 is a difficult task because multiple populations of a variety of ages are present in this region. "Slow runaways" have not escaped far beyond the cluster, and thus are included in the IMF for R136. For these reasons, the IMF slope measurements presented here represent the true IMF slope.

Even a cluster as young as Danks 1, 1.5 Myr, contains post-MS objects (WNLh stars, O supergiants, Davies et al. 2012b). Evolutionary models predict that at 2 Myr, a star of initial mass ~60 $M_{\odot}$ will be the most massive object remaining on the main sequence (Maeder & Meynet 2005). Detailed atmosphere models of post-MS supergiants, such as those found in Danks 1 and in the Arches clusters, allow for an estimation of the initial mass of these objects. With the inclusion of detailed atmosphere models, a slope measurement across a wided mass range is possible. However, detailed atmosphere modeling is beyond the scope of the current work presented here.

6.5. Assumption of Coevality

The stellar clusters in this sample were chosen to be younger than 8 Myr, as indicated by the lack of red supergiant stars. With the exception of Mercer 20, which contains a yellow hypergiant and mid-O supergiants, there is no evidence for an age spread larger than ~2 Myr in any of the clusters presented here. The error on the age determination is roughly +/- 1 Myr for each cluster. It is shown in Chapter 4 that varying the age of each cluster does not significantly alter the slope measurement.

The IMF is modeled as the result of a single burst of star formation for each cluster. For simplicity, the duration of this burst is assumed to be a delta function, i.e. an instantaneous burst. This implies that all stars in the cluster formed at the same time, which is not necessarily the case. Should each cluster contain a population of massive stars that formed over a large spread, the resulting IMF would be steeper than a single burst population.

Multiple epochs of star formation in a single region are likely common. For example, Davies et al. (2012b) suggest that the presence of Danks 2 in the G305 star forming region triggered the formation of Danks 1. The triggering timescale would be on the order of ~2 Myr in the G305 region. Hamaguchi et al. (2010) present evidence for two major episodes of star formation in the Carina Nebula, the most recent episode triggered by the prior. These authors estimate an age difference between the two epochs of star formation in the Carina Nebula on the order of 3-30 Myr. Pre-MS isochrone calculations predict – and observations confirm - that high mass stars form more quickly than low mass stars. This age difference is used by Davies et al. (2012b) to determine the age limits on the clusters Danks 1 and Danks 2, for

example. The Monte Carlo simulations described in Section 4.2 assign an age to each star in a synthetic cluster drawn from a Gaussian distribution of 0.5 Myr, centered on an average age. These simulations recover the input IMF slope quite well, indicating that an age spread of 0.5 Myr does not have an effect on the measured slope.

Extended Green Objects (EGOs) found in the GLIMPSE survey are tracers of high mass star formation (Cyganowski et al. 2008). No evidence for current massive star formation as probed by EGOs is present in the mid-IR images of the Galactic clusters in this sample. The current epoch of massive star formation appears to have ended in the Galactic clusters in this sample. Evidence for on-going massive star formation in R136 is the subject of current studies. The core cluster, R136, in 30 Dor is surrounded by a halo of older stars. It is possible that older stars along the line of sight to R136 contaminate the IMF. Analysis of two control fields serves as a better constraint on the contaminating population towards R136.

6.6. Effects of Unresolved Binaries

Unresolved binary systems can play a role in shaping the inferred IMF. Two extremes can be considered: 1) every observed star is an equal mass binary or 2) every observed star is single. In reality, it is more likely the mass ratio (M_{low}/M_{high}) of binary systems is randomly drawn from a population between 0 and 1. One represents the case of an equal mass system while 0 represents the case of a single star.

For the case of 100% equal mass binaries, the slope of the IMF does not change. The luminosity of each unresolved system is higher than the true luminosity of each single star by a systematic offset. This offset results in a shifting of each true mass bin to a higher mass bin. Stolte (2003) finds that ~30% of individual mass estimates are overestimated when correction for randomly distributed binaries are taken into account. This serves to flatten the IMF slope towards a "top heavy" distribution.

6.7. "Super" Star Clusters in the Milky Way

Several groups have estimated the number of young, massive clusters in the Milky Way to be roughly 100 (e.g. Hanson et al. 2008, Ivanov et al. 2010). These authors define young, massive clusters (YMCs) or "Super Star Clusters" as those clusters similar to R136 and the Arches: masses around or above 10^4 $M_\odot$ and ages roughly 2 Myr. At present, only a handful of such clusters are observed. Table 31 lists these clusters, and includes some clusters with slightly advanced ages. All four red supergiant clusters (RSGC) were identified via the red supergiant population alone; the MS in these clusters remains undetected.

Table 31 Known Galactic YMCs		
Name	Mass	Reference
Trumpler 14	10,000 $M_\odot$	Ascenso et al. 2007a
Westerlund 2	10,000 $M_\odot$	Ascenso et al. 2007b
Mercer 30	10,000 $M_\odot$	this work; de la Fuente et al. in prep
NGC3603	12,500 $M_\odot$	Harayama et al. 2008
Mercer 81	14,500 $M_\odot$	this work; Davies et al. 2012a
Arches	20,000 $M_\odot$	Figer et al. 1999a,b
Quintuplet	20,000 $M_\odot$	Figer et al. 1999b, 2002
Galactic Center	20,000 $M_\odot$	Martins et al. 2007
RSGC4	20,000 $M_\odot$	Negueruela et al. 2010
RSGC1	30,000 $M_\odot$	Figer et al. 2006
RSGC3	32,000 $M_\odot$	Clark et al. 2009
RSGC2	40,000 $M_\odot$	Davies et al.
Westerlund 1	50,000 $M_\odot$	Brandner et al. 2008

Estimates of the number of young, massive clusters in the Galaxy are based on extrapolation of a locally derived cluster mass function or application of the global star formation rate of normal spiral galaxies. The discovery of Mercer 81 was serendipitous in that it is located behind a chance asterism of bright stars on the sky. From an original sample of 23 carefully selected clusters, two are newly discovered globular clusters (Mercer 3 and Mercer 5) and two are more massive than 10^4 $M_\odot$ (Mercer 30 and Mercer 81). Five clusters contain evolved massive stars, part of the intermediate-mass population of Galactic clusters. From the results presented here and the previously known YMCs in the Galaxy, it can estimated that the current census of these clusters is 30-50% complete. This suggests a total YMC population of 25-45, far fewer than estimated in previous work.

7. Conclusions

To date, the slope of the IMF in the solar neighborhood and in nearby (< 3 kpc) stellar clusters is found to be consistent with the Salpeter slope (e.g. Bastian et al. 2010). Though derived through somewhat different methods, primarily the use of infrared instead of optical observations, the results presented here are consistent with the majority of the literature. The earlier review of Massey (2003) finds similar results, mainly citing the works of Massey et al. (1998a) and Massey & Hunter (1998); it may worth noting that as imaging capabilities and stellar modeling have improved, the measured slope of the IMF in some clusters has changed. For the Cyg OB2 association, the measurement of the slope of the IMF has undergone a considerable progression from -0.9+/-0.2 (Massey et al. 1995b) to -1.6+/-0.1 (Knodlseder 2000) then to -1.27+/-0.16 (Wright & Drake 2010).

Bartko et al. (2010) and Lu et al. (2013) find a flattened or "top heavy" initial mass function in the Galactic Center region. Measurements of the IMF in the Galactic center represent the only clear deviation from a nearly universal IMF at intermediate to high masses. Bartko et al. (2010) use IR observations from VLT/SINFONI, covering a portion of the Galactic center region, to derive an IMF with an extremely steep slope, $dN/dm \sim m^{-0.45+/-0.3}$, for the mass interval 7-60 $M_{\odot}$. Do et al. (2013) and Lu et al. (2013) present Keck II/OSIRIS integral field IR spectroscopy of the same region as Bartko et al. (2010), including a larger field of view. These authors derive an IMF of $dN/dm \sim m^{-1.72+/-0.2}$, or Γ = -0.72+/-0.2, via a Bayesian inference method, finding that the area of the sky considered by other authors is not representative of the hot star population. Namely, Lu et al. (2013) point out that Bartko et al. (2010) do not include the clock-wise disk of massive stars in their analysis, nor do they include the S-star cluster inwards of r<0.8". Though Lu et al. (2012) find considerably steeper slope than Bartko et al. (2010), these results still represent a significant deviation from the Salpeter slope.

When applying an IMF to unresolved population in external galaxies, care must be taken to incorporate results from Mercer 70 and the Galactic Center. It remains possible that top heavy IMFs are common in extreme starbursts where the natal material can be quickly cleared away by the winds of massive stars, effectively halting low mass star formation. Advances in simulations of massive star cluster formation would serve to clarify this situation.

7.1. The Slope of the IMF

The slope of the IMF over an intermediate to high mass range is found to be consistent with the canonical Salpeter value and other slope values in the literature.

Figure 102 presents the IMF slope for each cluster in the context of the mass range over which the slope was measured, reproduced from Figure 100 in the previous section. Here, the plot limits have been expanded in order to produce a better comparison to Figure 2 of Bastian et al. (2010), reproduced in Figure 2 of this work, which itself is a representation of the "alpha plots" from Scalo (1998) and Kroupa (2002). Though the plot displays some scatter in the IMF slope, comparison of Figure 102 with the similar plot of Bastian et al. (2010) reveals that the measurements presented here are well within the scatter found in the literature (though Bastian et al. 2010 do emphasize that the scatter in their Figure 1 may seem larger than the typical literature values, as their review is concentrated on deviations from "typical" values).

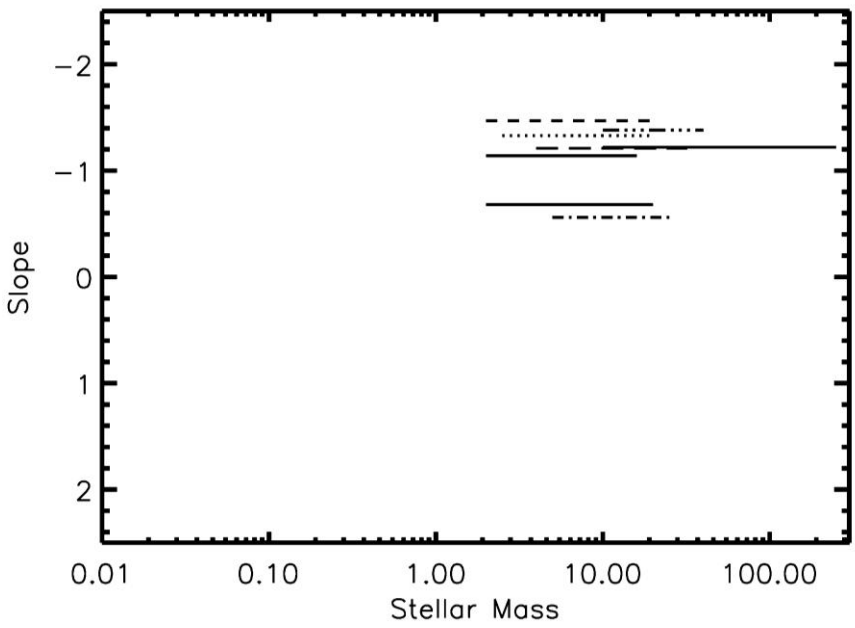

Figure 102 IMF Slope vs. Mass Range

7.1.1. R136

Recent work by Selman et al. (2011) presents the results of a Bayesian analysis of the slope of the IMF in NGC 2070, the central cluster in the Tarantula Nebula or 30 Doradus in the Large Magellanic Cloud (LMC). These authors find a power-law slope of Γ = -1.17+/-0.05, consistent with Salpeter and the results presented here.

7.2. Upper Mass Cut-Off

Figer (2005) find evidence in the Arches cluster for an upper mass cut-off of 150 $M_{\odot}$, by identifying a cliff-like feature in the Arches IMF. This author interpolates the measured IMF (Γ = -0.9) and a Salpeter IMF (Γ = -1.35) beyond 150 $M_{\odot}$ to predict that 33 or 18 stars respectively should be present. The missing population of stars more massive than 150 $M_{\odot}$ firmly support the upper mass cut-off found in Figer (2005).

In addition to the star counting method employed by Figer (2005), Oey & Clarke (2005) make a statistical argument for an upper mass cut-off of 150 $M_{\odot}$, based on a compilation of clusters in the literature, These authors assume a Salpeter-like IMF.

Crowther et al. (2010) suggest the upper mass limit of 150 $M_{\odot}$ is an underestimate, citing evidence for stars in R136 with masses well above this limit. These authors derive higher stellar temperatures than previous estimates, leading to larger bolometric corrections, absolute magnitudes, and larger initial

masses. Though Crowther et al. (2010) disard binarity as a possibility for these "super canonical" mass estimates, see the earlier discussion of R136.

Unfortunately, no cluster in the sample presented here is young enough and massive enough to fully populate the highest mass bins of the IMF. For this reason, no evidence for an upper mass limit, as found in the Arches cluster by Figer (2005), is identified. The cluster R136 appears to contain stars heavier than the canonical upper mass limit of 150 $M_{\odot}$, this can be attributed to binarity or the merger of two very massive stars. Additional investigation of the very massive stars in R136 is required.

8. Future Work

Future work could improve the results presented here and provide a better understanding of many aspects of this project, e.g. X-ray emission from massive stars, modeling of medium resolution spectra, and spectrophotometric monitoring of suspected highly variable stars, to name a few.

8.1. Improved Sample Size

In order to significantly improve on the results presented here, a larger sample of young, massive clusters should be considered. Given the low number of Galactic YMCs predicted and the fairly homogenous metallicity of the Milky Way, expanding the sample to the LMC and SMC would be ideal. The sample should consist of a consistent data set, ideally NIR imaging and follow up NIR spectroscopy. With the upcoming decommissioning of VLT's ISAAC, a suitable replacement for spectroscopy in the south will be required. IRTF/SpeX, Keck/NIRSPEC, and (likely) Gemini N/GNIRS will provide coverage of northern and low southern latitude clusters.

On-going NIR imaging from the VISTA Variables in the Via Lactea (VVV Survey) has identified promising new cluster candidates (e.g. Borissova et al. 2011; Chene et al. 2012). The clusters VVV-Cl073, FSR 1530, [DBS2003] 179 (Borissova et al. 2012), and NGC 6357 (which hosts the massive clusters Pismis 24 and AH03 J1725-344) would be ideal candidates for IMF slope measurement via the treatment presented here. Initial investigation of the PDMF over an intermediate mass range (up to the MS turn-off) for four low to intermediate mass clusters in the VVV survey indicates results consistent, within errors, with the canonical slope of the IMF (Chene et al. 2012). The results of the VVV study are consistent with the results presented for the sample defined here. In one low mass (M_{total}=660+/-150 $M_{\odot}$) cluster,VVV-Cl009, the slope of the PDMF is found to be -0.7+/-0.2, similar to what is found for clusters on the lower mass end of the sample presented here. The age of this cluster is also consistent with Mercer 20 and Mercer 70, 4-6 Myr (Chene et al. 2012). These results suggest that the VVV survey contains a

number of young, potentially massive star clusters hosting MS and evolved massive stars, ideal for inclusion in a larger sample designed to measure the slope of the IMF.

8.2. Improvement of Cluster Membership Determination

Cluster membership is defined through a statistical subtraction in the work presented here. Cool stars observed spectroscopically were removed by hand, as these objects often had no counterpart in the corresponding control field. There are better methods for determining cluster membership of individual stars, including radial velocity measurements and proper motion measurement.

A star's radial velocity can be measured from spectroscopy, as was done for some stars in this project (e.g. Mc30-2, de la Fuente private communication). There will exist some small scatter around an average cluster radial velocity, with non-cluster members lying significantly (greater than 2-3 sigma) away from this average. Obtaining spectra of sufficient resolution and SNR of every star in a cluster is very difficult, especially at the low-mass (photometrically faint) end. Additionally, some clusters in this sample are quite distant (up to 11 kpc), resulting in intrinsically fainter apparent magnitudes.

Proper motion measurements can be obtained by re-observing the same area of the sky at a later point in time. For the most distant clusters, Mercer 30 and Mercer 81, a second epoch of imaging would serve to identify foreground stars. Foreground stars will move farther in the plane of the sky than clusters members, as the foreground population is located closed than the clusters. Identifying common motions in the somewhat closer clusters allows for determination of cluster membership. Proper motion measurements are somewhat flawed, however. In all cases, cluster stars and fore- and background stars, some subset of objects will not move in the plane of the sky, but towards or away from the observer.

Combing proper motion measurements with radial velocity measurements is the best way to constrain cluster membership for stellar clusters. While statistical subtraction of likely fore- and background stars is reliable method for the purpose of this work, improvements can be made.

8.3. Investigation of Mass Segregation

Wide-field NIR imaging extending well beyond the NIC3 field of view around Mercer 70 and Mercer 20 would be ideal to investigate the nature of the full spatial extent of these clusters. Evidence for mass segregation can be identified in the form of a radially varying Γ or via construction of a radial mass function, containing information beyond what can be found in a radial density distribution. Given the high density of, extinction towards, and position on the sky of Mercer 20 and Mercer 70, the best telescope/instrument combination for follow-up would be Keck II/NIRC2 for Mercer 20 and VLT/NACO for Mercer 70. Mosaicked imaging would be required in order to cover a large enough field to properly

characterize the spatial extend of both clusters. Control fields at different locations than the HST/NIC3 control fields are required.

8.4. X-ray follow-up

Three clusters in this sample are prime targets for X-ray observations. Successful identification of point sources associated with massive stars in Danks 1, Danks 2, and Mercer 81 are discussed earlier in this work, proving the usefulness of X-ray follow-up. Likely colliding wind binaries are identified in these clusters, which will be the subject of future papers. X-ray follow-up observations of Mercer 20, Mercer 30, and Mercer 70 are warranted. These three clusters are likely to contain X-ray emitting objects, e.g. soft X-ray emission from single O stars, hard X-ray emission from CWBs, non-thermal emission from post-SN stellar remnants. Identifying CWB MS stars will allow for a better IMF slope measurement. The age of all three clusters argues for post-SN state, allowing for the identification of a lower limit on the mass of any post-SN stellar remnants, as is done for the magnetar in Westerlund 1 by Muno et al. (2006) and for SGR1900+14 by Davies et al. (2009).

In order to truly justify follow-up observations of other clusters, a more robust X-ray analysis of the Chandra X-ray Observatory (CXO) observations of Mercer 81 and the G305 star forming complex are required. For Mercer 81, the large distance to the cluster and high extinction impede the collection of large numbers of X-ray photons. For Danks 1 and Danks 2, however, the observations contain enough incident photons that low resolution spectral analysis is possible. The G305 star forming region hosts other massive stars coincident with thermal X-ray emission. Preliminary analysis (See DATA ANALYSIS section) reveals thermal emission lines consistent with hot plasmas for sources in Danks 1 and "halo" sources selected on basis of known spectral type. Further spectral modeling of each source is required to determine if the hot plasma component is the result of self-shocking in clumpy winds or shocks from colliding wind binaries. No evidence for non-thermal emission is found in sources in Danks 1 or Mercer 81 (note that Danks 2 lies on the CXO/ACIS chip gap).

Identification of strong X-ray point sources with no infrared counterpart is the first step in locating post-SN stellar remnants. For Mercer 81, no such sources have been identified. For the G305 complex, the situation is complicated by ongoing star formation at the periphery of the cavity excavated by the two central clusters, which hosts many pre-MS stars (known to be strong, variable X-ray sources).

8.5. FS CMa Stars

Mc70-14 is identified as a rare class of B[e] star, a FS CMa object. Mercer 20 hosts a spectroscopically similar object, Mc20-16, while Mercer 81 contains a photometrically similar star, Mc81-28, which has no spectroscopic information available at this time. These objects are the subject of a recent VLT/ISAAC

proposal aimed at studying FS CMa stars belonging to coeval populations, in order to determine the evolutionary phase of these enigmatic objects.

An archive search for photometrically similar objects in other young massive clusters using HST filters and ground-based narrow-band filters could prove fruitful in identifying additional FS CMa stars for follow-up spectroscopy. Follow-up spectroscopic observations of any candidate FS CMa stars belonging to clusters, beyond those identified here which are part of the aforementioned VLT/ISAAC proposal, would be highly useful in providing statistical constraints on the expected number of these B[e] stars, ideally for predicting how many of these stars should exist in the Milky Way.

8.6. DB9 and the Surrounding Medium

The discovery of the B[e] star in DB9, including the spectrum and photometry, will be the subject of a letter to a refereed journal (e.g. The Astrophysical Journal). As evidenced by Figure 64, DB9 lies near the center of a complex, IR bright region. It is possible that the dusty nebula surrounding DB9 was formed over the course of the evolution of the central star, DB9-1, as it shed its outer layers in the slow, dense winds of a red supergiant phase (Kastner et al. 2006). Another very bright IR point source exists to the southwest of DB9-1, potentially an embedded OB star or small cluster. Spectroscopy of the point-source population in this region is vital to understanding the evolutionary status of the B[e] star DB9-1. Follow-up observations of stars in the region around DB9 will be the subject of an IRTF/SpeX proposal for Semester 2013B.

IRTF/SpeX spectra of stars in DB9 contain multiple diffuse interstellar bands (DIBs), many of which are common to the CygOB2 region. Closer examination of DIBs in DB9, especially the measurement of the EW of each identified DIB, and comparison with the EW and shape of DIBs in CygOB2 spectra are required for determining if these two regions are located aat the same distance, as is assumed in this work. The IRTF/SpeX library can be searched for spectra of objects in the CygOB2 association in order to make the best measurements of the EW of DIBs in the 0.8-2.4 micron spectral range possible.

Modeling of the spectral energy diagram of DB9-1 will provide additional clues to the history of this object and a better understanding of the B[e] phenomenon. Ideally, a computation of dust mass in nebula/bubble will allow for an estimate of the mass lost during the red supergiant phase.

8.7. Modeling and Spectra

In order to expand the IMF slope measurement beyond the main sequence turn off, CMFGEN grid modeling then detailed modeling of spectroscopically observed hot stars in each cluster can be used to determine the parameters (including initial mass) of evolved objects.

Radial velocity measurements for each spectroscopically observed hot star in each cluster provide a much more robust constraint on the distance to each cluster than spectrophotometric distance estimates. This method is outlined in Davies et al. 2007 (see their Figure 7) and is used to determine the distance to Cl 1900+14 (Davies et al. 2009), Mercer 81 (Davies et al. 2012a), and the Danks 1 and 2 clusters (Davies et al. 2012b) by adopting the Galactic rotation curve of Brand & Blitz (1993).

The IRTF/SpeX spectral atlases for cool stars (Cushing et al. 2005; Rayner et al. 2009) provide an excellent source for spectral classification of cool stars observed by IRTF/SpeX for this work. Comparison of the spectra of cool stars in Mercer 17 and [BDS2003] 52 to template stars from the IRTF/SpeX atlases will allow for the determination of both spectral type and luminosity class. If it is possible to determine radial velocity offsets, distances to these cool stars will also be established. For [BDS2003] 52, it will be possible to determine if the cool star population represents a pre-MS belonging to the cluster or characterizes the fore- and background contamination towards the cluster. For Mercer 17, spectral typing of observed stars will be the deciding factor in determining if Mercer 17 is a bona fide (but somewhat dispersed) cluster or a chance stellar over-density along the line of sight.

8.8. R136

Dedicated photometric/spectroscopic monitoring of the central stars in R136 to search for variability is highly recommended. Long base-line, months to years, monitoring would most beneficial as the X-ray properties are consistent with a large separation but still unresolved binary population. This is partially ongoing as part of the VLT FLAMES Tarantula Survey (Evans et al. 2011), but does not include R136-a1.

9. References

Aareseth, S. J. & Hills, J. G., 1972, A&A, 255

Ascenso, J., Alves, J., Vicente, S., & Lago, M. T. V. T., 2007a, A&A, 476, 199

Ascenso, J., Alves, J., Beletsky, Y., & Lago, M. T. V. T., 2007b, A&A, 466, 137

Banerjee, S., Kroupa, P., & Oh, S., 2012a, ApJ, 746, 15

Banerjee, S., Kroupa, P., & Oh, S., 2012b, MNRAS, 426, 1416

Bartko et al. 2010, ApJ, 708, 834

Bastian, N., Covey, K. R., & Meyer, M. R., 2010, ARA&A, 48, 339

Beech, M. & Mitalas, R., 1994, ApJS, 95, 517

Benjamin, R. A., et al. 2003, PASP, 115, 952

Bestenlehner, J. M., et al. 2011, A&A, 520, 14

Bica, E., Dutra, C. M., Soares, J., & Barbuy, B., 2003, A&A, 404, 223

Borissova, J., Ivanov, V. D., Minniti, D., Geisley, D., & Stephens, A. W., 2005, A&A, 435, 95

Borissova, J., et al., 2011, A&A, 532, 131

Borissova, J.,Georgiev, L., Hanson, M. M., Clarke, J. R. A., Kurtev, R., Ivanov, V. D., Penaloza, F., Hillier, D., J., & Zsargo, J., 2012, A&A, 546, 110

Brand, J. & Blitz, L., 1993, A&A, 275, 67

Brandner, W., Clark, J. S., Stolte, A., Waters, R., Negueruela, I., & Goodwin, S. P., 2008, A&A, 478, 137

Bressert, E., et al., 2012, A&A, 542, 49

Brott, I., de Mink, S. E., Cantiello, M., Langer, N., de Koter, A., Evans, C. J., Hunter, I., Trundle, C., Vink, J. S. 2011, A&A, 520, 115

Campbell, M. A., Evans, C. J., Mackey, A. D., Gieles, M., Puls, J., Ascenso, J., Bastian, N., & Longmore, A. J., 2010, MNRAS, 405, 421

Carney, B.W., Lee, J.-W., & Dodson, B., 2005, AJ, 129, 656

Chene, A.-N ., et al., 2012, A&A, 545, 54

Chlebowski, T. & Garmany, C. D. 1991, APJ, 368, 241

Clark, J. S., Muno, M. P., Negueruela, I., Doughert, S. M., Crowther, P. A., Goodwin, S. P., & de Grijs, R., 2008, A&A, 477, 147

Clark, J. S., Negueruela, I., Davies, B., Larionov, V. M., Ritchie, B. W., Figer, D. F., Messineo, M., Crowther, P. A., & Arkharov, A. A., 2009, A&A, 498, 109

Clark, J. S. & Steele, I. A., 2000, A&AS, 141, 65

Clarke, C. J. & Pringle, J. E., 1992, MNRAS, 255, 423

Clarke, C. J. & Bonnell, I A., 2008, MNRAS, 388, 1171

Cohen et al. 2011, MNRAS accepted (arXiv1104.4786)

Crockett, R. M., et al. 2008, MNRAS, 391L, 5

Crowther, P. A., Hadfield, L. J., Clark, J. S., Negueruela, I., & Vacca, W. D., 2006, MNRAS, 372, 1407

Crowther et al. 2010, MNRAS, 408, 731

Cushing, M. C., Rayner, J. T., & Vacca, W. D., 2005, ApJ, 623, 115

Cushing, M. C., Vacca, W. D., & Rayner, J. T., 2004, PASP, 116, 362

Cyganowski, C. J., et al., 2008, AJ, 136, 2391

Davies, B., Figer, D. F., Kudritzki, R.-P., MacKenty, J., Najarro, F., & Herraro, A., 2007, ApJ, 671, 781

Davies, B., Figer, D. F., Law, C. J., Kudritzki, R.-P., Najarro, F., Herraro, A., &MacKenty, J. W., 2008, ApJ, 676, 1016

Davies, B., Figer, D. G., Kudritzki, R.-P., Trombley, C. Kouveliotou, C., Wachter, S., 2009, ApJ, 707, 844

Davies, B., Clark, J. S., Trombley, C., Figer, D. F., Najarro, F., Crowther, P. A., Kudritzki, R.-P., Thomspon, M., Urquhart, J. S., & Hindson, L., 2012b, 419, 1871

Davies, B., de la Fuente, D., Najarro, F., Hinton, J. A., Trombley, C., Figer, D. F., & Puga, E., 2012a, MNRAS, 419, 1860

de la Fuente, D., Najarro, F., Davies, B., & Figer, D. F., 2012, Highlights of Spanish Astrophysics VII (arXiv:1210.1781)

de Wit, W. J., Testi, L., Palla, F., Vanzi, L., & Zinnecker, H. ,2004, A&A, 425, 937

de Wit, W. J., Testi, L., Palla, F., & Zinnecker, H., 2005, A&A, 437, 247

Do, T., et al., 2013, ApJ accepted (arXiv:1301.0539)

Drew, J. E., et al., 2005, MNRAS, 362, 753

Dutra, C. M. & Bica, E., 2001, A&A, 376, 434

Dutra, C. M., Bica, E., Soares, J., & Barbuy, B., 2003, A&A, 400, 533

Eckstrom, S., et al., 2012, A&A, 537, 146

Eddington, A. S., 1926, The Internal Constitution of Stars

Evans, C. J., et al., 2011, A&A, 530, 108

Fanaroff, B. L. & Riley, J. M., 1974,MNRAS, 167, 31

Figer, D. F., 2005, Nature, 434, 192

Figer, D. F., McLean, I. S., & Najarro, F., 1997, ApJ, 486, 420

Figer, D. F., McLean, I. S., & Morris, M., 1999a, ApJ, 514, 202

Figer, D. F., Morris, M., Geballe, T. R., Rich, R. M., Serabyn, E., McLean, I. S., Puetter, R. C., & Yahil, A., 1999b, ApJ, 525, 759

Figer, D. F., et al., 2002, ApJ, 581, 258

Figer, D. F., MacKenty, J. W., Robberto, M., Smith, K., Najarro, F., Kudrizki, R.-P., & Herrero, A., 2006, ApJ, 643, 166

Fich, M. & Blitz, L., 1984, ApJ, 279, 125

Ferraro , F. R., Montegriffo, P., Origlia, L., & Fusi Pecci, F., 2000, AJ, 119, 1282

Froebrich, D. & Ioannidis, G., 2011, MNRAS, 418, 1375

Froebrich, D., Scholz, A., & Raftery, C. L., 2007, MNRAS, 374, 399

Frogel , J. A., Persson, S. E., & Cohen, J. G., 1981, ApJ, 246, 842

Gagne, M., Sksala, M. E., Cohen, D. H., Tonnesen, S. K., ud-Dula, A., Owocki, S. P., Townsend, R. H. D., & MacFarlane, J. J., 2005, ApJ, 628, 986

Gagne et al. 2011, arXiv1103.1149

Georgy, ., Eckstrom, S., Meyney, G., Massey, P., Levesque, E. M., ,Hirschi, R., Eggenberger, P., & Maeder, A., 2012, A&A, 542, 29

Gies, D. R., 1987, ApJS, 64, 545

Groh, J. H., Meynet, G., & Eckstrom, S., 2013, A&A, 550, 7

Gvaramadze, V. V., Kniazev, A. Y., Kroupa, P. & Oh, S. 2011, A&A, 535, 29

Habibi, M., Stolte, A., Brandner, W., Hu(beta)mann, B., & Motohara, K., 2012, A&A submitted (arXiv:1212.3355)

Hamaguchi, K., et al. 2007, ApJ, 663, 522

Hamaguchi, K., et al., 2010, AIPC, 1248, 17

Hanson, M. M., Kudritzki, R.-P., Kenworthy, M. A., Puls, J., & Tokunaga, A. T., 2005, ApJS, 161, 154

Hanson, M. M., Kurtev, R., Borissova, J., Georgiev, L., Ivanov, V. D., Hillier, D. J., & Minniti, D., 2010, A&A, 516, 35

Hanson, M. M. & Popescu, B.,.2008, IAUS, 250, 307

Harayama, Y., Eisenhauer, F., & Martins, F. 2008, ApJ, 675, 1319

Harfst, S., Portegies Zwart, S., & Stolte, A., 2010, MNRAS, 409, 628

Henkel, Gueten & Haschick 1986

Hillier, D. J. & Miller, D. L., 1998, ApJ, 496, 407

Hoare, M. G. et al. 2005, IAUS, 227, 370

Hunter, D. A., O'Neil, E. J., Lynds, R., Shaya, E. J., Groth, E. J. & Holtzman, J. A. 1996, ApJ, 459, 27

Ivanov, V., 2010, JENAM, 135

Kashi & Soker 2010, ApJ, 723, 602

Kastner, J. H., Buchanan, C. L., Sargent, B., & Forrest, W. J., 2006, ApJ, 638, 29

Kleinmann, S. G. & Hall, D. N. B., 1986, ApJS, 62, 501

Knodlseder, J., 2000, A&A, 360, 539

Koen, C., 2006, MNRAS, 367, 1735

Kroupa, P., 2002, Science, 295, 82

Kroupa, P., 2001, MNRAS, 322, 231

Kroupa, P., 2005, Nature, 434, 148

Kogure, T. 2009, ASPC, 404, 212

Kuchinski, L. E., Frogel, J. A., Terndrup, D. M., & Persson, S. E., 1995, AJ, 109, 1131

Kurtev, R., Borissova, J., Georgiev, L., Ortolani, S., & Ivanov, V. D., 2007, A&A, 475, 209

Kurucz, R. L., 1991, Solar interior and atmosphere, 663

Lada, C. J. & Lada, E. A., 2003, ARA&A, 41, 57

Lemiere, A., Slane, P., Gaensley, B. M., & Murray, S. 2009, ApJ, 706, 1269

Leonard, P. J. T. & Duncan, M. J., 1990, AJ, 99, 608

Longmore, A. J., Kurtev, R., Lucas, P. W., Frobrich, D., de Grijs, R., Ivanov, V. D., Maccarone, T. J., Borissova, J., & Ker, L. M., 2011, MNRAS, 416, 465

Lu, J. R., Do, T., Ghez, A. M., Morris, M. R., Yelda, S., & Matthews, K., 2013, ApJ accepted (arXiv:1301.0540)

Lucas, P. W., et al., 2008, MNRAS, 391, 136

Maeder, A. & Meynet G.,1988, A&AS, 76, 411

Maeder, A. & Meynet, G., 1994, A&A, 287, 803

Maeder, A. & Meynet,G., 2000, ARA&A, 38, 143

Maeder, A. & Meynet, G., 2003, A&A, 422, 225

Marsh Boyer, A. N., McSwain, M. V., Aragona, C., & Ou-Yang, B. 2012, AJ, 144, 158

Maiz Apellaniz, J. & Ubeda, L., 2005, ApJ, 629, 873

Maiz Apellaiz, J., Walborn, N. R., Morrell, N. I., Niemela, ,V. S., & Nelan, E. P., 2007, ApJ, 660, 1480

Martins, F. & Plez,B., 2006, A&A, 457, 637

Martins, F., Genzel, R., Hillier, D. J., Eisenhauer, F., Paumard, T., Gillessen, S., Ott, T., & Trippe, S., 2007, A&A, 468, 233

Massey, P., 1998, ASPC, 142, 17

Massey, P., 2003, ARA&A, 41, 15

Massey, P. & Hunter, D. A., 1998, ApJ, 493, 180

Massey, P., Johnson, K.E., & Degioia-Eastwood, K., 1995a, ApJ, 454, 151

Massey, P., Lang, C. C., Degioia-Eastwood, K., & Garmany, C. D., 1995b, ApJ, 438, 188

Mauerhan, J. C., Van Dyk, S. D., & Morris, P. W., 2011, AJ, 142, 40

Mercer, E. P., et al., 2005, ApJ, 635, 650

Messineo M., Davies, B., Ivanov, V. D., Figer, D. F., Schuller, F., Habin, H. J., Menten, K. M., & Petr-Gotzens, M. G., 2009, ApJ, 697, 701

Miroshnichenko, A. S., 2007, ApJ, 667, 497

Miroshnichenko, A. S., et al., 2009, ApJ, 700, 209

Moffat et al. 2002, ApJ, 573, 191

Morris, P. W., Eenens, P. R. J., Hanson, M. M., Conti, P. S., & Blum, R. D., 1996, ApJ, 470, 597

Muno, M., et al., 2006, ApJ, 636L, 41

Nayakshin, S. & Sunyaev, R., 2005, MNRAS, 364L, 23

Negueruela, I., Gonzalez-Fernandez, C., Marco, A., Clark, J. S., & Martinez-Nunez, S., 2010, A&A, 513, 74

Oey, M. S., 1996, ApJ, 465, 231

Oey, M. S. & Clarke, C. J., 2005, ApJ, 620, L43

Oey, M. S., King, N. L., & Parker, J. W. 2004, AJ, 127, 1632

Oey, M. S. & Massey, P., 1995, ApJ, 452, 210

Oskinova, L. M., Ignace, R., Hamann, W.-R., Pollock, A. M. ., & Brown, J. C., 2003, A&A, 402, 7550

Pang, X, et al. 2012, ApJ accepted (arXiv:1212.4566)

Parker, J. W. 1992, PASP, 104, 1107

Pflamm Altenburg , J. & Kroupa, P., 2006, MNRAS, 373, 295

Pittard & Stevens ,2002, A&A, 388, L20

Portegies Zwart, S. F., Makino, J., McMillan, S. L. W., & Hut, P., 1999, A&A, 117

Portegies Zwart, S. F., Pooley, & Lewin 2002, ApJ, 574, 762

Poveda, A., Ruiz, J., & Allen, C., 1967, BOTT, 4, 86

Rayner, J. T., Cushing, M. C., & Vacca, W. D., 2009, ApJS, 185, 289

Richards, E. E., Lang, C. C., Trombley, C., & Figer, D. F., 2012, AJ, 144, 89

Rieke, G. H., Rieke, M. J., & Paul, A. E., 1989, ApJ, 336, 752

Rogers , F. J. & Iglesia, C A., 1994, Science, 261, 50

Russeil, D., Adami, C., & Georgelin, Y. M., 2007, A&A, 470, 161

Salpeter, E. E., 1955, ApJ, 121, 161

Sana H., et al., 2012, A&A accepted (arXiv:1209.4638)

Scalo, J. M., 1998, Fundamentals of Cosmic Physics, 11, 1

Schaerer, D., Meynet, G., Maeder, A., & Schaller, G., 1993, A&AS, 98, 523

Schaller, G., Schaerer, D., Meynet, G., Maeder, A.,1992, A&AS, 96, 269

Schnurr et al. 2008, MRNAS, 389L, 38

Selman, F. J., Espinoza, P., & Melnick, J., 2011, ASPC, 440, 39

Shara, M. M., Moffat, A. F. J., Gerke, J., Zurek, D., Stanonik, K., Doyon, R., Artigau, E., Drissen, LK, Villar-Sbaffi, A., 2009, AJ, 138, 402

Shekov, S. A., Gagne, M., & Skinner, S. L. 2011, ApJ, 727,17

Skinner, S. L., Zhekov, S. A., Gudel, M., SChmutz, W., & Sokal, K. R., 2010, AJ, 139, 825

Skrutskie, R. M., et al. 2006, AJ, 131, 1163

Snell, R. L. & Bally, J., 1986, ApJ, 303, 683

Stothers, R. B., 1992, ApJ, 391, 706

Steele, I. A. & Clark, J. S., 2001, A&A, 371, 642

Stevens et al. 1992, ApJ, 386, 265

Strader, J. & Kobulnicky, H. A., 2008, AJ, 136, 2102

Stolte, A., 2003, PhDTh

Townsley, L. K., 2009, AIPC, 1165, 225

Townsley et al. 2006, ApJ, 131, 2164

Townsley et al. 2011, ApJ, 194, 16

Urquhart, J. S., Busfield, A. L., Hoare, M. G., Lumsden, S. L., Clarke, A. J., Moore, T. J. T., Mottram, J. C., Oudmaijer, R. D. 2007a, A&A, 461, 11

Urquhart, J. S., Busfield, A. L., Hoare, M. G., Lumsden, S. L., Oudmaijer, R. D., Moore, T. J. T., Gibb, A. G., Purcell, C. R., Burton, M. G., Marechal, L. J. L. 2007b, A&A, 474, 891

Vacca, W. D., Garmany, C. D. & Shull, J. M. 1996,ApJ, 460, 914

Valenti, E., Ferraro, F. R., & Origlia, L., 2004, MNRAS, 354, 815

Valenti , E., Ferraro, F. R., & Origlia, L., 2007, AJ, 133, 1287

Vink, J. S., 2006, ASPC, 353, 113

Vink, J. S., de Koter, A., & Lamers, H. J. G. L. M., 2000, A&A, 362, 295

Vink, J. S., de Koter, A., & Lamers, H. J. G. L. M., 2001, A&A, 369, 574

Vink, J. S., Muijers, L. E., Anthonisse, B., de Koter, A., Grafner, G., & Langer, N., 2011, A&A, 521, 132

Weidner, C. & Kroupa, P., 2004, MNRAS, 348, 187

Whitmore, B. C., Zhang, Q., Leitherer, C. et al. 1999, AJ, 118, 1551

Wright, N. J. & Drake, J. J., 2009, proceedings of IAU Symposium 266 (arXiv:0909.4613)

Zavagno, Deharveng & Caplan 1994

Zhu, Q., Davies, B., Figer, D. F., & Trombley, C., 2009, ApJ, 702, 929

Zinnecker, H. & Yorke, H. W., 2007, ARA&A, 45, 481

10. Appendix A: HST/NIC3 Images

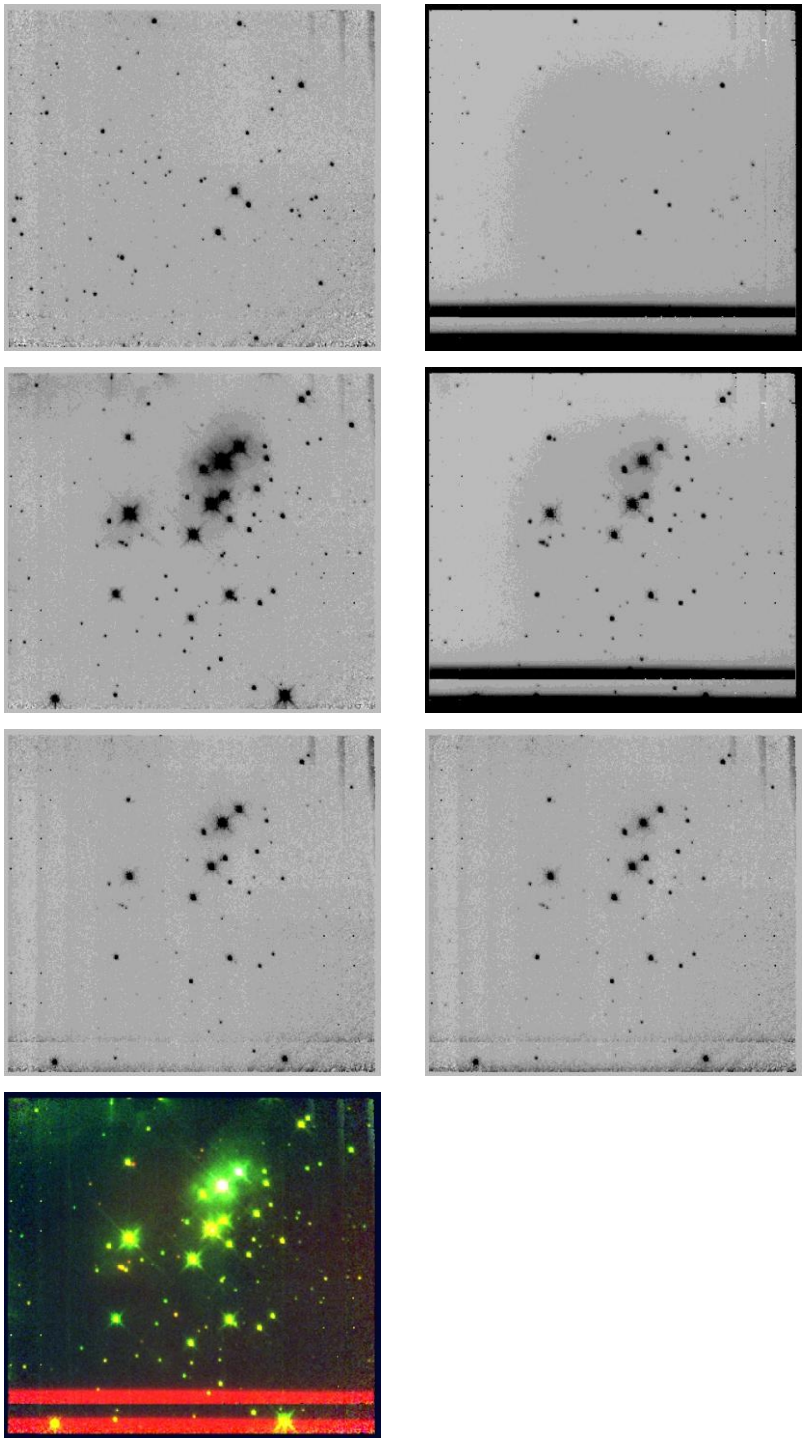

Figure 103 [DB2001] Cl 20; from top left to bottom right: F160W control field, F222M control field, F160M target field, F222M target field, F187N target field, F190N target field, 3-color HST image (F222M in red, F160W in green, and F187N-F190N in blue)

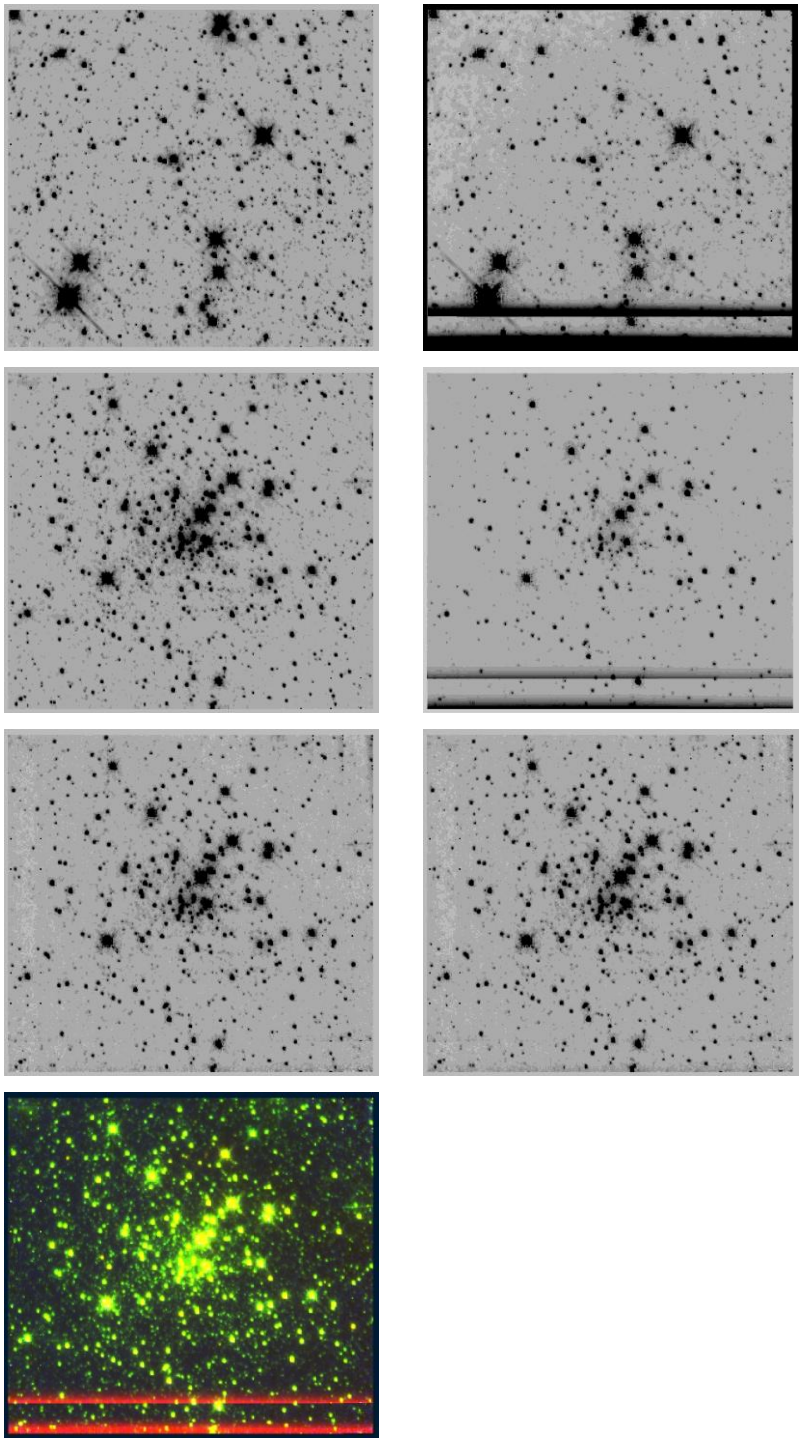

Figure 104 Mercer 5, panels are the same as Figure 103

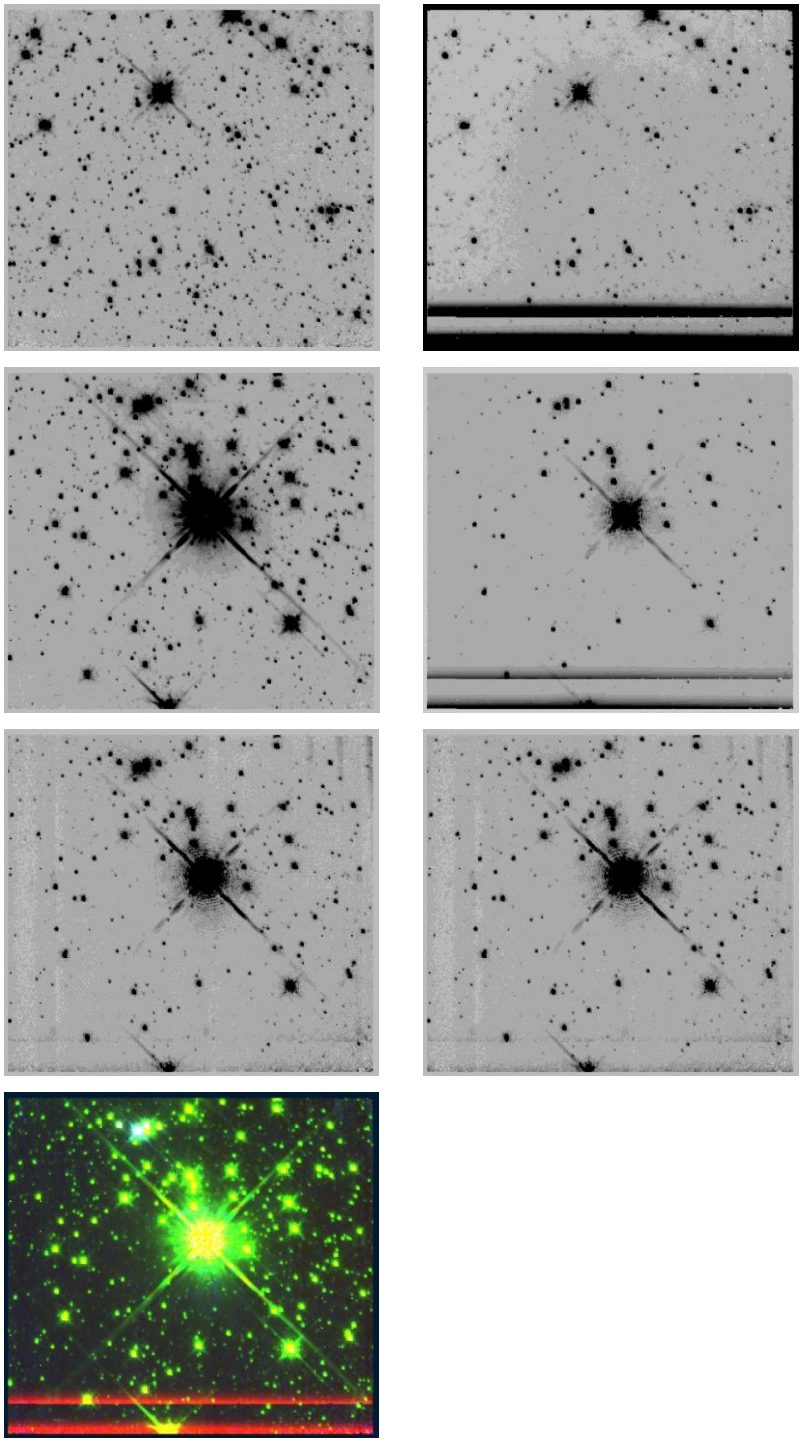

Figure 105 Mercer 20, panels are the same as Figure 103

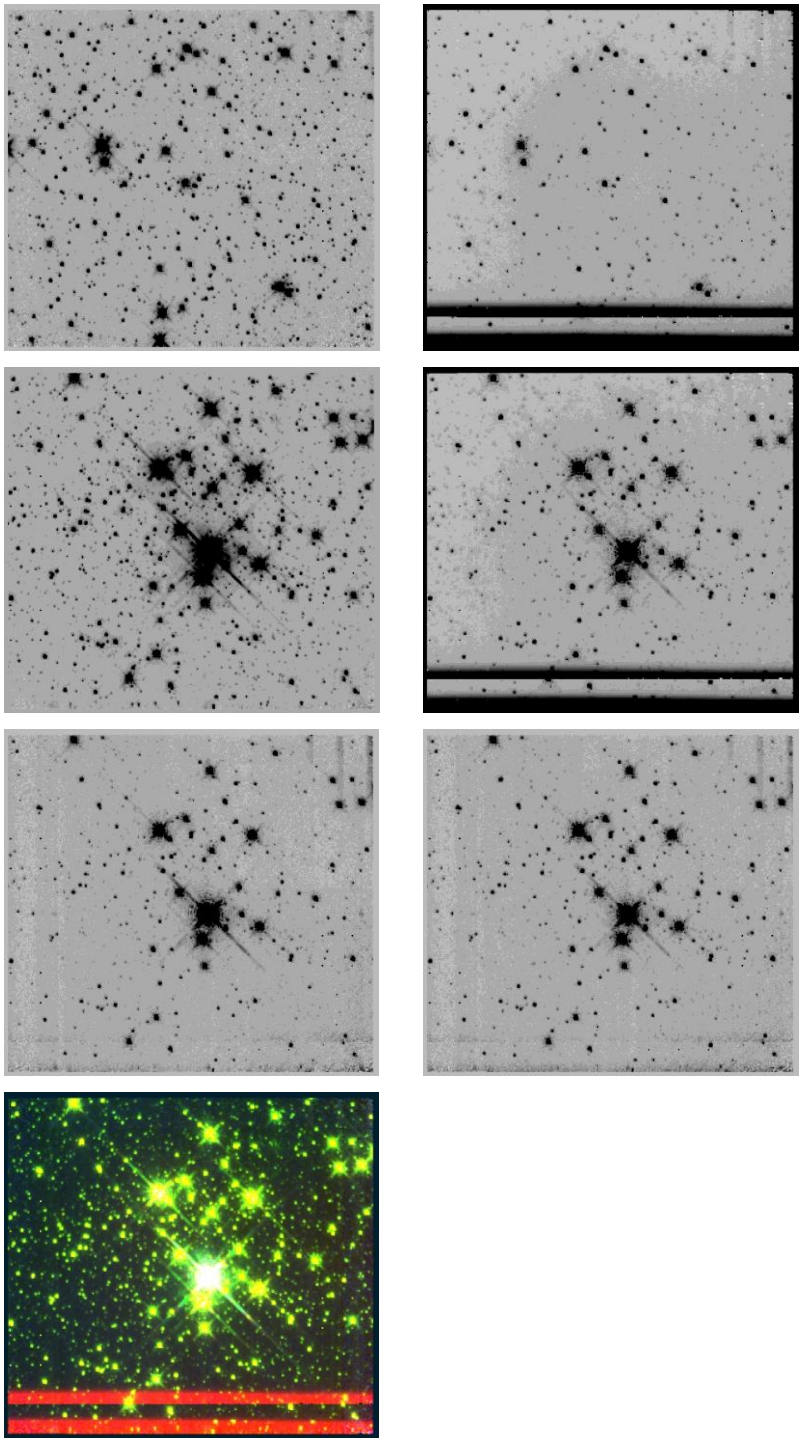

Figure 106 Mercer 23, panels are the same as Figure 103

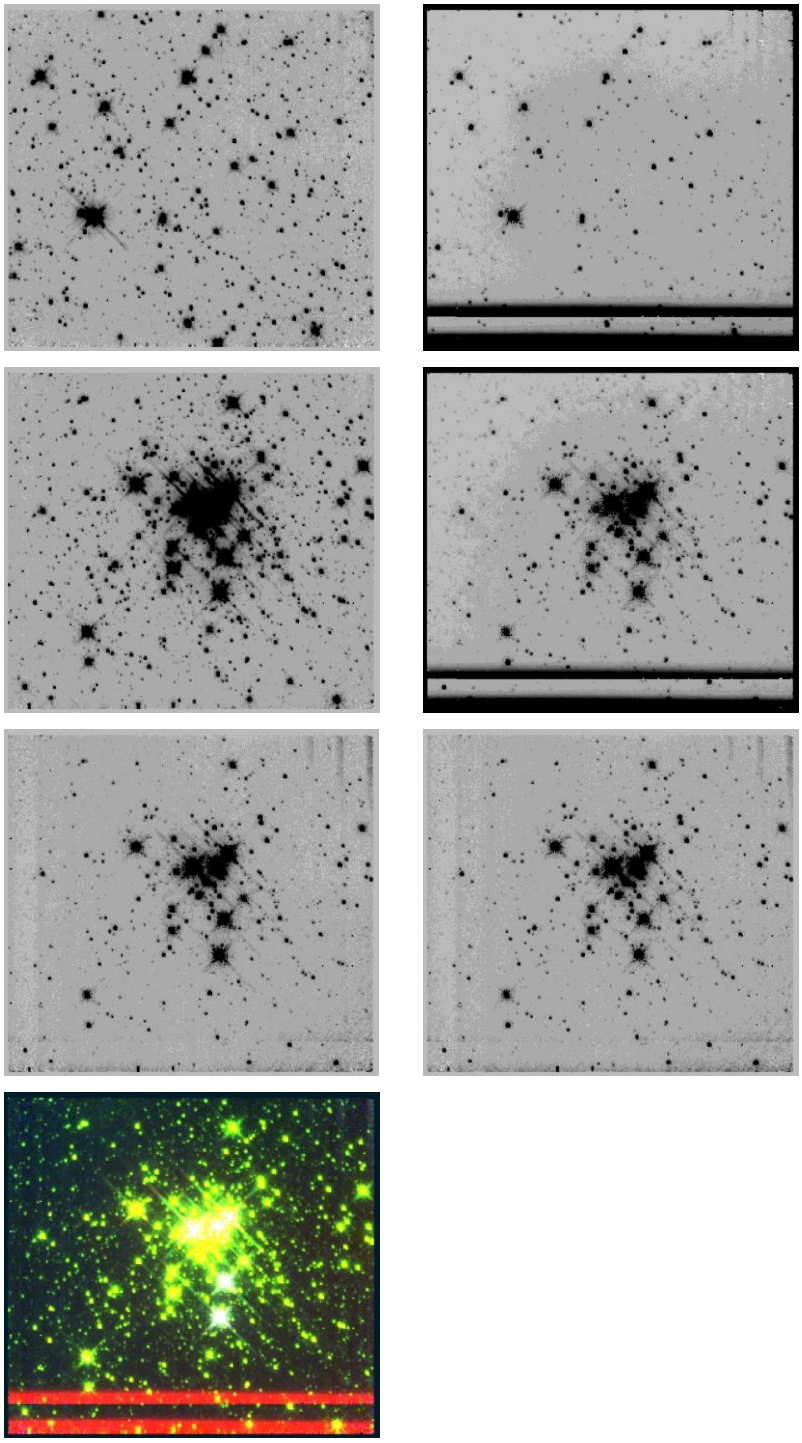

Figure 107 Mercer 30, panels are the same as Figure 103

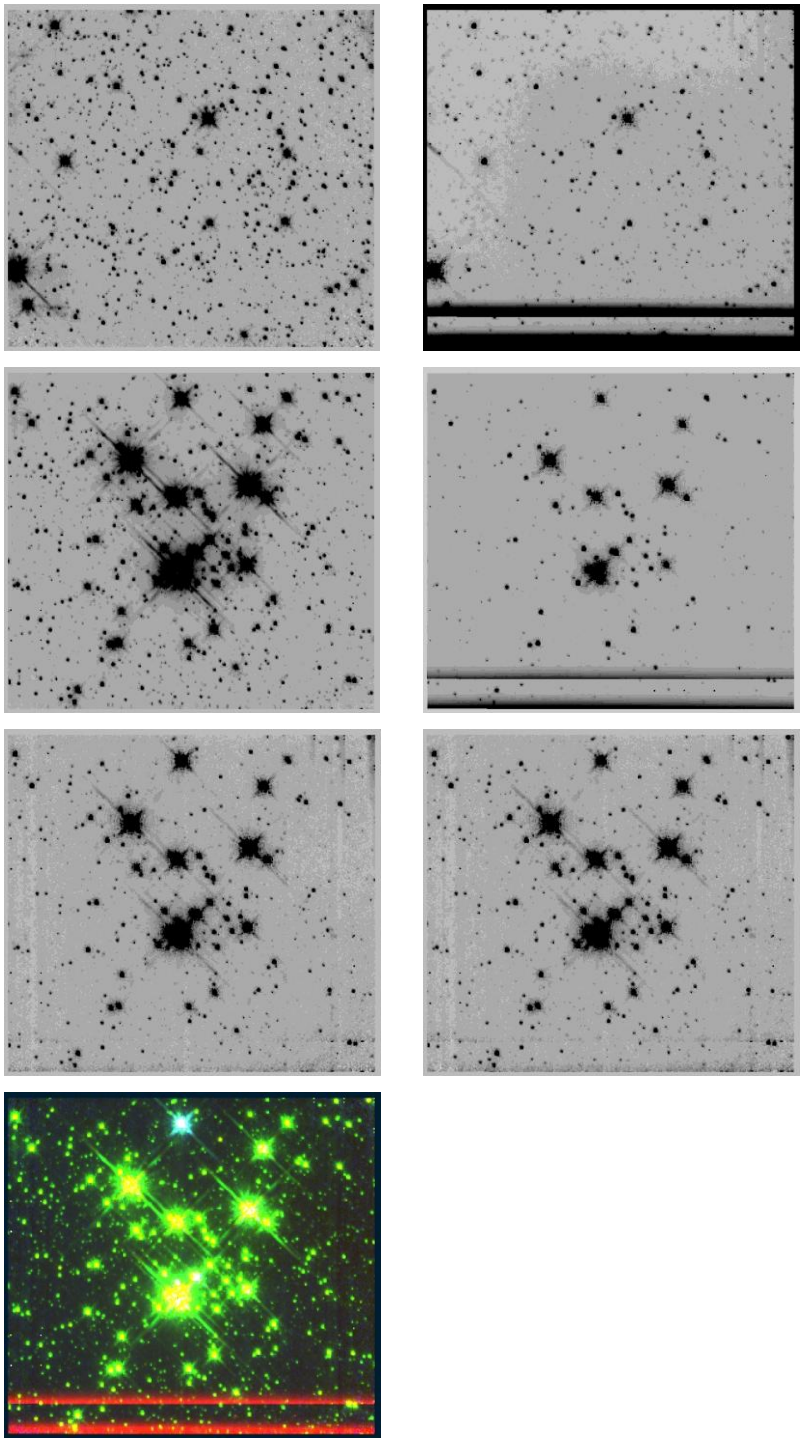

Figure 108 Mercer 70, panels are the same as Figure 103

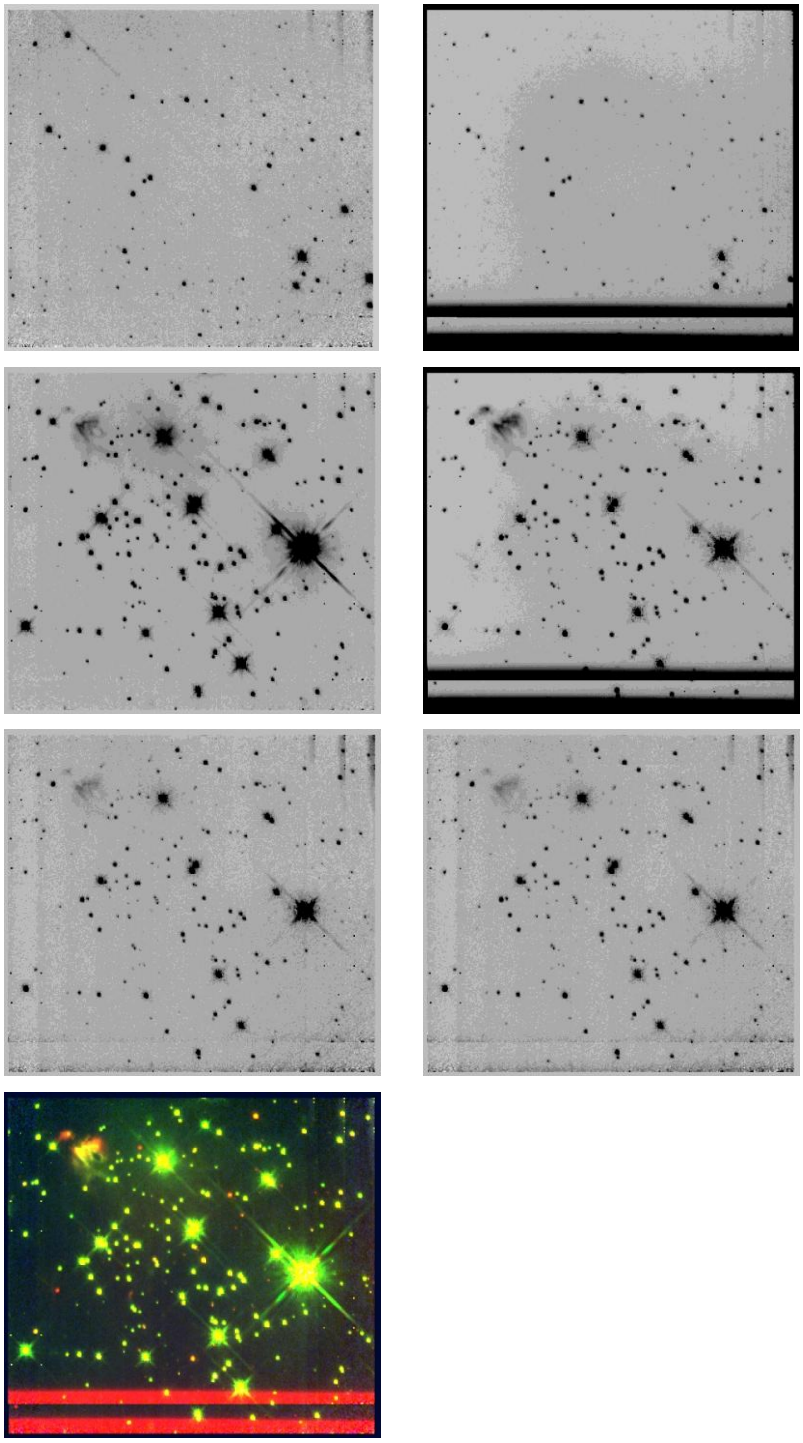

Figure 109 Mercer 14, panels are the same as Figure 103

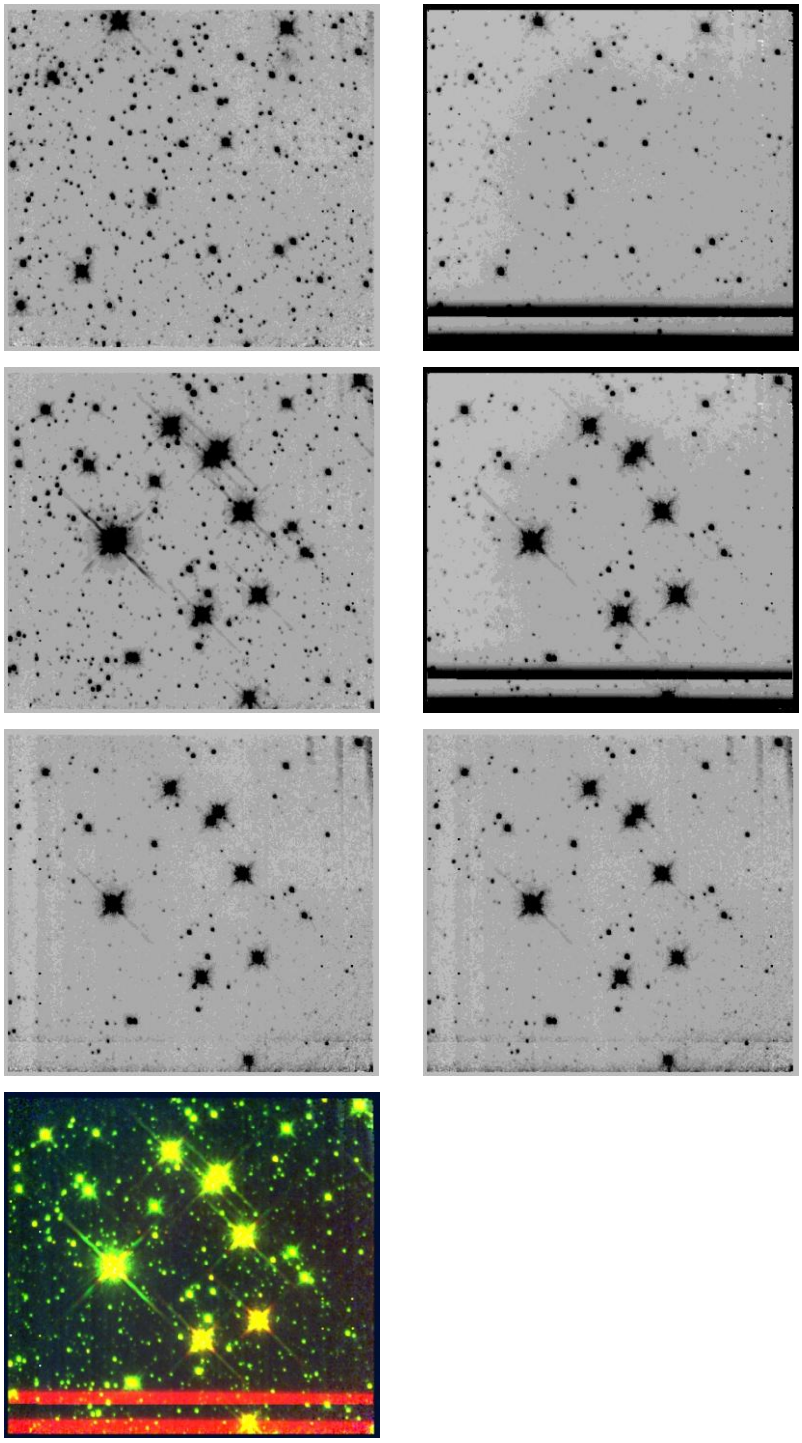

Figure 110 Mercer 17, panels are the same as Figure 103

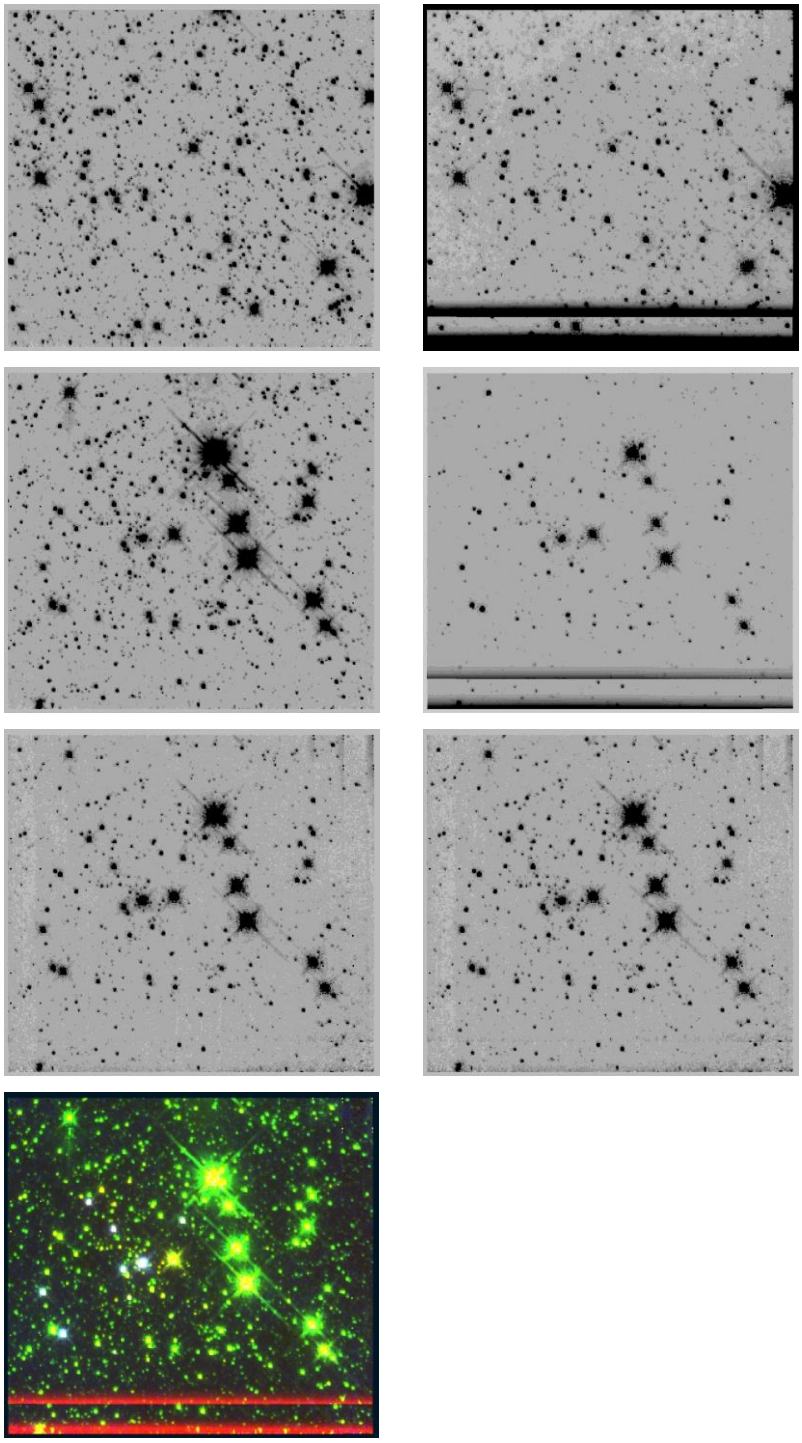

Figure 111 Mercer 81, panels are the same as Figure 103

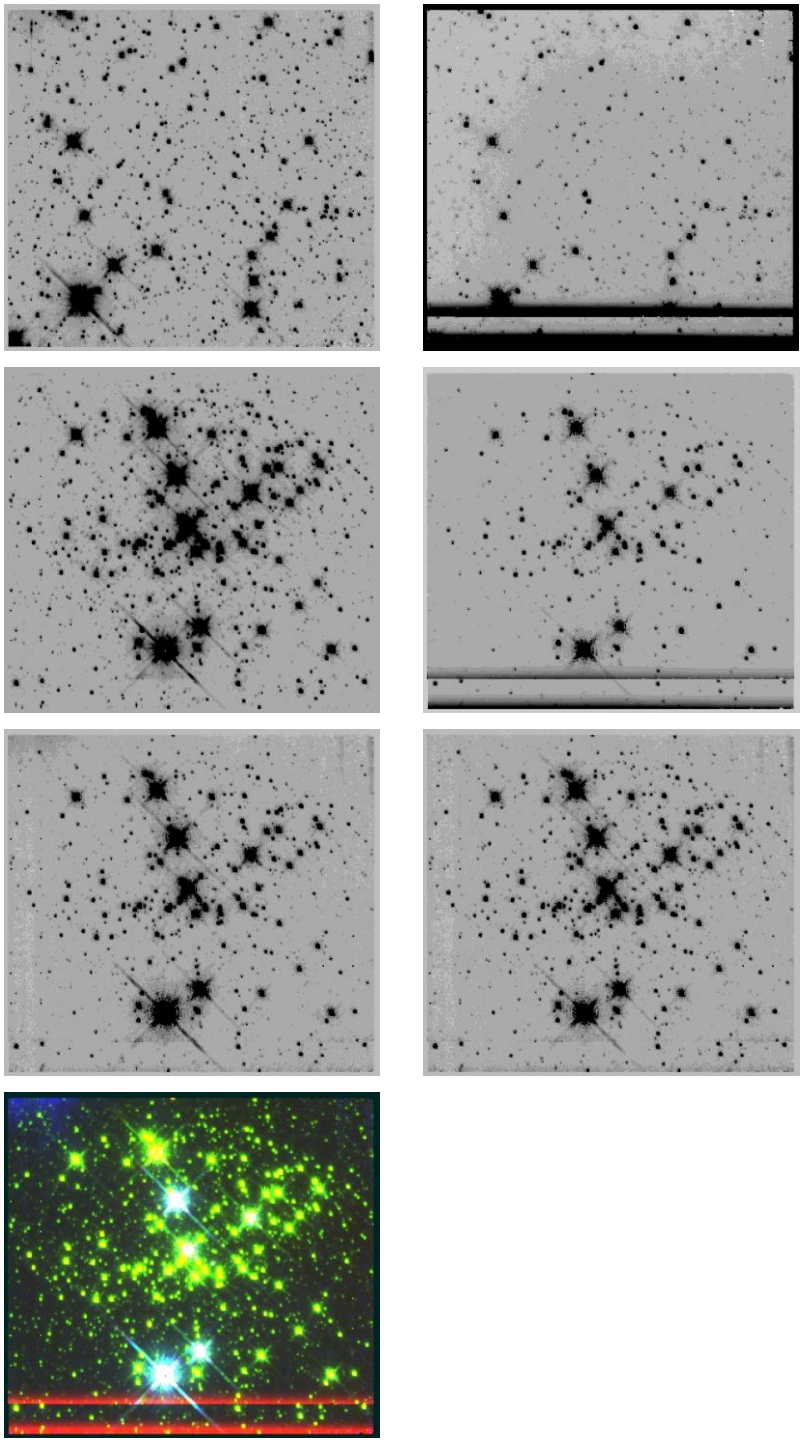

Figure 112 Danks 1, panels are the same as Figure 103

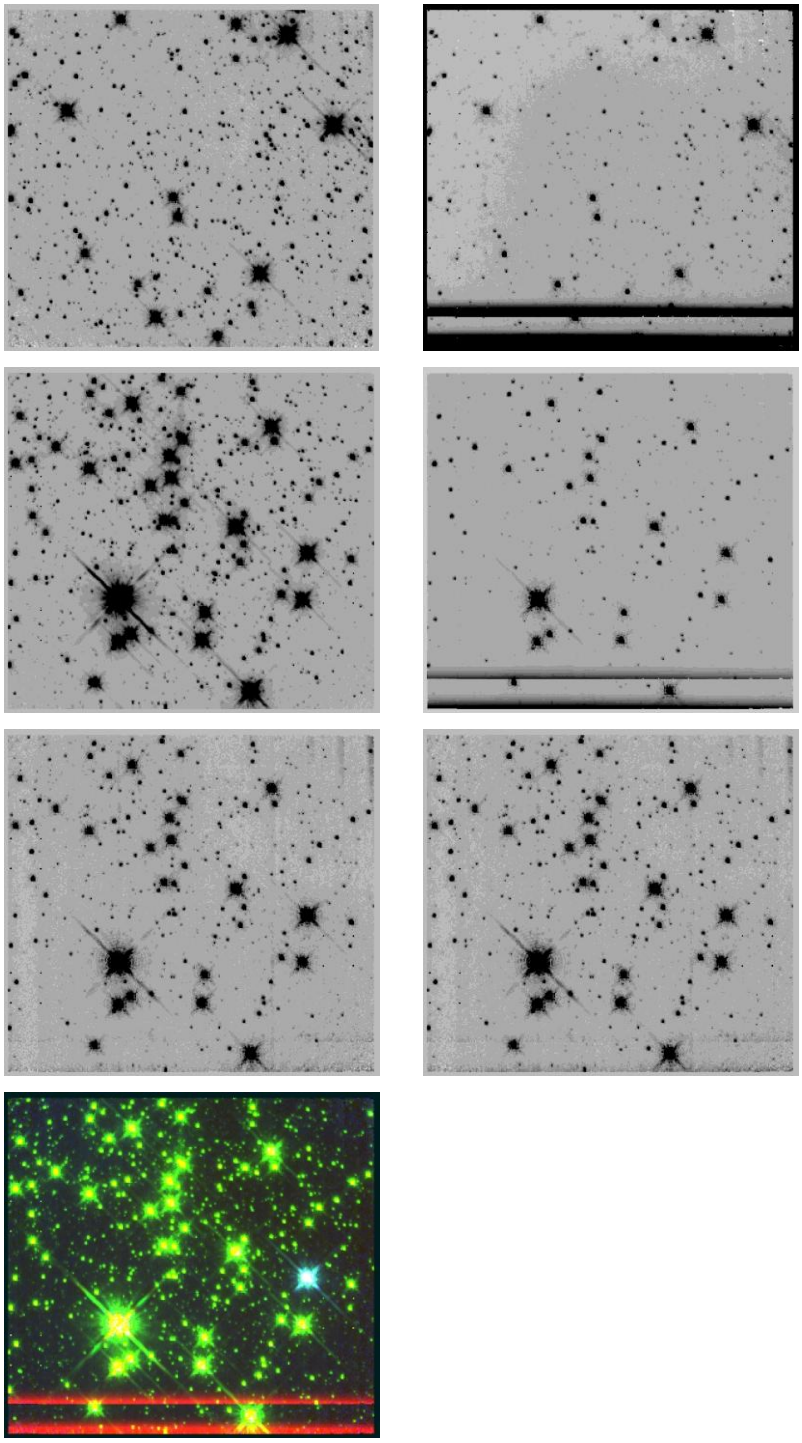

Figure 113 Danks 2, panels are the same as Figure 103

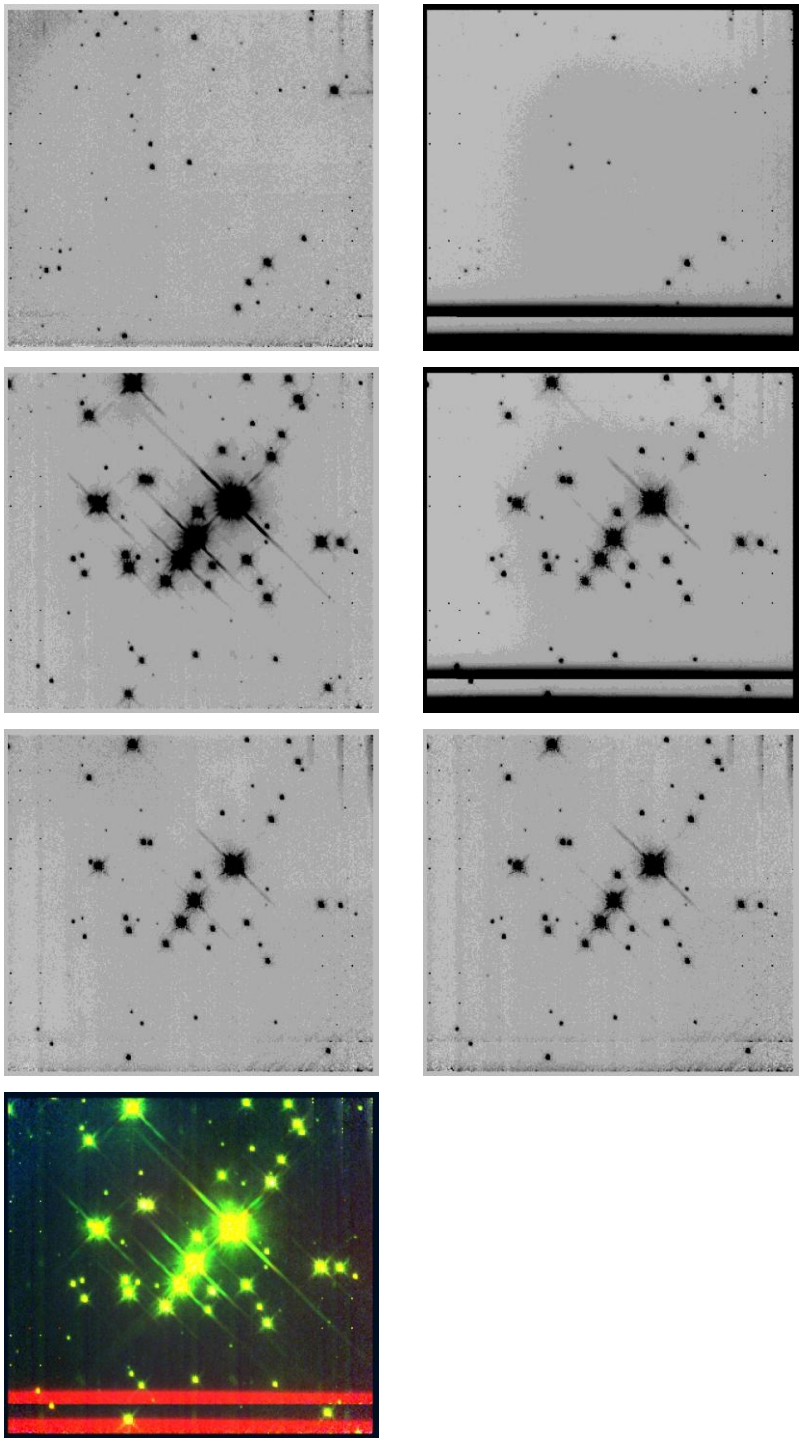

Figure 114 [BDS2003] 52, panels are the same as Figure 103

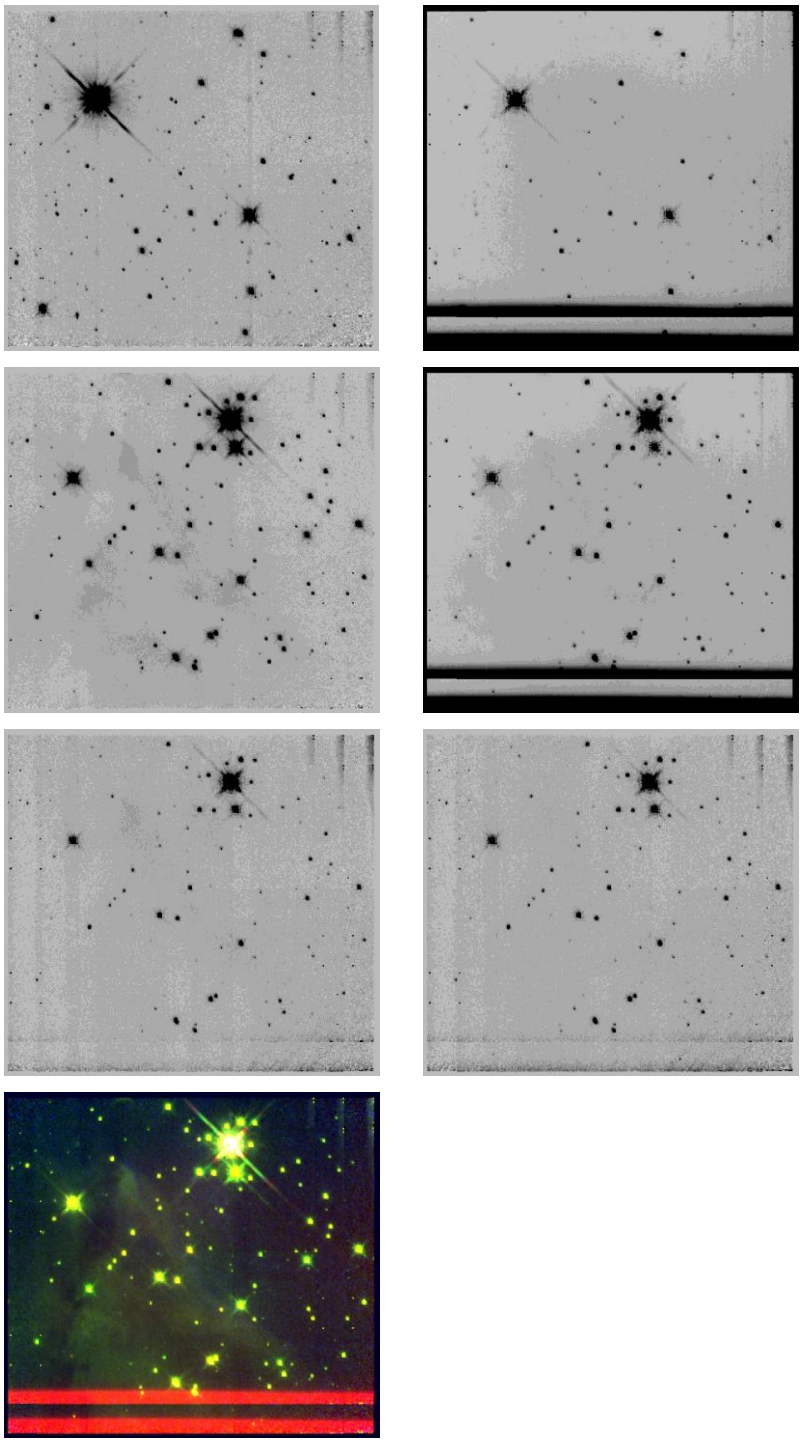

Figure 115 [DB2001] Cl 9, panels are the same as Figure 103

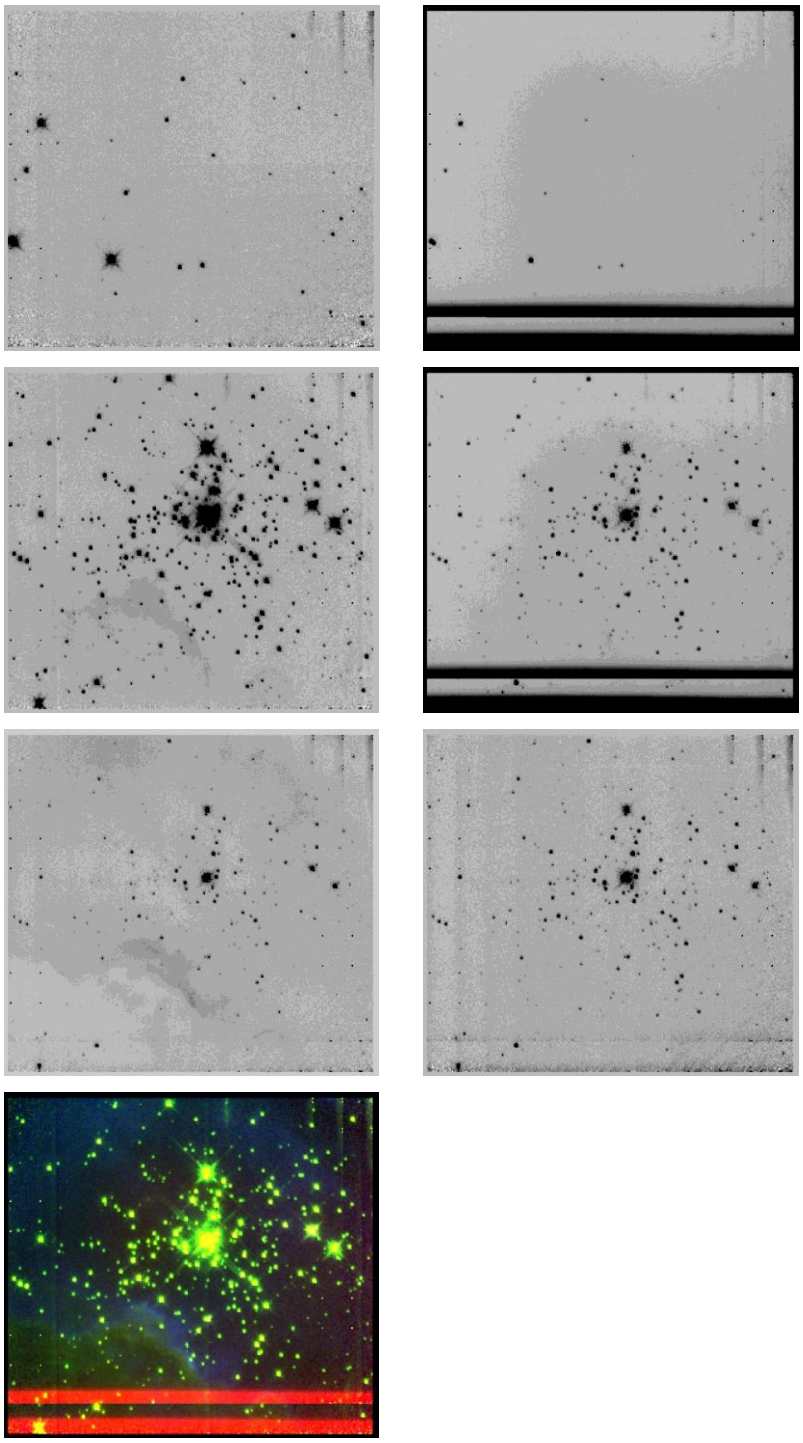

Figure 116 [BDS2003] 66, panels are the same as Figure 103

11. Appendix B: WISE Images

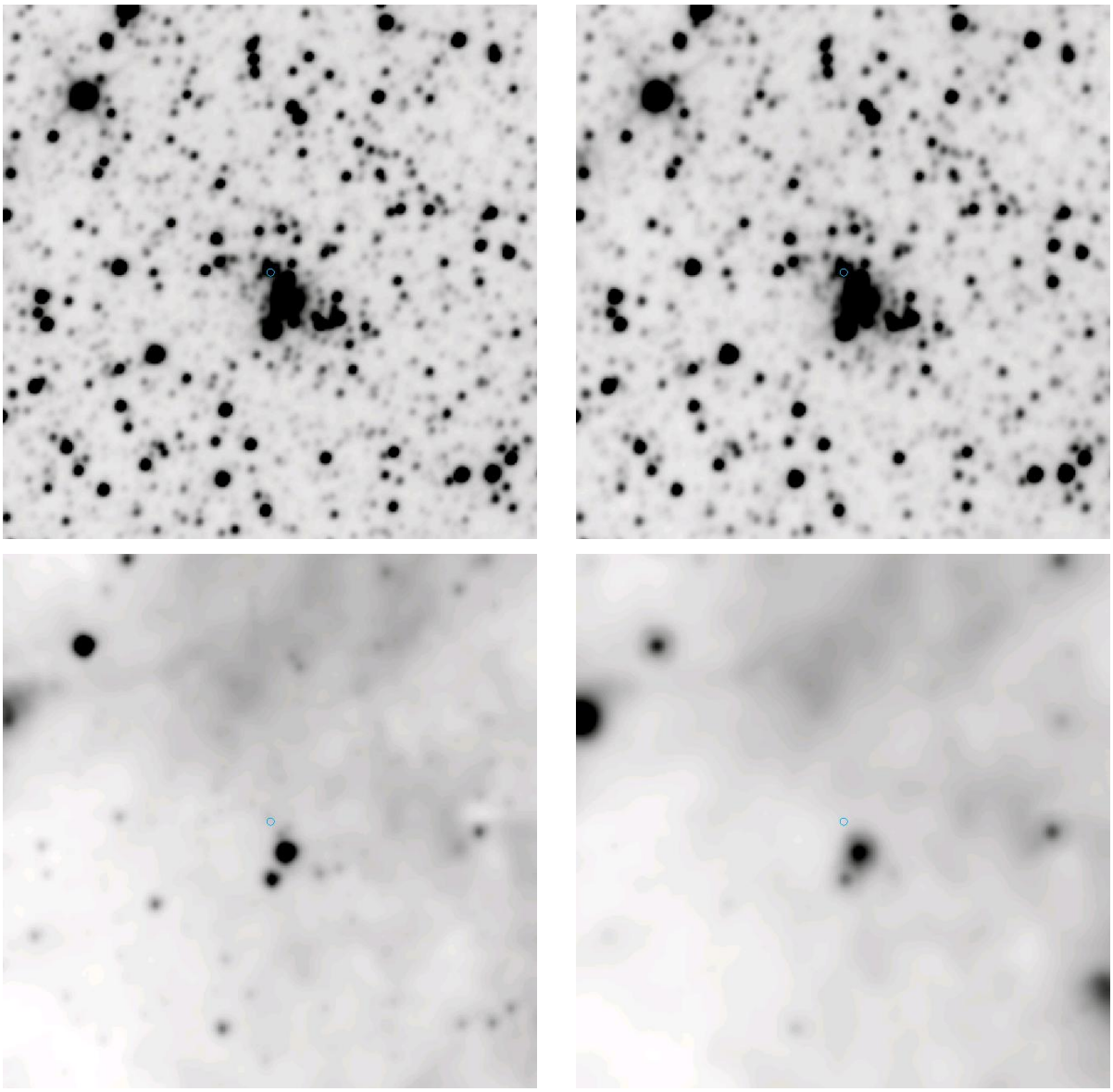

Figure 117 WISE observations of Mercer 20. Top left: band 1; Top right: band 2; bottom left: band 3; bottom right: band 4. The cluster center is indicated by a small blue circle.

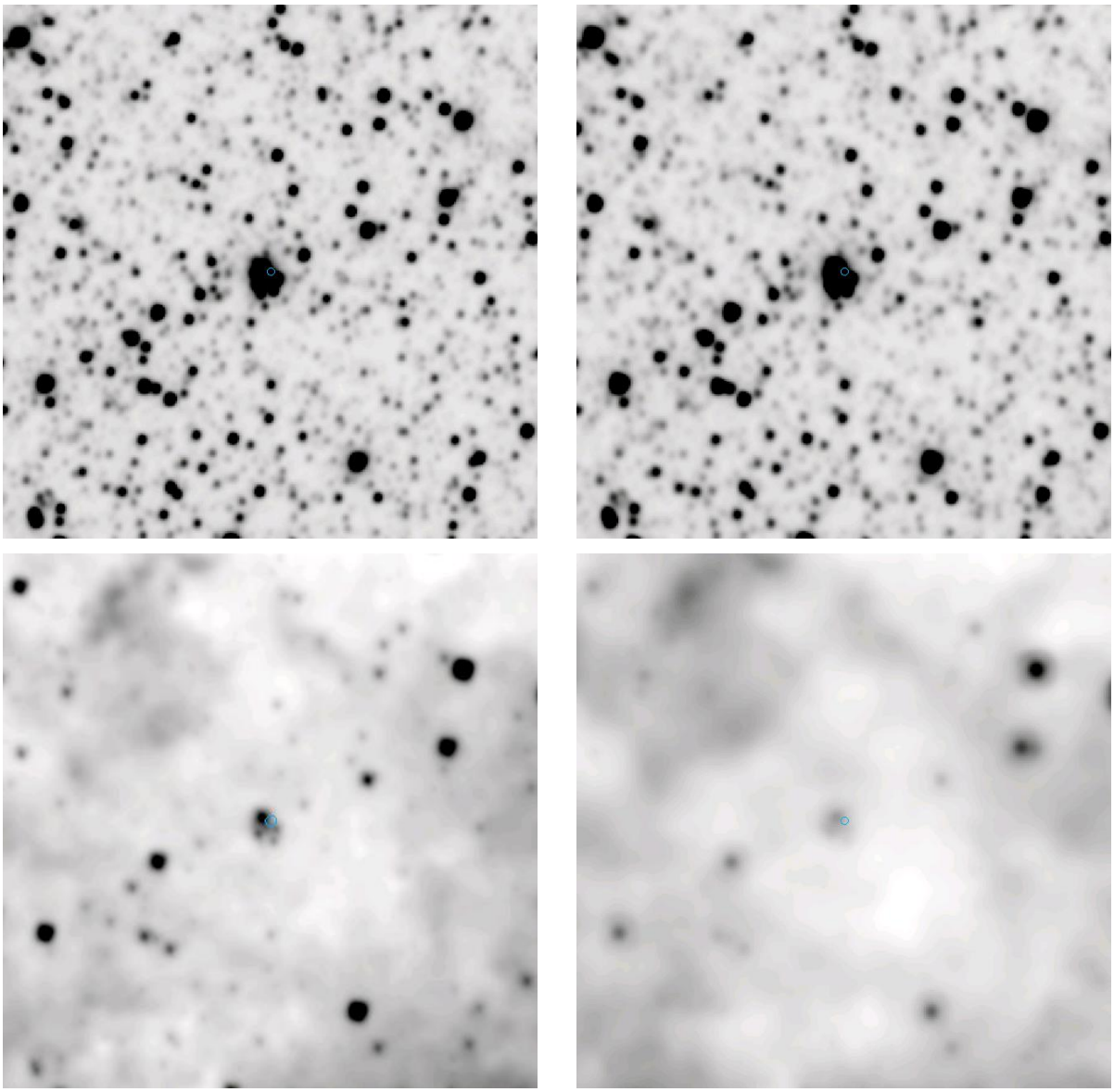

Figure 118 WISE observations of Mercer 70. Top left: band 1; Top right: band 2; bottom left: band 3; bottom right: band 4. The cluster center is indicated by a small blue circle.

12. Appendix C: IRTF/SpeX Spectra of FS CMa B[e] Stars

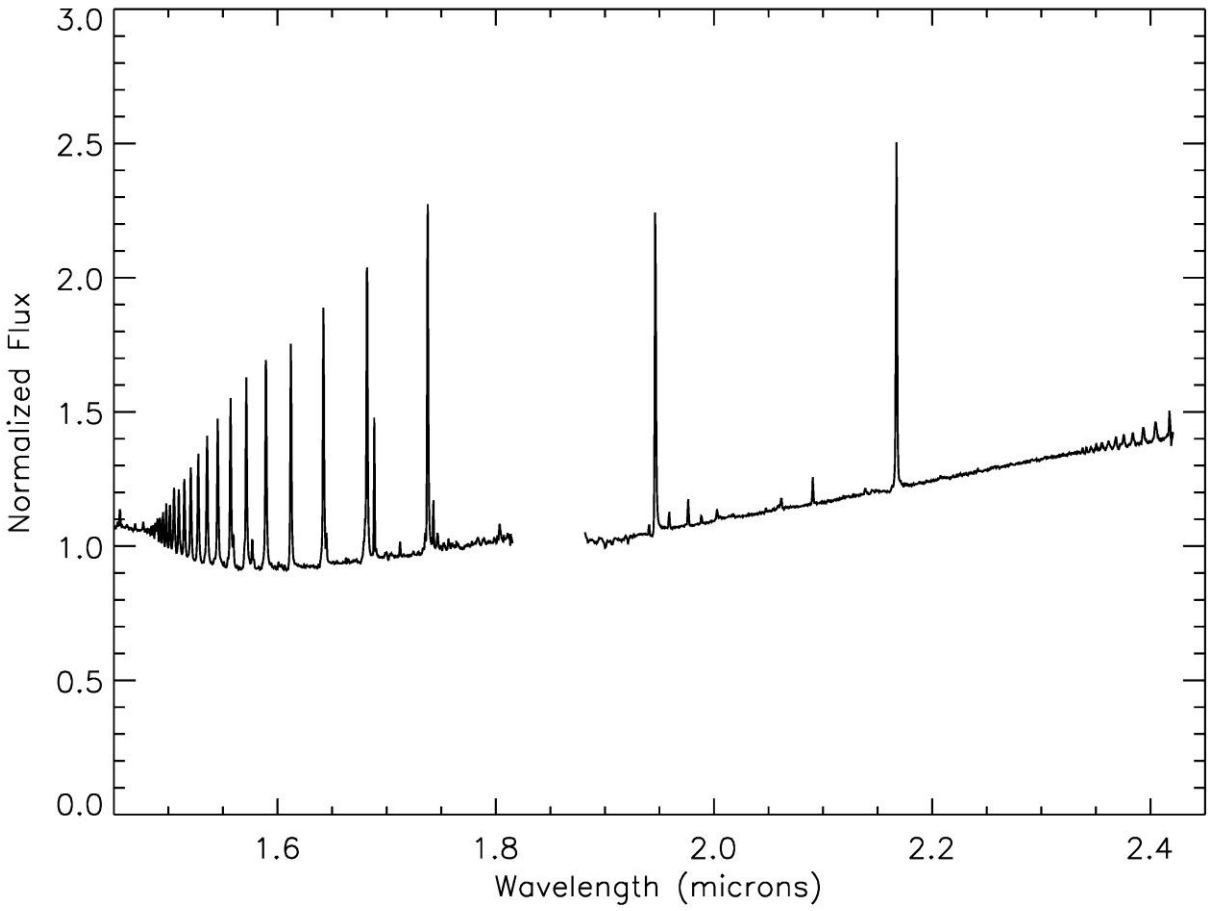

Figure 119 Spectrum of FS CMa

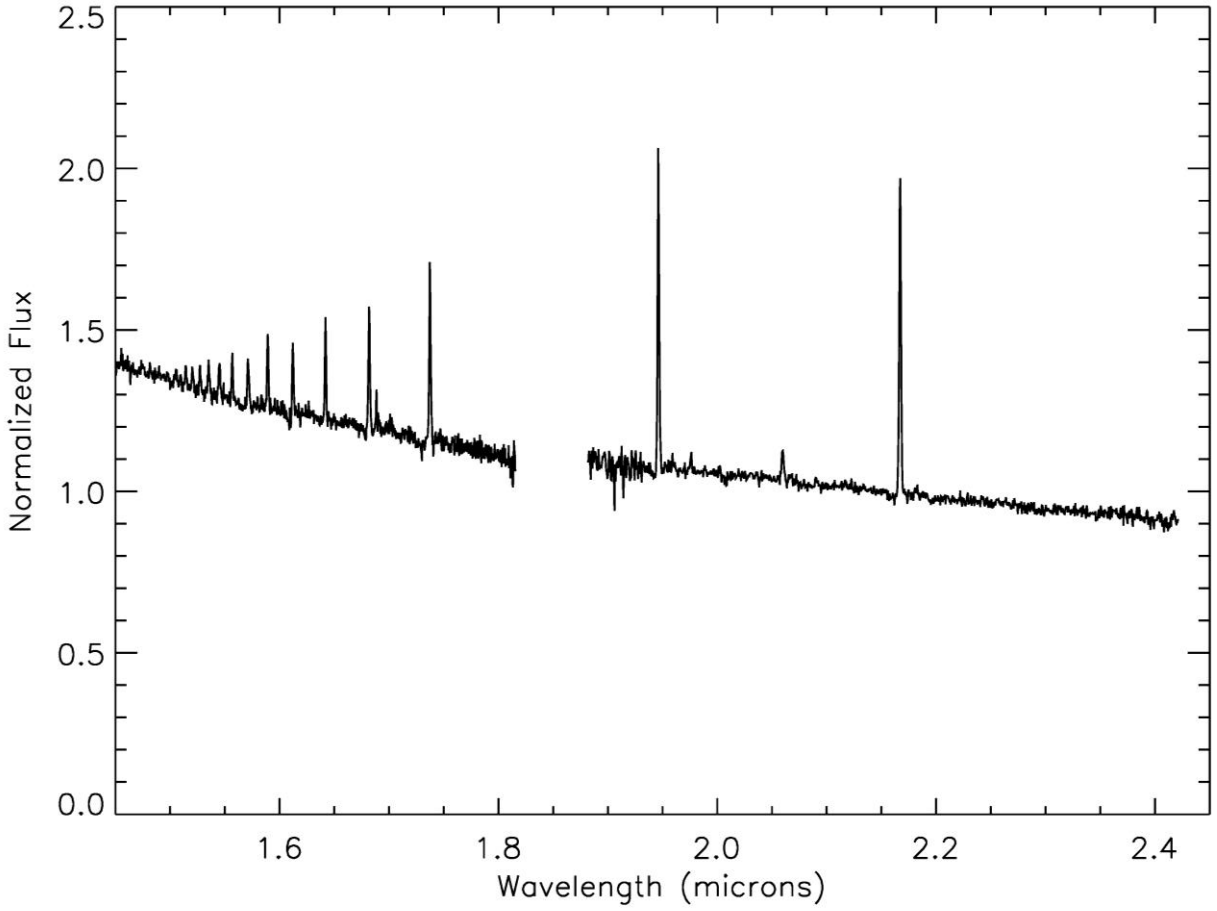

Figure 120 Spectrum of IRAS06071+2925